Tool Wear and Weld Quality Characterization in Friction Stir Welding of Similar and Dissimilar Steel

A thesis submitted in partial fulfillment of the requirement for the degree of

Doctor of Philosophy

By

Avinish Tiwari

DEPARTMENT OF MECHANICAL ENGINEERING
INDIAN INSTITUTE OF TECHNOLOGY GUWAHATI
GUWAHATI-781039, ASSAM, INDIA
JANUARY-2021

Dedicated

To

My Family

Department of Mechanical Engineering
Indian Institute of Technology Guwahati
Guwahati-781039, Assam

DECLARATION

I hereby certify that the information presented in the dissertation "**Tool Wear and Weld Quality Characterization in Friction Stir Welding of Similar and Dissimilar Steel**" submitted to "**Indian Institute of Technology**" for the degree of "**Doctor of Philosophy**" is a work of pure authenticity carried out under the supervision of **Prof. Pankaj Biswas**. To the best of my knowledge, the content of this thesis work is free from any act of plagiarism. Any part of this work has not earlier been submitted for the award of any degree, diploma, associateship, fellowship, or it's equivalent to any institution.

Avinish Tiwari
Roll No. 156103019
Department of Mechanical Engineering
Indian Institute of Technology Guwahati
Assam-781039, INDIA

Department of Mechanical Engineering
Indian Institute of Technology Guwahati
Guwahati-781039, Assam

CERTIFICATE

It is certified that the work presented in the thesis entitled ‘**Tool Wear and Weld Quality Characterization in Friction Stir Welding of Similar and Dissimilar Steel”** submitted by **Mr. Avinish Tiwari**, a student in the Mechanical Engineering Department, Indian Institute of Technology Guwahati, Guwahati, Assam, India for the award of the degree of Doctor of Philosophy has been carried out under my supervision. This work has not been submitted previously elsewhere for the award of any other degree or diploma.

Prof. Pankaj Biswas
Department of Mechanical Engineering
Indian Institute of Technology Guwahati
Guwahati, Assam-781039, INDIA

ACKNOWLEDGEMENT

Firstly, I would like to express my deep appreciation and sincere gratitude to my thesis supervisor, Prof. Pankaj Biswas for his guidance and support, critical review of my work, and most importantly, for his great patience and enthusiasm. I honestly devote this thesis to him for providing me irreplaceable inspiration and for being more than a supervisor.

I want to extend my gratitude to the present and the former HOD mechanical engineering, IITG, Guwahati for extending various facilities in the mechanical department during the tenure of my doctoral program. I am also indebted to my doctoral committee members Prof. P. S. Robi, Prof. S. Senthilvelan and Prof. S. K. Majumder for their insightful comments and valuable suggestions. I would also like to express my thanks to Prof. Sachin D. Kore of the Department of Mechanical Sciences, IIT Goa for helping me in various possible ways. I would also like to express my sincere thanks to Prof. U. S. Dixit for his valuable comments and suggestions during my research work.

My special thanks to Mr. N. K. Das, assistant workshop superintendent (AWS) for helping me in various ways possible ways during experimentation work. I also wish to express my sincere thanks to Mr. S. Sarma, Mr. S. Ahmed, Mr. J. Basumatary, Mr. N. Borah, Mr. D. Chetri, Mr. N. Saikia, Mr. M. Sarma, Mr. B. Chandan, Mr. U. Gohain, and Mr. M. C. Medhi for their help and support in conducting the experiments.

I am thankful to the senior researchers of college A. K. Rajak, P. Singh, R. Kumar, K. K. Gajrani who helped me get started with my research work. I also extend my gratitude to my lab mates Siabal, Pardeep, Saurav, Sagar, Deepak, Lakshmi, and Sanjay, for keeping the workplace joyful and lively. In last my special thanks to my dear friends Ajit, Sudip, Saptarshi, Asutosh, Raktim, Bikash, Shranish and Saurav Datta, who maintained the research life cheerful. I also extend my sincere thanks to the Naval Research Board (NRB), DRDO India for financial support.

Lastly, I am grateful for the unconditional love, support, and constant encouragement of my family members.

Avinish Tiwari

Indian Institute of Technology Guwahati

ABSTRACT

Friction stir welding of steel is more challenging that demands the development, modification, and improvement of the existing FSW techniques and tool technology. Unlike conventional fusion welding of steel, FSW of steel can eradicate the problems regarding melting and solidification i.e. porosity, blowholes, hot cracks, rapid grain growth, heat-affected zone softening, and segregation of elements, and difficulty in selection of filler material. FSW of steel is investigated by using advanced tool materials like Polycrystalline cubic boron nitride (PCBN), tungsten rhenium (W-Re), and tungsten cobalt (W-Co) alloys. Regardless of the high cost of these tool materials, another problem is the limited tool life due to high plunging force and high temperatures involved during the process. Moreover, improper parameter selection results in insufficient consolidation of plasticized material and consequently generate volumetric defects.

The present study explored the FSW process of low carbon steels (UNS G10060, DH36) and dissimilar steels (UNS G10080 and UNS S30400) using tungsten carbide tool material. It is found that the welded joints and tool life are significantly affected by the alloying compositions of steel and process operating conditions. There are various process parameters like rotational speed, traverse speed, plunge depth, tool tilt angle, which controls the weld quality. These process parameters are not considerably explored in literature, and the knowledge available on this is contradictory. From the experimental investigation of UNS G10060 steel welded samples, it is found that welded structures resulted in refined grain microstructure, high strength, and high microhardness of the weld joint. The ferrite grains in thermomechanically affected zone (TMAZ) are finest grains that developed due to the grain refinement and sufficient plastic deformation to promote dynamically recrystallized microstructure. The average grain size in thermomechanically affected zone is significantly less than the stir zone (SZ).

Due to FSW's asymmetry, FSW of dissimilar steels was explored with an additional parameter i.e., tool offset towards the softer material placed on the retreating side. The key factors that determine the joint quality in the FSW of dissimilar steel are mainly (i) the mechanical effects (i.e., interlocking at macroscale and diffusion at microscale) caused by tool and (ii) the thermal effects (i.e., metallurgical bonding caused by frictional heat and plastic deformation). During FSW of dissimilar steel, complex and chaotic material flow is visualized

due to differences in the real elemental composition during FSW of dissimilar steels. Tool particles are entrapped in the weld zone, more specifically in the SZ, due to high peak temperature.

Furthermore, a coupled heat and material flow model is investigated for FSW of DH36 steel by incorporating non-Newtonian viscosity and heat flux. The asymmetric and skewed temperature distribution is observed at the advancing trailing side, which is reduced at the high traverse heat input ratio (THIR). It is found that temperature, strain rate, and material flow are maximum on the shoulder-workpiece interface, decreasing through the plate thickness. Material flow mainly occurs at the retreating side, while mixing of material is observed at the advancing side.

During FSW of steel, high temperature and stresses resulted in different types of tool wear and degradation mechanism for Tool A (WC-6wt. % Co) and Tool B (WC-10wt. % Co). It is seen that tool A underwent catastrophic failure, whereas in tool B, progressive wear is observed. Different degradation mechanisms, such as oxidation adhesion, abrasion, crack initiation, and diffusion are observed. At the high rotational speeds, a decreased strength of the binder phase due to the high temperatures may have contributed to severe tool wear through grain pull-outs. During the FSW of DH36 steel, preheating has significantly softened the material ahead of the tool. The workpiece's preheating reduced the tool wear by 58% and plunge force by 31.6% compared to the conventional FSW process.

Key words: *Friction stir welding, Tungsten carbide tool, steel alloys, similar welding, dissimilar welding, computational fluid dynamic modeling*

Contents

DECLARATION......v

CERTIFICATE......vii

ACKNOWLEDGEMENT......ix

ABSTRACT......xi

NOMENCLATURE......xxi

LIST OF FIGURES......xxvii

LIST OF TABLES......xxxiv

Chapter 1 1

1 INTRODUCTION 1

1.1 BACKGROUND AND MOTIVATION 1

1.2 LIMITATIONS OF FSW PROCESS 5

1.3 RESEARCH OBJECTIVES 5

1.4 CONTRIBUTION TO THE THESIS 6

1.5 OUTLINE OF THE THESIS 7

Chapter 2 9

2 LITERATURE REVIEW 9

2.1 INTRODUCTION 9

2.2 FRICTION STIR WELDING OF STEEL......9

2.3 FRICTION STIR WELDING OF DISSIMILAR STEELS 14

2.4 TOOL MATERIALS 15

2.5 AUXILIARY ENERGY ASSISTED FRICTION STIR WELDING TECHNIQUES......22

  2.5.1 Laser-assisted FSW......23

  2.5.2 Ultrasonic assisted FSW 24

2.5.3 Induction assisted FSW....25

2.5.4 Arc assisted FSW....25

2.6 NUMERICAL MODELING IN FRICTION STIR WELDING....26

2.7 MAJOR RESEARCH GAPS FROM THE LITERATURE REVIEW....28

Chapter 3....31

3 METHODOLOGY....31

3.1 INTRODUCTION....31

3.2 EXPERIMENTAL DETAILS....31

3.2.1 Material selection....31

3.2.2 Experimental setup....32

3.3 NUMERICAL MODELLING OF FSW PROCESS....34

3.3.1 Model description....35

3.3.2 The governing equations....36

3.3.3 Material properties and material model....37

3.3.4 Meshing....39

3.3.5 Boundary conditions....40

3.4 SOLVER AND DISCRETIZATION SCHEME....44

3.5 SUMMARY....44

Chapter 4....45

4 FSW OF LOW CARBON STEEL PLATES WITH TUNGSTEN CARBIDE TOOL....45

4.1 INTRODUCTION....45

4.2 MATERIALS AND METHODOLOGY....45

4.3 RESULTS AND DISCUSSION....48

4.3.1 Surface assessment....49

4.3.2 Microstructural characterization....50

4.3.3 Tensile properties 55

4.3.4 Micro-hardness 56

4.3.5 Tool wear characterization...57

4.4 SUMMARY 58

Chapter 5..79

5 FRICTION STIR WELDING OF DISSIMILAR STEEL 61

5.1 INTRODUCTION 61

5.2 MATERIALS AND METHODOLOGY 61

5.3 RESULTS AND DISCUSSION 62

5.3.1 Metallography analysis 62

5.3.2 Mechanical properties 68

5.3.3 Tool wear characterization..73

5.4 SUMMARY 76

Chapter 6 79

6 CFD MODELLING FOR PREDICTION OF THERMAL HISTORY AND MATERIAL FLOW DURING FSW OF DH36 STEEL 79

6.1 INTRODUCTION 79

6.2 MATERIALS AND METHODOLOGY 79

6.3 RESULTS AND DISCUSSION 80

6.3.1 Temperature contour 80

6.3.2 Fluid flow results 85

6.4 SUMMARY 93

Chapter 7 95

7 FRICTION STIR WELDING OF DH36 STEEL USING TWO DIFFERENT TOOL COMPOSITIONS 95

7.1 INTRODUCTION 95

7.2 MATERIALS AND METHODOLOGY 95

7.3 RESULTS AND DISCUSSION 97

7.3.1 Characterization of degradation mechanisms in tool material A (WC-6 **wt.** %Co) 97

7.3.2 Characterization of degradation mechanisms in tool material B (WC-10 **wt.** %Co)..101

7.4 SUMMARY 109

Chapter 8 111

8 EXPERIMENTAL INVESTIGATION OF PLASMA ASSISTED FRICTION STIR WELDING OF DH36 STEEL 111

8.1 INTRODUCTION 111

8.2 MATERIALS AND METHODOLOGY 111

8.2.1 Experimental setup...112

8.2.2 Transient temperature and force measurements 114

8.2.3 Metallographic and mechanical properties characterization...........................114

8.3 RESULTS AND DISCUSSION 115

8.3.1 Surface appearance and force evaluation...115

8.3.2 Weld thermal history and the weld microstructures 117

8.3.3 Microhardness distribution 123

8.3.4 Tensile properties...124

8.3.5 Tool performance evaluation..126

8.4 SUMMARY 128

Chapter 9 131

9 CONCLUSIONS AND THE FUTURE SCOPE OF THE WORK 131

9.1 CONCLUSIONS OF THE PRESENT WORK 131

9.2 SCOPE OF FUTURE WORK 133

Appendix A 155

A.1 FSW machine specifications 155

A.2 Machine’s specifications used for characterization 157

Appendix B 158

B.1 List of parameters used in the simulation 158

B.2 An analytical model for the heat generation in the tapered pin profile FSW tool 159

NOMENCLATURE

❖ Notations

$\boldsymbol{Q_{ss}}$	Heat generation from shoulder surface (W)
$\boldsymbol{Q_{pb}}$	Heat generation from pin bottom surface (W)
$\boldsymbol{Q_{pt}}$	Heat generation from pin tapered surface (W)
$\boldsymbol{Q_{sl}}$	Heat generation by sliding condition (W)
$\boldsymbol{Q_{st}}$	Heat generation by sticking condition (W)
$\boldsymbol{Q_{T}}$	Total heat generation at tool work interface (W)
$\boldsymbol{\dot{Q}_{1}}$	Heat generation by frictional heating (W)
$\boldsymbol{\dot{Q}_{2}}$	Heat generation by viscous dissipation (W)
$\boldsymbol{q_{ss}}$	Heat flux at the shoulder surface ($\mathrm{W/m^2}$)
$\boldsymbol{q_{pb}}$	Heat flux at the pin bottom surface ($\mathrm{W/m^2}$)
$\boldsymbol{q_{tp}}$	Heat flux at the pin tapered surface ($\mathrm{W/m^2}$)
$\boldsymbol{q_{T}}$	Total heat flux at the tool interface ($\mathrm{W/m^2}$)
$\boldsymbol{R_{1}}$	Shoulder radius (mm)
$\boldsymbol{R_{2}}$	Pin base radius at shoulder (mm)
$\boldsymbol{R_{3}}$	Pin tip radius or pin radius at free end (mm)
$\boldsymbol{H}$	Pin Height (mm)
$\boldsymbol{h}$	Variable pin height (mm)
$\boldsymbol{\delta h}$	Infinitesimal pin height at a distance of h (mm)
$\boldsymbol{h_{ts}}$	Heat transfer coefficient at the top surface ($\mathrm{W/m^2K}$)
$\boldsymbol{h_{sw}}$	Heat transfer coefficient at the side walls ($\mathrm{W/m^2K}$)
$\boldsymbol{h_{bp}}$	Heat transfer coefficient at the backing plate ($\mathrm{W/m^2K}$)

$\boldsymbol{l}$	Length of the plate (mm)
$\boldsymbol{w}$	Width of the plate (mm)
$\boldsymbol{t}$	Plate thickness (mm)
$\boldsymbol{C_{pwp}}$	Workpiece specific heat at constant pressure $(\mathrm{J/kg-K})$
$\boldsymbol{K_{wp}}$	Workpiece thermal conductivity $(\mathrm{W/m-K})$
$\boldsymbol{C_{ptl}}$	Tool specific heat at constant pressure $(\mathrm{J/kg-K})$
$\boldsymbol{K_{tl}}$	Tool thermal conductivity $(\mathrm{W/m-K})$
$\boldsymbol{T}$	Temperature (K)
$\boldsymbol{T_{amb}}$	Ambient temperature (K)
$\boldsymbol{T_{pk}}$	Peak temperature (K)
$\boldsymbol{T_{m}}$	Melting point of DH36 steel (K)
$\boldsymbol{R_{g}}$	Universal gas constant $(\mathrm{J/kg-mol-K})$
$\boldsymbol{Z_{n}}$	Zener- Holloman parameter (s^{-1})
$\boldsymbol{Q_{e}}$	Activation energy $(\mathrm{kJ/mol})$
$\boldsymbol{A_{e}}$	Material constant (s^{-1})
$\boldsymbol{n_{mat}}$	Material constant
$\boldsymbol{f_{m}}$	Arbitrary constant indicates extent of atomic mixing
$\boldsymbol{P}$	Plunging pressure (MPa)
$\boldsymbol{P_{1}}$	Plunging pressure at tapered pin surface (MPa)
$\boldsymbol{F}$	Frictional force (N)
$\boldsymbol{N}$	Normal force (N)
$\boldsymbol{F_{F}}$	Z force in conventional FSW (N)
$\boldsymbol{F_{P}}$	Z force in plasma assisted FSW (N)

A_1	Critical temperature at which austenite begins to form (K)
A_3	Transformation of ferrite to austenite completes (K)
V_v	Voltage (V)
I_a	Current (A)
x	x- coordinate (mm)
y	y- coordinate (mm)
z	z- coordinate (mm)
u	x- velocity (mm/s)
v	y- velocity (mm/s)
w	z- velocity (mm/s)
u_S	X velocity of material at shoulder workpiece interface (mm/s)
v_S	Y velocity of material at shoulder workpiece interface (mm/s)
V_θ	Local velocity of a point on tool with the origin fixed at the tool axis (mm/s)
U	Welding speed (mm/s)

❖ Greek Letters

δ	Extent of slip
δ_o	Initial value of slip
ρ	Density (kg/m^3)
μ_{fluid}	Fluid viscosity (Pa − s)
$\dot{\epsilon}$	Effective strain rate (s^{-1})
τ_{yield}	Yield shear stress (MPa)
σ_{yield}	Yield strength of workpiece based on von-Mises yield

	criteria (MPa)
σ_{flow}	Flow stress of material (MPa)
μ	Coefficient of friction
ω	Rotational speed (rad/s)
ω_o	Local rotational speed (rad/s)
σ_b	Stefan Boltzmann constant (W/m^2K^4)
φ	Traverse heat input ratio
λ	Fraction of total generated heat transferred to the workpiece
θ	Arbitrary rotation angle (degree)
α_l	Pin cone angle (degree)
α_{mat}	Material constant $(MPa)^{-1}$
α_c	Constant
α_a	Acicular ferrite
α_w	Widmansttaen ferrite
α_p	Polygonal ferrite
α_f	Ferrite
α_{fc}	Perlite
γ_a	Austenite
η_{mech}	Fraction of mechanical energy due to sticking friction converted to heat
η_p	Efficiency of plasma preheating source
β	Facing angle of diamond indentor
ε_{se}	Surface emissivity of material
ψ	Viscous dissipation

∇	Del operator

❖ Non-Dimensional Number

- Traverse Heat Input Ratio (THIR)

❖ Acronyms and Abbreviations

CFD	Computational fluid dynamics
FDM	Finite difference method
FVM	Finite volume method
FEM	Finite element method
ALE	Arbitrary Lagrangian-Eulerian
CEL	Coupled Eulerian and Lagrangian
FSW	Friction stir welding
HFSW	Hybrid friction stir welding
FSSW	Friction stir spot welding
LFSW	Laser-assisted friction stir welding
PFSW	Plasma assisted friction stir welding
UFSW	Ultrasonic assisted friction stir welding
IFSW	Induction assisted friction stir welding
TFSW	TIG assisted friction stir welding
FSP	Friction stir processing
TMCP	Thermo-mechanical control processes
A. S.	Advancing side
R. S.	Retreating side
SZ	Stir zone
WN	Weld nugget

TMAZ	Thermo-mechanically affected zone
HAZ	Heat affected zone
DRX	Dynamic recrystallization
CDRX	Continuous dynamic recrystallization
DDRX	Discontinuous dynamic recrystallization
Tool B	Tungsten carbide with 10 weight percent cobalt $(\mathrm{WC} - 10\ \mathrm{wt.\%\ Co})$
Tool A	Tungsten carbide with 6 weight percent cobalt $(\mathrm{WC} - 6\ \mathrm{wt.\%\ Co})$
PCBN	Polycrystalline cubic boron nitride
HSLA	High strength low alloy steel
HSS	High strength structural plates
BM	Base material
$\mathbf{HV_{0.5}}$	Vickers micro hardness at 5N load
UTM	Universal tensile testing machine
YS	Yield strength
UTS	Ultimate tensile strength
EDS	Energy dispersive spectroscopy
FESEM	Field emission scanning electron microscope
XRD	X-Ray diffractometer
TS	Traverse speed
RPM	Revolution per minute
PD	Plunge depth
TTA	Tool tilt angle
ASTM	American society for materials and testing

LIST OF FIGURES

Figure 1.1 (a) Illustration of FSW process (b) metallurgical process during FSW (c) schematic cross-section of a typical FSW weld showing based metal with three distinct weld zones: (A) base metal, (B) heat–affected, (C) thermo-mechanically affected and (D) stirred (nugget) zone 2

Figure 2.12 (a) Laser assisted FSW experimental setup (Casalino et al. 2012) (b) ultrasonic assisted FSW experimental setup (Shi et al. 2015) (c) induction assisted FSW experimental set-up (Álvarez et al. 2014) (d) arc assisted FSW process (Constantin et al. 2018) 22

Figure 3.1 (a) Illustration of FSW machine, (b) experimental setup used in the present study, (c) fixture developed to perform experiments, (d) tool dimensions, and (e) tool holder dimensions 33

Figure 3.2 Boundary conditions of the FSW process used in present computational model .. 35

Figure 3.3 Meshed geometry of 3D model 39

Figure 3.4 Fractional slip (δ) variation with the tool radii, and (b) variation of friction coefficient (μ) with tool radial distance 42

Figure 3.5 Velocity of a point on tool shoulder 43

Figure 4.1 (a) Shows the schematic diagram of the FSW process, and (b) FSW tool mounted on the tool holder 46

Figure 4.2 (a) Transient thermal history at different locations, and (b) force curve during the plunge, dwell stage, and traverse stage of welding. 48

Figure 4.3 (a) Visual appearance of the welded joints, and (b) macrograph of the transverse cross-section of the welded samples 49

Figure 4.4 Microstructure of low carbon steel indicating ferrite and perlite structures with ferrite as major content: (a) optical microstructure; and (b) FESEM microstructure indicating perlite structure as alternative layers of ferrite and cementite 50

Figure 4.5 Microstructures obtained by optical microscope: (a) weld nugget indicating concentric ring structures also known as onion rings, (b) banded structures beneath the tool shoulder indicating intense plastic deformation at high temperatures; and (c) defect prone region in the AS-TMAZ of the weld zone 50

Figure 4.6 (a) Optical microstructure of the base material and weld produced at 600 rpm and 132 mm/min traverse at different locations i.e. SZ, AS-TMAZ, RS-TMAZ, AS-HAZ, HAZ-RS, and (b) grain size variation in WNZ, TMAZ-AS and TMAZ-RS 52

Figure 4.7 Microstructure at the bottom region in the advancing: (a) optical image indicating dark bands similar to those obtained at the top surface, and (b) FESEM image indicating dispersed perlite 53

Figure 4.8 (a) SEM micrograph of base material; (b) SEM micrograph of the weld stir zone at 600 rpm and 90 mm/min (The pearlite distribution and tungsten (W) particles in the ferrite rich matrix can be observed FESEM micrograph), (c) EDS analysis indicating the tungsten particles in the weld nugget of the weld 1, and (d) XRD pattern of SZ indicating similar peaks of ferrite before and after welding condition 54

Figure 4.9 (a) Tensile properties of weld joints; (b) tensile specimens before fracture; (c) fracture tensile specimens, (d) tensile properties variation with the rotational speed at a traverse speed of 132 mm/min, and (e) tensile properties variation with traverse speed at a rotational speed of 600 rpm...55

Figure 4.10 FESEM image of the fractured tensile surface of weld 5: (a) micro cracks were observed at low magnification, and (b) high magnification showing a cluster of fine dimples along with coarse dimples...56

Figure 4.11 (a) Schematic representation of micro-hardness evaluation points along ND-TD direction, microhardness contour of (b) weld 1; and (c) weld 2 (Schematic is drawn not to scale) 56

Figure 4.12 Microstructure of the WC-10 % Co tool: (a) before welding; and (b) after welding 57

Figure 4.13 Surface roughness values: (a) tool pin surface, and (b) tool shoulder surface 58

Figure 5.1 Schematic representation of: (a) dissimilar FSW butt joints, (b) tool offset toward the softer material i.e. UNS G10080 steel, (c) FSW of SS304 and UNS G10080 in progress (Schematic is drawn not to scale) 62

Figure 5.2 Microstructural view of weld cross-section: (a) cross-sectional macrostructure, (b) base material, (c) TMAZ-MS showing substructures and grain refinement (d) HAZ-MS, (e) banded structure at the top surface of the weld, (f) vortex swirl, and (g) interface between MS and SS304 at the pin bottom 63

Figure 5.3 Weld micrograph: (a) FESEM micrograph at the bottom region, and (b) transition behavior of SS304 and MS in the deformed region 64

Figure 5.4 EDS analysis across the interface between the two alloys: (a) joint interface separating SS304 and mild steel, (b) EDS analysis, (c) swirl formation in the AS, and (d) EDS line spectrum indicating larger peaks of Ni and Cr in SS304 rich matrix 65

Figure 5.5 EDS analysis in the stir zone of the weld joint indicating tool debris in UNS S30400 rich regions 66

Figure 5.6 FESEM micrograph and EDS analysis of weld 4 at different locations in the weld zone (a-b) SZ, (c-d) weld interface region, and (e-f) hook region 67

Figure 5.7 Tool particles in the weld zone: (a) tool particle of 25 μm in the swirl region, and (b) at a distance from the interface near TMAZ on the advancing side, i.e., stainless steel 304 side 68

Figure 5.8 Microhardness mapping at the weld cross-section: (a) weld 1, (b) weld 2, (c) weld 3, and (d) weld 4 68

Figure 5.9 Tensile test results: (a) tensile strength and yield strength of welded specimens and base materials, (b) tensile specimens showing fracture location in the UNS G10080 steel base material, and (c) comparison of % elongation of weld joints with the base material 70

Figure 5.10 Fractured tensile specimen: (a) showing fracture location in the UNS G10080 steel base metal, (b) macro fracture appearance, (c) localized fracture morphology, and (d) presence of fine and coarse dimples at the fracture surface 70

Figure 5.11 Impact toughness of the welded joints and the base materials 71

Figure 5.12 Impact specimen of weld 4: (a) fractured impact specimen, (b) macro fracture surface appearance, (c) micrograph showing lower and upper fracture surface region, and (d) typical ductile dimples observed in the upper region indicated a mixed fracture mode 72

Figure 5.13 EDS analysis at the fractured surface of impact specimen 72

Figure 5.14 XRD spectrums of base materials and the weld joint (a) stir zone of the weld joint, (b) SS304, and (c) UNS G10080 73

Figure 5.15 Oxidation of the tool edge after performing the welds: (a) FESEM micrograph, (b-d) energy dispersive spectra at different locations showing tungsten and oxygen as major element 74

Figure 5.16 Tool wear characterization: (a) surface roughness at the tool shoulder, (b) surface roughness at the tool pin, (c) FESEM micrograph at the tool shoulder indicating scratches and Fe adhesion, (d) FESEM micrograph indication Fe adhesion and abrasion, and (e) EDS analysis reflecting higher peaks of Fe on tool shoulder surface 75

Figure 5.17 XRD phase analysis of tungsten tool before and after welding condition indicating the oxide phase $WO3$ 76

Figure 6.1 Temperature contour of the case 1 (i.e., rotational speed of 600 rpm and traverse speed of 60 mm/min) 81

Figure 6.2 (a) Temperature contour in the transverse direction (Y-axis) and longitudinal (X-axis), (b) thermal contour indicating temperature distribution at different locations, and (c) temperature profile along the leading trailing frame and AS-RS frame 82

Figure 6.3 Peak temperature variation with (a) coefficient of friction, and (b) mechanical efficiency........ 83

Figure 6.4 (a) Downward z force and temperature data recorded by non-contact infra-red (IR) camera, (b) peak temperature comparison for different welding conditions, (c) thermal contours, and (d) temperature distribution along Y axis for different welding parameters 84

Figure 6.5 (a) Dynamic viscosity variation in the AS-RS frame and leading-trailing edge, (b) comparison of dynamic viscosity in the AS and RS, and (c) strain rate variation at $z =$ 0.21 mm and $z = 2$ mm 86

Figure 6.6 shows the comparison of spatial distribution of dynamic viscosity at rotational speed $\omega = 600$ rpm and U= 1 mm/s at three different planes along thickness (a) z = 0.21 mm, (b) z = 1.8 mm, and (c) z = 3.61 mm........ 87

Figure 6.7 (a) Velocity contour variation of case 1, (b) velocity plot of case 1 , (c) case 4, and (d) case 5. 88

Figure 6.8 (a) Velocity vectors, (b) velocity vectors at the interface of tool and workpiece, (c) velocity vector in the AS-RS region for case 1 i.e. $\omega = 600$ rpm, and $V = 60\ \mathrm{mm/min}$ in YZ-plane 89

Figure 6.9 (a) Streamlines, and (b) pathlines for case 1 i.e. ω = 600 rpm and V = 60 mm/min 90

Figure 6.10 (a) Comparison of surface temperature at 2.5 mm from the tool shoulder edge (15 mm from the weld centerline, (b) temperature validation at 9 mm from centerline inside the channel, (c) temperature validation at 15 mm from weld centerline, and (d) temperature validation at 20 mm from weld centerline 91

Figure 6.11 (a) Welding of DH36 plates with tungsten carbide tool for case 1, (b) top surface appearance of welded plate, (c) bottom surface appearance ,(d) vickers microhardness profile at 500 gF along the transverse cross-section, (e) tensile properties of the welded specimen, and (f) fracture surface of tensile specimen indicating a cluster of fine dimples 92

Figure 6.12 Material flow by the action of tool pin and tool shoulder (a) cross section macrograph of welded specimen, (b) schematic diagram of material transportation, (c) material inflow at AS, (d) vortex swirl at SZ in the bottom region, (e) juncture point indicating the material mixing from the top region and bottom region, and (f) material outflow at the RS..93

Figure 7.1 Schematic representation: (a) tool designation, (b) monitoring of FSW process using non-contact IR camera, and (c) pin tip and shoulder cross-section for post-weld inspection (Schematic is drawn not to scale) 96

Figure 7.2 Characterization of tool A: (a) crack generation, (b) pores and cracks leading to intergranular fracture, (c) crack propagation towards the outer edge, and (d) chip formation and crack initiation at the tool edge 98

Figure 7.3 Micrograph of tool pin and EDS analysis 99

Figure 7.4 (a) Tool shoulder edge of tool A, (b) EDS analysis at the layer formation, (c) micrograph at the shoulder surface showing scratches and abrasion, and (d) EDS analysis at the shoulder contact surface...100

Figure 7.5 Weld joint characterization: (a) top surface appearances of the welded plates at different welding conditions, and (b) transient thermal history of the welding condition using non-contact infrared (IR) camera (The scan was made along the welding direction) 101

Figure 7.6 (a) Microstructure images of tool representing tungsten carbide and cobalt binder before welding and after welding, and (b) illustration of the oxidation behavior and swelling of W-Co alloys at elevated temperatures 102

Figure 7.7 Tool wear characterization at non-contact shoulder surface: (a) sub layer formation at non-contact surface due to massive oxidation at elevated temperature, (b) FESEM micrograph indicating different locations for EDS analysis, and (c–e) EDS analysis indicating W, O and Co elements with higher percentage of Co and O elements on the sublayer 103

Figure 7.8 (a) Fragmentation and adhesion phenomenon at the tool pin, and (b) indentation mark at tool shoulder after hardness measurement ($HRC150$) 104

Figure 7.9 Projected profile of tool pin..105

Figure 7.10 Tool wear characterization: (a) weight loss versus weld length, (b) surface roughness after each weld run at tool pin, and (c) surface roughness at tool shoulder surface after each weld run...106

Figure 7.11 Tool shoulder characterization: (a) surface roughness measurement, (b) FESEM micrograph showing abrasion and adhesion wear at the shoulder contact surface, and (c) EDS analysis indicating Fe adhesion on the shoulder contact surface...107

Figure 7.12 Tool pin characterization: (a) surface roughness measurement at tool pin surface, (b) FESEM micrograph indicating non uniform topology with circular grooves, and (c–e) EDS analysis indicating Fe adhesion on the tool pin...108

Figure 7.13 XRD patterns showing different phase's formation on the tool (a) XRD peaks indicating WC and Co peaks before welding, and (b) XRD peaks indicating different oxide and carbide phases after welding...109

Figure 8.1 Plasma assisted friction stir welding (PFSW) process: (a) illustration of preheating stages of PFSW process, and (b) plasma heat source layout ahead of the FSW tool 112

Figure 8.2 Schematic diagram of the thermocouple layout used to record transient thermal history during welding 114

Figure 8.3 (a) Weld top surface appearance at different welding conditions, and (b) the corresponding downward axial force during the welding...115

Figure 8.4 Micrograph appearance of weld joints at the top surface: (a) weld 1, (b) weld 2, (c) weld 3, and (d) weld 4...117

Figure 8.5 Thermal analysis: (a) effect of plasma preheating current, i.e., 13A, 15A, and 17A at a location of 5 mm from the weld line, (b) peak temperatures, and (c) weld cooling rate $T65$for different welding conditions 118

Figure 8.6. Microstructural comparison in the middle of the stir zone under PFSW and conventional FSW: (a) weld 1, (b) weld 2, (c) weld 3, and (d) weld 4 120

Figure 8.7 Comparison of optical and FESEM micrograph of FSW (i.e., weld 1) and PAFSW (i.e., weld 2): (a) schematic diagram for the heat-affected zone, (b) optical micrograph of intercritical HAZ indicating pearlite dissolution in HAZ region, (c) subcritical HAZ of weld 1 ($G *$: globular cementite), (d) FESEM micrograph of SCHAZ of weld 1,(e) ICHAZ of weld 2 (f) SCHAZ of weld 2, and (g) FESEM micrograph of SCHAZ of weld 2 122

Figure 8.8 Energy dispersive spectrum analysis showing the tungsten (W) percentage in the SZ: (a) weld 1, (b) weld 2, (c-e) elemental mapping indicating tool debris in the SZ, (f) spectrum for weld 3, and (g) spectrum for weld 4 123

Figure 8.9 Comparison of microstructure and Vickers microhardness maps: (a) weld 1, (b) weld 2, (c) weld 3, and (d) weld 4. 124

Figure 8.10 Tensile test results: (a) YS and UTS, (b) fracture location, (c) percentage elongation up to fracture point, and (d) FESEM images of fracture surfaces 125

Figure 8.11 Impact test results: (a) comparison on impact toughness of welded specimen with the base material, (b) fracture location of impact specimens, and (c) fracture surface of impact specimens 126

Figure 8.12 Macro characterization of tool: (a) comparison of weight loss, (b) FSW tool profiles (c) 3D surface and surface roughness (Ra) at shoulder for tool 1 (d) tool illustration showing shoulder contact edge and contact surface (e-h) FESEM and EDS analysis showing edge oxidation, and (h) EDS line scan reflecting Fe adhesion on the shoulder contact surface 127

LIST OF TABLES

Table 2.1 Summary of friction stir welded joint at different process conditions 11

Table 2.2 Summary of tool materials and key findings during FSW of steel alloys 18

Table 3.1 Chemical composition of UNS G10060, UNS G10080, stainless steel (UNS S30400), and DH36 steel (wt.%) 32

Table 3.2 Details of tungsten carbide tool materials used for FSW 33

Table 3.3 The peak temperature obtained for all three meshes 40

Table 4.1 Mechanical properties and chemical composition of low carbon steel 46

Table 4.2. Selection of lower and upper limits of traverse speed and rotational speeds and its effect on weld quality..47

Table 4.3. FSW process parameters for the present investigation...48

Table 6.1 Welding conditions for the present CFD model 80

Table 7.1 Details of tungsten carbide tool materials used for FSW of DH36 steel.................96

Table 7.2 Welding operating conditions for different tool materials tool A and tool B..........97

Table 8.1 Chemical composition of DH36 steel (wt. %)...112

Table 8.2 Details of plasma preheating parameters 113

Table 8.3 Welding parameters used in the present study..113

Chapter 1

1 INTRODUCTION

1.1 BACKGROUND AND MOTIVATION

Joining is an essential processing step as it is required to mitigate the complexity of manufacturing large structures. Welding is one of the permanent joining processes which produces complex products that are difficult to manufacture as a single component. It is defined as the joining of two different materials with the application of heat and with or without the application of pressure. Various welding processes are used on a large scale for different applications. Generally, fusion welding processes enjoy the status of the most preferred joining techniques in the industries. Fusion welding processes require several consumables including filler metal and fluxes during welding and release toxic fumes, harmful gases, and radiations that adversely affect the environment. Additionally, the fusion-welded zone and heat-affected zone suffer deterioration of the advantageous effects of the previous processing on the base materials. The other side of fusion welding is that the large heat input associated with the process alters the microstructure, deteriorates the mechanical properties, promotes solidification cracking related to the segregation of alloying elements, expedites hydrogen embrittlement, and creates blowholes at the weld nugget (WN). Not only this, additional work like the post-cleaning of slag from the welded joint, and the distortions induced due to large heat input of conventional fusion welding techniques led to the search for advanced welding technology. Thus fusion welding must be checked with a clean alternative process and with superior quality. This lead to the development of alternatives solid-state welding techniques with gradual reductions in heat input being made. Owing to such qualities, the solid-state joining technique has gained huge attention for joining similar and dissimilar materials in recent years.

Friction stir welding (FSW), a solid state welding process, was introduced in 1991 by The Welding Institute (TWI) UK. It is one of the derivatives of friction welding, which uses frictional heat and plastic dissipation energy to produce the weld. This process appears to be promising prospects for next-generation globalization of FSW, i.e., application of FSW for all types of metals. Initially, it was invented for welding of low melting point materials like aluminum and magnesium alloys. However, with advancements in understanding the process and tool materials technology, FSW has also been successfully investigated on high strength materials like steels, copper, nickel, and titanium alloys. Wear-resistant tool material and process parameters are investigated to join these high strength materials. Figure *1.1* depicts the schematic representation of various stages during the FSW process i.e. the plunge, dwell, welding, and tool retracing/pull-out phases.

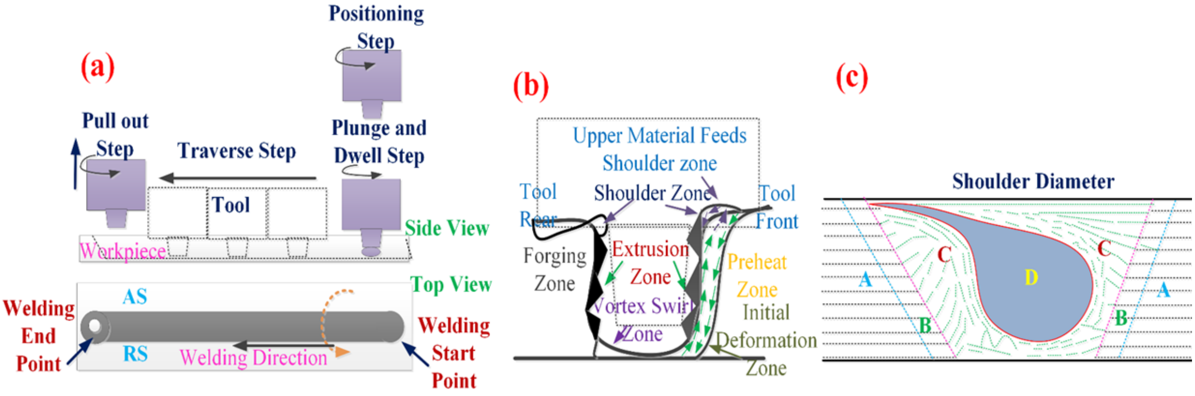

Figure 1.1 (a) Illustration of FSW process (b) metallurgical process during FSW (c) schematic cross-section of a typical FSW weld showing based metal with three distinct weld zones: (A) base metal, (B) heat–affected, (C) thermo-mechanically affected and (D) stirred (nugget) zone

The non-consumable FSW tool (relatively harder material than the workpiece) consisting of the pin and the shoulder is plunged into the weld line of the materials to be welded. After plunging and certain dwell period, tool is traversed along the weld line to produce the weld joint as shown in Figure *1.1*(a). The two sides of the weld joint line are termed as advancing and retreating sides based on the welding direction and tool motion. On the advancing side, the tool rotation and translation are in the same direction while tool rotation and weld direction are opposite to each other at the retreating side. In FSW, heat is generated due to the combined action of frictional heating and plastic dissipation energy. The necessary heat generation and material flow required to produce the weld is controlled by FSW process parameters such as rotation speed, traverse speed, tool tilt angle, and tool geometry. The formation of the weld zone is illustrated in Figure *1.1*(b). Material flow during FSW is very complex but can be explained as a simple extrusion process at the tool work interface. With the progress of the welding process, the softened material is transported from the front of the tool pin to the trailing region where it is forged into a joint, and within this region, the softened material will be extruded, thus the deformation mainly occurs here. Thus, a set of complex deformation processes and their interactions at high temperature, high strains and strain rates conditions determine the weld zone's characteristic microstructures (Cam, 2011). In general, as depicted in Figure *1.1*(c), the transverse section of the weld indicates three distinct regions i.e., a dynamic recrystallized zone (also known as weld nugget), thermo-mechanically affected zone (TMAZ), heat affected zone (HAZ), and base metal. SZ of FSW joints is characterized by grain refinement subjected to intense material stirring in this zone. TMAZ is a region that undergoes plastic deformation at the "local" level coupled with a temperature rise that is lower than that of the weld nugget. Heat affected zone in the FSW process is similar to the heat-affected zone of the fusion welding process which is affected by the heat only.

Welding operations in the shipping and marine industries represent a significant share of the production costs (Sampath, 2006). It allows the construction of various complex profiles. The solid-state FSW process removes the melting and solidification related defects and cause less metallurgical changes in the HAZ, which is a significant concern of the welded structures (Mishra & Ma, 2005). At present gas metal arc welding (GMAW), with covered electrode, is mostly used for the joining of steel (Konkol & Mruczek, 2007; Nathan et al. 2015). Unlike conventional fusion welding techniques, where the higher tensile strength depends on the selected electrodes, FSW produces overmatched tensile strength due to grain refinement (Cam, 2011). It is noteworthy to mention here that weldability of steel significantly affected by carbon content and alloying element composition. The use of friction stir welding (FSW) could lead to savings in, post-weld processing, post-weld heat treatments, and reductions in inspection costs. The absence of ultraviolet or electromagnetic hazards, reduced energy requirements, elimination of consumables and superior weld quality are some of the key benefits that attracts the FSW process in the shipbuilding industries (Konkol & Mruczek, 2007; Steuwer et al. 2012a, 2012b).

The main reason for the success of FSW of softer alloys was the abundance of reusable tools, less peak temperature, and low process load & spindle torque. During FSW of harder materials like steel, the peak temperature, downward force, and spindle torque on the tool either lead to premature failure of the tool or excessive wear during welding. Also, only a limited choice of tool material is available which are highly expensive and difficult to manufacture. The tool design and geometry which can sustain high plunging load at elevated temperatures are needed to be investigated. At present, the most commonly used tool materials are refractory materials such as tungsten cobalt alloys and other ceramics like PCBN. Even the tool made up of refractory material is also susceptible to wear and degradation. Furthermore, due to the difference in the tool material's mechanical, thermal, and chemical properties, it also alters the weld quality (Lakshminarayanan et al. 2010; Lienert et al. 2003). During the FSW of steel, tool performance, durability, and high production cost are major issues which need to be resolved. Though many studies (Cam, 2011; Padhy et al. 2015) have been performed with various potential solutions on the problem of tool wear, the problem of tool wear and degradation of tool persists.

Tool wear is common phenomenon observed in FSW of high strength materials. However from scientific perspective, it is an intricate unresolved issues that has attracted researchers remarkably in the past two decades. Considerable progress has been achieved in every aspect of tool fabrication, microstructure modification, and tribological properties modification in the past two decades, although the problem of tool wear still persist. The pioneering work of Gan et al. (2007), gave some fundamental insights in tool wear and degradation phenomena. Previous researchers also investigated few strategies like an oversized pin, maintaining slow plunge rates, a pilot hole at the plunge position, use of a partial-penetration at the plunge stage, and preheating of workpiece to control the wear and catastrophic failure of tool at plunge stage. However, these strategies do not resolve the problem completely, so more in-depth knowledge is highly essential.

Among these strategies, energy assisted FSW (EFSW), is extensively used to reduce tool wear and increase productivity. EFSW of harder material has the potential benefits like lesser load requirements and high tool life. Even a local preheat at the place of tool plunge is reported to reduce the tool wear and forces generated during FSW of steel and other harder materials (Padhy et al. 2015). Though many thermally assisted FSW variants have been investigated, only a few have addressed high strength steel. The plasma-assisted FSW has advantages like low cost, high efficiency, focused arc, made it more suitable to use as compared to other thermal energy-assisted FSW processes. It is also noteworthy to mention here that in EFSW, over preheating can generate defects that open the field for further improvements to make it a more reliable process. Welding parameters and preheating parameters has complex interaction that affect the heat generation rate, peak temperatures, material flow and tool forces during the EFSW process. Till now, there have been significant improvements in controlling the process but still the knowledge available is insufficient.

In summary, ‘Friction Stir Welding (FSW)’ is primarily used on wrought or extruded Aluminum and particularly for structures that need very high weld strength. It is capable of joining aluminum alloys, copper alloys, titanium alloys, mild steel, stainless steel and magnesium alloys and recently even polymers. Additionally, joining of dissimilar metals such as aluminum to magnesium alloys, etc. can be achieved. FSW has a huge scope in joining steel in shipbuilding and marine industries due to huge demand in low distortion welded structures. FSW attracts in joining of steel due to reduced pre-weld preparation and rework, manpower savings, low distortion, and high-quality welds. The present work is the major thrust on the application of FSW process to low carbon steel, dissimilar steels, and high strength steel alloys for shipbuilding and other heavy industries. To achieve the goal, present study deals with the design and development of the experimental setup, selection of tool material and tool geometry and investigation of process window in which successful welds can be produced. Tool wear is common issue reported in earlier literatures extensively however wear and its mechanism have not been addressed. To overcome the issues of tool wear, an additional plasma heat source was added for FSW of DH36 steel.

1.2 LIMITATIONS OF FSW PROCESS

- FSW is slower than few conventional fusion welding process.
- It is less flexible than manual arc welding processes.
- It requires large downward force to plunge the tool and large clamping force to hold the work piece.
- Keyhole is left at the end of the welding process.
- Tool wear is a main issue in friction stir welding of high strength materials like steel, Inconel and titanium alloys.
- High process forces and high temperature generates during FSW of high strength materials that limits the choice for tool material.

1.3 RESEARCH OBJECTIVES

Based on the detailed literature review and the research gaps found in the published literature the following objectives were identified:

- The primary objective is to develop the experimental setup and determine the process conditions that lead to the successful application of the FSW of steel using tungsten carbide (WC-10 wt. %Co) tool material.
- Investigations on friction stir welding of dissimilar steel alloys i.e. stainless steel and mild steel at different tool rotational speeds and tool offsets.

- Friction stir welding of high strength low alloy steel (i.e. DH36 steel) using two different tool material compositions. Investigations of wear mechanism of tungsten tool during FSW of DH36 steel by qualitatively and quantitatively.
- Development of a numerical coupled thermal and material flow model to predict the thermal history and flow fields during FSW of DH36 steel.
- Development of a plasma-assisted FSW process, characterization of weld quality and tool wear during FSW of DH36 steel.

1.4 CONTRIBUTION TO THE THESIS

In the present thesis both experimental and numerical investigations were carried out. The important contributions of this research work are as follows:

- From the mechanical characterization of the FSW joint it is observed that tensile strength increases with an increase in traverse speed and a decrease in rotational speed. The "onion ring", "banded structure" and the "swirl" formation are observed in the weld zone. At AS, material flow is more complex and chaotic at both top and bottom regions than the material flow on the RS. The SZ on the advancing side (SZ-AS) had a band structure with deeply etched lines. The microstructures of the thermomechanically affected zone consisted of the finest grains size of 7.9 μm as compared to the stir zone size of 14.75 μm. Friction stir welded specimens lead to a greater YS/TS ratio for each welding condition.
- In dissimilar FSW of UNS SS30400 and UNS G10080 steel, rotational speed and tool offset are important parameters that significantly affect the weld quality. Successful joints are produced beyond the tool offset of 0.6 mm at rotational speeds of 600 rpm and 875 rpm. The effect of tool offset was more significant at low rotational speed as compared to high rotational speed. Complex intermixing was observed in the weld region with higher intermixing on the advancing side. The bonding mechanism of dissimilar FSW of stainless steel and mild steel were both mechanical and metallurgical bonding.
- Two different compositions of tool materials were selected to produce weld on DH36 steel at different rotational speed and traverse speed. From the investigation, it is found that the peak temperatures rather than stresses are more detrimental to the life of the tungsten tool. Oxidation, abrasion, adhesion, diffusion, and chipping are the active tool

wear mechanisms for the disintegration of the tungsten carbide cobalt tool. Tool wear is significantly reduced at low rotational speed and high traverse speed due to the low temperature generated at these conditions.

- A 3D numerical coupled thermal and material flow model was developed to predict the peak temperature and flow behavior in the weld zone during FSW of DH36 steel. An asymmetry and skewness of temperature are observed at the advancing trailing frame which reduced at high traverse heat input ratio.
- To reduce tool wear, PFSW was investigated for high strength shipbuilding steel. It is observed that the tool wear was reduced by 56 % on using plasma preheat sources ahead of the FSW tool. The heat input and cooling rate subsequently changed the grain morphology which results in higher ductility and high impact toughness of the welded joints.

1.5 OUTLINE OF THE THESIS

The present thesis is organized into 9 chapters with references and the appendices at the end.

Chapter 1 deals with the background, brief introduction, and motivation of the present research work.

Chapter 2 deals with a brief literature review on the joining of similar and dissimilar steel. Research work in the area of auxiliary energy-assisted FSW is also discussed.

Chapter 3 reveals the procedures, methods used for conducting the experiments. This chapter also outlines the methodology for CFD modelling of the FSW process.

Chapter 4 presents preliminary experimentation to find the process window, tool material and tool geometry during FSW of low carbon steel. (**Published**)

Chapter 5 deals with the joining of dissimilar steels i.e. stainless steel (UNS S30400) and mild steel (UNS G10080). (**Published**)

Chapter 6 deals with the various mechanism associated with the wear and degradation of tungsten carbide tools during FSW DH36 steel. (**Published**)

Chapter 7 highlights a 3D computational fluid dynamic model for temperature distribution and material flow during FSW of DH 36 steel. (**Published**)

Chapter 8 exhibits the effect of plasma preheating on weld quality as well as tool life during FSW of DH36 steel. **(Accepted)**

Chapter 9 represents the concise conclusions and future scope of the present work.

:--------------------*--------------------*----------------------:

Chapter 2

2 LITERATURE REVIEW

2.1 INTRODUCTION

FSW of steel has become one of the exciting research fields in the last 20 years (Lienert et al. 2003; Mishra & Ma, 2005; Reynolds et al. 2003; Thomas et al. 1999), after the development of tools that have sufficient strength for performing welding trials. Although numerous studies are reported in review articles (Cam, 2011; Mishra & Ma, 2005; Padhy et al. 2015), FSW of steel is not progressed rapidly, unlike Al-alloys. The main reason for limited FSW on steel are (a) high process temperature (~1100 °C) that results in tool low life (b) costly tool materials (c) abundance of conventional fusion welding process (d) phase transformation phenomenon in steel at these elevated process temperatures and (e) lastly the variety of commercial grades of steel alloys which require a large set of initial experiments to optimize the FSW process window for a set of desired properties. In this literature review, FSW and energy-assisted FSW of steel alloys are discussed in detail. The literature pertinent to FSW of steel is categorized into different sub-sections as described below.

2.2 FRICTION STIR WELDING OF STEEL

Welding of steel alloys are generally affected by the alloying composition and process temperature attained, which widely affect the microstructure development and weld joint properties (Cui et al. 2007; Cui, et al. 2007; Fujii et al. 2008; Fujii et al. 2006; Husain et al. 2015). Friction stir welding is a solid-state in nature that enables controlling these factors (i.e., heat input and cooling rate) and producing superior weld quality (Chung et al. 2010; Wei & Nelson, 2012). Nathan et al. (2015) investigated the weld joint quality during high strength low alloy steel by using three different welding processes. It is found that the weld joint produced by FSW is superior in terms of mechanical properties. In review articles by (Cam, 2011; Mishra & Ma, 2005; Rai et al. 2011), important issues like tool materials, tool geometry, and tool wear in friction stir welding are softer and harder alloys are discussed. The peak temperature and weld cooling rate are significantly influenced by the process parameters i.e., rotational speed and weld traverse speed. Peak temperature was reported in the range of 1090 ℃ (Ghosh et al. 2011; Lienert 2003; Thomas et al. 1999). Thomas et al. (2009) reported that low carbon steel with an initial microstructure of ferrite and pearlite transformed into a ferritic and bainitic structure in the weld nugget. Ueji et al. (2006) have studied the FSW of ultrafine-grained low carbon steel. They reported that tool rotation rate influenced microhardness at weld nugget, grain boundary characteristics, the morphology of ferrite grains, and carbide distribution. Cui et al. (2007) performed FSW of steel below its recrystallization temperature by controlling the process parameters. They produced successful welds in high carbon steel at 100 and 200 rpm at the welding speed of 25 mm/min. In FSW of carbon steels, it was difficult to distinguish the thermo-mechanically affected zone (TMAZ) due to phase transformation. In another endeavor, they compared FSW of steel with different carbon contents (Cui et al. 2007). It was obtained that the steel with different carbon content yielded different microstructure after welding. Saeid et al. (2008) studied the effect of traverse speed on mechanical and microstructural properties on stainless steel. The SZ grain size was reduced on increasing the welding speed. The peak temperature is observed to drop with increasing traverse speed. (Reynolds et al. 2003) investigated the effect of traverse speeds on mechanical properties and microstructure of FS welded micro-alloyed steel. Lienert et al. (2003) studied the feasibility of FSW of steel with acceptable tensile properties. On increasing welding speed, the cooling rate also increases, which leads to greater amounts of displacive transformation products in the weld zone and thus hardness values of the weld nugget. Husain et al. (2015) investigated Friction stir welding of carbon steel at different rotational speeds. Either increase or decrease in tool rpm beyond 1000 rpm reduced the joint efficiency. It was found that hardness values decreased marginally in the heat-affected zone. Ozekcin et al. (2004) performed FSW on L80 and X80 steel at two rotational speeds and two Z-axis load. FSW process can be used to tailor the mechanical properties like microhardness of the weldment by controlling the welding process parameters like rotation speed, and Z-axis load. Ghosh et al. (2011) investigated Friction stir welding on advanced high-strength M190 steel at a different traverse speed of 0.21 mm/s, 0.85 mm/s, and 1.69 mm/s. Their study was mainly focused on the effect of heat input and cooling rate on the microstructure and mechanical properties of the joint. Total heat input was reduced, and the cooling rate was increased with the increase of tool traverse speed. Lakshminarayanan et al. (2010) studied microstructure and mechanical characterization in FSW of AISI 1018 steel. The weld joint exhibited higher strength and hardness than the base material. However, their study was limited to single parameter combination i.e., rotational speed of 1000 rpm and traverse speed of 50 mm/min. Summary of friction stir welding of steel alloys at different process conditions is summarized in Table *2.1*

Table 2.1 Summary of friction stir welded joint at different process conditions

Workpiece	**Parameter Investigations**	**Remarks**	**References**
Ultrahigh carbon steel	Travel speed of 1.27 mm/s & rotational speed of 400 rpm, PCBN tool had a shoulder diameter of 14 mm	Defect-free welds were obtained in 2.3 mm thick steel plates. Welding was performed at 3 process parameters although only 1 parameter was reported due to difficulty in analysis.	(Sato et al. 2007)
SAF 2205 duplex stainless steel	The rotational speed of 800 rpm, WC-based material had a shoulder diameter of 16 mm	A groove defect was observed due to insufficient heat input obtained at a traverse speed of 250 mm/min. Process temperatures was reduced on increasing traverse speed.	(Saeid et al. 2008)
316L SS	RPM, TS, force, polycrystalline cubic boron nitride, PCBN)	15 mm thick plates were welded by tool pin having 5 mm length. Defect-free welds were obtained at only 35 kN downward force. The stir zone exhibited refined grains and equiaxed grain structure.	(Chen et al. 2009)
HSLA-65 steel	Traverse speed	The effect of traverse speed and rotational speed on microstructure and microhardness was done. No quantitative study regarding peak temperatures.	(Barnes et al. 2012)

	two tool materials (W-25%Re and PCBN)		
X80 pipeline steel relative	(PCBN) CS4	It was found that with a decrease in heat input the bainitic structure in the hard zone becomes finer and so hard zone strength increases.	(Aydin & Nelson, 2013)
ODS and RAFM Steels	PCBN, SD = 25.4 mm	Grain size was reduced and hardness was altered on decreasing heat input during FSW of the RAFM steel.	(Yu et al. 2015)
AISI 316L stainless steel	Rotational speed WC–Co cermet SD = 16 mm	Grain size was reduced on decreasing heat input to the weld The lower tool rotational speed, or equivalently, with the lower heat input, led to the higher hardness and strength.	(Hajian et al. 2015)
DH36 steel	PCBN &W-Re	The effect of centerline deviation was investigated.	(Tingey et al. 2015)
HSLA65 steel	Tool shoulder diameter, WC–Co	Different tool diameters were investigated for the joining of steel. Successful joints were observed at a suitable D/d ratio.	(Nathan et al. 2016b)

structural steel grade St52 (EN S355JR grade) plates	Tungsten carbide	The defect-free joints were obtained on a 4 mm thick plate by using a 3.8 mm pin length. A hardness as high as 350 HV was observed within the weld nugget with mainly Widmanstatten ferrite as a predominant phase in the nugget zone.	(Küçükömero et al. 2018)
AISI 410S ferritic stainless steel	Rotational speed and Z force, PCBN, conical shoulder diameter of 25 mm	Successful welds on 4 mm thick plates were obtained using a pin length of 3.7 mm. At low rotational speed and low forging, force defected joints were produced.	(de Queiroz Caetano et al. 2018)

2.3 FRICTION STIR WELDING OF DISSIMILAR STEELS

The excellent properties of dissimilar steel components welded by friction stir welding (FSW) make it suitable for many potential applications in automobile, chemical, petrochemical, electrical, electronics, structural, and shipbuilding industries (Wang et al. 2019). The challenges faced during the existing conventional welding of dissimilar steels are mainly due to the differences in carbon content and alloying elements' compositions. The traditional fusion welding techniques can easily generate various defects like porosity, blowholes, hot cracks, the rapid growth of grain, heat-affected zone softening, and alloying elements segregation due to improper selection of filler materials, welding process, and its operating parameters (Matlan et al. 2018; Murr, 2010; Singh et al. 2018; Vashishtha et al. 2017).

Few important findings from the previous studies of friction stir welding of dissimilar steel alloys have been discussed. Thomas et al. (1999) reported a feasibility study on the FSW of steel way back in 1999. Choi et al. (2010) studied FSW of two different carbon steels SK5 and SPHC. It was reported that placing the stronger steel on the weld's advancing side resulted in a smaller weld nugget with more martensitic transformation. Cheng et al. (2013) successfully carried out FSW of ferritic ductile iron and low carbon steel. A defect-free weld was obtained when low carbon steel was placed on the advancing side. The tensile fracture location was shifted from the welding zone to the low carbon steel side after heat treatment. Chung et al. (2011) studied the effect of workpiece material position and tool plunging in dissimilar FSW F82H and SUS304 steels. The weld joint interface showed unmixed regions when the tool was shifted toward the advancing side in the softer material during dissimilar FSW of SUS304/F82H steels. Choi et al. (2011) demonstrated successful dissimilar FSW of low carbon steel (SHPC) and high carbon steel (SK85). Martensite was observed in the weld region with a higher fraction at the higher rotational speed. Zhou et al. (2018) investigated the effect of tool pin profile in dissimilar FSW of aluminum and copper. The joint produced by the threaded pin sustained the maximum shear tensile fracture load. Jafarzadegan et al. (2013) studied (Zandsalimi et al. 2018) investigated dissimilar FSW of stainless steel and aluminum alloy the FSW between two different grades of steel, i.e. SS304 and st37 steels. It was found that the tensile fracture occurred in st37 steel with ductility and strength higher than st37 steel base material. Logan et al. (2016) investigated FSW of duplex stainless steel (DSS) and low-alloy structural steel. High hardness values were obtained in the SZ of DSS. The high hardness in the region was due to severe strain-induced deformation and significant grain refinement observed at this location. The micro/macrostructure analysis showed the void defects in the stir zone of duplex stainless steels. Tool eccentricity is one of the most important parameters in FSW and has been studied by previous authors in the joining of similar materials (Mao et al. 2014; Tingey et al. 2015) and dissimilar materials (Zandsalimi et al. 2018) (Yaduwanshi et al. 2017) welding. (Tingey et al. 2015) studied the effect of tool centerline offset in FSW of DH36 steel. Three different types of fracture mechanisms were observed in the tensile test of the welded joints. Tensile fracture was ductile up to a certain tool deviation on both AS and RS, beyond that the failure mechanism turned to brittle fracture. Mao et al. (2014) investigated the influence of tool pin eccentricity in FSW of AA7075 aluminum alloy. It was observed that the tool pin offset up to a certain point (i.e., 0.2 mm) produced joint with the highest tensile strength and sufficient elongation due to grain refinement and the better joint interface. Yaduwanshi et al. (2017) studied the effect of tool deviation on the weld quality in dissimilar FSW of aluminum and copper. They studied complex material mixing and the formation of intermetallic layer thickness as a function of tool offset. They achieved the sound surface quality and higher strength at a rotational speed of 900 rpm, a traverse speed of 120 mm/min, and fixed offset. The serrated-type interface was produced at the fixed offset value, while below and above the fixed offset value, the voids and micro-cracks were produced. It is observed that the tool deviation from weld centerline has played significant role in producing sound quality weld in FSW of dissimilar materials.

2.4 TOOL MATERIALS

In joining the high strength materials by the friction stir welding (FSW) process, the FSW tool is a key component. Although FSW of high strength materials has been initiated for more than two decades ago, high tool wear and the lack of cost-effective tools limit the commercialization of the process. Several studies have addressed the issues of tool degradation in joining of high strength materials like steel, nickel, and titanium alloys (Cam 2011; Lemos et al. 2017). To improve tool performance, an understanding of the tool wear mechanism is mandatory. However, a limited number of published literature (Choi et al. 2009; Gan et al. 2007; Thomas et al. 1999) are available on the tool wear in FSW of high strength materials. The tool material, composition, and its thermos-physical properties affect the FSW process in various aspects. Furthermore, tool geometry and the operating process parameters are prominent issues that influence the weld quality and tool life. The tool geometry affects the heat generation and material flow and at the same time, it impacts the stresses developing in the tool.

Although the benefits of FSW in steel are clear (Cam, 2011), the applications are limited due to severe tool degradation. The available choices of tool material for high strength materials are PCBN and WC alloys (Rai et al. 2011; Zhang et al. 2012). PCBN is a preferred tool material for FSW of steels because of its high strength and hardness as well as its stability at elevated temperatures. A recently published study (da Cunha et al. 2018) on the FSW of GL E36 shipbuilding reported that PCBN tool successfully produced welds without any physical loss in the tool dimensions and size. However, the PCBN tools also have a limitation of brittle fracture at higher traverse speed (Konkol & Mruczek 2007). Another choice is the WC-based tool, which is less costly than the PCBN tool but undergoes more wear due to its lower strength and hardness at elevated temperatures (Rai et al. 2011).

Few attempts were made to improve the tribological behavior of the tool material by tailoring the material composition (Iqbal et al. 2016; Miyazawa et al. 2011; Park et al. 2012) and providing an additional coating on the tool (Batalha et al. 2012; Gan et al. 2007). Still, further investigation would be required to improve the wear resistance and strength at elevated temperatures. Tool wear was investigated in aluminum alloys (Tarasov et al. 2014), steel (Choi et al. 2009a), titanium alloys (Fall et al. 2016; Farias et al. 2013; Wang et al. 2014), nickel alloys (Hanke et al. 2017), and cast AI359-20% SiC matrix composites (Ashish et al. 2016; Shindo et al. 2002) using experimental techniques and FEM-based model (Hasan et al. 2017). Initially, (Tarasov et al. 2014) investigated wear mechanism of alloy steel tool during FSW of aluminum alloys. Tool metal fragments were pulled out at the contact surface by the hot diffusion mechanism. Furthermore, tool degradation was also reported as tool particles in the stirred zone of the weld joint. During FSW of mild steel (Lakshminarayanan et al. 2010) and Inconel 625 alloy (Song & Nakata 2010), tool particles were found in the weld zone, and it was described as the physical wear from the tungsten carbide tool. Diffusion is another degradation mechanism observed by Siddiquee & Pandey (2014) during FSW of stainless steel plates using the WC alloy tool. A similar result was obtained by Wang et al. (2014); they also noticed an enhanced diffusion of tool particles in the weld nugget during FSW of Ti6Al4V alloy using the WC tool. Hanke et al. (2017) investigated the degradation mechanism of the PCBN tool during FSW of Ni-base alloy 625. Diffusion of boron nitride (BN) particles inside the weld zone indicated the existence of hot diffusion wear. At higher process temperatures, BN grain pulled out from the tool due to the softening of the binder phase resulted in the tool's excessive mechanical wear. Similarly, small BN wear particles were observed inside the stir zone during

FSW of Ni-base alloy 600 (Sato et al. 2008). Furthermore, the surface interaction between tool and the welded metal was responsible for the adhesion as well as tool wear (Siddiquee & Pandey, 2014). Gan et al. (2007) investigated degradation of tungsten tools during FSW of L80 steel. They found that the strength of the pin material should be higher than 400 MPa at 1000 °C to avoid mushrooming effect in WC tool. Plastic deformation and wear are the two main contributors for the degradation of WC tools. Tool material composition, tool geometry, i.e., shoulder surface, and pin geometry characteristics have also significant influence on tool wear rate. Pradeep et al. (2013) reported the influence of different tool geometries on the wear in WC-alloy tools during FSW of steel. Tool with concave shoulder and conical pin had shown the minimum tool degradation as compared to other profiles. Similarly, Liu et al. (2005) investigated the wear of WC tools in FSW of aluminum matrix composites (AMCs). Maximum radial wear was reported at the position of about one third pin length from the root of the pin. Lemos et al. (2017) presented valuable insights on various aspects of tool materials and tool design in joining of high strength Ni- based alloys. Table *2.2* summarized the details of different tool materials and tool design for FSW of different grades of steel alloys.

Table 2.2 Summary of tool materials and key findings during FSW of steel alloys

Tool Details	**Material**	**Remarks**	**References**
PCBN and W-Re	Low carbon steel and stainless steel, 12 mm and 15 mm plates of LCS and SS	Successful welds were produced in dissimilar steel and similar steels. Peak temperatures were reported in order of 1200 °C. Characteristics zones like SZ, TMAZ and HAZ were reported in the weld zone. No comments were made on tool performance during similar and dissimilar welding of steel.	(Thomas et al. 1999)
PCBN and Tungsten -Re	6.3 mm thick AISI1018 steel.	Process temperatures were reached at around 1100 °C. Tool wear was observed in W tools. Their study revealed that PCBN tool were failed during the initial stage of welding.	(Lienert et al. 2003)
60% PCBN (Q60 tool) while the other had 70% PCBN (Q70 tool), where the balance was W–Re in both cases	HSS and UHSS	Q70 tool provided the best combination of wear resistance and joint strength, lasting for 1200 welds, versus 700 welds for the Q60 tool. Successful welds were made that resulted in higher tensile strength than the base material.	(Miles et al. 2006, 2009, 2011)
Carbide specifications: (K10, 94%WC-6% Co), Equilateral triangle tip profile with 5 mm in diameter and 2.8 mm in height	AISI 304 steel, 3 mm	A pressurized air-cooled setup was used for the tool. Successful welds were obtained in 3 mm thick plates with refined grain microstructure in the SZ. No comments were made on the tool wear.	(Meran & Canyurt, 2010)

Two tool materials (W-25% Re and PCBN)	HSLA-65 steel	Tungsten-rich bands were observed in the weld produced at low traverse speed of 50 mm/min. The abrasive wear was the predominant wear mechanism on the tool shoulder and tool pin. PCBN tool suffered significantly less wear than the W-Re tool.	(Barnes et al. 2012)
Tool materials included tungsten carbide (WC), tungsten–iron (W-Fe), and tungsten–molybdenum (W-Mo) were investigated	5.5 thick Maraging steel	Significant wear and degradation were reported in WC and W-Fe tools. Tool wear was minimum in tungsten molybdenum tool.	(Meshram et al. 2013)
W-25% Re pin	Mild steel	The tool reaction forces and torque were recorded. No evidence of mechanical wear of the tool was found in the SEM analysis.	(Iqbal et al. 2014a; 2014b, 2016)
90% W, 95% W, and 99% W	HSLA65, 5 mm thick high strength low alloy	99% W and 1% La_2O_3 withstood high temperature and stresses and shown negligible wear. In the other endeavor, it was found that the tool diameter of 5 times the plate thickness resulted in the defect-free joint.	(Nathan et al., 2016b, 2016a)
Tungsten based alloy, Tapered pin geometry with SD=25 mm	Structural steel, structural steel and stainless steel	Welded joints shown higher hardness in the SZ. Tensile strength of the dissimilar joints were higher than structural steel and lower than the stainless steel. In another endeavor of FSW of structural steel, it was observed that PWHT of	(Sharma & Dwivedi, 2017b, 2017a)

		the FSW joint resulted in grain coarsening and tempering of the martensite.	
PCBN, Convex shoulder	HSLA steel	Heat input and backing plate material were varied and its effect on microstructure was investigated. It was observed that there is linear relationship between weld cooling rate and both post-weld lath width. Cooling rate controls the weld nugget microstructure and width of lath structure.	(Nelson & Rose, 2016)
$Si_3 N_4$ material	1.4 mm thick, Dual-phase steel	The temperature on the RS was higher than that of the AS. Hard phases were reported in the SZ. Post-processing of tool and tool degradation was not discussed.	(Kim et al. 2014)
(Cemented carbide specifications: K10 has 1,650 HV hardness and made up of 94 wt. % WC-6wt.% Co), Triangular Pin, 2.7 mm pin length for 3 mm thickness plate	AISI430 stainless steel	Successful welds were obtained in the process window. Process force and temperature were recorded. Tensile strength of the welded joints were higher than the base material. No comments were made on the tool wear and deformation.	(Bilgin & Meran, 2012) (Bilgin et al. 2015)
PCBN, scrolled shoulder with SD = 25.4 mm, 5.84 mm pin length with 30° taper and step spiral threads)	API X80 HSLA steels	12.7 mm thick HSLA plates were successfully welded using PCBN tool. No information on tool wear and degradation was provided.	(Tribe & Nelson, 2015)

PCBN and Tungsten -Re	EH46 steel grade plate of 14.8 mm thickness	Plunge depth had more significant effect on heat input than rotational speed. The probe side surface significantly influenced the material flow and heat generation.	(Al-moussawi et al. 2017)

2.5 AUXILIARY ENERGY ASSISTED FRICTION STIR WELDING TECHNIQUES

During FSW of high strength materials, tool wear, tool deformation and unpredictable tool breakage is not completely solved. These difficulties have led to explore a new approach known as hybrid or assisted FSW approach by availing supplementary heating/softening to the workpieces. Till now no standard terminology is available to refer to the above new variants of FSW. Based on the mode of assistance, these hybrid FSW/ energy-assisted FSW/energy-enhanced FSW/ auxiliary energy-assisted FSW processes are classified into two categories broadly (*i*) thermal energy-assisted FSW and (*ii*) mechanical energy-assisted FSW. The present literature review summarized an elementary idea of the various auxiliary energy-assisted FSW processes, their experimental set-ups, and the influence of the auxiliary energy on the FSW process, its parameters, and the weld joint properties, and to some extent the microstructure characterization of the energy assisted friction stir welded joint. Figure *2.1* shows different experimental setups for the energy-assisted FSW process.

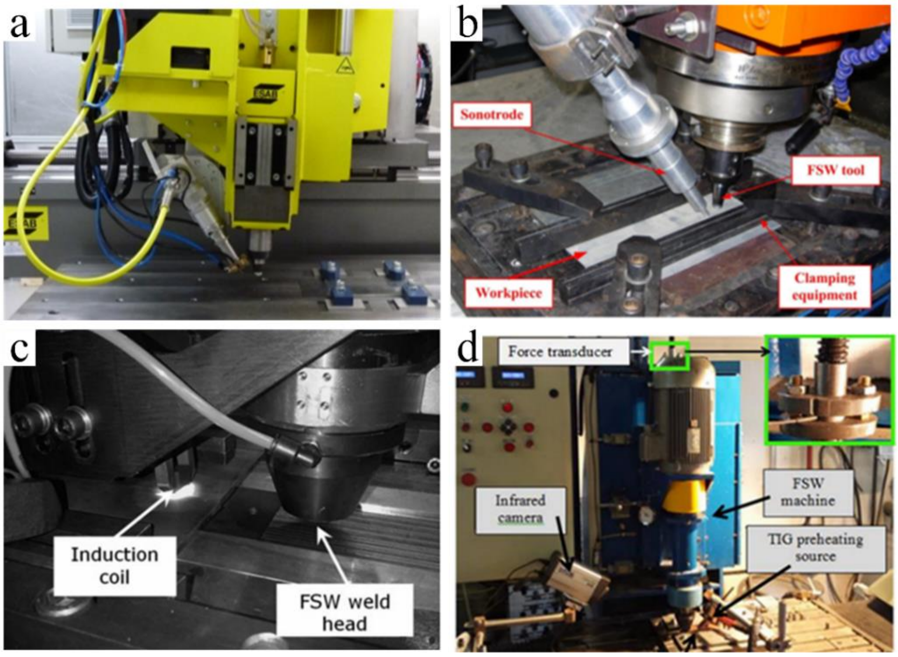

Figure 2.1 (a) Laser assisted FSW experimental setup (Casalino et al. 2012) (b) ultrasonic assisted FSW experimental setup (Shi et al. 2015) (c) induction assisted FSW experimental set-up (Álvarez et al. 2014) (d) arc assisted FSW process (Constantin et al. 2018)

Based on the classification UFSW is the only mechanical energy-assisted FSW process that was used significantly in the joining of softer materials (Ahmadnia et al. 2015; Amini & Amiri, 2014; Liu & Wu, 2016; Liu et al. 2018; Park et al. 2009; Shi et al. 2015). On the other hand, direct preheating of the workpiece by an additional heating source like Laser, TIG, Plasma, and Induction heating were investigated in the joining of several similar and dissimilar materials. Thermal methods investigated earlier are induction heating (Álvarez et al. 2014, 2016; Mohan & Gopi 2018; Padhy et al. 2015; Sun et al. 2014), laser heating (Able & Pfefferkorn, 2005, Ahmad et al. 2019a; Campanelli et al. 2013; Casalino et al. 2012a; Chang et al. 2011; Fei et al. 2018; Fujii et al. 2008; Kheireddine et al. 2013; Merklein 2008; Song et al. 2009; Sun et al. 2013; Sundqvist et al. 2017), and arc (Bang et al. 2016; Constantin et al. 2018; Mehta & Badheka 2017; Mili et al. 2017). The details of individual energy-assisted FSW processes are described in subsequent sections 2.5.1 to 2.5.4.

2.5.1 Laser-assisted FSW

Laser assisted FSW (LFSW) is the most commonly used variant of the hybrid FSW process in which a laser source is used ahead of the FSW tool to preheat the workpiece. LFSW includes a conventional FSW machine integrated with a laser source whose focal point maintains some distance ahead of the tool. Figure *2.1*a shows the experimental set up of LFSW (Casalino et al. 2012). Laser preheating reduced the welding forces and torque, thus reducing the FSW fixture's overall stiffness requirement. This allowed the weld formation with a significantly lower tool deliverance energy, which corresponds to a higher productivity rate (Able & Pfefferkorn, 2005; Casalino et al. 2012). Hence it has been widely used in the welding of various similar materials (Campanelli et al. 2013; Song et al. 2009; Sun et al. 2013) and dissimilar materials (Chang et al. 2011). Among various laser sources, Nd: YAG fiber laser (Chang et al. 2011; Fei et al. 2016; Sun et al. 2013) and CO_2 laser (Padhy et al. 2015) are widely used. In lap joint, force and torque were not reduced to the extent of the butt joint as reported in earlier studies (Padhy et al. 2015). Álvarez et al, (2016) reported tool forces were reduced by 33 % and 40 % in LAFSW during the plunge and welding stages compared to conventional FSW. LFSW produced defect-free welds in wide range of parameters (Casalino et al. 2012) and enhanced mechanical properties like tensile strength (Sun et al. 2013), microhardness (Fujii et al. 2008), and fatigue properties (Able & Pfefferkorn, 2005) of the weld joint. Sun et al.(2013) reported that the hard phases (i.e. martensite and bainite) were prevented up to a high traverse speed of 600 mm/min which generally occurred at the traverse speed of 300 mm/min in weld microstructure. The heat input to the weld was increased significantly when the laser source was shifted from AS to RS. Song et al. (2009) observed that the mechanical properties like microhardness and tensile strength were increased in LFSW of Inconel alloy. Both transverse and longitudinal tensile specimens were plastically deformed significantly before the failure took place in the base material. A higher cooling rate would lead to a more refined grain structure was explained by a longitudinal tensile test. Merklein (2008) produced tailored joint between 1 mm thick DC04 steel and AA6061 sheets using LFSW. It was reported that traverse speed reached to 2000 mm/min which is technically impossible in FSW. These welded samples had shown high tensile strength and which was 80% of AA6061 base material. Dissimilar materials i.e. AA6061 T6 and AZ31were joined using Laser-assisted FSW by Chang et al. (2011). Defect-free joints were obtained with LAFSW at 2 KW power only with nickel foil. The addition of nickel foil was in line with the higher tensile strength around ~66% of the magnesium base metal. Casalino et al. (2012) found that the void defects were absent in LFSW of AA2024 T3 and AA6061 T6. The edge tearing was absent in LFSW due to better plasticization of the material. Although LFSW is a widely studied process among all the auxiliary energy-assisted, it also has disadvantages like bulky setup, high cost, and skilled operator.

2.5.2 Ultrasonic assisted FSW

Ultrasonic assisted FSW (UFSW) is the only variant that uses mechanical energy to soften the workpiece material. Figure *2.1*b shows the experimental setup of ultrasonic enhanced FSW. This process includes an ultrasonic energy source integrated with a conventional FSW machine. In UFSW, high-frequency ultrasonic vibrations are used to soften the workpiece and enhance the plastic deformation. In earlier literature, it is observed that UFSW increases peak temperature, material plasticization and subsequently enhance the weld quality (Ahmadnia et al. 2015; Amini & Amiri 2014; Liu & Wu 2016; Liu et al. 2018; Lv et al. 2018; Park et al. 2009; Zhong et al. 2017). (Shi et al. 2015, 2018) observed ultrasonic vibration reduced the voids and tunnel defects. Moreover, Ultrasonic energy reduces the requirement of frictional heat by complementing the softening however increases the net heat input by additional plastic deformation. UFSW reduced the downward welding force than conventional FSW (Amini & Amiri 2014; Park et al. 2009). Amini & Amiri (2014) also reported that tensile strength and percentage elongation were increased by 10% and 15% respectively during UFSW of AA6061. Lv et al. (2018) found that the process temperatures, weld width, and the mechanical interlocking features were improved in UFSW. Liu & Wu (2016) found that the ultrasonic vibration increased the width of the plastically deformed zone by 10% during FSW of 2024 T4 aluminum alloy. In addition to that, the width of the heat-affected zone (HAZ) was reduced in ultrasonic-assisted FSW. Ahmadnia et al. (2015) investigated the effect of ultrasonic energy and process parameters on the mechanical and tribological properties of AA6061 using UFSW. US vibration power of 400 W resulted in the maximum tensile strength and Erichsen number, as well as the minimum surface roughness of the welded joint.

2.5.3 Induction assisted FSW

Induction heating is a process where an electrically conductive workpiece is placed in a varying electromagnetic field. The variable magnetic field induces an electric current inside the conductive workpiece and thus results in the workpiece's resistance heating. In the IFSW set-up, the FSW machine and the induction coil are fixed such that the weld line falls under the electromagnetic field of the induction coil. This eliminates high tool force requirement, heavy clamping system, and reduces the power and size of the FSW machine. Induction assisted FSW has been successfully studied in the welding of aluminum alloys as well as high-temperature materials like steel Álvarez et al. (2014). Figure *2.1*c shows various parts of the experimental setup of Induction assisted FSW. An important feature of the induction heating process is that the heat is generated inside the object itself via heat conduction. The advantage of Induction assisted FSW is that the resistance heating plasticizes the workpieces, reduces the plastic deformation resistance and contamination issues. It reduced the chances of weld defects due to well-controlled heat input and result in improved weld quality. It also promotes high traverse speed and hence the increased productivity. (Álvarez et al. 2014, 2016; Cam 2011; Mohan & Gopi 2018; Padhy et al. 2015). Álvarez et al. (2014) found that the welding forces were reduced by 31% during the plunge stage and welding speed was further increased in induction assisted FSW of steel. Tensile strength and hardness of the weld were increased due to plasticization and intense deformation of the material during Induction assisted FSW. The IFSW also has some disadvantages like difficulty in controlling the current flow, the spark generation, and heating of all the conductive materials involved in the current path.

2.5.4 Arc assisted FSW

Based on the arc source used for preheating, AAFSW processes can be further classified into two categories. The preheating torch was fixed by integrating a plasma arc source (Yaduwanshi et al. 2017) or a tungsten inert gas (TIG) welding arc (Bang et al. 2012, 2013) with the FSW machine. The details of arc assisted FSW process are provided in the forthcoming sections

2.5.4.1 TIG assisted FSW

TIG assisted FSW (TFSW) was investigated by several researchers in the joining of similar and dissimilar materials. Experimental setup of TFSW is shown in Figure *2.1*d. In dissimilar materials, preheating was done at the harder material side. TFSW enhanced material plastic flow and material mixing. Bang et al. (2012) during TFSW of AA6061T6 and stainless steel STS304 resulted in better mechanical properties of welded joint. The stir zone is mostly confined to softer alloy i.e. AA6061 T6. Microhardness is found maximum in the HAZ and TMAZ side of steel than the steel itself because of the work hardening of the steel. Transverse tensile strength was reached up to 93 % of the aluminum alloy. In another endeavor of (Bang et al. 2013), TIG assisted FSW of dissimilar materials like AA6061 and titanium alloy Ti-6Al-4V were investigated. Tensile strength of weld was increased and the fracture mode was shifted to ductile behavior in TFSW. Joo (2013) found that the tensile strength (~91 %) of the magnesium alloy during TFSW of magnesium AZ31B to SS400 mild steel. This was due to the enhanced material plastic flow and partial annealing effect in the magnesium which also enhanced the weld elongation. Chen & Kovacevic (2004) performed TAFSW on a dissimilar combination of materials like 1018 steel to 6061 aluminum alloys. The tool offset of 1 mm towards the softer aluminum side enhanced the weld quality, temperature history, microstructure, and microhardness. Choi et al. (2011) produced defect-free weld in hybrid FSW of high carbon steel. A marginal increase in mechanical properties in terms of hardness and elongation was observed however tensile strength almost remained unchanged. Scutelnicu et al. (2011) observed that the plunge forces were reduced significantly during TIG assisted FSW of copper. The peak temperature of TFSW was around 100 °C higher than conventional FSW.

2.5.4.2 Plasma assisted FSW

PFSW is a rarely used variant of the hybrid FSW process in which a constricted plasma arc is used to preheat the workpiece material. The additional plasma preheating supplement the original FSW heat input and causes an increase in the process temperature. This consequently leads to adequate plasticization of the workpieces. In the joining of similar materials, the source was focused on the weld line while in the joining of dissimilar material arc was focused on the harder material (Yaduwanshi et al. 2016). The advantages of PFSW are its low-cost setup, constricted arc, greater energy concentration, and arc stability.

2.6 NUMERICAL MODELING IN FRICTION STIR WELDING

The Friction stir welding (FSW) process is highly complex in nature due to its nonlinear coupled behavior of the physics involved. Complex physical interaction occurring simultaneously during the FSW process, including the thermal, mechanical, and coupled interactions. Heat flow and material flow during the FSW process depend on the thermo-physical properties of the workpiece material, the tool material, tool-workpiece interaction, and the welding condition. The interactions between the materials, affect the weld thermal (heating and cooling) cycles, the material flow, and the weld joint characteristics of the friction stir welded joints. From the beginning, the FSW technique has been extensively investigated by numerical techniques and the experimental characterization to optimize the process and to obtain sound weld quality (Assidi & Fourment 2009; Mishra & Ma 2005; Neto & Neto 2013). Numerical simulations can develop a more in-depth understanding of the complex physics of the FSW process. Several attempts are made to establish numerical models based on the coupled nature of the process (Colegrove & Shercliff 2006; Dialami et al. 2016; Micallef et al. 2013; Shi et al. 2014). Previous numerical modeling attempts were primarily focused on the thermal analysis and were unconcerned to the material transportation behavior (Schmidt & Hattel, 2004, 2005). (Frigaard et al., 2001) developed a 3D thermal model for FSW of aluminum alloys. The numerical simulation was compared with the experimentally recorded temperature readings. (Chao et al., 2003) proposed a model for heat transfer analysis for FSW of aluminum alloys by inverse modeling of boundary conditions. It was found that mechanical efficiency during FSW was 80 % and heat transferred into the tool material was only 5 %. (Song & Kovacevic, 2003) proposed a 3D heat transfer model is used to simulate the welding temperatures during FSW of aluminum alloys. The temperature distribution obtained by the FEM simulation was close to the experimental results. (Khandkar et al., 2003) investigated a 3-dimensional heat transfer model in the transient state during FSW of aluminum alloys. Heat generation was calculated by the experimental values of torque obtained during welding. Simulation results were matching with the experimental ones by correcting the heat transfer coefficient of the backing plate material. In short, initially developed thermal models ignored the heat transfer aspect by material flow and plastic deformation during the FSW process. However, in the past few years relatively more advanced model considering the aspects of convective heat transfer using coupled heat and material flow is developed. (Cho et al., 2015; Cho et al., 2013) used a coupled 2D heat and material flow model to demonstrate the peak temperatures during FSW of AISI304 steel. It was observed that the temperature distribution across AS and RS of the weld joint were asymmetric in nature and the high temperature was observed across the advancing side. (Seidel & Reynolds, 2003) proposed 2D material flow model in the laminar approach considering non-Newtonian fluid flow behavior. However, the developed model could not match satisfactorily on comparing with the experimental results due to over assumptions for the simplification of the complex FSW process. (Ulysse, 2002) proposed a 3D model for heat and material flow to predict the thermal history during FSW. The model allowed the prediction of thermal history with the variation in the process parameters with a slight deviation with the experimental ones. (Colegrove et al., 2007; Colegrove & Shercliff, 2006) investigated the 3D model for heat flow and material flow analysis for FSW of aluminum alloys. The simulated model predicted the heat and material flow analysis for different tool geometry through coupled thermal/flow analysis. (Nandan et al., 2007; Nandan, Roy, & Debroy, 2006; Nandan, Roy, Lienert, et al. 2006) proposed coupled heat and material flow model considering, viscoplastic 3D fluid flow model during FSW of different materials like AA-6061 (Nandan, Roy, & Debroy, 2006), stainless steel SS304 (Nandan, Roy, Lienert, et al. 2006), and AISI1018 (Nandan et al., 2007). In-depth analysis of peak temperature, weld thermal cycles, velocity streamline were investigated. It was found that the temperature obtained in the numerical simulation were close to the experimentally measured ones. (Assidi et al. 2010) proposed a 3D model using the ALE approach by considering two different friction model. It was seen that the coulombs friction model is more accurate in predicting the temperatures and forces generated on the tool. (Arora et al., 2009a) developed a heat flow model and evaluated the strains and strain rates during the FSW of 2XXX series aluminum alloy. The ranges of strain and strain rates were calculated for different welding conditions. Moreover, (Arora et al., 2009b) reported that an analytical approach can be easily used to predict the spindle torque and process temperatures during FSW. From the available literature, it is observed that computational fluid dynamics (CFD) is extremely useful for modelling FSW process because of its ability to deal with complex heat flow using coupled thermal and fluid flow analyses.

2.7 MAJOR RESEARCH GAPS FROM THE LITERATURE REVIEW

From the above-detailed literature review, it is observed that FSW has potential to join steel alloys. Due to limited & expensive tool material and severe tool wear & degradation, FSW of steel is not commercialized and such implementation would still require higher levels of FSW technology. Numerical modeling based on discretized techniques like finite element, finite difference methods, and finite volume methods were used to understand complex phenomena and prediction of temperature, material flow, and residual stresses during welding. Moreover, previously investigated FEM based model doesn’t deal with the advective term both for momentum and temperature during FSW. During FSW of steel heat transfer by convection cannot be ignored and hence a more advanced coupled thermal, and material flow model is required to analyze thermal and plastic flow field phenomenon.

It may be inferred that several aspects on FSW of steel are investigated and also published work gave a very mixed and inconsistent impression about the weld quality. Apart from a feasibility study, optimization of process parameters and development of process envelope are required. The selection of tool material, optimizing the tool design to reduce the wear and deformation still needs to investigate. Although, a lot of issues are addressed in FSW of similar steel, the available knowledge on FSW of dissimilar steel is very limited. Moreover tool wear is reported in FSW of steel, however studies focused on tool wear mechanism are rarely investigated in published literature. In addition, the experimental investigations on plasma assisted FSW of steel are not reported. Accordingly research gaps are set to enhance the fundamental information available on FSW of steel and are enlisted as below:

- ❖ Information available in the literature for FSW of steel is limited unlike aluminum alloys. Moreover, reported literature gives a mixed and complicated information on microstructural evolution and mechanical characterization of welded joints.
- ❖ Previous investigations were focused on the feasibility of dissimilar steel only. Effect of process parameters like rotational speed, traverse speed and tool tilt angle were not studied systematically.
- ❖ Limited studies are performed on coupled thermal and material flow modelling on FSW of steel alloys.
- ❖ No systematic study is carried out to investigate the degradation of tungsten tool during FSW of steel**.** Focused studies on tool wear and degradation are highly required for the assessment of tool material and tool design.
- ❖ Most of the previous studies used laser and ultrasonic source as preheat source. Efforts can be made in the direction of hybrid FSW technologies in joining of high strength steel.

:-------------------*-------------------*---------------------:

Chapter 3

3 METHODOLOGY

3.1 INTRODUCTION

This chapter deals with the experimental procedures, methods, and mathematical model to fulfill the objectives as stated in chapter 1. The chapter is divided into two sections (i) experimental details and (ii) mathematical model. Section-I is further subdivided into two sections i.e., 3.2.1 material selection, 3.2.2 experimental setup. In section-II, mathematical model provides a sequence of information of CFD models to study the temperature distribution and material flow during FSW of DH36 steel. The mathematical model provides detailed information regarding material model, contact condition, heat generation, meshing, mesh sensitivity analysis, and boundary problems.

3.2 EXPERIMENTAL DETAILS

3.2.1 Material selection

The plate material studied in this work are mild steel (UNS G10060 & UNS G10080), stainless steel (UNS S30400), and shipbuilding grade DH36 steel. The chemical composition ($wt.\%$) of UNS S304, UNS G10080, UNS G10060 are summarized in Table *3.1*. To demonstrate the reliability of FSW process, three different grades of steel are selected. The reason for selecting DH36 steel is due to its huge application in shipbuilding industries. In commercial ship construction industries, there are five different grades of steel employed besides the usage of composite materials and aluminum series (Fowler et al. 2016; Konkol & Mruczek, 2007). The most commonly used grade, Grade DH36, is specified with a minimum of 352 MPa (51 ksi) yield strength and 490 MPa (71 ksi) ultimate tensile strength (Sampath, 2006). From the metallography point of view, the DH36 steel has a higher average carbon content than the D grade steel and hence a higher pearlite content, which reduce the ductility of the plate, and make it less susceptible to distortion (Sampath, 2006). The fine grain size and high toughness of DH36 steels is due to addition of elements (i.e. Molybdenum, Vanadium, Niobium, and Titanium) in micro amount and thermomechanically controlled manufacturing process (TMCP). TMCP is a combination of deformation and thermal processes that change the microstructure during production itself. These processes affect the strain, strain rate, temperature, and the cooling rate of the material. These effects change the grain size and the grain morphology of the material. The higher-strength DH36 also results in improved weldability, formability, along with high toughness (Sampath, 2006). Both the ferrite (α_f) and pearlite (α_{fc}) often appear as bands in the microstructure and the ferrite structure is characterized by an equiaxed grain morphology.

Table 3.1 Chemical composition of UNS G10060, UNS G10080, stainless steel (UNS S30400), and DH36 steel (wt.%)

Chemical composition						
UNS G10060	Carbon	Manganese	Sulphur	Phosphorous	Silicon	Copper
	0.06	0.52	0.033	0.031	0.01	0.04
UNS G10080	0.08	0.51	0.03	0.03	0.02	0.06
UNS S30400	Carbon	Manganese	Sulphur	Phosphorous	Silicon	Copper
	0.038	1.02	0.002	0.028	0.32	0.09
	Nickel	Chromium	Molybdenum	Iron		
	8.2	18.1	0.04	Rest		
DH36	Carbon	Manganese	Sulphur	Phosphorous	Silicon	Copper
	0.146	1.51	0.001	0.007	0.22	0.14
	Titanium	Vanadium	Niobium	Aluminum	Iron	
	0.003	0.003	0.03	0.017	Rest	

Tool material selection for the present study was a challenging task concerning tool cost and tool strength at elevated temperature. In the present investigation, two different tungsten carbide-based composites were investigated in the joining of different grades of steel. The details of tool properties are summarized in Table *3.2*.

3.2.2 Experimental setup

Welding experiments were performed on a semiautomatic FSW machine with 25 kW spindle drive motor power as shown Figure *3.1*a. A hydraulic power pack system was fitted that provided maximum z force of $55-58$ kN (working range) during welding condition. The machine frame was robust, thus it did not deflect significantly during the FSW experiments. The available traverse speeds and rotational speeds are in the range of 20 mm/s to 300 mm/s and 300 and 1800 rev/min respectively. The clamping of the test pieces was done such that the movement of the plates was restricted under both plunging and translational movement of the tool as depicted in Figure *3.1*b.

Table 3.2 Details of tungsten carbide tool materials used for FSW

Properties (Room Temperature)	**Values**	
	Tool A	**Tool B**
Composition (wt. %)	WC-6 wt.%Co	WC-10 wt.%Co
Hardness	75 HRC	81 HRC
Rupture Stress	2460 N/mm^2	3740 N/mm^2

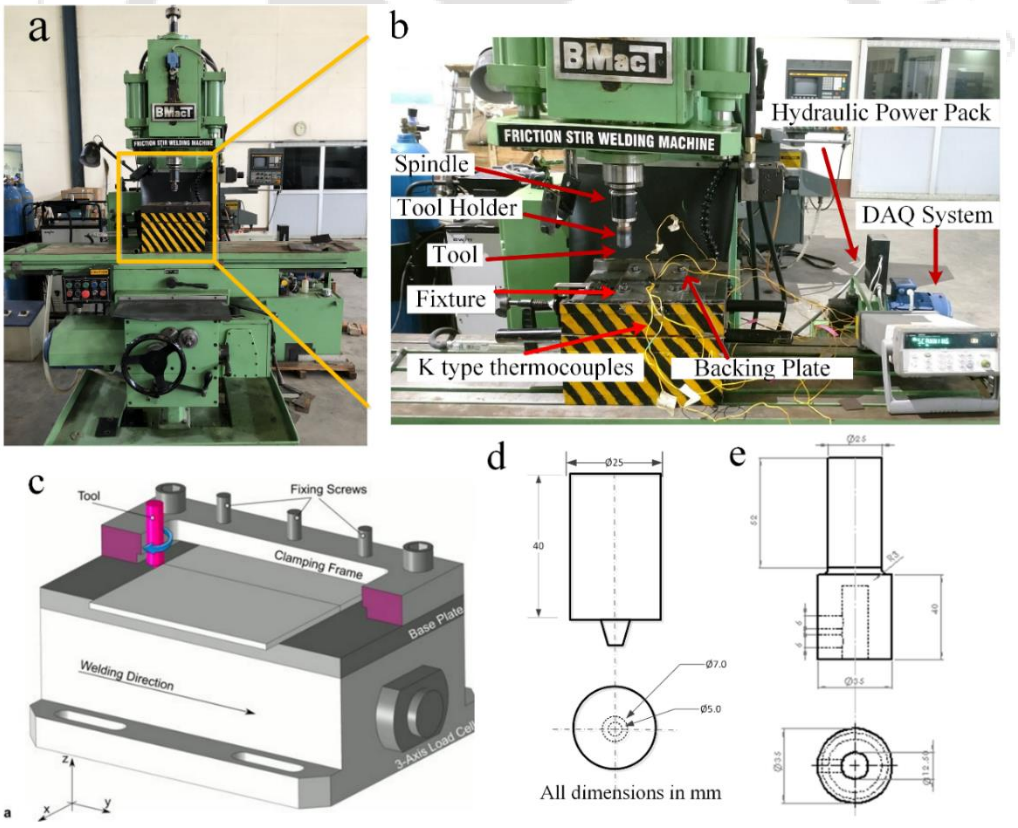

Figure 3.1 (a) Illustration of FSW machine, (b) experimental setup used in the present study, (c) fixture developed to perform experiments, (d) tool dimensions, and (e) tool holder dimensions

The robust experimental fixture is designed and developed to perform the experiment which is shown in Figure *3.1*c. The low carbon steel plates were secured with work holding fixtures on the machine traverse table. The designs was aimed to constrain the motion in X, Y and Z direction during welding. The Y axis motion was constrained with horizontal clamps and the x axis motion was clamped by the stopper fixed at the end position. The fixture has mainly four main components i.e. backing plate, clamping plate, stopper and alignment bolts. It had all the necessary features required to clamp the work plate rigidly and arrest the motions in X, Y and Z directions during welding. The tool designs is chosen since this design showed the most consistent weld quality and minimum tool wear during FSW of high strength low alloy steel (DH36). Schematic diagram of tool and tool holder geometry is shown in Figure *3.1*d and Figure *3.1*e respectively. The shoulder diameter selected for the present investigation was 25 mm. The tool pin was tapered from 7 mm at the shoulder to 5 mm at the free end. The tools were tested in robust conditions i.e. in an ambient atmosphere without providing and shielding gases any pressurized cooling during welding. The tool was fixed in the tool holder made up of mild steel with the help of a grove screw. The tool and tool holder assembly is fixed in the arbor. For PFSW, the plasma torch was fixed with the FSW machine spindle for preheating or interpass heating during the FSW of DH36 steel. The plasma torch can move at a fixed welding speed, the same as the traverses speed during welding. Transferred arc mode (i.e. between a tungsten electrode and the workpiece plate) is employed with DCEN polarity in conduction mode in the present investigation, the direct current straight polarity (DCEN) mode is used. Pure argon gas (99.95%) is used as a plasma gas as well as a shielding gas during the welding process. The plasma and shielding gasses' flow rate is maintained at 0.6 L/min and 12 L/min, respectively.

The above-mentioned information is a broad description of the experimental procedures like FSW machine setup, FSW fixture, backing plate material, tool materials and plasma assisted FSW setup. Details of various machines used and their specifications are summarized in Appendix A.

3.3 NUMERICAL MODELLING OF FSW PROCESS

Numerical modeling provides an adequate and in-depth understanding of the weld behavior which is necessary to ensure the efficiency, safety, and reliability of such joints. It provide useful information regarding process variables without performing the actual experiments. Physical testing is expensive, time-consuming and requires large number of resources and trials. The basic topics in FSW's numerical modeling are the temperature field, material flow, and the residual stresses. For the metallurgical point of view, thermal history of the weld is needed to connect the weld hardness data, microstructural features to welding parameters and the material transfer can throw insights in the underlying mechanism for joint formation. The modeling considering appropriate boundary conditions can lead to self-optimization of the process conditions. Previous literature suggested that previous models were primarily focused on FSW of aluminum alloys, and only a few studies are investigated on steel alloys (Nandan et al. 2008). Additionally, during the FSW of high-strength materials like steel, the importance of materials flow during FSW cannot be neglected in the heat transfer calculations. Hence present study deals with an Eulerian approach using commercial CFD code, ANSYS FLUENT, to understand the temperature characteristics and material flow behaviors. The details of numerical model is described for the present CFD based FSW simulation of DH36 steel.

3.3.1 Model description

In the present study, a 3D, coupled heat and material flow model is investigated in laminar approach under steady state condition. The simulation is performed on the commercial available computational fluid dynamics (CFD) software ANSYS®. Eulerian frame work is studied in which tool is fixed at the middle portion, and tool-plate is generated as a single part of the domain geometry as shown in Figure *3.2*.

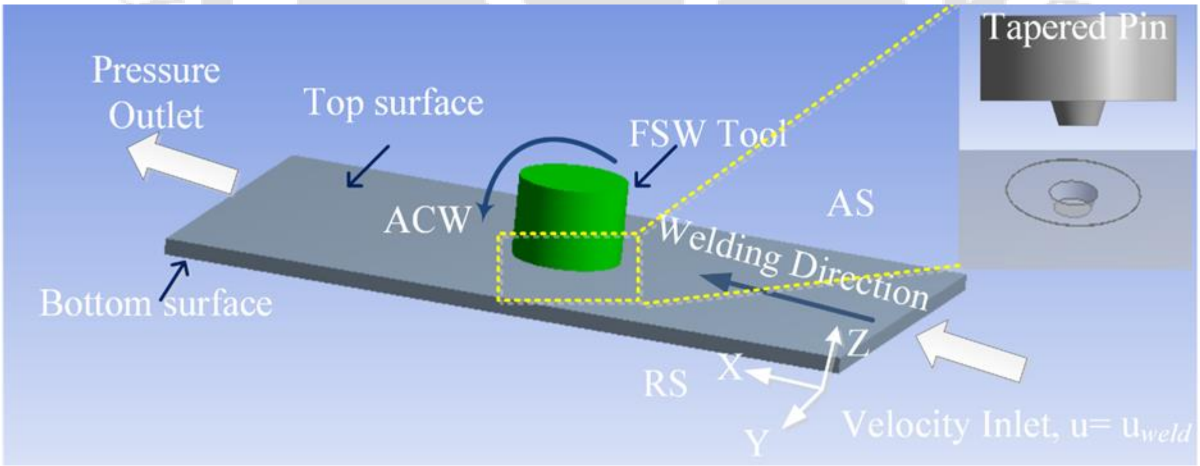

Figure 3.2 Boundary conditions of the FSW process used in present computational model

A 3 dimensional Cartesian system for the work plate and the tool is established. The origin is set at the intersection point between the tool axis and the axis of bottom plate. The x axis indicates the direction of welding and the z-axis indicates the tool axis and the thickness of workpiece material. The tool has given rotational motion and interior domain has set to move with the welding speed by providing the same at the velocity inlet side. On the other hand, opposite end of the plate is set at zero pressure to avoid the reverse flow at the pressure outlet. Plate side walls along with top and bottom walls were given the same velocity as the velocity inlet. The welding is performed in steady state case which is justified by the fact that the weld profile and properties remain roughly constant during the welding phase. Except for the initial and the final periods of welding, i.e., during tool–pin insertion and extraction, the heat generation occurs at a constant rate if the tool rotates and moves forward at a constant speed.

3.3.2 The governing equations

The Navier–Stokes equations are solved for the incompressible, non-Newtonian fluid in single-phase fluid flow representing the quasi-static thermal and fluid flow boundary problem. The conservation equation (Nandan et al. 2007) for continuity, momentum and energy are summarized below,

The continuity equation is expressed as:

$$\vec{\nabla} \cdot \rho\overrightarrow{(V)} = 0 \qquad \textbf{(3.1)}$$

The momentum equation is written as:

$$\rho(\vec{V}.\nabla)\vec{V} = -\nabla \mathrm{p} + \mu\nabla^2(\vec{V} + \overrightarrow{V^T}) \qquad \textbf{(3.2)}$$

where ρ, p μ and V are the density, fluid pressure, viscosity, material flow velocity respectively.

The energy equation is expressed as:

$$\rho C_P(\vec{V}\cdot\vec{\nabla}T) = K\nabla^2 T + \dot{Q}_1 + \dot{Q}_2 \qquad \textbf{(3.3)}$$

where K is thermal conductivity, T is temperature $\dot{Q}_1$ is the heat generation by friction heating including sliding and sticking conditions and $\dot{Q}_2$ is the viscous plastic dissipation heat source due to plastic deformation near the tool vicinity in the shear zone. A rough estimate of the viscous dissipation of momentum per unit volume, $\dot{Q}_2$, is calculated as $f_m\ \mu_{fluid}\psi$, where ψ is given by:

$$\psi = 2\left(\left(\frac{\partial u_1}{\partial x_1}\right)^2 + \left(\frac{\partial u_2}{\partial x_2}\right)^2 + \left(\frac{\partial u_3}{\partial x_3}\right)^2\right) + \left(\frac{\partial u_1}{\partial x_2} + \frac{\partial u_2}{\partial x_1}\right)^2 + \left(\frac{\partial u_1}{\partial x_3} + \frac{\partial u_3}{\partial x_1}\right)^2 + \left(\frac{\partial u_3}{\partial x_2} + \frac{\partial u_2}{\partial x_3}\right)^2 \quad \textbf{(3.4)}$$

where f_m is an arbitrary constant that indicates the mixing amount in the system at atomic level and μ_{fluid} is the viscosity of the fluid (Nandan et al. 2007).

3.3.3 Material properties and material model

In this study DH36 steel is considered as the base material. The density of the steel plate is taken as $7860\ \mathrm{kg/m^3}$ (Incompressible material). Temperature-dependent thermo-physical properties, thermal conductivity (k_{wp}) and specific heat (C_{pwp}) for the shipbuilding (DH36 steel) are adapted from the available literature (Al-Moussawi et al. 2017).

$$k_{wp} = 23.6 + 51.96e^{-2.03T/1000} \quad \textbf{(3.5)}$$

$$C_{pwp} = 689 + 46.2e^{3.78T/1000} \qquad \text{For } T < 700\ °C \quad \textbf{(3.6)}$$

$$C_{pwp} = 207 + 294.4e^{1.41T/1000} \qquad \text{For } T > 700\ °C \quad \textbf{(3.7)}$$

Temperature-dependent thermo-physical properties i.e. thermal conductivity (k_{tl}) and specific heat (C_{ptl}) for the tungsten tool material are adapted from the available literature (Nandan et al. 2008).

$$k_{tl} = 0.3671 - 2.29 \times 10^{-4}T + 1.25 \times 10^{-7}T^2 \quad \textbf{(3.8)}$$

$$C_{ptl} = 158 + 1.06 \times 10^{-1}T - 1.63 \times 10^{-5}T^2 \quad \textbf{(3.9)}$$

Non Newtonian viscosity is the most significant factor for heat generation in coupled heat and material flow modelling. The viscoplastic material model correlates the deviatoric stress tensor and the strain rate tensor. Non-Newtonian viscosity is assumed to change with the temperature and strain rate. Seidel & Reynolds (2003), Ulysse (2002) and Colegrove and Shercliff (2006) used the viscoplastic fluid flow model to calculate the temperature fields. The viscosity as a function of flow stress and strain rate is given as:

$$\mu_{fluid}=\frac{\sigma_{flow}}{3\dot{\in}} \qquad \textbf{(3.10)}$$

where the flow stress σ_{flow} is considered as perfectly plastic model, as suggested by Sellars & Tegart (1972) and further modified by Sheppard & Wright (1979).

The flow stress is obtained from the relationships provided in literature (Hasan et al. 2017; Shi et al. 2014) which is described as:

$$\sigma_{flow} = \frac{1}{\alpha_{mat}} sinh^{-1} \left(\frac{Z_n}{A_i}\right)^{\frac{1}{n_{mat}}} = \frac{1}{\alpha_{mat}}\left[\left(\frac{Z_n}{A_i}\right)^{\frac{2}{n_{mat}}} + \left(1 + \left(\frac{Z_n}{A_i}\right)^{\frac{2}{n_{mat}}}\right)\right] \qquad \textbf{(3.11)}$$

where Z_n is the Zener-Holloman parameter, used to calculate the temperature-dependent strain rate which is given as:

$$Z_n = \dot{\varepsilon}\left(\frac{Q_e}{R_g T}\right) \qquad \textbf{(3.12)}$$

where Q_e and R_g are the activation energy and universal gas constant. The constitutive constants A_i, n_{mat} and α_{mat} which represent material characteristics can be obtained from the hot working (extrusion) process. The values of constitutive constants were taken from the work of Tello et al. (2010).

The effective strain is expressed as:

$$\dot{\epsilon} = \sqrt{\frac{2}{3}\varepsilon_{ij}\varepsilon_{ij}} \qquad \textbf{(3.13)}$$

where $\epsilon^{\cdot}{}_{ij}$ is strain rate tensor can be represented as:

$$\epsilon^{\cdot}{}_{ij} = \frac{1}{2}\left(\frac{\partial u_j}{\partial x_i} + \frac{\partial u_i}{\partial x_j}\right) \qquad \textbf{(3.14)}$$

Therefore, the final expression for the material viscosity is expressed as:

$$\mu_{fluid} = \frac{1}{3\dot{\epsilon}\alpha_{mat}}\left[\left(\frac{Z_n(T, \alpha_{mat})}{A_i}\right)^{\frac{1}{n_{mat}}} + \left(1 + \left(\frac{Z_n}{A_i}\right)^{\frac{2}{n_{mat}}}\right)\right] \quad \textbf{(3.15)}$$

3.3.4 Meshing

A rectangular plate (200 mm × 100 mm × 4 mm) with a cylindrical tool with tapered pin (i.e. 7 mm at the pin root and 5 mm at the pin tip) is used. The meshing is done using tetragonal elements with a high degree of refinement at the workpiece-tool interface to obtain high accuracy in the output fields, i.e., temperature, strain rates, viscosity, and path lines, as shown in Figure *3.3*. Moreover, the skewness and aspect ratio is kept low and high degree of orthogonality is maintained. The design and number of mesh elements are determined considering both the efficiency and accuracy of the computation. Further, a grid independence test is carried out using three different mesh sizes, ranging from 281386 to 400000 elements. It is obtained on further refinement of mesh from 281386 to 400000 elements, no reasonable changes are obtained in the output temperature results.

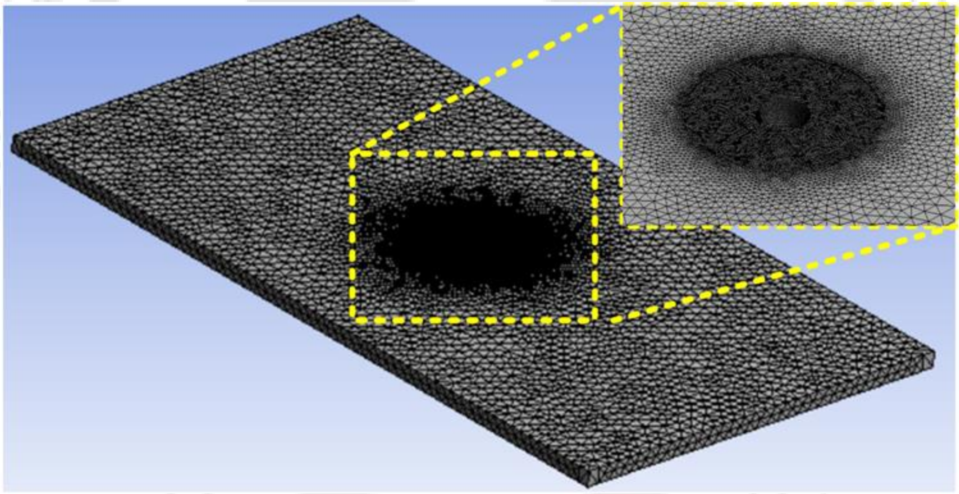

Figure 3.3 Meshed geometry of 3D model

Apart from element type, the size of an element plays a vital role in determining the accuracy and computational time. Finer mesh leads to higher computation time while coarser produces inaccurate results. Mesh optimization is necessary in maintaining the accuracy of the results simultaneously the reduced computational time. Therefore to strike a balance between the accuracy and computational time, mesh sensitivity is carried out where mesh size is varied from coarser to finer elements. The computed temperature ($\frac{T}{T_{amb}}$) for the same set of parameters and their output responses are compared. Three different sizes of mesh as shown in Table *3.3* are considered and non-dimensional temperature output responses are compared.

Table 3.3 Peak temperature obtained for all three meshes

Mesh	**No. of elements**	**Non Dimensional Temp. Factor ($\frac{T}{T_{amb}}$)**
Grid 1	280000	4.5417
Grid 2	340000	4.5473
Grid 3	400000	4.5503

From the results obtained in Table *3.3*, it is clear that no significant variation is further observed on increasing the number of mesh elements. Hence for the present simulation Grid 1 is selected to maintain the accuracy in the output fields as well as less computational time.

3.3.5 Boundary conditions

3.3.5.1 Heat partition at the tool work interface

Due to considerable difference in the thermal conductivity between the workpiece and the tool material, heat loss or transferred to the tool material cannot be ignored. The partition of the heat between the tool material and workpiece is also considered in the previous literature (Nandan et al. 2007; Pal & Phaniraj 2015). The heat flux boundary at shoulder-workpiece contact interfaces is express as

$$k\frac{\partial T}{\partial \vec{n}} = \lambda Q_{tsi} \quad \textbf{(3.16)}$$

$$\lambda = \frac{J_{wp}}{J_{wp} + J_{tl}} \quad \textbf{(3.17)}$$

$$J = \sqrt{k\rho C_p} \quad \textbf{(3.18)}$$

where subscripts wp and tl denote the workpiece and the tool. λ and J are the heat fraction entering the workpiece and the heat generation at shoulder workpiece contact interface respectively. K , C_p and ρ are the thermal conductivities, specific heat capacities and density of the materials respectively i.e., workpiece and tungsten tool. Based on the values of K and C_p of both tool and workpiece, the value of heat fraction is 0.401. The obtained fraction heat value is close to the fractional heat in the published work of FSW of low carbon steel (Nandan et al. 2007).

3.3.5.2 Heat flux at tool shoulder and workpiece interface

In the steady-state analysis, for thermal and fluid flow model, the heat flux is applied to the tool-workpiece contact surface i.e. shoulder region, pin lateral region and the pin bottom region. The model incorporates the heat generation by frictional heat considering both sliding and sticking friction. Frictional heat flux incorporates both the sliding and sticking friction at contact interface (Nandan et al. 2006). The expression for the heat flux at the contact boundary surface is as follows:

$$Q_1(r) = \frac{3Q_{ss}r}{2\pi(R_1^3 - R_2^3)} \tag{3.19}$$

Q_1 (W/m^2) is total heat considering the frictional heating, R_1 and R_2 is are the outer and inner radius of tool shoulder. The heat generation rateQ_{tsi} at the contact interface is expressed as:

$$Q_{tsi} = [(1-\delta)\eta_{mech}\tau_{yield} + \delta\mu P](\omega \mathrm{R}_1 - \mathrm{U}\sin\Theta) \tag{3.20}$$

where η_{mech} indicates the efficiency of mechanical work converted into the heat energy; P is the normal pressure obtained when the downward force is divided by the area of tool shoulder; the maximum shear stress τ_{yield} for yielding is assumed in accordance with the distortion energy/ von Mises theory for plane stress. R_1 is the radius of tool shoulder and ω is the tool rotational speed. U is traverse speed during welding, θ is the angle lies between position vector r and velocity vector U. The velocity $(\omega R_1 - U\sin\Theta)$ represents the local velocity of a point on tool with the origin fixed at the tool axis. The other constants in the heat equation i.e. μ and δ indicates the spatially variable frictional coefficient and spatially variable fractional slip respectively. Frigaard et al. (2001) chosen the coefficient of friction as 0.4 for considering both partial sticking and sliding friction. In present investigation, as shown in Figure *3.4*a, extent of slip δ is given as:

$$\delta = \left\{1 - exp\left(-\frac{\omega r}{\delta_o \omega_o R_1}\right)\right\} \tag{3.21}$$

where δ denote the spatially variable fraction-slip , $\delta_{\circ}$ is an arbitrary constant, ω is local rotational speed at a local distance r in the contact region. ω_o and R_1 are the rotational speed and the tool shoulder radius respectively. A typical value of rotational speed, ω , is used to non-dimensionalize the tool rotational speed of, ω_o. Moreover, Figure *3.4*b shows the spatially variable friction coefficient μ ,as suggested by Arora et al. (2009), is evaluated as:

$$\mu = \mu_{\circ}\, exp(-\frac{\omega r}{\omega_o R_1}) \quad \textbf{(3.22)}$$

Here, $\mu_{\mathbf{o}}$ is the arbitrarily friction coefficient and its value is taken to be 0.3. ω_o and R_1 are the rotational speed and the tool shoulder radius respectively.

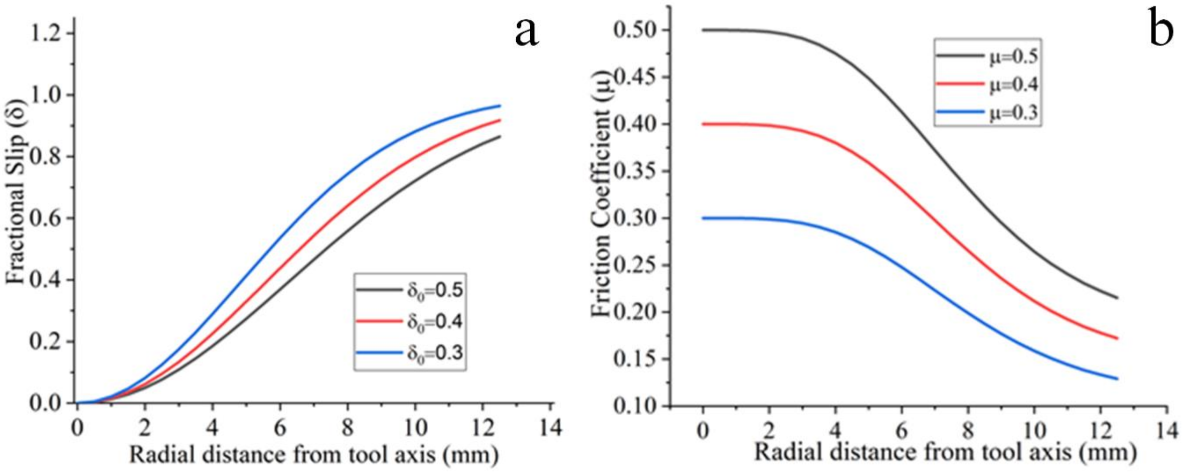

Figure 3.4 Fractional slip (δ) variation with the tool radii, and (b) variation of friction coefficient (μ) with tool radial distance

3.3.5.3 Representation of material flow

As shown in Figure *3.5*, the speeds with which material moves at shoulder workpiece interface, u_s, and v_s along the welding direction and normal to the welding direction in the plane of the of the plate being welded, are given by:

$$u_s = (1-\delta)(\omega R_1 \sin\theta - U) \quad \textbf{(3.23)}$$

$$v_s = (1-\delta)\omega R_1 \cos\theta \quad \textbf{(3.24)}$$

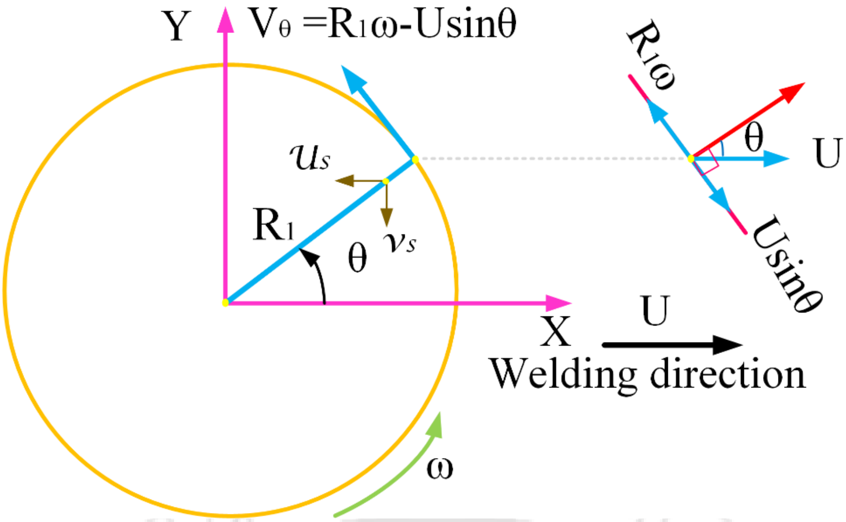

Figure 3.5 Velocity of a point on tool shoulder

3.3.5.4 Heat losses at the walls

The heat losses at the plate edges i.e. top walls, (excluding the shoulder workpiece contact region) included the convection and radiation heat loss during the welding, while side walls and the bottom walls included the heat transfer by convection with higher convection coefficient at the bottom side. The boundary condition at top wall (in the range $> R_1$) and bottom wall are given as:

$$k\frac{\partial T}{\partial \vec{n}} = h_t(T - T_{amb}) + \varepsilon_{se}\sigma_b(T^4 - T_{amb}^4) \tag{3.25}$$

$$k\frac{\partial T}{\partial \vec{n}} = h_b(T - T_{amb}) \tag{3.26}$$

$$k\frac{\partial T}{\partial \vec{n}} = h_s(T - T_{amb}) \tag{3.27}$$

where T_{amb} is the ambient temperature, ε_{se} is the surface emissivity, σ_b is the Stefan-Boltzmann constant ($5.67 \times 10^{-8}\ \mathrm{W/m^2K^{-4}}$). Here h_t, h_b and h_s are the convective heat transfer coefficient at top surface, bottom surface and side walls respectively ($\mathrm{W/m^2K^{-1}}$). In the present investigation, conduction heat transfer at bottom plate and side walls is assumed to high convection heat loss condition. The convection heat loss at the backing plate is varied from 750 to 2100 $\mathrm{W/m^2K^{-1}}$) to get the reasonable temperature gradient across the plate. Schmidt (Schmidt & Hattel, 2004) proposed the range of heat transfer coefficient for backing plate as 1000-2000 $\mathrm{W/m^2K^{-1}}$) for more realistic temperature. The final value of heat convective transfer coefficient h_b was considered to 2000 $\mathrm{W/m^2K^{-1}}$ by inverse analysis method in order to maintain the uniformity in the temperature gradient along the thickness direction. Along with backing plate heat convection coefficient, a convective heat transfer boundary condition is assumed at side walls with an average value of convective heat transfer coefficient h_s as 200 $\mathrm{W/m^2K^{-1}}$) to compensate the heat loss by conduction.

3.4 SOLVER AND DISCRETIZATION SCHEME

The governing equations are discretized by following the finite volume discretization approach. Pressure based solver is used for the constant density problem (due to the prevailing Boussinesq approximation in the flow domain). The convection-diffusion terms of the governing equations are solved using the second-order upwind scheme. Pressure–velocity coupling which is used to calculate the velocity and temperature fields, is solved following the Semi-Implicit Method for Pressure Linked Equations (SIMPLE) algorithm. The simulations are initialized with the flow domain having zero velocity and ambient temperature. The Relaxation factor that prevents the simulations' divergence is set as 0.5 for the momentum equation, and 0.9 for the energy equation respectively. The convergence criteria of the numerical simulations are maintained as 10^{-6} for the momentum, and energy equations and 10^{-4} for the continuity equation.

3.5 SUMMARY

This chapter provided the thorough procedure of experimental investigation and mathematical models to reach the objectives stated in Chapter 1. In addition to that details of material and methods, and experimental procedures are also provided. The material model, governing equations, mesh details, grid independence test, contact condition boundary conditions, solver and discretization scheme are also discussed. Experimental and numerical results fulfilling the objectives of the present thesis will be discussed in the forthcoming chapters.

:-------------------*-------------------*---------------------:

Chapter 4

4 FSW OF LOW CARBON STEEL PLATES WITH TUNGSTEN CARBIDE TOOL

4.1 INTRODUCTION

This chapter deals with the friction stir welding of low carbon steel (UNS G10060 steel) using a tungsten carbide tool. The weld characterization is done by performing elementary mechanical testing, i.e., Vickers microhardness test at the transverse cross-sectional surface and the tensile test to evaluate the transverse tensile properties. The primary area of interest is to investigate the different structural features (onion rings, banded structure, lamellar bands, and vortex swirls) in the weld zone at different welding conditions. In addition to that, microstructure evolution at several locations inside the weld zone (i.e., SZ, AS-TMAZ, RS-TMAZ, AS-HAZ, and RS-HAZ) zone is characterized by using an optical microscope, SEM equipped with EDS and XRD analysis. The mean line intercept method is used to calculate the average grain size in the SZ and TMAZ of the weld zone. FSW joints revealed that grain morphology depended on various temperature, strain, and strain rate dependent phenomenon like dynamic recovery, dynamic recrystallization, and grain growth which are mainly controlled by welding process parameters like rotational speed and traverse speed. The macroscopic analysis demonstrated that chances of defect generation at higher weld traverse speed are relatively more due to insufficient heat input to provide flowability of plasticized material.

4.2 MATERIALS AND METHODOLOGY

In this study, friction stir butt joints are made on 4 mm thick steel plates along the rolling direction. The properties and composition of the base plate is described in Table *4.1*. The plate's dimensions are 185 mm ×50 mm ×4 mm $(l \times w \times t)$ and plates are cleaned by acetone to avoid contamination in the weld zone. Tungsten carbide tool with flat shoulder (25 mm diameter) and tapered pin (7−5 mm) is used. The other parameters, i.e., backward tool tilt angle and tool plunge depth are kept constant at 2° and 0.2 mm, respectively. Different stages FSW process and tool holder assemble are shown in Figure *4.1*a and b.

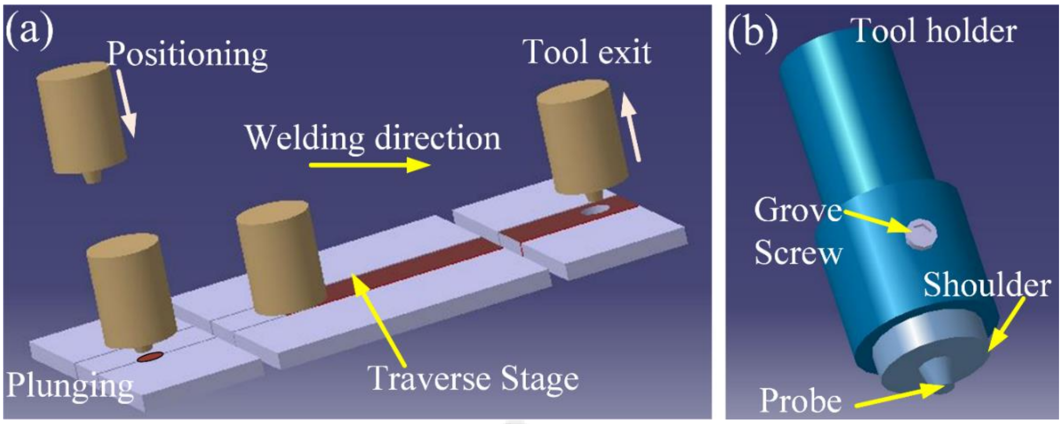

Figure 4.1 (a) Shows the schematic diagram of the FSW process, and (b) FSW tool mounted on the tool holder

The correlation between tool dimensions, process parameters, and process temperatures are considered from the preliminary investigation (Tiwari et al. 2019b; Tiwari et al. 2019a) and available literature (Karami et al. 2016; Lakshminarayanan et al. 2010) to narrow down the welding parameter domain. Welding parameters are chosen in such a way that the joint should be free from defects, as described in Table *4.2*.

Table 4.1 Mechanical properties and chemical composition of low carbon steel

Chemical Composition		**Mechanical Properties**	
Element	**Weight %**		
C	0.06	YS (MPa)	254
Mn	0.4	UTS (MPa)	323
P	0.031	% Elongation	13.7
S	0.033	Hardness ($HV_{0.5}$)	91
Si	0.01		
Fe	Rest		

The welding parameters for the present investigations are reported in Table *4.3*. Within the chosen working range of parameters, the joints are free from defects. Samples are cut transverse to the welding direction for metallographic and mechanical testing. Metallographic samples are polished on a rotating disc polishing machine to mirror finish using diamond paste. Specimens are then etched with Nital solution (5% nitric acid) and Murakami reagent

(5g $Fe_3\,(CN)_6$, 5g NaOH, and 50 ml distilled water) for steel and tungsten tools, respectively. Microstructural analysis is carried out using an optical microscope and field emission scanning electron microscope (FESEM) equipped with energy dispersive spectroscopy (EDS). Vickers microhardness is evaluated at the transverse cross-section at a load of 0.5 N for a dwell time of 15 s. Tensile properties are evaluated at 1 mm/min on the universal tensile testing machine.

Table 4.2. Selection of lower and upper limits of traverse speed and rotational speeds and its effect on weld quality

Process parameter	**Parameter range**	**Top surface**	**Weld quality**	**Remarks**
Rotation speed (higher side)	>875 rpm & 280 mm/min		Improper joint.	Excessive wear of tool pin
Rotation speed	875 rpm & 180 mm/min		Improper joint at the root of the weld	Tool pin wear at the end of weld
Rotational speed	600 rpm & 180 mm/min		Good quality weld	-
Rotational speed (lower side)	300 rpm & 180 mm/min		Good quality weld	-
Traverse speed (higher side)	600 rpm & 280 mm/min		Defect on the AS of the joint	Improper consolidation due to less heat input.
Traverse speed	600 rpm & 40 mm/min		Good quality weld	-
Traverse speed	300 rpm & 40 mm/min		Good quality weld	-
Traverse speed (lower side)	300 rpm & <20 mm/min		Excessive flash and Improper joint at the root of the weld	Improper joint

Table 4.3. FSW process parameters for the present investigation

Weld ID	Rotational Speed (rpm)	Traverse Speed (mm/min)
Weld 1	600	90
Weld 2	600	132
Weld 3	600	180
Weld 4	450	132
Weld 5	300	132

4.3 RESULTS AND DISCUSSION

Figure *4.2* shows the transient thermal history of the weld 1 and the process force recorded during the welding condition. Peak temperature recorded by thermocouples at a location of 15 mm, 20 mm, and 30 mm from the weld center line on the advancing side (AS) is 290, 182, and 120 °C. The peak temperature decreased gradually with an increase in distance from the weld center toward the sheet's edge. As a result, it showed different microstructure in different weld zones. The maximum temperature recorded on the retreating side (RS) at the same locations is 17%, 29%, and 37% less than the advancing side (AS).

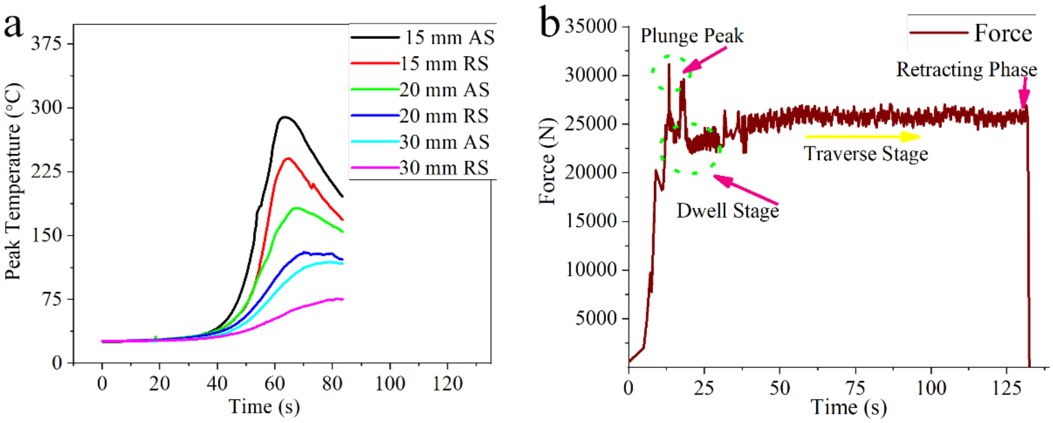

Figure 4.2 (a) Transient thermal history at different locations, and (b) force curve during the plunge, dwell stage, and traverse stage of welding

Figure *4.2*b shows the axial downward force during all three welding stages, i.e., plunge, dwell, and traverse stage. The axial force must ensure a certain plunge of the tool shoulder in the workpiece material to avoid open tunnel defects (insufficient plunging) or excessive burr generation (excessive plunging). Peak value of 33.6 kN is observed during the plunge stage.

Average axial loads of 25.7 kN is recorded during the traverse stage. Maximum fluctuations (i.e., spikes) of ±1.5 kN are observed in the axial force curve during the weld traverse stage. These spikes in the process force lead to compliance of discrete stick-slip condition that occurs during welding. The axial force is approximately the same for all the conducted experiments, which must adhere to the temperature- viscosity variation laws.

4.3.1 Surface assessment

Figure *4.3* shows the top surface appearance and macrographs of the weld cross-section of the welded samples. The top surface appearance of the welded plates is a good indicator that the forces involved during the process are stable, and the absence of flash after joining proved that the parameters set was suitable to maintain the stirred material within the joint. The macrographs show that the weld zone is not symmetric about the weld centerline, as indicated in Figure *4.3*b. From the macrographs, it is possible to conclude that the process parameters rotational speed and traverse speed have a more significant effect on the overall weld beads geometries. There is complete consolidation at the weld root for all welding conditions.

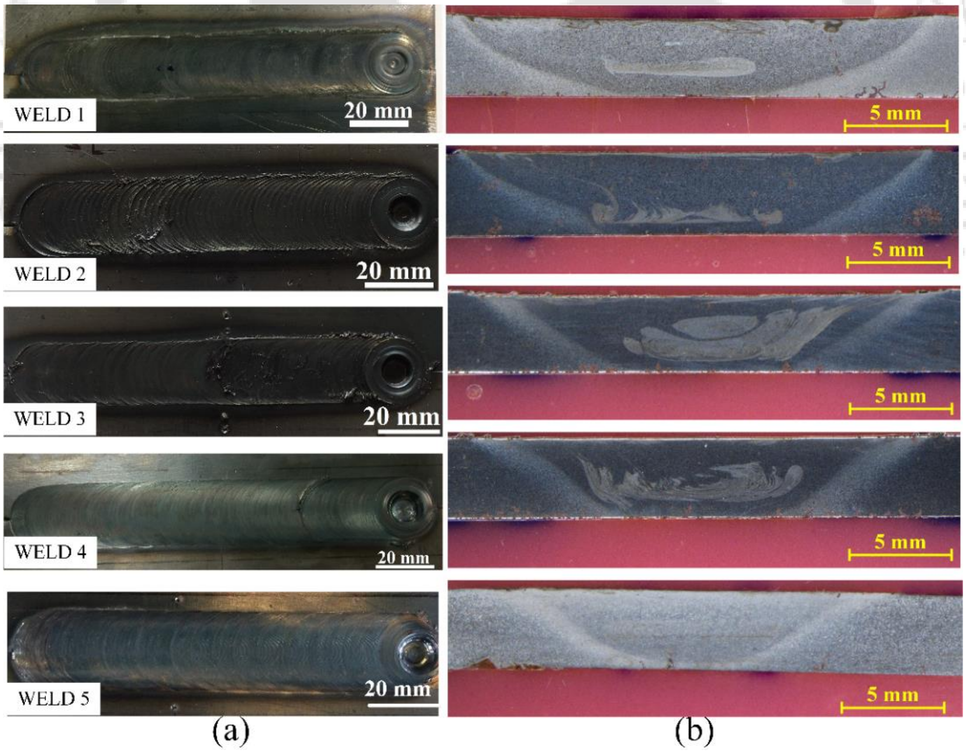

Figure 4.3 (a) Visual appearance of the welded joints, and (b) macrograph of the transverse cross-section of the welded samples

4.3.2 Microstructural characterization

The microstructure of the parent metal (Figure *4.4*a and Figure *4.4*b) is composed of ferrite (α_f) with a small pearlite (α_{fc}) amount. The pearlitic microstructure is revealed by its characteristic appearance of alternating layers of ferrite (α_f) and cementite(Fe_3C).

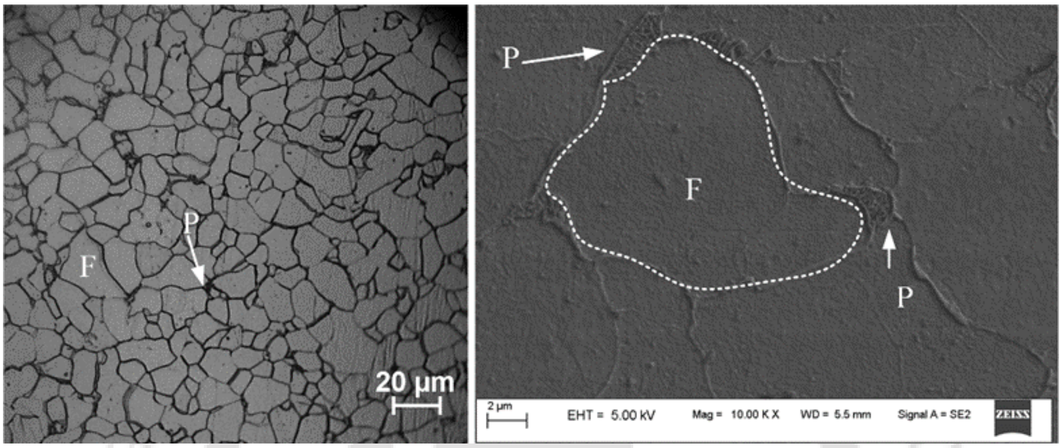

Figure 4.4 Microstructure of low carbon steel indicating ferrite and perlite structures with ferrite as major content: (a) optical microstructure; and (b) FESEM microstructure indicating perlite structure as alternative layers of ferrite and cementite

Figure *4.5* presents the low-magnification microstructural morphology of the welded sample.

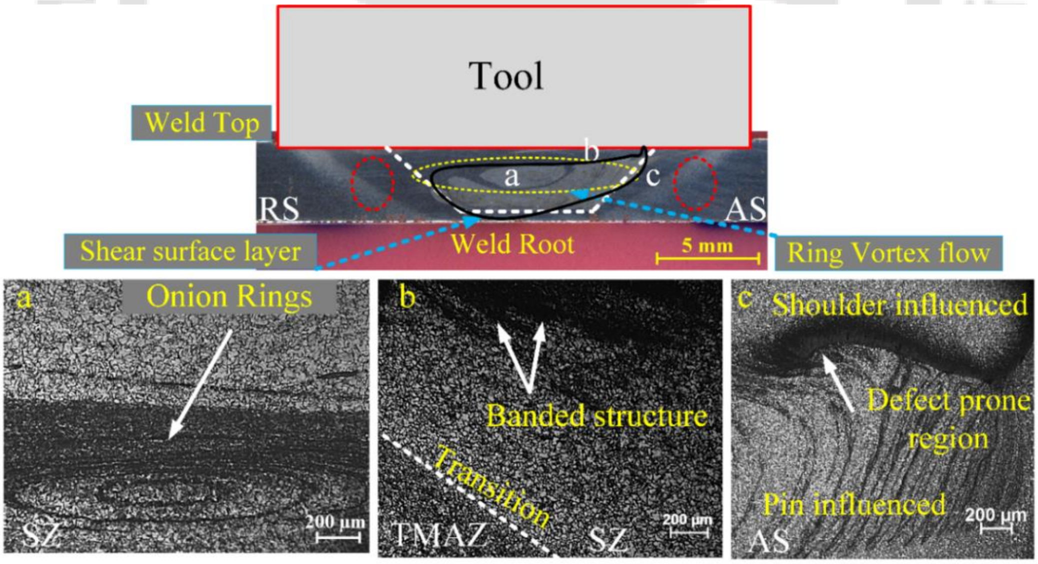

Figure 4.5 Microstructures obtained by optical microscope: (a) weld nugget indicating concentric ring structures also known as onion rings, (b) banded structures beneath the tool shoulder indicating intense plastic deformation at high temperatures; and (c) defect prone region in the AS-TMAZ of the weld zone

The weld zone has a relatively wider nugget zone and a visually discrete transition between the WNZ, TMAZ, and HAZ in FSW of low carbon steel. The weld nugget is the zone deformed by the tool pin during welding. Due to intense deformation at peak temperatures this zone is sometimes referred as the dynamically recrystallized zone (DXZ). In DXZ, there is sufficient strain energy and peak temperatures to promote recrystallization of grains (Mishra & Ma, 2005). In the FSW process, material movement is a complex phenomenon and is studied extensively for FSW of softer materials. Kumar & Kailas (2008) and Saeid et al. (2008) also studied in FSW of steel alloys. In general, FSW's material flow consisted of two regions: 'pin-driven flow' and 'shoulder-driven flow'. This results in the banded circular ''sub- regions'', which is generally a result of plastic flow and recrystallization of the base material. These structures can sometimes take the form of concentric rings in the nugget region and are generalized broadly as ''onion rings". Onion rings are most predominant at the center of the weld nugget zone as shown in Figure *4.5*a. Similar consecutive rings were also reported by Wan et al. (2014) in FSW of aluminum alloys. Figure *4.5*b shows swirls of dark-etching regions visible near the top of the FSW's stir zone. These banded structures indicate the high heat generation, extensive plastic deformation, and the downward forging of material by tool shoulder. It is observed that these band spacing changes with the changes in tool traverse and rotational speeds. These band spacing signifies how much the tool moves in the welding direction per weld rotation of the FSW tool. The similar banded structure are also reported previously by Nathan et al. (2016b) in friction stir welding of high strength low alloy (HSLA) plates. Figure *4.5*c shows the mixing of the shoulder and pin driven material flow. On the advancing side, the tool rotation and translation are in the same direction and cause chaotic flow and complex mixing. Material flow on the retreating side (RS) is not complex, unlike the advancing side (AS) since the material is simply deformed by tool rotation, but no significant mixing takes place on RS (Klingensmith et al. 2005).

Figure *4.6* shows the optical micrograph of the as-received base metal and distinct weld zones and Figure *4.6*b displays the grain size variation at different weld zones. Several noticeable areas are observed in the weld joint, including the weld nugget zone, the thermo-mechanically affected zone on the retreating side (TMAZ-RS) and the advancing side (TMAZ-AS), heat affected zone on the advancing side (HAZ-AS) and the retreating side (HAZ-RS) and the base metal (BM).

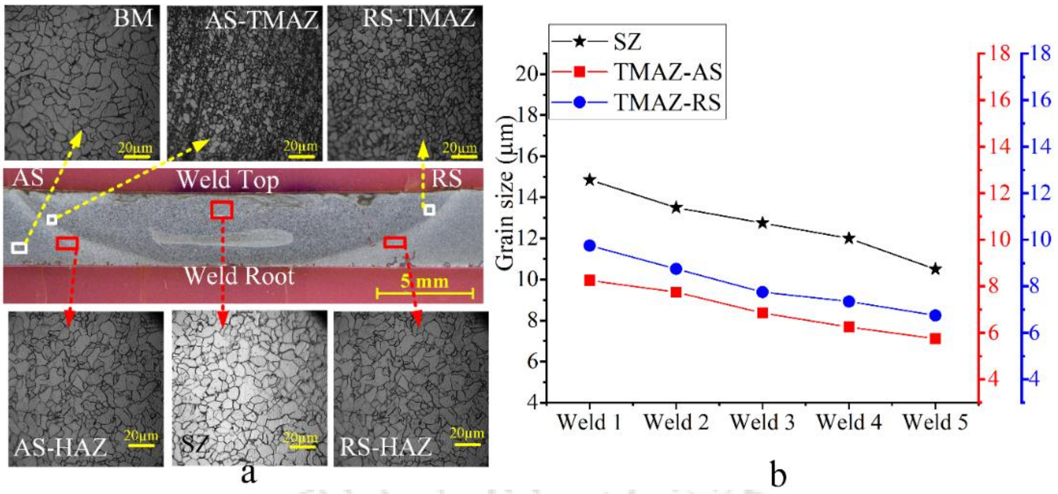

Figure 4.6 (a) Optical microstructure of the base material and weld produced at 600 rpm and 132 mm/min traverse at different locations i.e. SZ, AS-TMAZ, RS-TMAZ, AS-HAZ, HAZ-RS, and (b) grain size variation in WNZ, TMAZ-AS and TMAZ-RS

The base material consist of ferrite (α_f) and pearlite $(\alpha_f + Fe_3C)$ structures. The average grain size of the base material is 22.45 μm. Though the lower heat input associated with FSW produces finer grains compared to higher heat input process like fusion welding, the intrinsic nature of dynamic recrystallization and plastic deformation also plays a significant role in grain refinement. Compared with the base metal (Figure *4.6*a), the grains are remarkably refined due to dynamic recrystallization at a high strain rate. The grain size in the weld nugget zone is 14.75 μm approximately. Moreover, irrespective of the welding condition, the primary ferrite phase is mainly observed without any evidence of phase transformation in the weld zone. Weld nugget zone clearly indicates a typical thermomechanical affected zone due to the absence of allotropic phase transformation during the cooling stage. The TMAZ shows mixed recrystallized and recovered microstructures with highly misoriented and smaller grains due to mechanical and thermal effects. The weld joint's HAZ-AS and HAZ-RS indicate the coarse ferrite grains with grain size slightly less than the base material. Figure *4.6*b presents the grain size variation in the WNZ, TMAZ- AS, and TMAZ-RS of welded joints. Grain size is decreasing gradually on increasing traverse speed and decreasing rotational speed. The coarse grain size in the SZ compared to TMAZ indicates that the occurrence of dynamic recrystallization followed by grain growth due to peak temperatures experienced in this zone. Comparing the retreating side (RS) with the advancing side (AS) of the joint, the grain size is found similar in the weld's heat affected zone, except at the thermo-mechanically affected zone, where the grain size is relatively smaller at the AS than the RS. In the TMAZ, the grain size of weld 1 is reduced to 7.9 μm and 9.45 μm in the AS and RS, respectively. Konkol & Mruczek

(2007) also reported the coarser ferrite grain size in SZ than the TMAZ during FSW of high strength low alloy steel.

Figure *4.7* shows the microstructure at the bottom region in the advancing side of the weld joint.

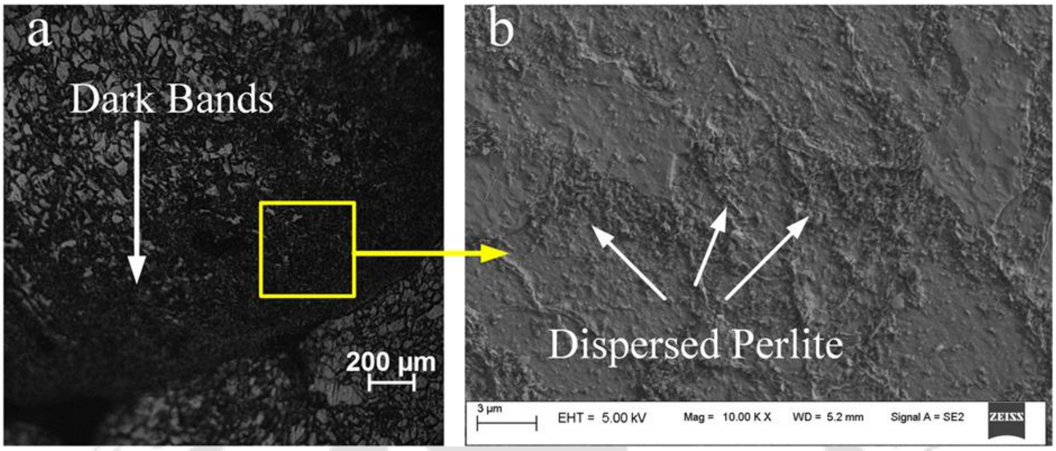

Figure 4.7 Microstructure at the bottom region in the advancing: (a) optical image indicating dark bands similar to those obtained at the top surface, and (b) FESEM image indicating dispersed perlite

Lamellar banded structures similar to those obtained at the weld top surface is observed at the AS. After FSW, pearlite (α_{fc}) is generally observed as nodules of alternate ferrite and cementite lamellae due to high transformation temperatures at the AS region. Pearlite transformation occurs in the narrow range of temperature i.e., between the temperatures 700–500 °C. This results in highly oriented and fine grains microstructure in the advancing region of the weld zone. During FSW, grain size reduction occurs by severe plastic deformation and dynamic recrystallization, resulting in no substantial increase in dislocation density (Ramesh et al. 2017).Moreover, the dislocations generated during FSW/FSP result in forming the substructures and the sub-grain by the combined effect of deformation, strain rate and temperature (Karami et al. 2016; Lienert et al. 2003). At surface (i.e. banded structure) and sub-surface (TMAZ-AS), the deformation was severe and resulted in higher nucleation sites, and ferrite + pearlite structure became finer as compared to the rest of the weld zone. This microstructural evolution is in accordance with that SZ and TMAZ-AS regions that can undergo different temperature and strain rate dependent mechanism such as dynamic recovery, dynamic recrystallization, and even grain growth along with dissolution or precipitation (Karami et al. 2016; Lienert et al. 2003; Mishra & Ma, 2005). These processes' cumulative effect determines the SZ's final microstructure (Chung et al. 2010). Figure *4.8* shows the FESEM EDS characterization of SZ of the welded joint.

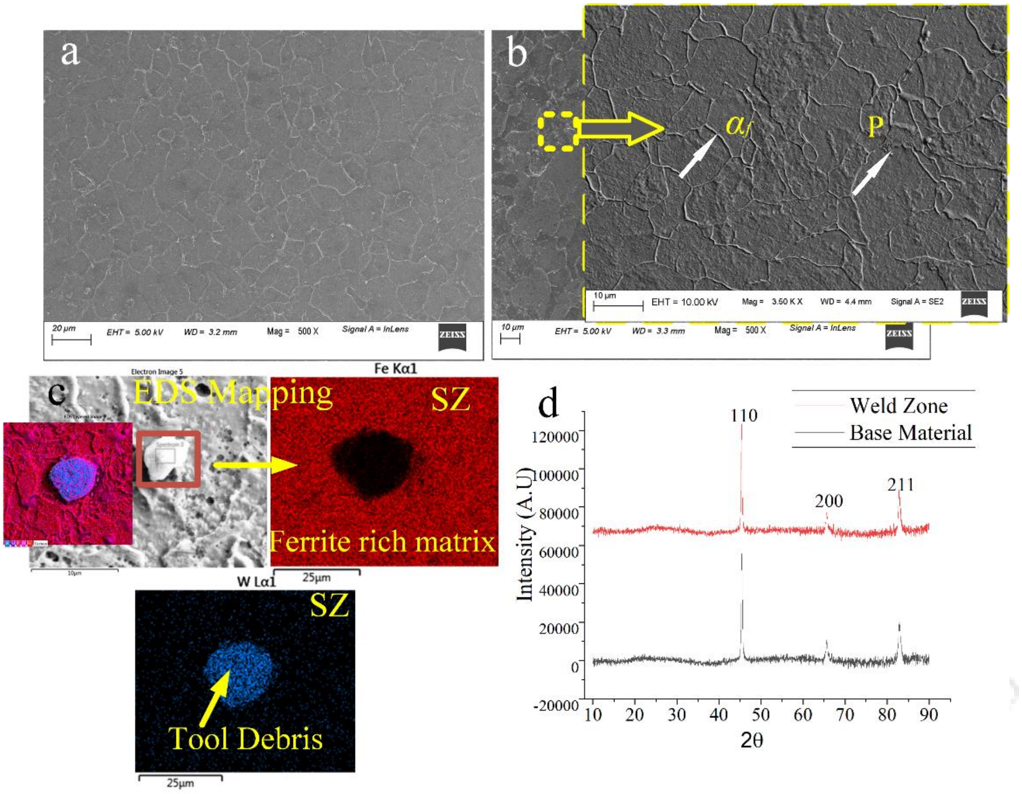

Figure 4.8 (a) SEM micrograph of base material; (b) SEM micrograph of the weld stir zone at 600 rpm and 90 mm/min (The pearlite distribution and tungsten (W) particles in the ferrite rich matrix can be observed FESEM micrograph), (c) EDS analysis indicating the tungsten particles in the weld nugget of the weld 1, and (d) XRD pattern of SZ indicating similar peaks of ferrite before and after welding condition

The high magnification scanning electron microscope (SEM) image shows that BM consists of ferrite and perlite structure, as shown in Figure *4.8*a. SEM images at the weld nugget also confirmed the ferrite perlite structure in the weld zone as indicated in the Figure *4.8*b. EDS analysis in the respective spectrum confirms the presence of tool wear debris i.e., W particles in the weld region, as shown in Figure *4.8*c. Softening of the ductile Co binder and mechanical interaction at tool-work interface may have attributed to the separation W particles from the tool. The concentration of tool particles is higher in the SZ and AS-TMAZ. The weld zone is further investigated by X-ray diffraction (XRD) analysis for phase identification, as shown in Figure *4.8*d. The peaks in XRD analysis are identified as ferrite (α_f) phases in the weld nugget. XRD phase analysis indicate almost similar ferrite peaks before and after welding condition.

4.3.3 Tensile properties

Figure *4.9* indicates the tensile test results of the welded joints and base material.

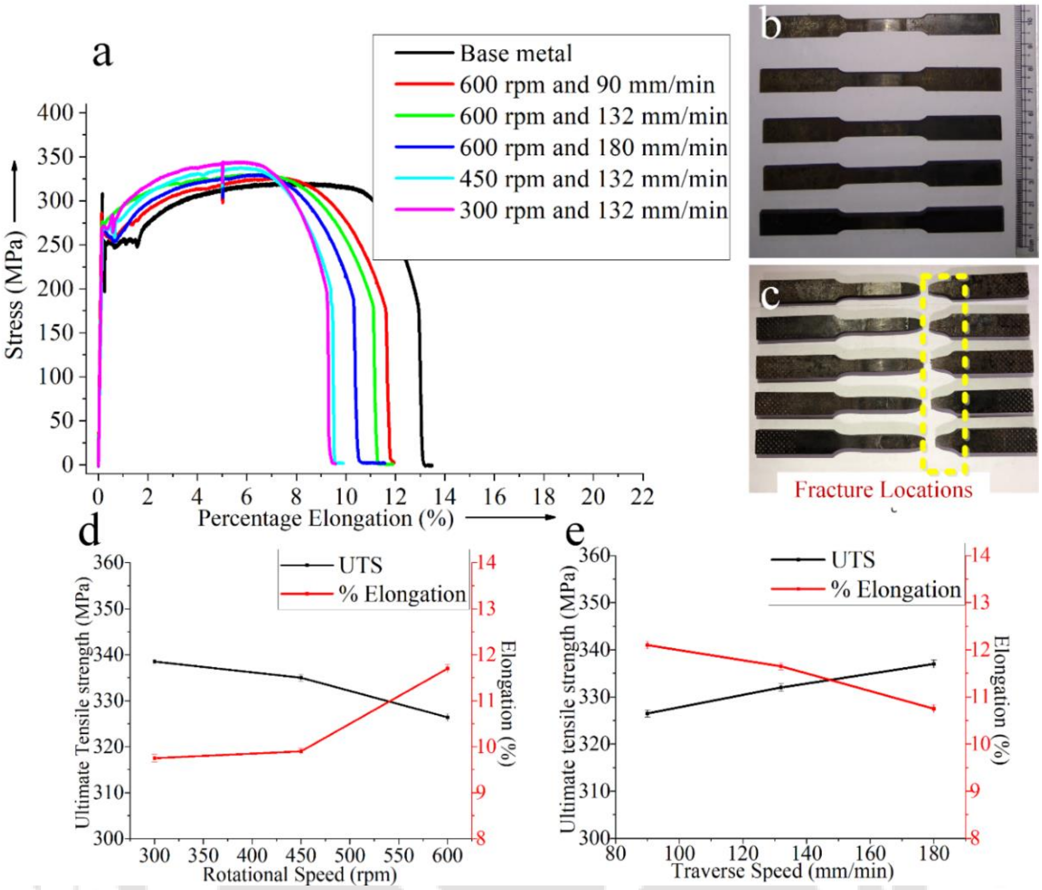

Figure 4.9 (a) Tensile properties of weld joints; (b) tensile specimens before fracture; (c) fracture tensile specimens, (d) tensile properties variation with the rotational speed at a traverse speed of 132 mm/min, and (e) tensile properties variation with traverse speed at a rotational speed of 600 rpm

The tensile strength increases slightly with increasing welding speed and decreasing rotational speed (i.e., decreasing heat input) due to refined grain microstructure. Due to the grain size variation being insignificant with the decreasing heat input, the UTS only slightly increased by less than 5%. (Saeid et al. 2008) also reported a decrease in tensile strength with the decrease in traverse speed. Results obtained are in good agreement with the results reported by Fujii et al. (2006), Cui et al. (2007), and Tiwari et al. (2019b). The weld 1 and weld 5 exhibit the maximum and minimum elongation, about 12.1%, and 9.85%, respectively, whereas the elongations for other welding conditions are varying in the range of $9.92 - 11.86\%$. Figure *4.10* shows the fractured surface appearance of the tensile specimen obtained by using a scanning electron microscope.

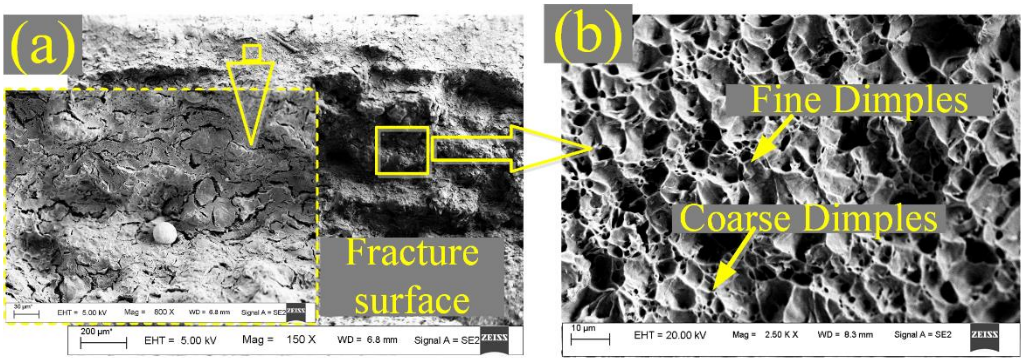

Figure 4.10 FESEM image of the fractured tensile surface of weld 5: (a) micro cracks were observed at low magnification, and (b) high magnification showing a cluster of fine dimples along with coarse dimples

Fracture surface morphology of tensile specimens is characterized by ductile dimples behavior. The modes of failure of the tensile tested parent metal and welded joints are ductile. It is concluded that tensile sample underwent sufficient plastic deformation and are evident from the fracture location and fractured surface as shown in Figure *4.10*. At low magnification, cracks are visible at the fracture location. A substantial dissimilarity is observed in the dimples size and alignment on the fracture surface of FSW joints. Fine and secondary dimples are the critical features of the superior tensile strength of FSW joint.

4.3.4 Micro-hardness

Microhardness values on the transverse cross-section of welded joints are summarized in *Figure* 4.11.

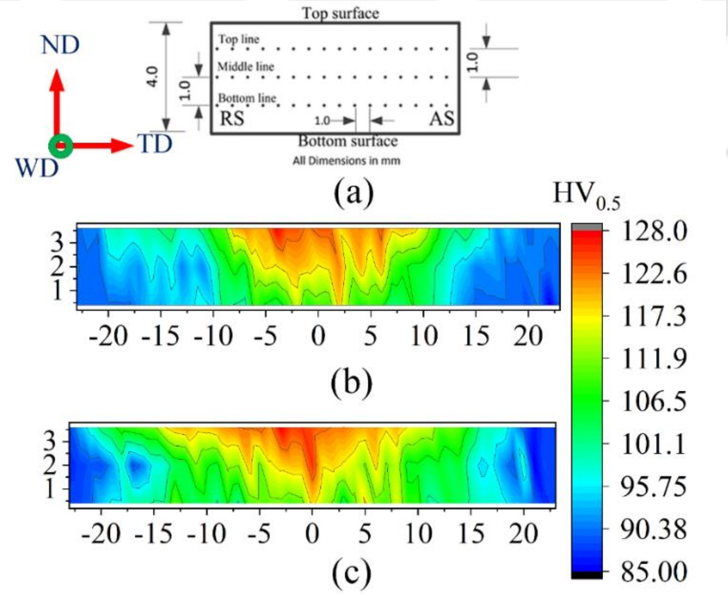

Figure 4.11 (a) Schematic representation of micro-hardness evaluation points along ND-TD direction, microhardness contour of (b) weld 1; and (c) weld 2 (Schematic is drawn not to scale)

The microhardness is measured at three different depths from the top surface (i.e., 1, 2, and 3 mm) in the normal-transverse (ND-TD) plane to observe the hardness variation across the transverse cross section. The hardness of the WNZ is slightly more than the base material because of grain refinement due to dynamic recrystallization (DRX) as discussed in microstructure in section 4.3.2. The maximum hardness in weld nugget of weld 1 and weld 2 is 123 and 127 $HV_{0.5}$ respectively. Average nugget hardness values of 131 $HV_{0.5}$, 135 $HV_{0.5}$, and 139 $HV_{0.5}$ are recorded in weld 3, weld 4 and weld 5, respectively. Lienert et al. (2003) and Lakshminarayanan et al. (2010), during FSW of low carbon steel (0.18 wt.%C) observed drastic change in hardness values in the weld nugget, unlike the variations observed in the present investigation. This could be ascribed to the evolution of ferrite phases in the weld nugget zone and that is absent during FSW of UNS G10080 steel. Hardness is high in the WN center than the TMAZ, contrary to the minimum grain size in the TMAZ. The obtained results of hardness distribution cannot be explained by the Hall Petch relation only. The higher hardness of the SZ than the TMAZ might be due to the presence of more dislocation density and formation of sub structures in the WNZ microstructure due to extensive deformation in the SZ (Karami et al. 2016). Moreover, it is observed that hardness is higher in HAZ than the base material, which is usually encountered in the fusion weld of particular steel.

4.3.5 Tool wear characterization

Tool wear is very common in the FSW of steel. It is expected to be a combination of chemical wear and mechanical wear mechanisms, likely to occur at high welding temperatures and stresses. Figure *4.12* shows the grain size distribution of the tool before and after the welding.

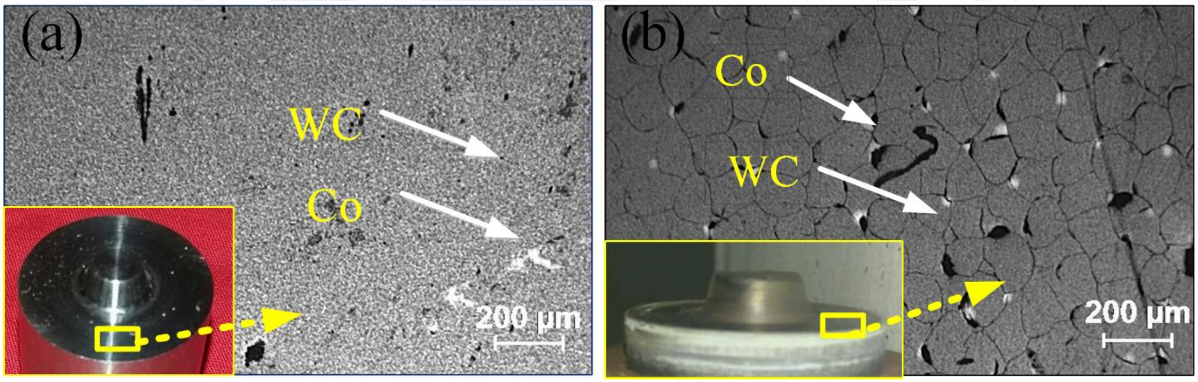

Figure 4.12 Microstructure of the WC-10 % Co tool: (a) before welding; and (b) after welding

The tool microstructure represents the bright and dark gray regions as WC and Co phases, respectively. Fine grains tungsten (W) particles are converted into coarse grain due to the weld thermal cycle. A greenish-blue layer is observed on the outer shoulder surface. This layer is formed due to the oxidation of tungsten carbide (WC) tools, which is expected since the welding is carried out in the absence of shielding gas. WC-Co alloys' oxidation behavior increases radically with the temperature above 600 °C, which is likely to occur in FSW of steel (Lofaj & Kaganovskii, 1995; Warren et al. 1996). The high process temperatures result in massive oxidation and the utmost degradation on the tungsten carbide (WC) tool's tribological properties. Moreover, at such a temperature level, the binder phase in a Co–W–C alloy, loosen the tungsten matrix since its melting point is lower than that of pure cobalt. Figure *4.13* indicates the surface roughness (i.e., R_a) at the tool pin and tool shoulder. Surface roughness at the tool pin is 0.245 µm, and the tool shoulder is 0.18 µm. Chipping of tool material and circular groves are observed on the tool pin and shoulder surface, respectively. The tool's good surface condition is required to avoid further abrasion and adhesion wear of the tool. The future work is essentially needed to assist a greater understanding of the tool degradation mechanism to produce a defect-free reproducible weld with higher tool life.

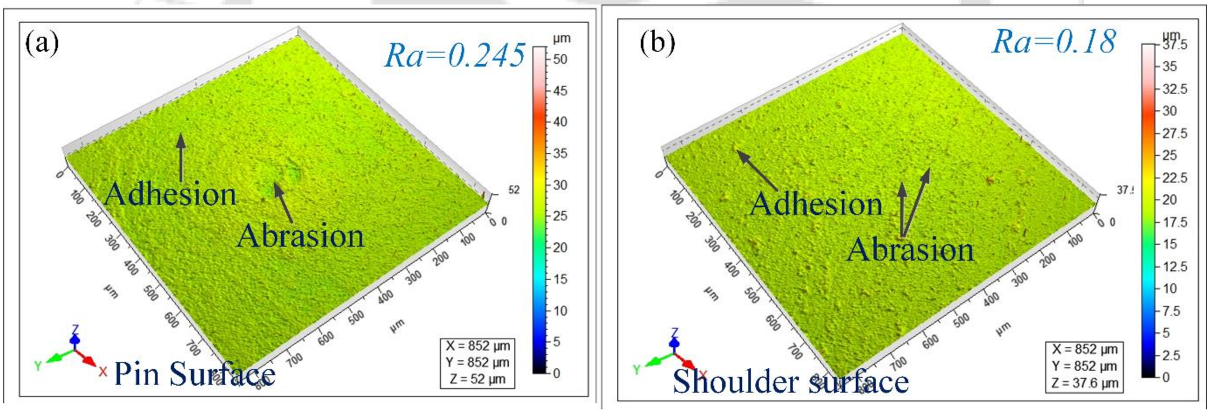

Figure 4.13 Surface roughness values: (a) tool pin surface, and (b) tool shoulder surface

4.4 SUMMARY

Friction stir welding of low carbon steel (%wt.C < 0.11) is demonstrated successfully using the tungsten alloy tool. The following conclusions are drawn

- The axial force recorded from the experimental investigation has an approximately value of 25.7 kN for all welding parameters, irrespective of the variation of the plastic stress in the operating temperatures range during FSW of low carbon steel.
- The “onion ring”, “banded structure,” and the “swirl” formation is observed in the weld zone. The thermomechanically affected zone's microstructures consisted of the finest

grains size of 7.9 μm as compared to the stir zone of 14.75 μm. The SZ on the advancing side (SZ-AS) has a band structure with deeply etched lines.

- The microstructural analysis of weld 1 confirmed the presence of tungsten particles. This indicated that high process temperatures are detrimental to tool life.
- The welded joints showed 106.2-112.4% in yield strength and 101.24-104.6% in tensile strength in comparison with the base material. The tensile strength of the low carbon steel joints increased with the increasing welding speed and decreasing rotation speed due to the grain refinement
- Increase in stir zone hardness values (123-139 $HV_{0.5}$) is attributed to the fine-grained structure, including substructures, like sub boundaries and dislocations, due to severe plastic deformation.
- The study demonstrated that WC-10wt. %Co tool is technically suitable for FSW of low carbon steel for structural applications over a large process window i.e., rotational speeds (300-600 rpm) and traverse speeds (90-180 mm/min). The study is further extended in welding of dissimilar steels, i.e., UNS S30400 and UNS G10080 steel using the same tool material composition.

:--------------------*--------------------*----------------------:

Chapter 5

5 FRICTION STIR WELDING OF DISSIMILAR STEEL

5.1 INTRODUCTION

This study deals with dissimilar friction stir welding between stainless steel (UNS S30400) and mild steel (UNS G10080). The challenges in conventional welding of dissimilar steels arise due to the differences in the compositions of alloying elements and carbon content that results in solidification defects and segregation defects. FSW of dissimilar steels needs a systematic investigation to produce defect-free welds by considering the discontinuity due to FSW's asymmetric nature. To address these issues, important parameters like tool rotational speed, tool traverse speed, tilt angle, and tool plunge depth are investigated for FSW of dissimilar steel. In addition, an important parameter, i.e., tool offset, is also analyzed to obtain defect-free weld. In previous literature, the complex relationship between microstructure and mechanical properties of dissimilar weld joints is not studied systematically. After performing welding, joints are characterized by tensile properties, microhardness, and impact toughness. The metallography is conducted to investigate the joining mechanism at macro and micro levels under optical microscope, field emission scanning electron microscope equipped with EDS. Results revealed that dissimilar materials are interleaved in some regions with finger-like projections that enhanced mechanical interlocking at the macroscale and metallurgical bonding at the microscale.

5.2 MATERIALS AND METHODOLOGY

The base materials used in this study are stainless steel (UNS S30400) and mild steel (UNS G10080). The nominal composition (in wt.%) of UNS G10080 is C (0.08), Mn (0.40), S (0.033), P (0.031) and balance Fe. The nominal composition (in wt.%) of UNS S30400 is Cr(18.1), Ni(8.2), C(0.008), Si(0.32), Mn(1.02), P(0.028), S(0.002) and balance Fe. The base material dimension of each plate is 200 mm × 60 mm × 4 mm ($l \times w \times t$). FSW was performed with a tungsten alloy tool consisting of flat shoulder with a diameter of 23 mm and pin length of 3.42 mm. The tool with tapered pin from 7 mm at the shoulder to 5 mm at the free end was used. The welding direction was parallel to the rolling direction of the plate.

Friction stir butt welding of dissimilar steels is schematically shown in Figure *5.1*. Unlike the conventional FSW, the tool pin was shifted toward the mild steel plate (as shown in Figure *5.1*b) to avoid grove and tunnel defects in the weld. This was done to avoid the formation of cavities or groove-like defects in AS which is reported in earlier literature. The rotational speed (rpm) and tool offset (mm) for the present investigation are as follows: weld 1(600, 0.6), weld 2 (600, 1.2), weld 3 (875, 0.6), and weld 4 (875, 1.2). The traverse speed for all levels was 90 mm/min. The other parameters, i.e., backward tool tilt angle and tool plunge depth, were kept constant at 2° and 0.2 mm, respectively. Figure *5.1*c shows the friction stir welding of dissimilar steels in progress.

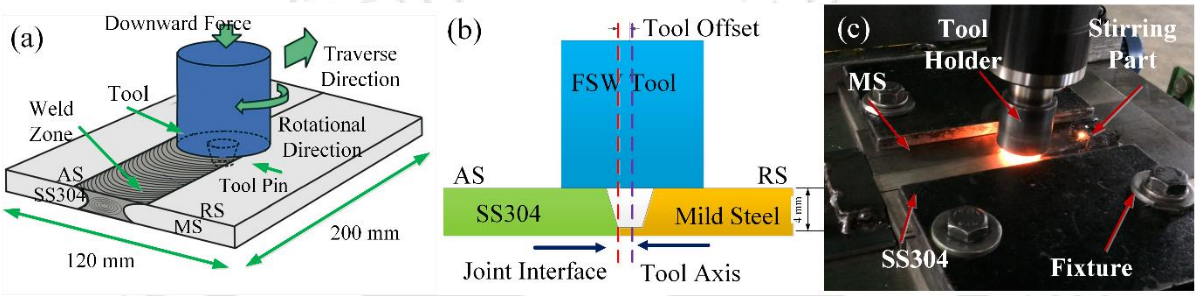

Figure 5.1 Schematic representation of: (a) dissimilar FSW butt joints, (b) tool offset toward the softer material i.e. UNS G10080 steel, (c) FSW of SS304 and UNS G10080 in progress (Schematic is drawn not to scale)

Tensile samples were cut from the welded plates using wire electric discharge machining (WEDM) as per the ASTM E8 standard. The tensile test was carried out at a crosshead speed of 1 mm/min on the universal tensile testing machine. Microhardness values ($HV_{0.5}$) was evaluated at an interval of 1 mm on the top, middle, and bottom layers of the welded joints. Sub size impact specimens were prepared as per the ASTM E23. The metallographic samples were polished to mirror finish using different grades of emery paper and alumina powder. The polished samples were etched for mild steel using 5% Nital solution (i.e., 5 ml HNO_3 and 95 ml ethanol) to reveal its microstructure and the material flow pattern. X-ray diffraction (XRD) analyses were also performed at room temperature in the continuous mode for 2θ values ranging from 10°-80°.

5.3 RESULTS AND DISCUSSION

5.3.1 Metallography analysis

Figure *5.2* shows the cross-sectional microstructure view of the weld 4 (875 rpm, 1.2 mm tool offset). Different distinguishable regions are identified within the welded region as shown in Figure *5.2*a.

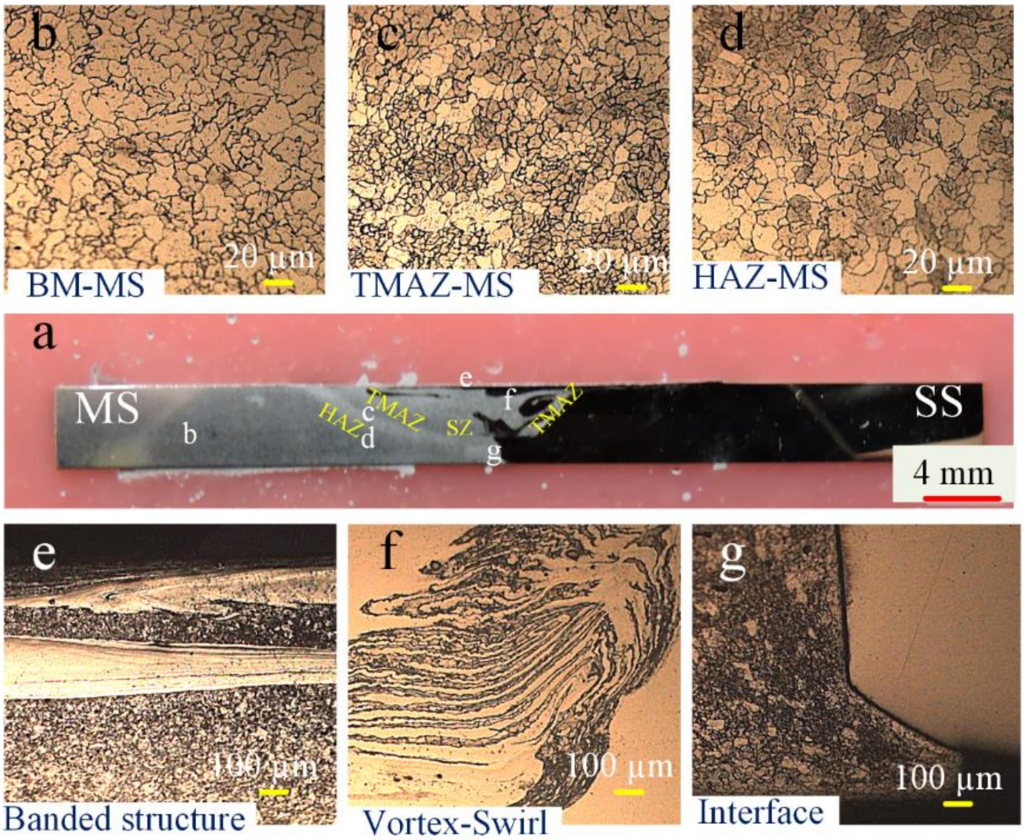

Figure 5.2 Microstructural view of weld cross-section: (a) cross-sectional macrostructure, (b) base material, (c) TMAZ-MS showing substructures and grain refinement (d) HAZ-MS, (e) banded structure at the top surface of the weld, (f) vortex swirl, and (g) interface between MS and SS304 at the pin bottom

The dissimilar welds exhibit regions, such as parent SS304 steel, thermomechanically affected zone (TMAZ) in the stainless steel in the advancing side of the weld, weld nugget, TMAZ in the mild steel at the retreating side of the weld, and heat-affected zone (HAZ) in the mild steel at retreating side. Weld cross-section displays a complex stirring flow on the interface of welded materials on either side of the weld centerline. It is also noticed that the stainless steel's sharp thin layers are stirred to the very extreme position of the thermomechanically affected region of mild steel at the top of the weld. Figure *5.2*b depicts the microstructure of the base material, indicating ferrite perlite structure. The grain sizes on the TMAZ of mild steel are observed to be smaller compared to the HAZ of MS as shown in Figure *5.2*c and Figure *5.2*d. The region shown in Figure *5.2*e indicates the banded structure in mild steel at the actual weld centerline. The intense heat input and material deformation result in forming the banded structures at the shoulder workpiece interface. At the SS304 and MS interface in the TMAZ of the AS, re-oriented flows are observed, which may be a result of the intense stirring effects of the tool pin, as shown Figure *5.2*f. This region shows the microstructure of different lamellae of both the steels and complex vortex flow pattern in the deformed region. The two materials are found to be interleaved in this region, with fingerlike projections. Guo and Shen (2019) also reported mixed lamella structures and vortex flow on the advancing side in dissimilar FSW of steel. Material flow is more disruptive on the AS than the RS due to the resultant tool velocity component. When two plates of dissimilar materials are joined, the swirls and vortex patterns are more evident due to real composition differences unlike in joining of similar materials. It is evident from the previous literature (Mishra & Ma, 2005; Nandan et al. 2007) that the peak temperatures are high on the advancing side than the retreating side of the weld joint. Figure *5.2*g shows the distinguishable interface between the MS and SS304, which is observed near the root of the weld. Appropriate selection of parameters restricts the formation of kissing bonds, tunneling, and weld defects, especially in this region. Al-Moussawi & Smith (2018) reported defects in this region due to insufficient heat input and material flow. Joint is further characterized under a high-magnification scanning electron micrograph as shown in Figure *5.3*a.

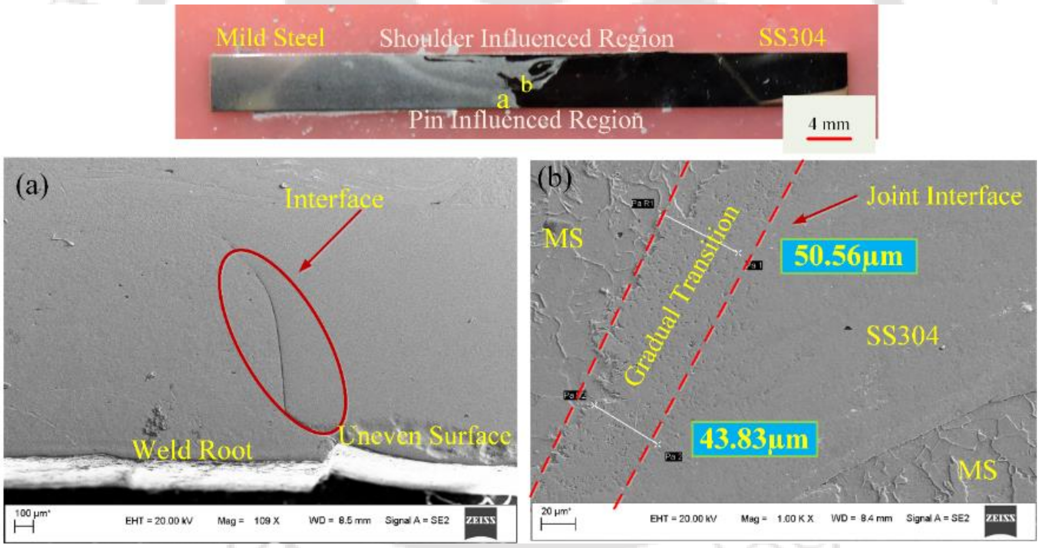

Figure 5.3 Weld micrograph: (a) FESEM micrograph at the bottom region, and (b) transition behavior of SS304 and MS in the deformed region

Defects like lower embedded, joint line remnant, and connectivity flaw are not observed, unlike reported by Stevenson et al. (2015). Logan et al. (2016) reported voids in the deformed region during FSW of dissimilar steel, resulting in the weld's reduced strength. Cheng et al. (2013) reported tunnel defect in the AS due to insufficient hot plastic flow during FSW of dissimilar steels. Two different types of transition behavior are observed, as shown in Figure *5.3*b. In some regions, the transition is sharp, whereas the transition is gradual in some other regions.

Gradual transition varied from 40 μm to 50 μm, as shown in Figure 5.3b. A sharp transition is observed toward the weld root side in the interleaved zone. Moreover, it can be noticed that the thickness of the transition layer slowly decreases from the top to the bottom region. Furthermore, an EDS line scan is performed to check the bonding mechanism of FS-welded dissimilar steels. Figure 5.4 shows the result of the FESEM micrograph and electro-dispersive spectroscopy (EDS) analysis.

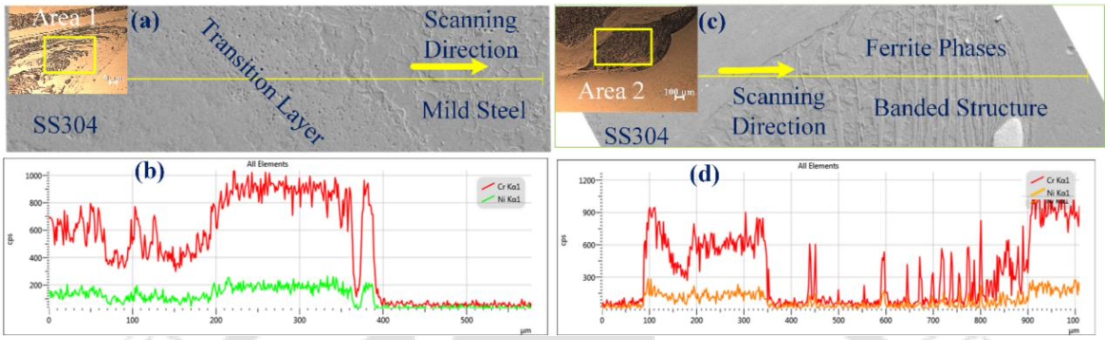

Figure 5.4 EDS analysis across the interface between the two alloys: (a) joint interface separating SS304 and mild steel, (b) EDS analysis, (c) swirl formation in the AS, and (d) EDS line spectrum indicating larger peaks of Ni and Cr in SS304 rich matrix

These are named as area 1 (close to TMAZ in AS) and area 2 (weld nugget interface region) marked with a yellow box in the optical micrograph region. Figure 5.4a and Figure 5.4c represent the microstructure regions in which EDS analysis is performed. The main elements observed in the interface are Ni and Cr, in the EDS line scan. Large peaks of Ni and Cr are observed in SS304 rich regions, which decrease in the UNS G10080 region as shown in Figure 5.4b and Figure 5.4d.The concentration profiles of the elements at the interface specify that stainless steel diffuses slightly in the softer mild steel alloy but negligible mild steel diffuses in the harder stainless steel alloy during welding. This is attributed to stainless steel's location on the advancing side and mild steel on the retreating side. The diffusion of such elements (Cr and Ni) indicates that the FSW of dissimilar materials is identified as mechanically bonded and chemically bonded, and these collectively contributed to the weld joint integrity. Jafarzadegan et al. (2013), Logan et al. (2016), and Klingensmith et al. (2005) also observed the diffusion of alloying material from one material to the other at the dissimilar materials interface due to the high strain and temperature-induced welding condition The key factors in FSW determining the joint quality in the dissimilar metallurgical bonding structure are mainly (i) the mechanical effects and (ii) the thermal effects. Mechanical effects are provided by the tool behavior which can effectively mix and transfer the dissimilar materials to be joined. The generated mixing structures enhance the mechanical interlocking at the macroscale and reduce the distance for elemental diffusion or solid solution at microscale. Thermal effects provided by friction heating and plastic deformation can promote the metallurgical bonding of dissimilar materials. It is observed that a good metallurgical bond and mechanical mixing are formed between the two materials. This is further confirmed by performing microstructural investigation of the mixed region (vortex swirl) as shown in Figure *5.5*.

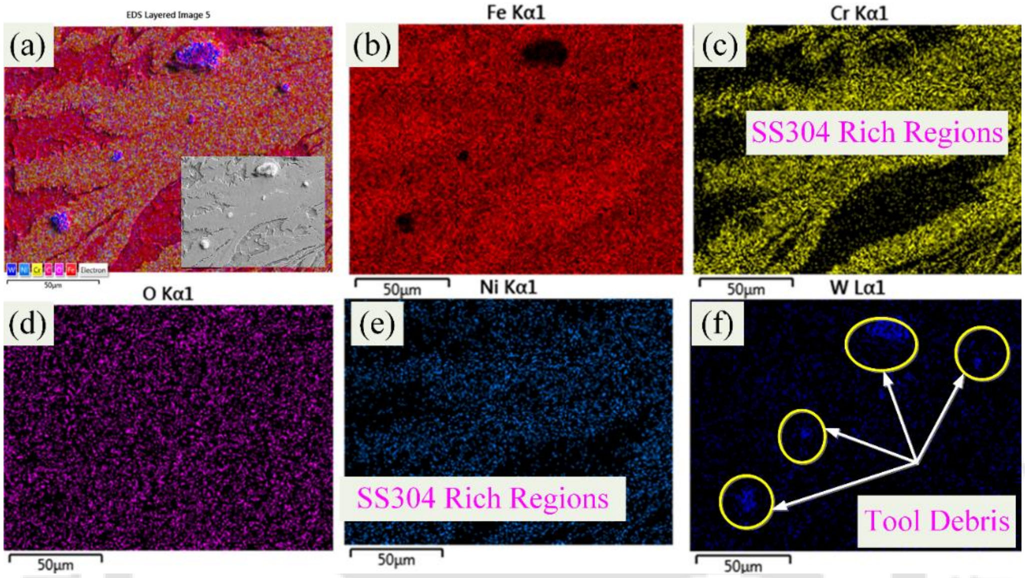

Figure 5.5 EDS analysis in the stir zone of the weld joint indicating tool debris in UNS S30400 rich regions

The EDS mapping supports the evidence of diffusion as the bonding mechanism between stainless steel and mild steel parent materials. The elemental mapping demonstrates the presence of iron (Fe), tungsten (W), nickel (Ni), chromium (Cr), and oxygen (O) elements, as depicted in Figure *5.5*b-e. The mixing occurs at the micron level due to the FSW process's typical nature in which each grain exhibits different levels of straining and temperature gradients. Furthermore, it is noticed that the tungsten particles are present in the weld microstructure, as shown in Figure *5.5*f. Tungsten-rich regions are observed due to the broken off/wear off tool particles embedded in the deformed zone. The weld micrograph is further investigated at different locations to observe the W traces. Figure *5.6*a demonstrates the complex swirl (randomly distributed stacked layers) micrograph due to intense material mixing in the weld nugget. It shows that the tungsten element takes up 55.5 % W, and iron takes up 4 % in the vortex swirl region, as shown in Figure *5.6*b.

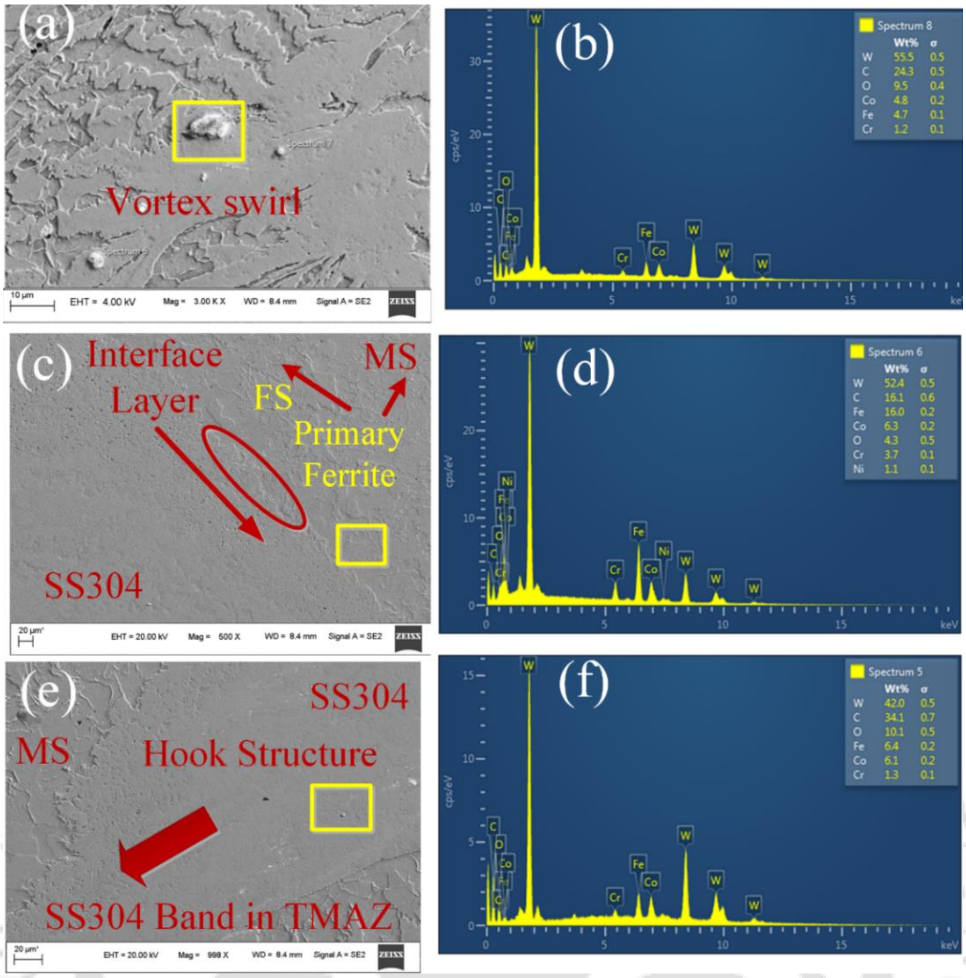

Figure 5.6 FESEM micrograph and EDS analysis of weld 4 at different locations in the weld zone (a-b) SZ, (c-d) weld interface region, and (e-f) hook region

As compared to the SS304 region, less amount of W particles are observed in the mild steel region. Figure 5.6c shows the tungsten particle in the gradual transition region. EDS spectrum in Figure 5.6d shows the elemental composition as 52.4% W and 16% Fe in the interface region. The tool particles are likely to occur in the deformed region due to the high temperature and high strain rate welding conditions. Figure 5.6c and Figure 5.6e also indicate the evidence of phase transformation occurred in the mild steel region. İpekoğlu et al. (2019) and Rahimi et al. (2019) also reported the ferrite-phase transformation and grain refinement in the SZ during FSW of steel. Saeid et al. (2008) reported grain refined microstructure due to dynamic recrystallization during FSW of stainless steel. Figure 5.6e shows the hook morphology due to characteristic material flow, which depends on tool geometry and operating parameters. However, on the macro-scale, the hook structure played an important role in mechanical interlocking at the welded joint interface. The elemental composition of W is 42% in the hook structure, as shown in Figure 5.6f. Tool particles are observed in various regions of different shapes and sizes. Figure *5.7* shows the results of particle size analysis of the tungsten tool in the weld zone.

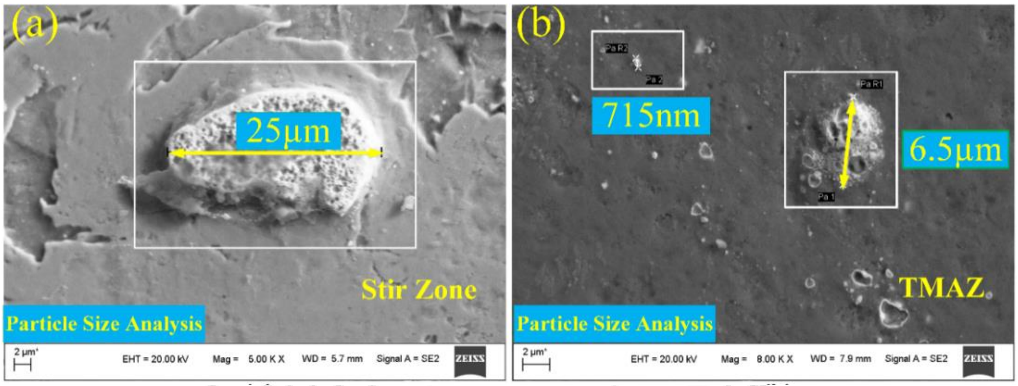

Figure 5.7 Tool particles in the weld zone: (a) tool particle of 25 μm in the swirl region, and (b) at a distance from the interface near TMAZ on the advancing side, i.e., stainless steel 304 side

The tool particles are varied in different sizes from a few nanometers to some micrometers. A maximum tool particle size of 25 µm is observed in the swirl region of the weld zone. Jafarzadegan et al. (2013) reported the tool particles reduced the joint strength significantly during FSW of dissimilar steels.

5.3.2 Mechanical properties

5.3.2.1 Microhardness distribution

Drastic variations in the microstructures within the deformed region of the FSWed stainless steel to mild steel resulted in an inhomogeneous distribution of microhardness as shown in Figure *5.8*.

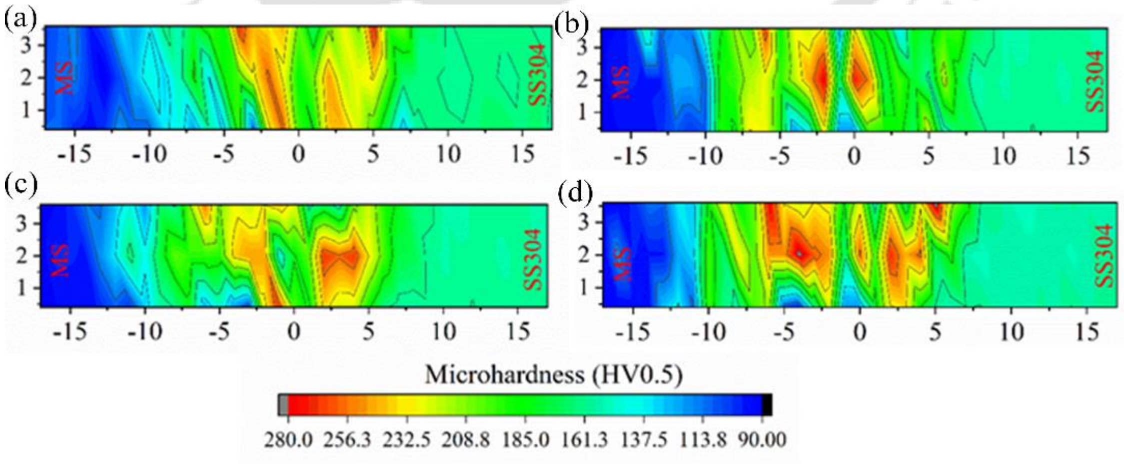

Figure 5.8 Microhardness mapping at the weld cross-section: (a) weld 1, (b) weld 2, (c) weld 3, and (d) weld 4

The microhardness of mild steel BM is about 88 $HV_{0.5}$ and stainless steel BM is 149 $HV_{0.5}$. The maximum hardness in the mild steel side was approximately 121–129 $HV_{0.5}$ in SZ, 106–116 $HV_{0.5}$ in TMAZ, and 95–102 $HV_{0.5}$ in the HAZ of the weld zone. HAZ hardness is increased slightly due to the work hardening (Guo & Shen, 2019). The SZ with acicular ferrite (α_a) and Widmanstatten ferrite (α_w) structure reached a maximum hardness of 281 $HV_{0.5}$. Hardness increases toward the deformed region as a result of increasing microstructural refinement. In weld 2 and weld 4, as shown in Figure *5.8*b and Figure *5.8*d, the hardness variation in the TMAZ and HAZ of the mild steel side is higher than that of weld 1 and weld 3. In the softer material, i.e., mild side, there is more fluctuation in the hardness values compared to the harder material, i.e., stainless steel. The hardness asymmetry is due to the inclusions of harder stainless steel and tool fragments scattered in the deformed zone of mild steel, as discussed in the microstructural section (shown in Figure *5.2*, 5.3, 5.4, and 5.5).

5.3.2.2 Tensile properties

Figure *5.9* shows the tensile properties of the welded samples and the base materials at room temperature. Both the tensile strength and percentage elongation of UNS S30400 are higher than the UNS G10080. All welded joints exhibited higher tensile strength than the weaker base material, i.e., mild strength. The maximum tensile strength of friction stir welded dissimilar joint (i.e., weld 4) is 341.54 MPa, which shows an increase of 7.6% than the mild steel. The strengthening mechanism of the dissimilar weld joints is attributed to grains size strengthening in SS304 and the phase transformation strengthening in mild steel, respectively (Wang et al. 2019). In addition to that, its corresponding elongation is 9.6%, which shows a decrease of 53.8% compared to mild steel, as shown in Figure *5.9*c. Tensile specimens fractured in the mild steel material for all welding conditions.

Figure *5.10*a and Figure *5.10*b show the fracture location and macroscopic appearance of the fractured specimen of weld 4 (joint with the maximum strength value).

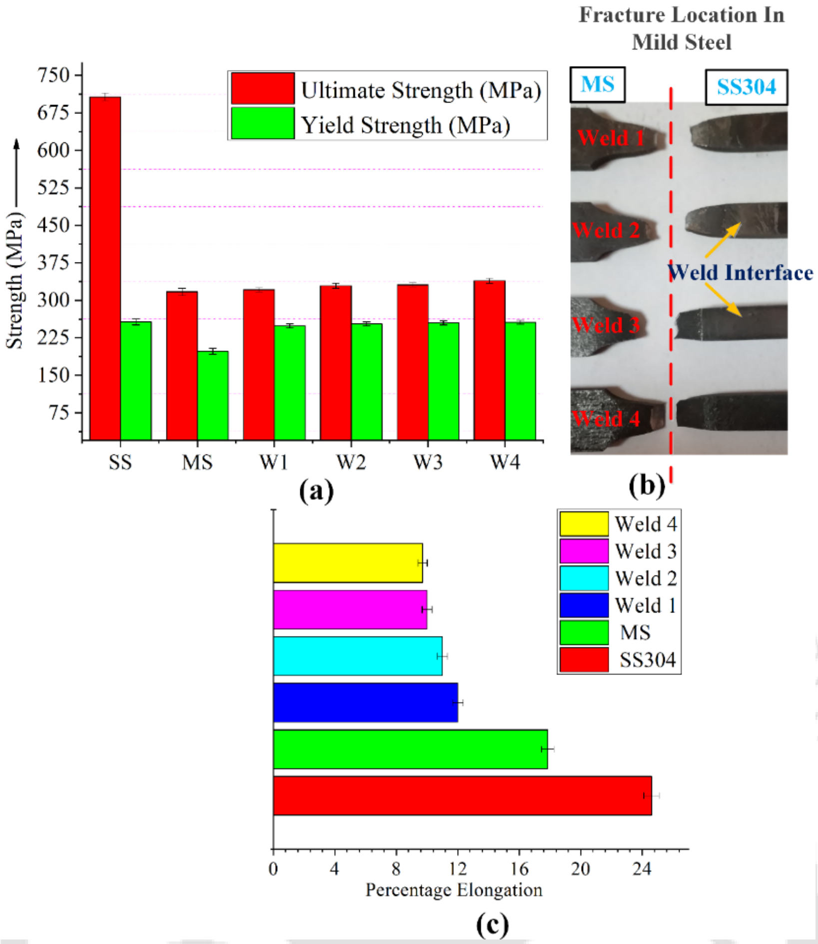

Figure 5.9 Tensile test results: (a) tensile strength and yield strength of welded specimens and base materials, (b) tensile specimens showing fracture location in the UNS G10080 steel base material, and (c) comparison of % elongation of weld joints with the base material

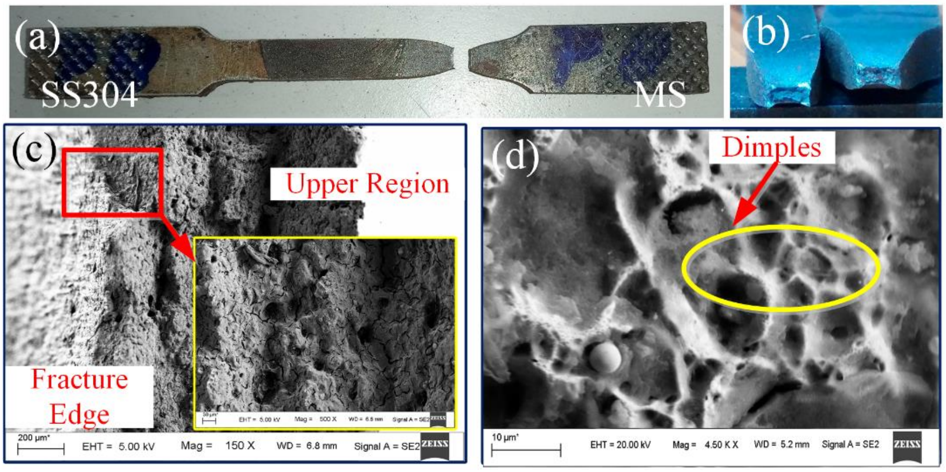

Figure 5.10 Fractured tensile specimen: (a) showing fracture location in the UNS G10080 steel base metal, (b) macro fracture appearance, (c) localized fracture morphology, and (d) presence of fine and coarse dimples at the fracture surface

Figure *5.10*c shows a localized fracture morphology, which consists of bundle of dimples indicating the ductile fracture in the middle region. Figure *5.10*d gives the enlargement of the localized ductile fracture surface marked in Figure *5.10*c. The presence of micro-and macro dimples suggests a characteristic ductile fracture (as shown in Figure *5.10*d). The distribution of dimples in the fracture surface is also inhomogeneous. These dimples are formed due to micro-and macro voids' coalescence, which results in a ductile-type failure during tensile testing. Figure *5.11* shows the impact energy stored by the welded samples at room temperature.

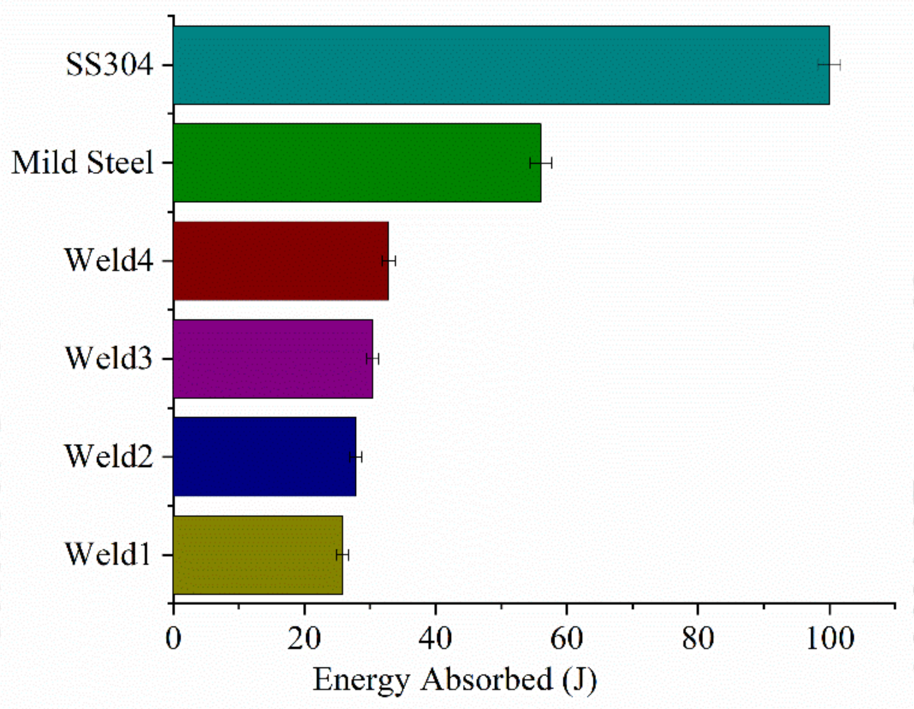

Figure 5.11 Impact toughness of the welded joints and the base materials

The weld joint's impact toughness is reduced from 58.5% to 49.6% of the mild steel on changing rotation speed from 875 to 600 rpm at the tool offset of 1.2 mm. This loss in impact toughness is due to less microstructural transformation in mild steel at low heat input weld conditions. Sekban et al. (2016) observed that the microstructural refinement during FSW process causes a significant increase in low carbon steel's impact toughness. During impact testing, all samples fractured in the welded portion. The fractured impact specimen of weld 4 is shown in Figure *5.12*.

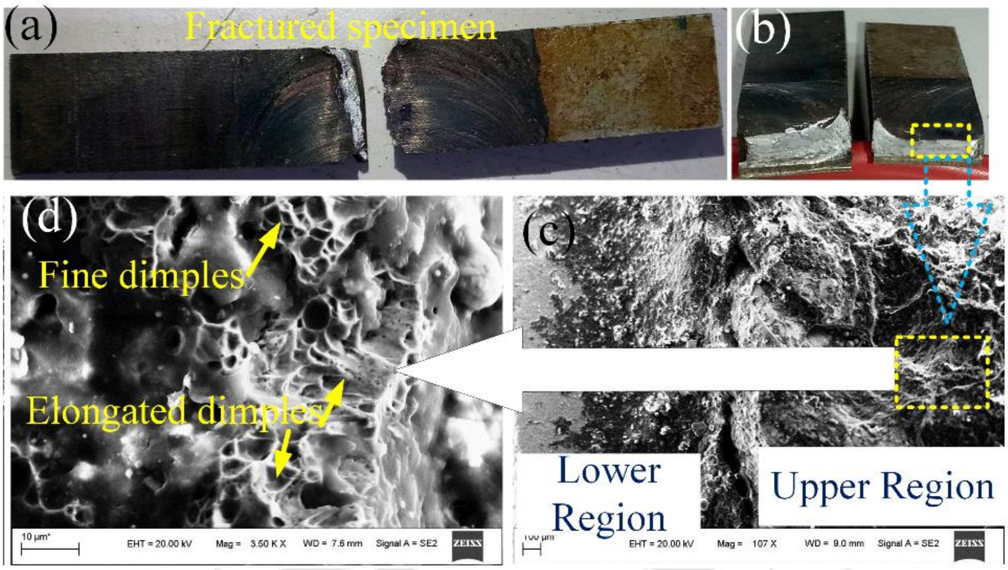

Figure 5.12 Impact specimen of weld 4: (a) fractured impact specimen, (b) macro fracture surface appearance, (c) micrograph showing lower and upper fracture surface region, and (d) typical ductile dimples observed in the upper region indicated a mixed fracture mode

Two distinct regions are observed on the fractured surfaces as shown in Figure *5.12*c. The upper region has a rough uneven surface due to a ductile mode of failure, while a smaller region near the root has a rough appearance indicating a brittle mode of failure, as shown in Figure *5.12*c. The presence of typical dimples structures in the upper region indicates the mixed ductile and brittle mode of fracture as shown in Figure *5.12*d. The presence of tool particles and distribution of the two alloys is confirmed by EDS analysis as shown in Figure *5.13*.

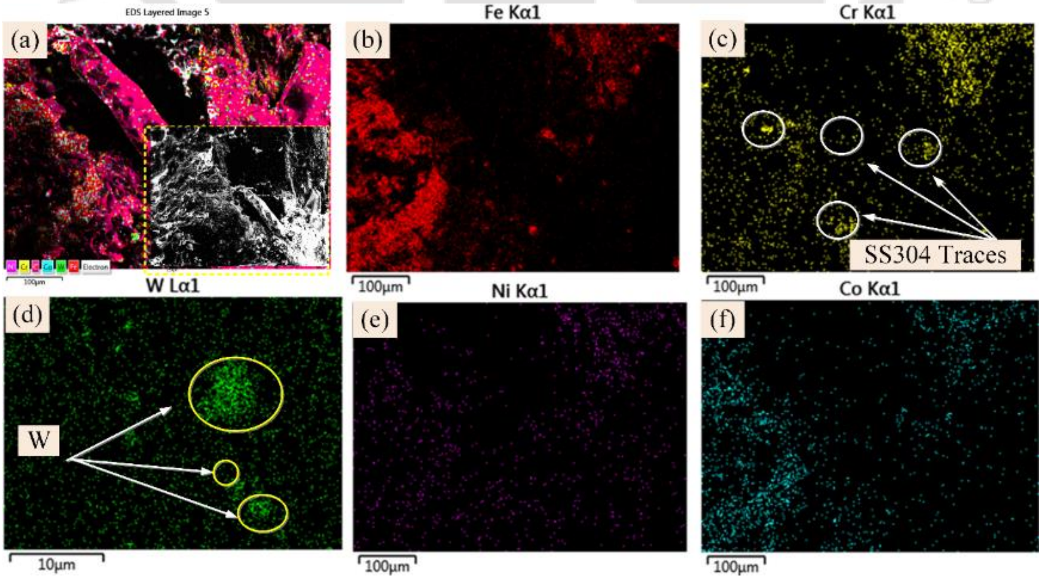

Figure 5.13 EDS analysis at the fractured surface of impact specimen

The elements, i.e., tungsten, chromium, and nickel, are found at the fractured surface. Further work is required to ascertain if these tungsten particles' presence is detrimental to the mechanical properties (like impact strength, and fatigue strength) of the weld joints. XRD phase analysis is carried out to examine the bulk-phase composition of the stir zone, as shown in Figure *5.14*.

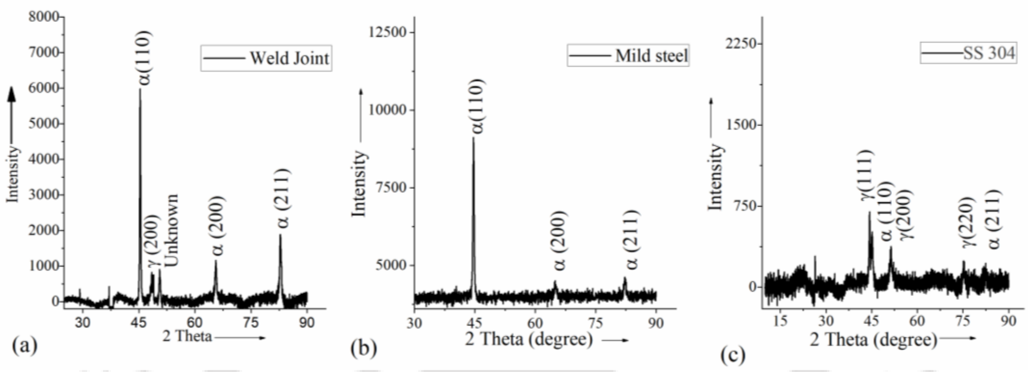

Figure 5.14 XRD spectrums of base materials and the weld joint (a) stir zone of the weld joint, (b) SS304, and (c) UNS G10080

As shown Figure *5.14*a, the XRD result from the weld stir zone shows ferrite, austenite, and carbide phases. As shown in Figure *5.14*b, the XRD result of the mild steel indicates ferrite phases as $\alpha 111, \alpha 200, \alpha 220,$ and $\alpha 211$. The XRD results of SS304 as shown in Figure *5.14*c shows that it mainly contains austenite phases such as $\gamma 111, \gamma 220\ \gamma 200,$ and ferrite $\alpha 211$. Generally, the ferrite structure is *bcc* for low carbon steel at room temperature. Few peaks of carbides are also precipitated during the weld cooling cycle due to the element diffusion (Guo & Shen, 2019). Few prominent lower intensity peaks correspond to the retained austenite in the weld zone microstructure. The obtained XRD results are matching with the results reported by Guo and Shen (2019).

5.3.3 Tool wear characterization

Tool wear is the most common phenomenon observed in FSW of high-strength materials like titanium, nickel, and steel alloys. Tool particles are also observed in the weld microstructure, as discussed in section 5.3.1. Jafarzadegan et al. (2013) and Lakshminarayanan et al. (2010) also reported the presence of tungsten tool particles in the weld zone microstructure. A bluish layer is formed at the tool's outer surface, indicating the tool's oxidation wear, which is in line with the published work (Tiwari et al. 2019b). Figure *5.15* demonstrates that the FESEM micrograph and energy dispersive spectra (EDS) of the oxide layer formed at the tool edge. EDS analysis indicates the elemental compositions of W, Co, and O at S3 is 62.7%, 27.6%, and 9.7%, respectively, as shown in Figure *5.15*d. Choi et al. (2009) reported oxidation wear as the dominant wear mechanism in FSSW of steel since the tool temperature exceeds 1000 °C, suggested that tungsten (W) particles are easily reacted with oxygen in the atmosphere to form different tungsten oxides. Figure *5.16* shows the characterization of the contact surface of the tool by surface roughness, scanning electron micrographs, and energy dispersive spectroscopy analysis.

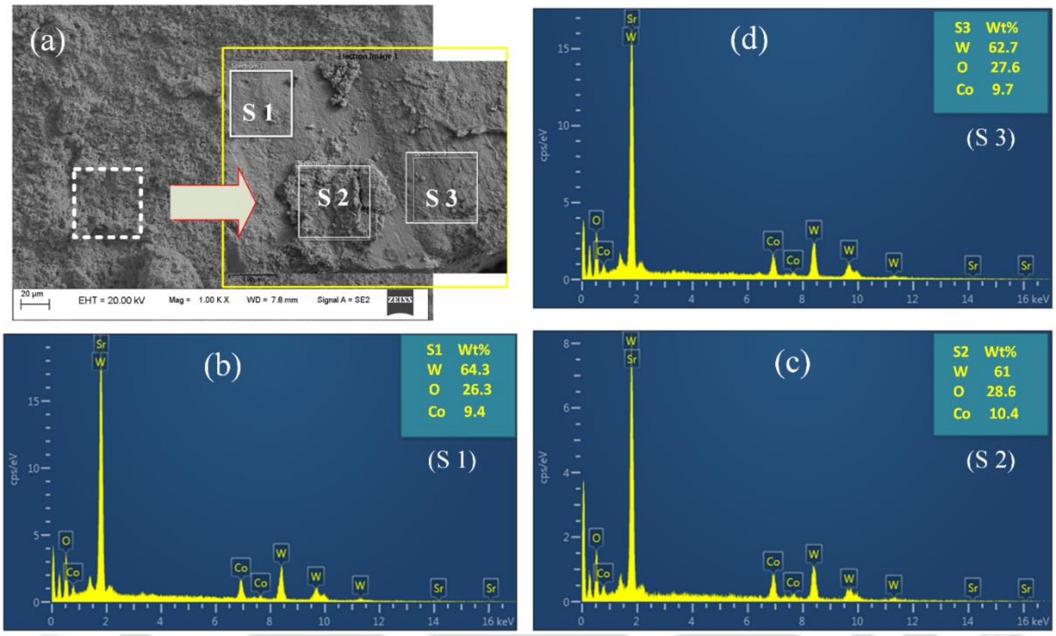

Figure 5.15 Oxidation of the tool edge after performing the welds: (a) FESEM micrograph, (b-d) energy dispersive spectra at different locations showing tungsten and oxygen as major element

Surface roughness (R_a) at the tool probe is 0.666 μm, and the tool shoulder is 0.595 μm as shown in Figure *5.16*a and Figure *5.16*b. These roughness values indicate that the tool probe is more prone to wear than the tool shoulder. Scanning electron micrograph illustrates the abrasion, scratches, and minor chipping at the tool contact surface as shown in Figure *5.16*c. EDS line scan (Figure *5.16*d and Figure *5.16*e) indicates Fe and O as the elements found on the shoulder contact surface, besides the primary elements, i.e., W and Co of tool material composition itself. Oxygen indicates the tool underwent an oxidation process, which is expected due to the absence of any shielding gas during welding. Fe element in the EDS analysis indicates the adhesion of workpiece material on the tool surface.

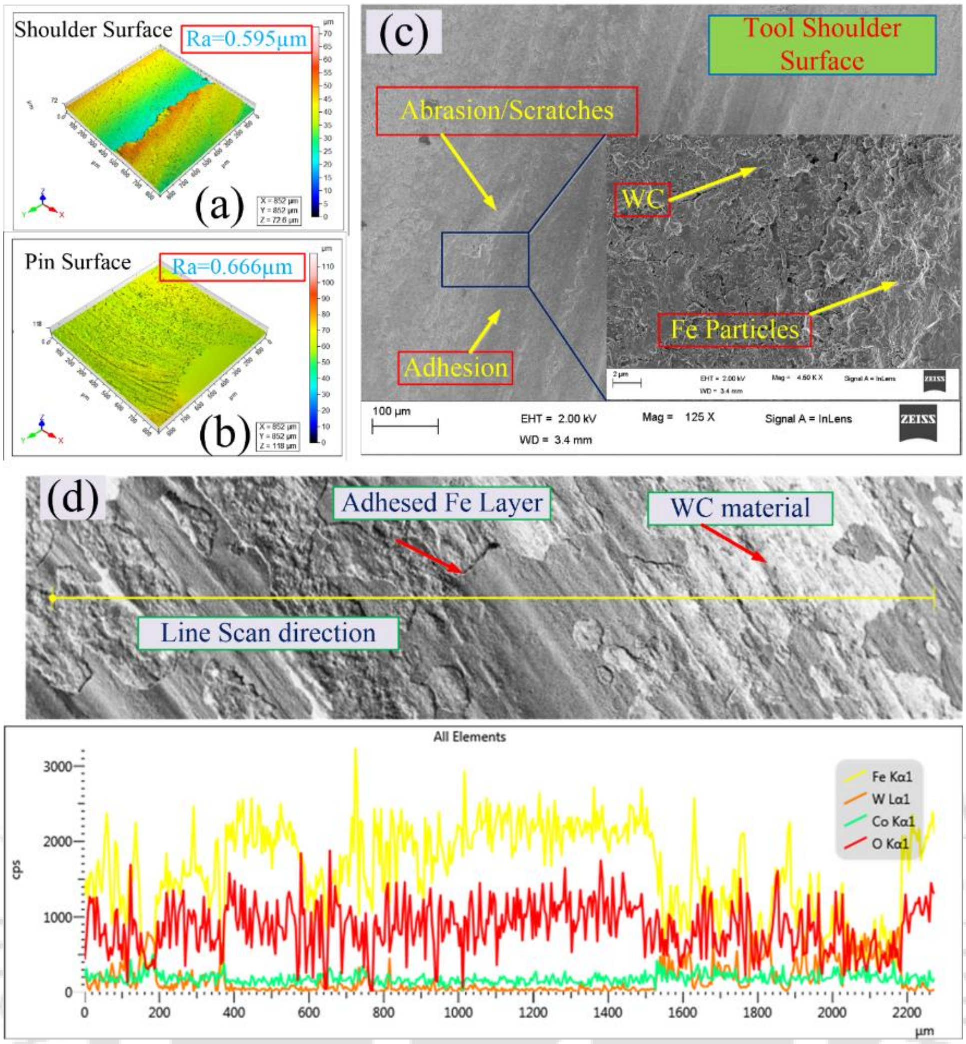

Figure 5.16 Tool wear characterization: (a) surface roughness at the tool shoulder, (b) surface roughness at the tool pin, (c) FESEM micrograph at the tool shoulder indicating scratches and Fe adhesion, (d) FESEM micrograph indication Fe adhesion and abrasion, and (e) EDS analysis reflecting higher peaks of Fe on tool shoulder surface

Figure *5.17* shows the XRD peaks of the tool before and after welding. The XRD peaks indicate carbide and oxide phases on the tool. The tool life degradation is associated with the formation of these oxide and carbide phases. Wear and deformation of tungsten tools are supposed to occur due to the high temperature attained during the FSW of steel. Warren et al. (1996) reported wear of tungsten carbide tool by oxidation and diffusion wear mechanisms. Gan et al. (2007) suggested that the tool pin material's tensile yield strength should be greater than 400 MPa at 1000 °C. From the above discussion, it can be concluded that the adhesion wear, abrasion wear, and oxidation wear are collectively responsible for the degradation of the tungsten tool. Therefore, the development of a cost-effective and reliable tool pin may be the most crucial aspect for friction stir welding of high strength materials like steel.

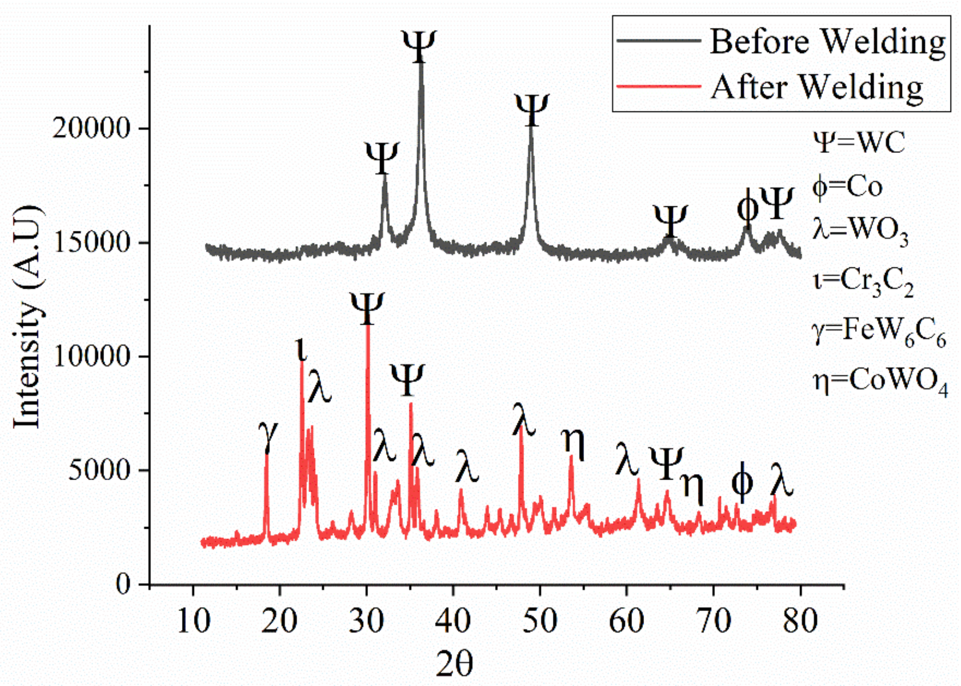

Figure 5.17 XRD phase analysis of tungsten tool before and after welding condition indicating the oxide phase WO_3

5.4 SUMMARY

Successful friction stir welds were produced between stainless steel and mild steel by using a WC-10 wt. % Co tool at rotational speeds (600, 875 rpm) and tool offsets (0.6, 1.2 mm). The following conclusions are drawn.

- Plastic deformation, material flow, and material mixing exhibited asymmetric characteristics at both sides of welds. Complex intermixing is observed in the weld region with higher intermixing on the advancing side. The two materials are interleaved with sharp and gradual transitions in some regions in the SZ. The bonding mechanism of dissimilar FSW of stainless steel and mild steel are both mechanical and metallurgical bonding.
- The YS and UTS of the joints are found to increase with the increase in tool rotational speed and tool offset distance. The maximum UTS for weld 4 is 107.6% of the UNS G10080 steel. The elongation to failure for weld 4 is 9.6% which showed a decrease of 53.8% as compared to UNS G10080. The presence of micro- and macro dimples on the fracture surface of the tensile specimen confirmed the typical ductile mode of failure.

- Microhardness contours correlated the microstructural changes in the different weld regions during FSW of dissimilar steels. The mild steel base material is softer than any other weld-affected zone, i.e., heat-affected zone (HAZ), TMAZ, and weld nugget which is consistent with the fracture location of tensile specimens. The hardness values in the deformed region, i.e., TMAZ and SZ of the welds are highly non-uniform due to complex material mixing in the weld zone.
- The maximum impact toughness for weld 4 is 41.5% less than the mild steel. Ductile dimple fracture is observed in the upper region of impact specimens.
- Tool particles of varying sizes are entrapment in the weld zone. FESEM–EDS analysis confirmed that abrasion, adhesion, and oxidation wear are responsible for the tungsten tool's wear and degradation.
- From the study, it is observed that tool wear is significantly increased in FSW of dissimilar steels than FSW of low carbon steel. The next chapter deals with the experimental and numerical study on high strength low alloy DH36 steel.

--------------------*--------------------*----------------------:

Chapter 6

6 CFD MODELLING FOR PREDICTION OF THERMAL HISTORY AND MATERIAL FLOW DURING FSW OF DH36 STEEL

6.1 INTRODUCTION

In FSW, owing to difficulties in measuring the peak temperatures and flow fields experimentally, an integrated thermal and material flow model is proposed to investigate the peak temperature and associated viscosity, strain rate, and material flow. The model incorporated the temperature-dependent material properties for both workpiece material and tool material. The material during the FSW process is assumed to behave as an incompressible, single-phase flow. The appropriate boundary conditions are considered in the simulation. Based on that, temperature distribution, velocity vector, strain rates, material viscosity are investigated for different sets of rotational and traverse speeds. The resulting temperature distribution and material flow is not symmetric along the joint line. Moreover the temperature distribution and flow patterns on the advancing and retreating sides are significantly different. Some distinctive 3D features of the flow field could be appreciated. The analysis is performed by using Fluent ANSYS 14. The proposed model is validated with the experimentally obtained temperature at different locations.

6.2 MATERIALS AND METHODOLOGY

In this study, experiments are performed to validate the simulated temperature profiles on DH36 plates using tungsten tool. The chemical composition and properties of the tool material are the same as reported in section 3.2.1. The dimensions of each work plate used for the experiment is same as those used for simulation, i.e., 100 mm × 50 mm × 4 mm ($l \times w \times t$). The diameter of tool and tool pin length is 25 mm, and 3.4 mm, respectively. The pin has a conical geometry with a diameter of 7 mm at the tool shoulder and 5 mm at the tip. The plunge depth of 0.2 mm is adopted during the experiment. The temperature history is recorded by Infra-Red (IR) camera. K-type thermal couples are attached at different locations away from the weld centerline on both the advancing side (AS) and the retreating side (RS). The thermocouple is inserted at a distance of 9 mm from the weld centerline, fitted in "L" shape channel to avoid any damage. The non-dimensionless parameter Traverse Heat Input Ratio (THIR) is calculated for each welding conditions and reported in Table *6.1*.

$$\varphi = \frac{R_1 \omega}{U} \tag{6.1}$$

where R_1 is the tool shoulder radius in mm, U is the traverse speed in mm/min and ω is the angular speed in rpm.

Table 6.1 Welding conditions for the present CFD model

Case ID	**Rotational speed (rpm)**	**Traverse speed (mm/min)**	**THIR**
Case 1	600	60	785.37
Case 2	600	90	523.58
Case 3	600	132	392.68
Case 4	450	60	589.03
Case 5	300	60	261.79

6.3 RESULTS AND DISCUSSION

6.3.1 Temperature contour

Figure *6.1* shows the thermal contour for the case 1 performed at 600 rpm and 60 mm/min. The melting point of DH36 steel is 1788-1798 K (Nemat-Nasser & Guo 2003).The important thing observed here is that the predicted thermal contours are less than the melting point (T_m), of the DH36 steel. Prasanna et al. (2010) and Zhu & Chao (2004) also reported maximum simulated temperature less than the melting point during FSW of steel workpiece material.

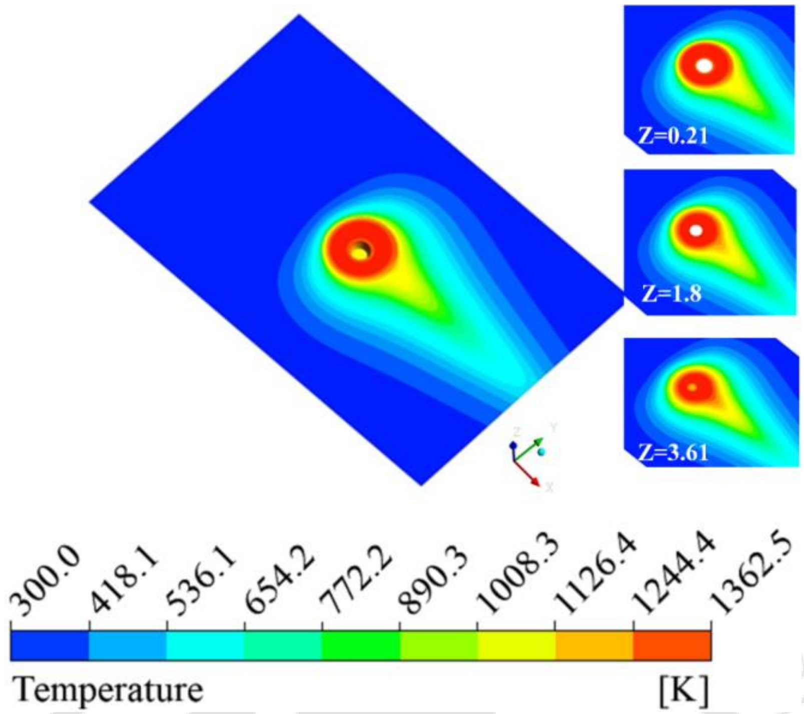

Figure 6.1 Temperature contour of the case 1 (i.e., rotational speed of 600 rpm and traverse speed of 60 mm/min)

Besides this, three $x-y$ planes are made to study the temperature contours at three different planes along with the plate thickness; the first plane (i.e., $z = 0.21$ mm) was at the top on the shoulder workpiece interface, the second plane (i.e., $z = 1.8$ mm) was at the mid surface of the plate, and the third plane (i.e., z = 3.61 mm) was at the root side of the pin. The peak values of temperature are seen on the top surface, i.e., shoulder-workpiece interface, and have a value of 1362.5 K. This result reveals contradiction with the results of Kadian & Biswas (2015) for the FSW of aluminum alloy AA7075 wherein it was reported that the peak temperature was observed at the pin tip workpiece interface. However, the obtained results are matching fairly with those reported by Toumpis et al. (2014) for the FSW of steel. During FSW, heat is generated by the three main factors (i) heat generation by friction (ii) heat generation by plastic deformation at the contact interface, and (ii) heat generation by viscous plastic dissipations in the shear zone. The heat loss ahead of the tool is significantly large during FSW of steel. The heat loss is less to the preheated workpiece behind the tool due to low diffusivity. In addition to that, the temperature at the midplane is about 1231.4 K. It is observed that the temperature is decreasing from the shoulder region towards the pin region. The minimum temperature is obtained near the root of the pin. This can be explained during FSW maximum heat is generated by shoulder rather than tool pin. The simulated peak temperature (1362.5 K) for case 1 is in the range of the peak temperature calculated experimentally by Lienert et al.(2003) and Selvaraj et al. (2013) for AISI1018 steel. Figure *6.2*a shows the temperature profile in the AS-RS frame and leading- trailing side frame of the workpiece material. Figure *6.2*b shows the line of temperature measurement in the x-direction (line $a - f$) and in y-direction (line h–m).

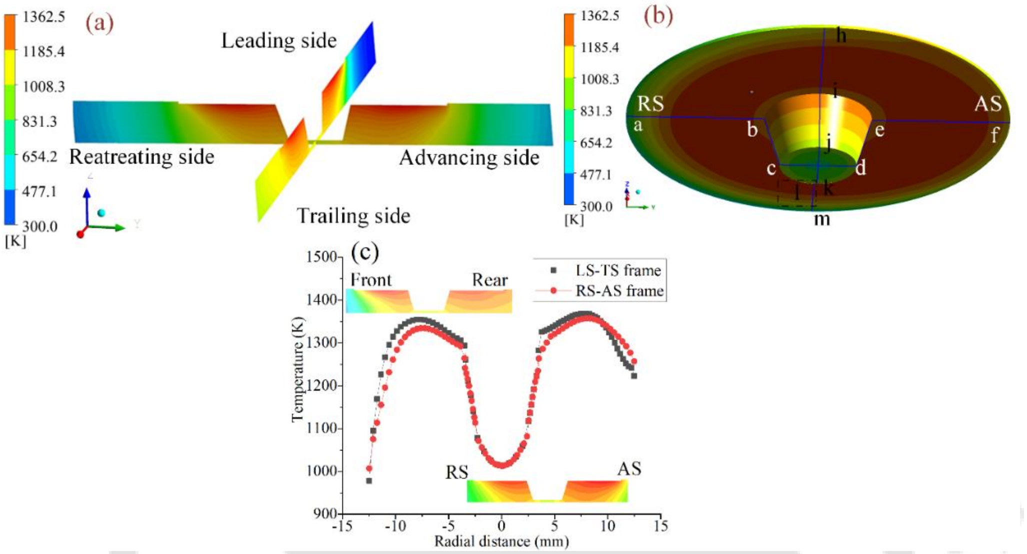

Figure 6.2 (a) Temperature contour in the transverse direction (Y-axis) and longitudinal (X-axis), (b) thermal contour indicating temperature distribution at different locations, and (c) temperature profile along the leading trailing frame and AS-RS frame

From the temperature profiles, as shown in Figure *6.2*c, the temperature from pin root edge increases, reaches a maximum, and decreases rapidly at the shoulder edge due to the high rate of heat loss from the backing plate and sidewalls. The lower temperature and sharp gradient at the shoulder periphery are associated with higher heat loss due to conduction. The temperature decreases along the pin side from pin root ($z = 0.2$ mm) to pin tip ($z = 3.6$ mm). In FSW, the tool shoulder generates maximum heat and distance away from the tool shoulder leads to a significant decrease in peak temperature value because of heat loss at the FSW machine bed. The reason for this is the comparatively lower temperature at the leading side. Unlike the leading side, the trailing side experienced severe plastic deformation and was surrounded by the hot plasticized material before it was forged to cool down.

Figure *6.3* illustrates the variation of peak temperature for case 1 with the variation of frictional coefficient and mechanical efficiency.

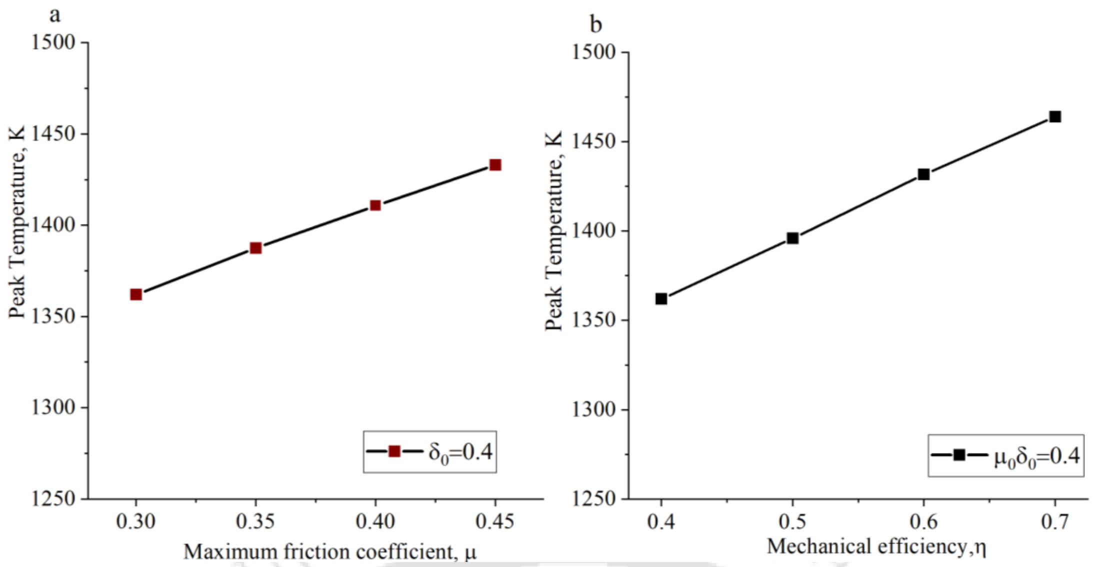

Figure 6.3 Peak temperature variation with (a) coefficient of friction, and (b) mechanical efficiency

It is found that maximum temperature is directly related to the coefficient of friction and mechanical efficiency. Figure *6.3*a depicts the increase in peak temperature value with the frictional coefficient. Figure *6.3*b shows the peak temperature variation with mechanical efficiency. It is observed that peak temperature increases as the mechanical efficiency are increased from 0.4. This is explained as on increasing the value of mechanical efficiency, the amount of work done gets increased. Manvatkar et al. (2015) also found that μ and δ have significant effect on simulated peak temperatures. The higher values of coefficient of friction resulted abnormal variation of temperature at the root of the weld. Parametric variations (i.e., case 2, case 3, case 4, and case 5) of friction stir welds are carried out by considering the above combination of values of coefficient of friction and mechanical efficiency.

The comparison of simulated peak temperatures for different welding conditions (mentioned in Table *6.1*) is depicted in Figure *6.4*.

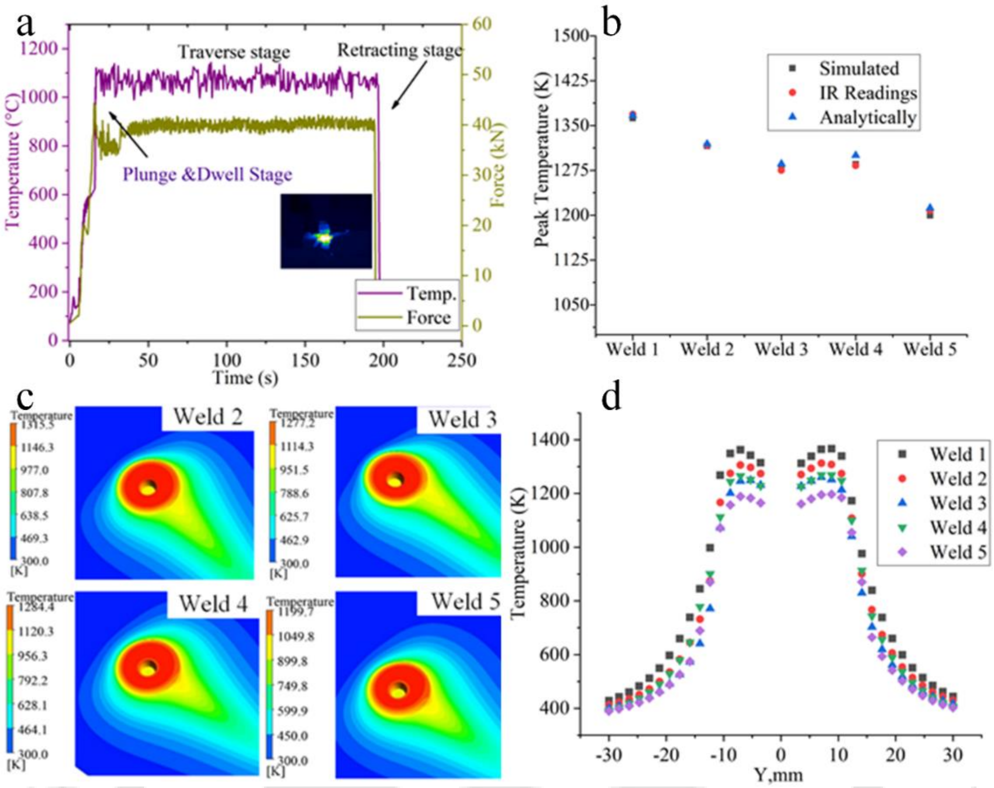

Figure 6.4 (a) Downward z force and temperature data recorded by non-contact infra-red (IR) camera, (b) peak temperature comparison for different welding conditions, (c) thermal contours, and (d) temperature distribution along Y axis for different welding parameters

Figure *6.4a* indicates the thermal profile recorded by the Infrared (IR) camera and the downward z-axis force for case 1. It is obtained that the downward z-axis force is maximum during the plunge stage which is reduced in the dwelling stage. The value of force is reduced from 43.65 kN at the plunge stage to 36.14 kN in the dwelling stage. The mixed sliding sticking nature leads to the generation of spikes during the process. The downward z force is further increased slightly during the traverse stage. In the traverse stage, the downward z force reached an average value of 39.25 kN. Figure *6.4*b shows the maximum temperature obtained at different welding conditions. In the FSW process, peak temperatures are dependent on rotational speed and traverse speed. The peak temperature (T_p) is also calculated analytically by the relationship as given in Eqn. 6.2.

$$\frac{T_p}{T_m} = K_c \left(\frac{\omega^2}{U \times 10^4} \right)^{\alpha_c} \tag{6.2}$$

where T_p is the maximum temperature reached, T_m is the melting point of the DH36 steel plate, ω is the angular velocity of the tool, U is the welding speed, and α_c $(= 0.04{-}0.12)$ and $K_c(=$

0.65−0.79) are constants. The above relationship predicted the peak temperature (T_p), which is obtained as 1093.4 °C for the weld 1. The above-mentioned equation is best fitted for the variation of traverse speeds and rotational speeds as shown in Figure*6.4*b. Moreover, as depicted in c, it can be concluded that low traverse speed (high THIR value) generates a more symmetrical temperature profile around the tool shoulder. Colegrove & Shercliff (2006) obtained that the weld zone (more specifically HAZ) increases with the increases in rotational speed and decreases with the increase in traverse speed. Additionally, on increasing weld traverse speed, it is found that the temperature asymmetry across the AS and the RS is increased, as shown in Figure *6.4*c. This can be explained at the advancing side, high relative velocity causing the higher heat generation through viscoplastic material shearing. Material is pushed more in the AS at the shoulder periphery due to differences in the velocity component at the advancing side. Similar asymmetric temperature across AS and RS and high asymmetry at higher weld traverse speed were also observed by Al-Moussawi et al. (2017) and Darvazi & Iranmanesh (2014). The obtained temperatures in Figure *6.4*d are in the range of 928–1089.5 °C. Temperature asymmetry along the AS and RS is 13.5% for case 1, 18.9% for case 2, 22.8% for case 3, 15.1% for case 4, 15.6% for case 5. When traverse speed increased, and rotational speed decreased, simulated peak temperatures decrease, as shown in Figure *6.4*d. The reason behind this is that the traverse motion of the tool also induces heat loss by convection. This can results in decreased cooling rates at low weld traverse speed than those with high traverse speed. Padmanaban et al. (2014) also observed similar results when traverse speed was increased during FSW of aluminum alloys. Simulated peak temperature variation with rotational speed and traverse speed can be explained as since during the FSW process the heat generation is inversely proportional to traverse speed and directly related to the rotational speed. Previous research also highlighted the similar trends in the coupled heat and material flow FSW simulation of stainless steel (Nandan et al. 2006) and mild steel (Nandan et al. 2007).

6.3.2 Fluid flow results

6.3.2.1 Viscosity distribution

During FSW, heat generation is due to three reasons (i) frictional heat (ii) plastic deformation, and (iii) viscous dissipation. Figure *6.5* shows a comparison of the dynamic viscosity in the AS-RS frame and leading- trailing frame of workpiece material. In the AS-RS frame, maximum viscosity is observed on the retreating side, while in the leading –trailing frame, viscosity is maximum in the leading side of the tool. Non-Newtonian viscosity at the leading side is slightly higher than the trailing side. The cut-off viscosity value at the boundary is $5.2\ \mathrm{MPa} - \mathrm{s}$ which is consistent with the previous research on the steel (Al-Moussawi et al. 2017). Figure 6.5c shows that strain rate seems to be symmetrical on both sides of the tool as the deformation and the material flow are largely dependent on tool rotational speed and the stick-slip condition at the interface. In present simulations, peak values of around 1500 s^{-1} are observed near the shoulder outer periphery for case 1. The simulation results predicted the local strain rate at z =2 mm ranges from about 80 to 260 s^{-1} as indicated in Figure 6.5c. Colegrove & Shercliff (2006), Al-Moussawi et al. (2017), Sadeghian et al. (2018), and Chen et al. (2018) also reported that the maximum values of strain rate can reach up to 1000 s^{-1} at the tool shoulder periphery at higher rotational speeds. The deformed material under the tool shoulder is found to be experiencing temperatures in the range of 1000-1100 °C and high strain rates in the order of (10–100 s^{-1}).

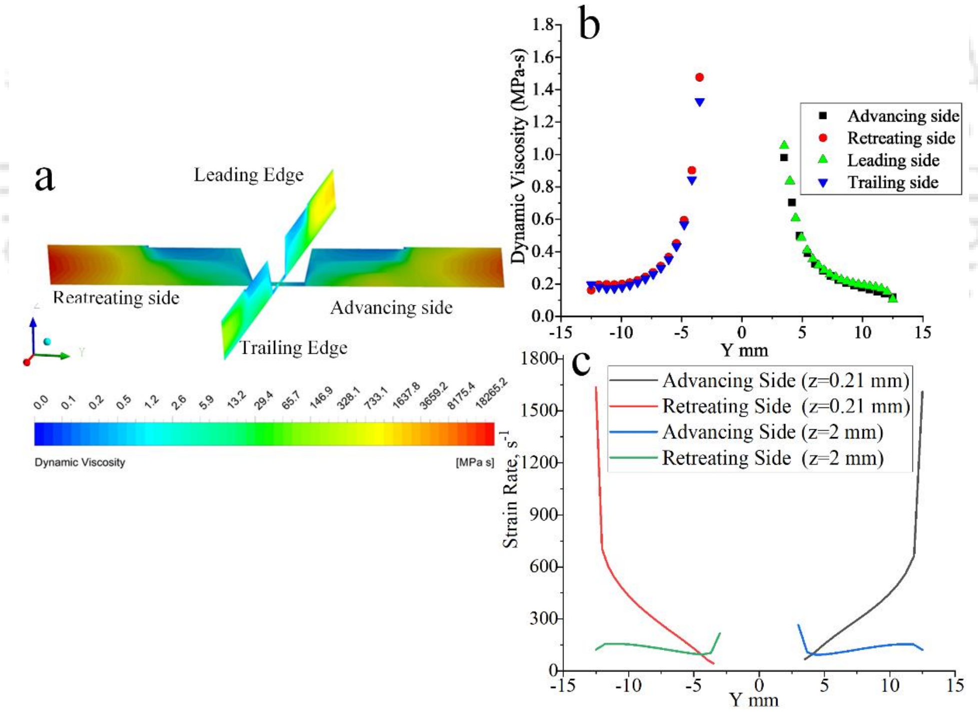

Figure 6.5 (a) Dynamic viscosity variation in the AS-RS frame and leading-trailing edge, (b) comparison of dynamic viscosity in the AS and RS, and (c) strain rate variation at $z = 0.21\ mm$ and $z\ = 2\ mm$

Figure 6.6 shows the spatial distribution of non-Newtonian viscosity at three different planes along Z direction ($\mathrm{z} = 0.21, \mathrm{z} = 1.\ 8$ and $\mathrm{z} = 3.61$ mm).

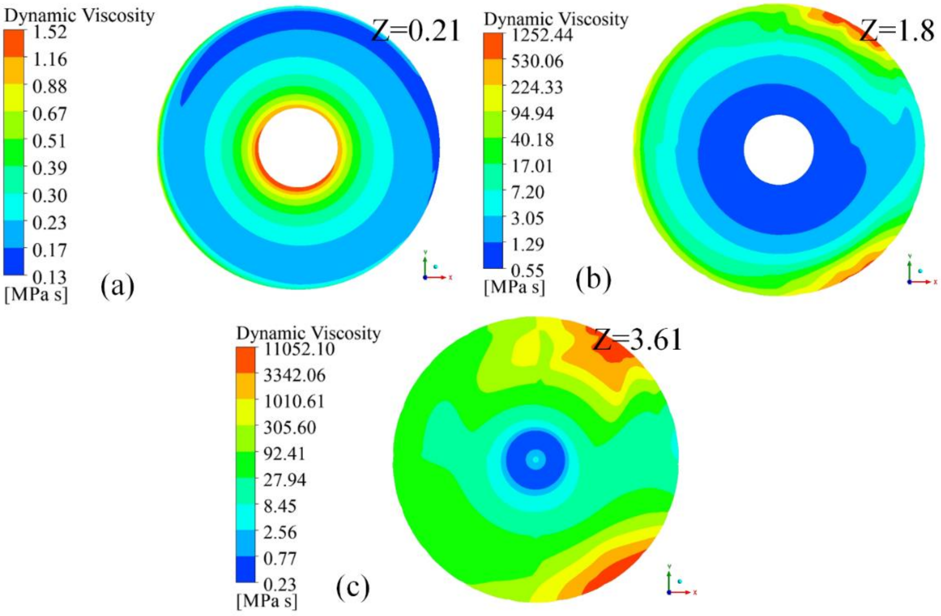

Figure 6.6 shows the comparison of spatial distribution of dynamic viscosity at rotational speed $\omega = 600$ rpm and U= 1 mm/s at three different planes along thickness (a) z = 0.21 mm, (b) z = 1.8 mm, and (c) z = 3.61 mm

Viscosity is maximum at the pin root edge $(z = 3.61\text{mm})$, which increases towards the shoulder contact interface. The viscosity is minimum at the advancing side. According to the viscoplastic material model, non-Newtonian viscosity is directly related to the flow stress and inversely related to the strain rate, as illustrated in Eqn. 3.15 (Chapter 3). The reason for lower viscosity at the AS is the maximum temperature associated with this region. On the plane $(z = 1.8\text{ mm})$, as shown in Figure *6.6*b, the semi-fluid region is seen due to drastic variation in the viscosity near the lateral surface of the tool pin. At the pin bottom interface $(z = 3.61\text{ mm})$, the viscosity gets increased, as depicted in Figure *6.6*c. The viscosity is minimum only at the pin center, and the viscosity is maximum near the tool pin edge. Al-Moussawi et al. (2017), Hasan et al. (2015) and Nandan et al. (2006) found similar trends of increasing viscosity from the shoulder-workpiece interface towards the probe end. Nandan et al. (2007) observed that the viscosity above 5 $Pa - s$ resulted in less material flow. The strain rate values are another aspect to explain the viscosity variation towards the probe end. It is clear that the viscosity is inversely related to the temperature and strain rate, so considering the strain and temperature values it can be explained that the viscosity is increased towards the probe end.

6.3.2.2 Velocity contour

The comparisons of velocity contour for case 1, case 4 and case 5 are demonstrated in Figure *6.7*.

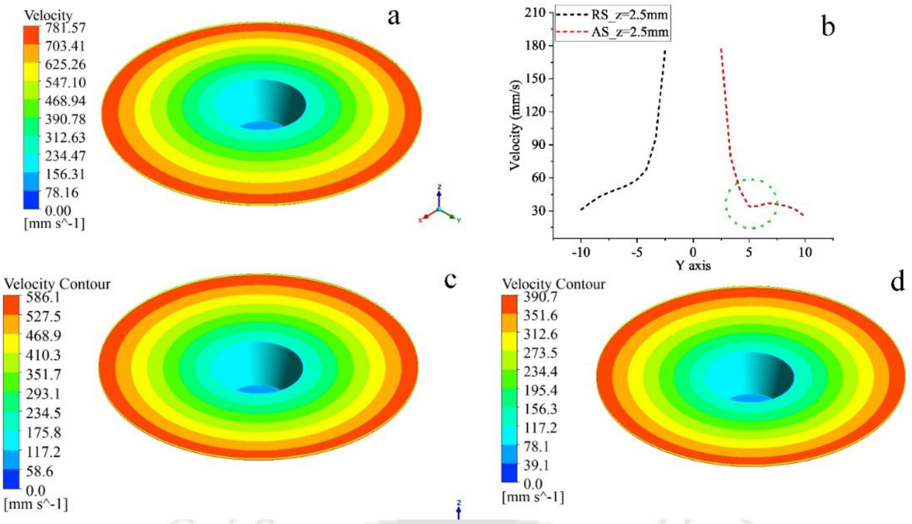

Figure 6.7 (a) Velocity contour variation of case 1, (b) velocity plot of case 1 , (c) case 4, and (d) case 5

From the velocity contour, it is seen, that the velocity is decreasing from the shoulder's outer edge towards the shoulder's inner edge. The velocity contour confirms that the velocity is maximum for case 1 as shown in Figure 6.7a. The effect of temperature on material flow is significant i.e. higher the material's temperature, the easier the plasticized material flows. Chen et al. (2018) reported similar order of velocity magnitude for the same boundary problem. Figure 6.7b shows that the velocity in the retreating side is greater than the advancing side. This can be explained as the material flow direction in the retreating side is the same as the rotation of the tool. Figure 6.7b explained that the velocity at the pin lateral surface ($z = 2.5\ \mathrm{mm}$) decreases from $180\ \mathrm{mm/s}$ to $30\ \mathrm{mm/s}$. The abrupt change in velocity is observed on the advancing side of the weld joint. Figure 6.7c and Figure 6.7d show the velocity contour for case 4 and case 5. From the combined analysis of the temperature distribution and velocity contour, it is obtained that the temperature is minimum at the bottom region and hence the flow velocity is slowest in this region. This makes the region more susceptible to defect formation, especially at high traverse speed. Visualizing the material movement during the FSW process provides a deep understanding of flow patterns and can reduce the chances of defect formation. The previous literature (Stevenson et al. 2015; Tingey et al. 2015;) reported that defects like wormhole and tunnel defects were likely to occur in this region and the tendency of the generation of these defect are increased at high traverse speed due to insufficient plasticization of material and material flow.

6.3.2.3 Velocity vectors, streamlines, and pathlines

Material flow is investigated by plotting the velocity vectors, streamlines, and pathlines at the tool and workpiece material interface. Figure *6.8* shows the velocity vectors at different planes.

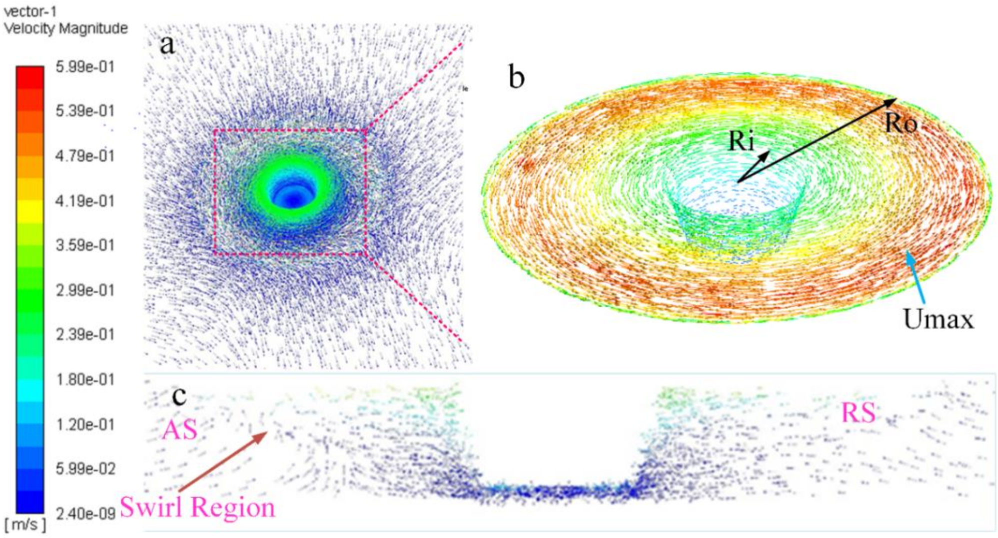

Figure 6.8 (a) Velocity vectors, (b) velocity vectors at the interface of tool and workpiece, (c) velocity vector in the AS-RS region for case 1 i.e. $\omega\ = 600\, rpm$, and $V\ = 60\, mm/min$ in YZ-plane

From Figure *6.8*a, it is observed that the flow of plastic material is different in different positions. The material starts contacting the tool pin in the RS and starts to rotate with the tool pin, and finally pushed into the wake behind the pin. In addition to that, the material viscosity is lower in the region where severe flow occurs. The relative velocity in contact with the tool is ranged from $2.4\mathrm{e}^{-9}$ to $0.599\ \mathrm{m/s}$. Toumpis et al. (2014) observed that the velocity on the tool/ workpiece interface was $0.366\ \mathrm{m/s}$ following the temperature distribution. Figure *6.8*b depicts that the velocity of the plasticized materials is minimum at the pin root edge (R_i) and increases towards the shoulder outer edge (R_o). Moreover, the material flow is strictly dominated by the rotation of the tool shoulder at the top surface and spiral movement in the downward direction by the stirring action of the tool pin. It signifies that the tool shoulder is a major source of heat as well as momentum transfer at the top portion of the weld. Figure *6.8*c shows that the material is flowing from the retreating side towards the advancing side and forged at the trailing side. The shoulder forces the material in the downward direction which combines with the upward flowing material by the tool pin. Zhang et al. (2007) reported swirl zone in the advancing side during material flow simulation and further added that the velocity of material flow increased with the increase in traverse speed. In FSW, material subjected to plastic deformation has significantly fast relative velocity. Also, the temperature gradient resulted in the flow velocity gradient distribution. The temperature has an obviously prominent effect on the flow of the plasticized material, the higher the temperature of plasticized material, the easier the material flow can occur. It is obvious as the temperature increases, the strength of the material reduces which enhanced flow of material during welding.

Material flow is further investigated by plotting the velocity streamlines and pathlines at the tool-workpiece interface, as shown in Figure *6.9*.

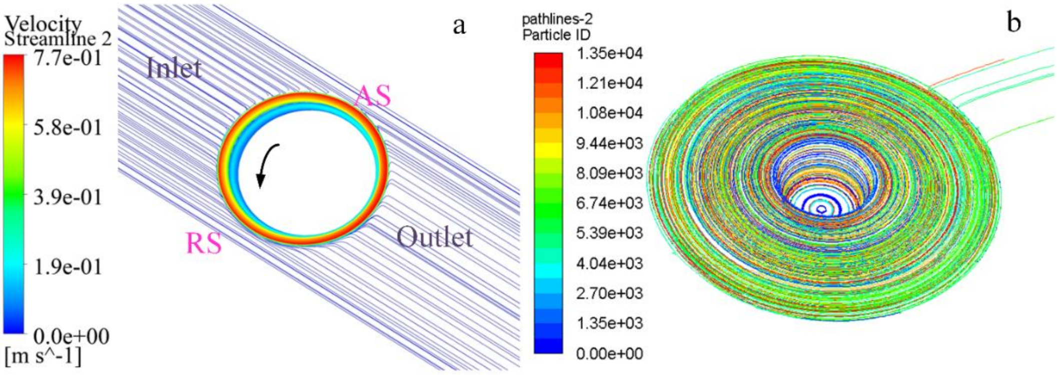

Figure 6.9 (a) Streamlines, and (b) pathlines for case 1 i.e. $\omega = 600\ rpm$ and $V = 60\ mm/min$

Figure *6.9*a shows that material enters the shoulder region from the advancing side with velocity the same as the welding speed, and then reflow in opposite direction. The streamlines are observed in the straight path away from the tool. In addition to that, the streamlines are segregating in the tool contact region. Moreover, the velocity streamlines are denser and closely packed circular lines near the tool pin, and this flow recirculates around pin length. These streamlines occupy the larger area at higher elevations (i.e. shoulder influenced) region due to the high momentum transfer. Similar trends in the streamlines at the tool shoulder and tool pin were also observed by Colegrove et al. (2007), Hasan et al. (2015), and Sun & Wu (2020). Figure *6.9*b depicts the traces of the material flow in the tool-workpiece interface region. The color of the line and the color bar value were used to differentiate the particles, and the ID of the particle respectively. It is seen that the plasticized material is transported in different regimes and deposited by the tool shoulder before it was cooled. Morisada et al. (2011) during FSW of aluminum alloys, experimentally investigated the material flow using tungsten tracers and X-ray technique. It was observed that the tool shoulder in FSW results in the maximum deformation which results in the formation of basin shape/inverted trapezoidal shape of the weld zone. It is reported in previous literature (Reynolds 2000) that the defects can be generated in the AS of the joint due to the formation of a stagnant zone. In another endeavor, (Morisada et al. 2014), also found that the velocity of tracers in aluminum is significantly higher than in the steel because of high shear stress in steel causing more resistance to flow. It is clear that during welding of high strength materials, significant plastic flow can only be achieved at low traverse speed.

The developed integrated thermal and material flow model was validated with the peak temperatures using thermocouples as depicted in Figure *6.10*. The refinements of the heat source model by considering the heat transfer coefficient at the bottom and side walls influence the temperature fields at different locations as described phenomenologically.

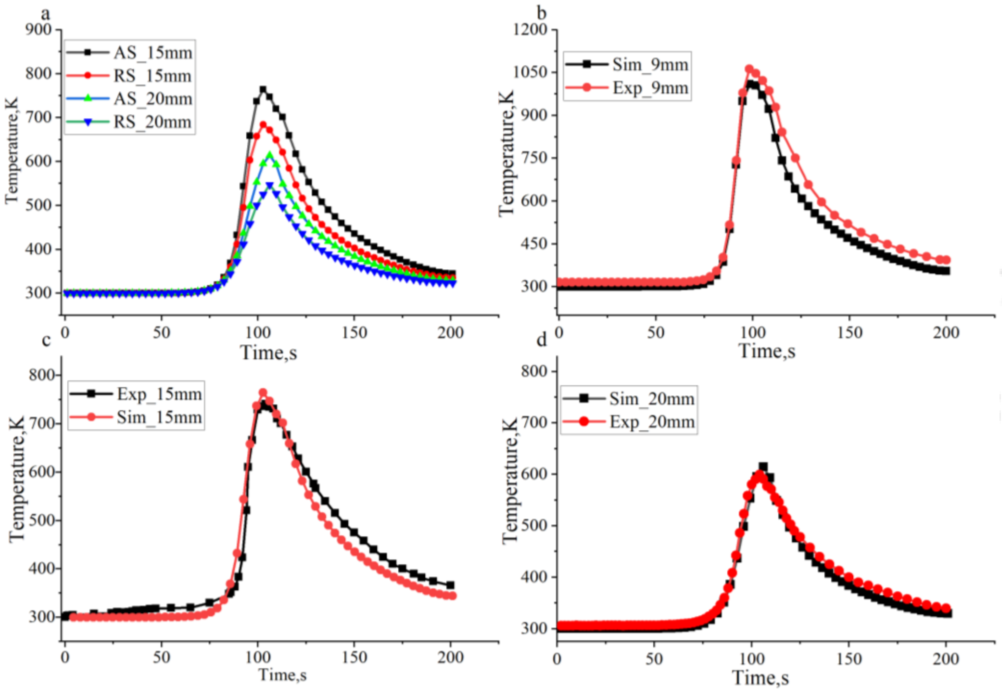

Figure 6.10 (a) Comparison of surface temperature at 2.5 mm from the tool shoulder edge (15 mm from the weld centerline, (b) temperature validation at 9 mm from centerline inside the channel, (c) temperature validation at 15 mm from weld centerline, and (d) temperature validation at 20 mm from weld centerline

As shown in Figure *6.10*a, the temperature distribution is asymmetric, and the maximum temperatures are found on the advancing side. Figure *6.10*b represents the experimental data and simulated temperature history inside the channel on the retreating side at 9 mm from the weld centerline. From Figure *6.10*b, it can be concluded that the peak temperatures were overmatched, with a percentage error of 8.24%. In another endeavor, the temperature was measured at the proximity of tool shoulder edge 15 mm (i.e., 2.5 mm from shoulder edge) and 20 mm far away from the weld line as shown in Figure *6.10*c and Figure *6.10*d. It is observed that the peak temperature showed good agreement with 5.21% and 5.68% at 15 mm and 20 mm from the centerline, respectively. Figure *6.11* shows the weld joint characterization by surface appearance, tensile properties, and microhardness of the weld produced at 600 rpm and 1 mm/s. Figure *6.11*a indicates the in-process monitoring and thermal recording of the welding. Figure*6.11*b and Figure*6.11*c display the surface appearance at the top and bottom side of the weld joint. It appears that the weld joint was free from any visible defects. Figure *6.11*d shows the hardness contour of the transverse cross-section. Hardness was maximum in the stir zone with peak values located at the top surface. The peak hardness value was 86% higher than the base material. The tensile test indicates the higher tensile strength and lower ductility as compared to the base material, as shown in Figure *6.11*e. The fractured sample indicates a cluster of dimples and voids on the fractured surface. It confirms the sufficient plastic deformation of the tensile specimen before fracture, as sown in Figure *6.11*f.

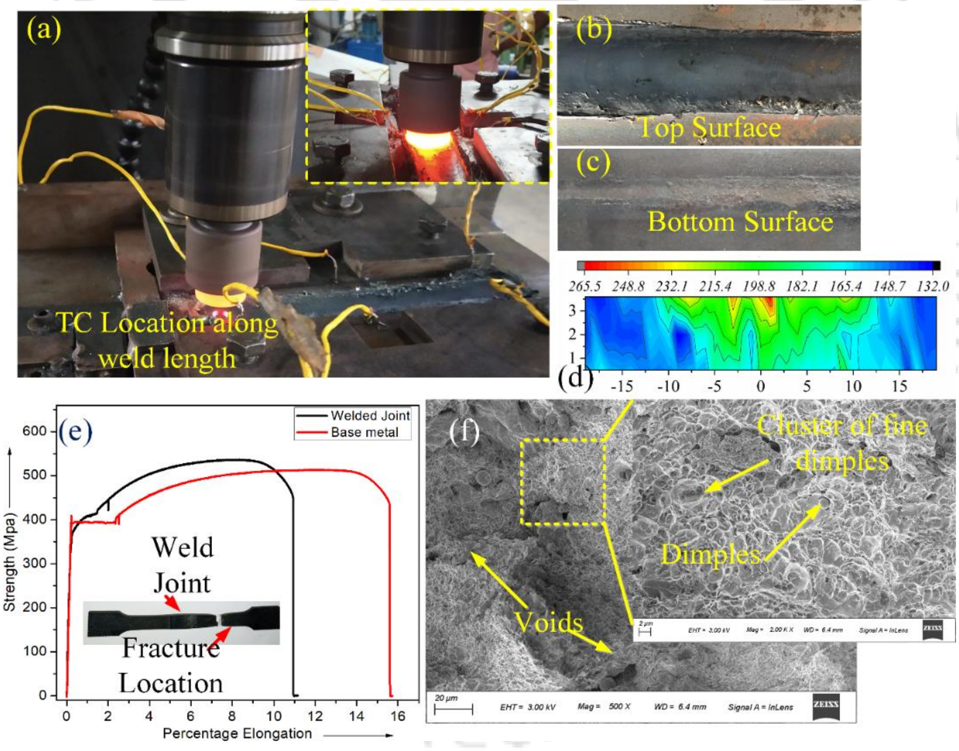

Figure 6.11 (a) Welding of DH36 plates with tungsten carbide tool for case 1, (b) top surface appearance of welded plate, (c) bottom surface appearance ,(d) vickers microhardness profile at 500 gF along the transverse cross-section, (e) tensile properties of the welded specimen, and (f) fracture surface of tensile specimen indicating a cluster of fine dimples

Figure *6.12*a shows the weld macrostructure at 600 rpm and 1mm/s. The weld zone formation during FSW depends on the tool geometry and weld process parameters. Figure *6.12*b illustrates the material transportation around the tool pin and tool shoulder. In FSW, material moves from leading side to the trailing side around the tool pin and forged back in the AS by the tool shoulder as depicted in Figure *6.12*b. Figure *6.12*c shows the inflow of material from the advancing side. Figure *6.12*d shows the complex vortex swirl and shear bands which are generated due to the vertical movement of material at the pin end. There is a combination of the deformed material's vertical and circular motion due to the rotational and traverse movement of the pin. The intensities of the formation of these vortex swirls and shear bands are more at low welding temperature. Figure *6.12*f shows the material outflow from the retreating side of the weld joint. At high process temperatures, the material flows more easily, which results in smoother mixing of material in the SZ.

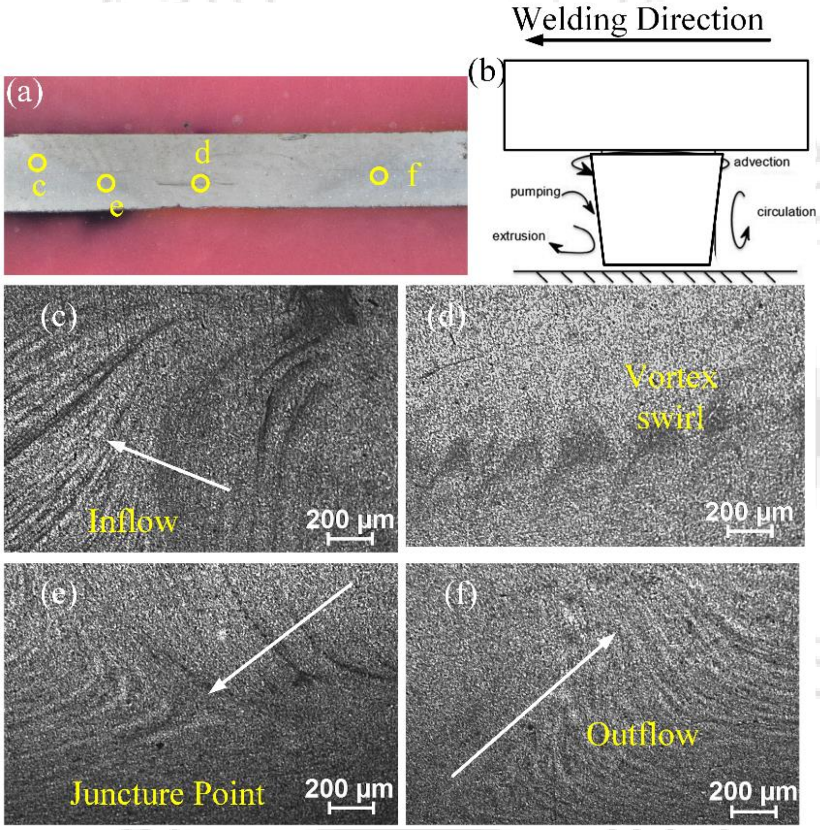

Figure 6.12 Material flow by the action of tool pin and tool shoulder (a) cross section macrograph of welded specimen, (b) schematic diagram of material transportation, (c) material inflow at AS, (d) vortex swirl at SZ in the bottom region, (e) juncture point indicating the material mixing from the top region and bottom region, and (f) material outflow at the RS

6.4 SUMMARY

The developed CFD model successfully demonstrated the material flow as well as the thermal analysis process during the FSW of DH36 steel. The following conclusions are drawn:

- The simulated profiles and experimental profiles are consistent in shape, but a little higher in magnitude at both 15 mm and 20 mm from the centerline. This difference in the measured and simulated temperatures are acceptable and within the accuracy of thermocouple readings.
- An asymmetry and skewness of temperature are observed at the advancing trailing frame. The maximum temperatures at AS is associated with the weld tool's tangential motion, which counters the slide of work-piece material on the tool advancing side leads to a peak temperature and high-temperature gradient on the advancing side.
- The shear stress at the leading-retreating side was higher than the advancing-trailing side due to low temperature at the leading-retreating side.
- The heat convection coefficient predominantly affects the temperature distributions. The temperature was increased with an increase in rotational speed and a decrease in traverse speed.
- High heat input ratios lead to a more uniform temperature gradient along the thickness direction. This indicates that the rotational speed has significantly more effect on heat generation than the traverse speed.
- The velocity streamlines indicated the drastic change of material flow at the shoulder edge. It is clear from the velocity streamline that the material flow zone is wider at the retreating side than the advancing side, which results from the difference in material deformation mode. The generated vector plots explained the asymmetry in the material flow, which resulted in the formation of vortex and swirl regions in the weld joint macrostructure.
- The peak strain rate is attained at the shoulder edge during the welding process. Strain rates are different in both the AS and RS of the weld joint. It is because of the difference in the relative velocity.

:--------------------*--------------------*----------------------:

Chapter 7

7 FRICTION STIR WELDING OF DH36 STEEL USING TWO DIFFERENT TOOL COMPOSITIONS

7.1 INTRODUCTION

In In this study, two different grades of tungsten carbide tools, i.e., tool A $(WC - 6\, wt.\%\, Co)$***and tool B*** $(WC - 10\, wt.\%\, Co)$ ***are used to join*** $DH36$ ***steel plates and tool wear is investigated. Tool wear is a continuous phenomenon that depends on the total distance traversed by the tool. This study is primarily focused on evaluating the effects of rotational speeds and traverse speeds on the tool wear. Pre- and post-welded tungsten carbide tools are characterized by using different techniques like weight measurement, surface roughness, thermography using a non-contact Infra-red (IR) camera, 3D coordinate measurement system, field emission scanning electron microscopy (FESEM) equipped with energy dispersive spectrometry (EDS), and X-ray diffraction (XRD). The primary areas of interest were to investigate the wear and characteristics of shoulder surface, pin top surface, pin length, and shoulder non-contacting surface. This study provided preliminary guidelines for wear and degradation and can serve as a guideline for selecting process parameters and, tool composition to arrest/mitigate the wear and degradation of the tungsten-based tool during FSW of*** $DH36$ ***steel.***

7.2 MATERIALS AND METHODOLOGY

In this work, FSW tools of tungsten carbide namely tool A (i.e., $\mathrm{WC} - 6\ \mathrm{wt.\%Co}$) and tool B ($\mathrm{WC} - 10\ \mathrm{wt.\%Co}$) are used to join DH36 steel plates. The chemical composition (in wt.%) is C (0.146), Mn (1.51), S (0.0001), P (0.007), Si (0.22), Cu(0.14), Ti (0.03), Va (0.003), Nb (0.03), Al (0.017) and balance Fe. Plates are cut in the dimensions $300\ \mathrm{mm} \times 100\ \mathrm{mm} \times 4\ \mathrm{mm}$. FSW tool is of the flat shoulder with a diameter of 25 mm and pin length of 3.42 mm. Figure *7.1* shows the schematic diagram of tool geometry designations used in the present study. Furthermore, on-line monitoring of the FSW process and surface temperatures are made using a non-contact temperature measurement system as illustrated in Figure *7.1*b. The scan is made along the welding direction. The tool pin is cut perpendicular to the Z-axis (i.e., tool axis) which is represented by section $a - a'$ as shown in Figure *7.1*c. Similarly, the tool shoulder section is cut parallel to the tool axis which is represented by section $b - b'$ for the metallographic characterization.

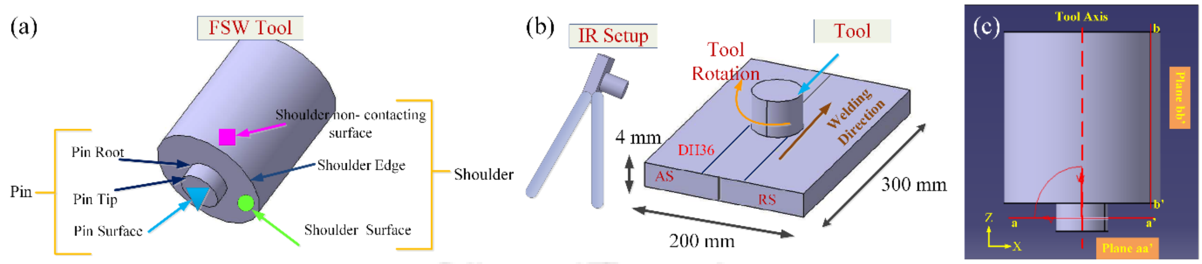

Figure 7.1 Schematic representation: (a) tool designation, (b) monitoring of FSW process using non-contact IR camera, and (c) pin tip and shoulder cross-section for post-weld inspection (Schematic is drawn not to scale)

Tool wear is a continuous phenomenon that increases with the distance covered and the tool work contact time. In the present study, multiple welding runs of each length 250 mm are performed without considering the effect of repetitive plunge time, dwell time and tool retract time. Mechanical properties, i.e., hardness and transverses rupture strength, are summarized in Table *7.1*.

Table 7.1 Details of tungsten carbide tool materials used for FSW of DH36 steel

Properties (Room Temperature)	**Values**	
	Tool A	**Tool B**
Composition ($wt.\%$)	$\mathrm{WC} - 6\ \mathrm{wt.\%Co}$	$\mathrm{WC} - 10\ \mathrm{wt.\%Co}$
Hardness	$75\ \mathrm{HRC}_{150}$	$81\ \mathrm{HRC}_{150}$
Rupture Stress	$2460\ \mathrm{N/mm}^2$	$3740\ \mathrm{N/mm}^2$

The welding operating parameters used in the present study are shown in Table *7.2*. These parameters are selected based on preliminary studies and from the published literature (Siddiquee and Pandey 2014; Lienert et al. 2003) to study the effect of rotational and traverse speeds on the tool degradation. Tool wear is characterized by both quantitatively and qualitatively techniques, i.e., visual inspection, weight measurements, profile measurements, surface roughness, FESEM-EDS analysis, and XRD analysis. For metallographic studies, samples are polished to obtain mirror finish using a $1-\mu m$ grade diamond paste and then etched by Murakami reagent (5 g $Fe_3(CN)_6$,5 g NaOH and 50 ml distilled water).

Table 7.2 Welding operating conditions for different tool materials tool A and tool B

Tool ID		**Welding conditions**	
		Rotational speed (rpm)	**Traverse speed (mm/min)**
Tool A		600	132
Tool B	TOOL 1	450	90
	TOOL 2	450	132
	TOOL 3	450	180
	TOOL 4	300	132
	TOOL 5	600	132

The etched surface is inspected under both the optical microscope and field-emission scanning electron microscopes (FESEM). A series of tool coordinates are recorded using a profile measurement instrument. The surface roughness parameter, i.e., average roughness (R_a) is measured on tool after each weld run. XRD phase analysis is carried out at a scanning speed of 2°/mm using X-ray diffractometer.

7.3 RESULTS AND DISCUSSION

7.3.1 Characterization of degradation mechanisms in tool material A (WC-6 wt. %Co)

Figure *7.2* shows the characterization of tool A after welding. Tool A is characterized qualitatively due to the catastrophic failure of tool material. Tool degradation in the form of pores, micro-cracks, and plastic deformation (due to slip and twinning) is observed as shown Figure *7.2*a. The stresses generated during the welding plunge stage result in crack initiation and propagation inside the tungsten carbide (WC) grains. The presence of pores and its subsequent enlargement affects the strength of the tool. According to Exner & Gurland (1970), high porosity leads to lower transverse rupture strength of the WC material. The grains underwent deformation by slip and twinning mechanisms, which lead to subsequent deformation near the tool edge. This results in partial bulging of the tool shoulder near the edge.

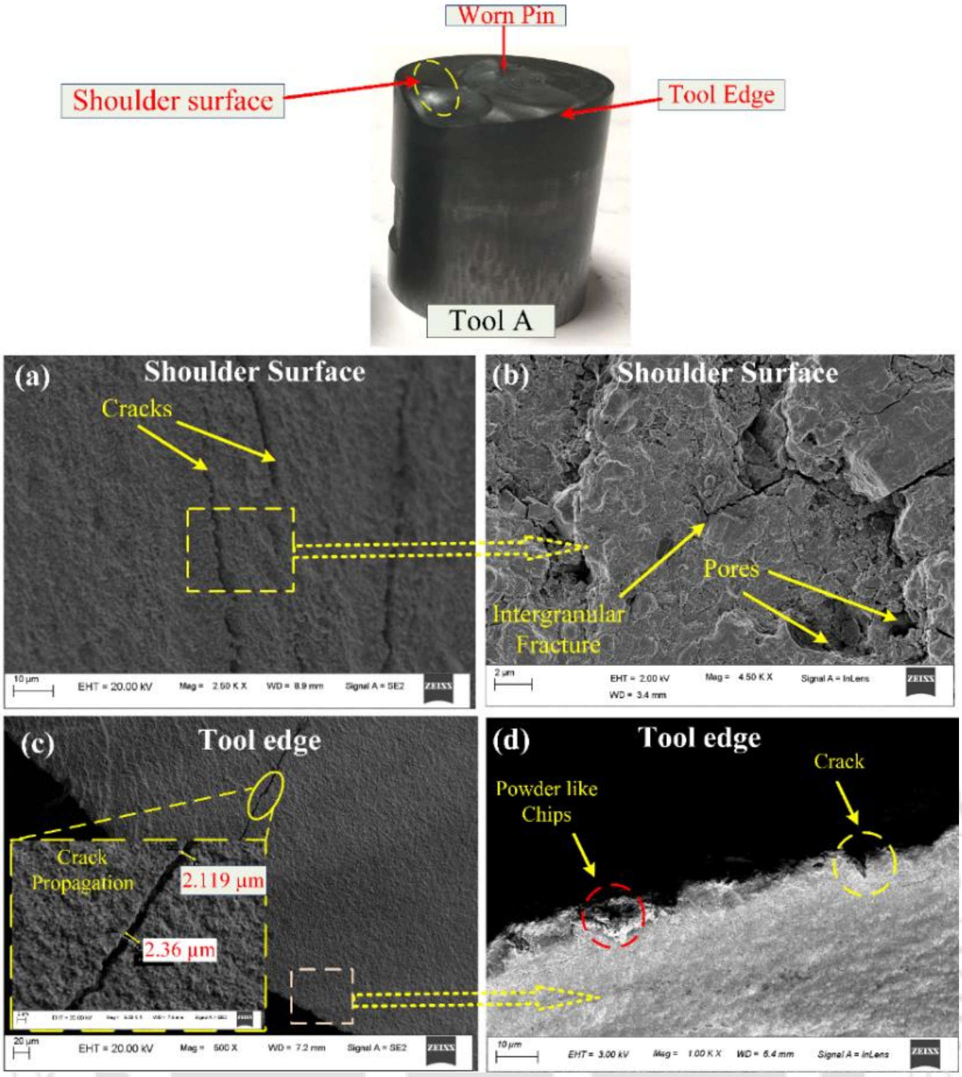

Figure 7.2 Characterization of tool A: (a) crack generation, (b) pores and cracks leading to intergranular fracture, (c) crack propagation towards the outer edge, and (d) chip formation and crack initiation at the tool edge

Figure *7.2*b indicates the pores and internal cracks that enhance the intergranular failure of the tool. Gan et al. (2007) and Thompson & Babu (2010) reported that slip and twinning mechanisms are responsible for the degradation of the WC tool by plastic deformation. The presence of voids, poor surface roughness, and internal cracks results in the premature failure of Tool A. Figure *7.2*c shows the crack initiation and propagation inside the WC grains. A crack of 2.2 μm width is observed at the fracture site of the pin root, which is propagated up to the shoulder's outer surface as shown in Figure *7.2*c. Wear at the tool's outer surface region is caused by chipping due to oxidation at the outer surface. Figure *7.2*d shows the chipping induced at the shoulder edges. These microchips at the surface can be sites for further crack initiation and may enhance the brittle failure mechanism. Pradeep & Muthukumaran (2015) also reported that intergranular failure and abrasion wear are responsible for the tool degradation. A sample is extracted from the worn-out tool pin, and EDS analysis is carried out as shown in Figure *7.3*. It is seen that the extracted pin surface has a non-uniform topology indicating massive wear of the tool pin. Figure *7.3*.2b–f shows the distribution of various elements obtained in the EDS analysis.

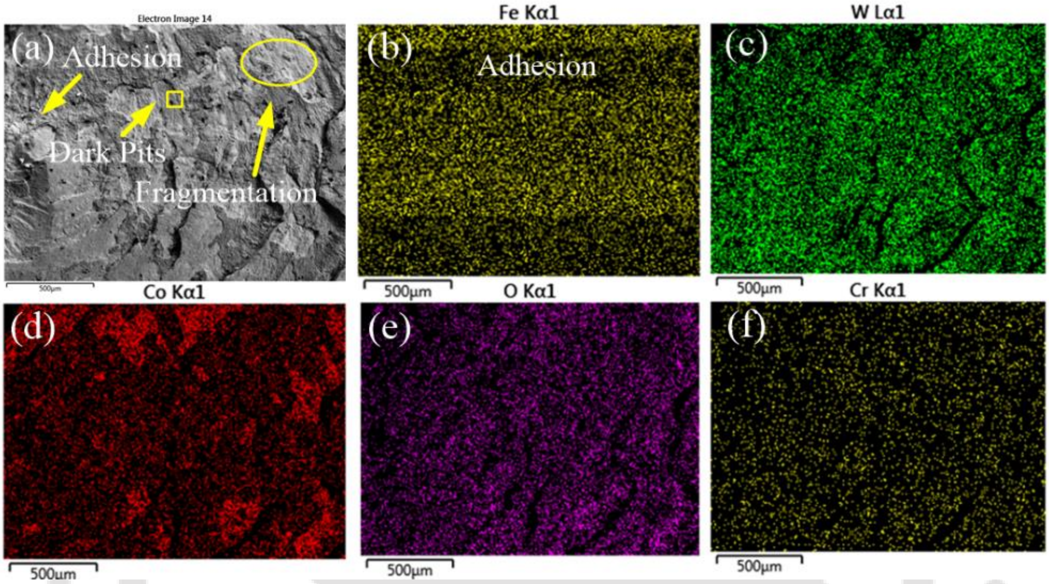

Figure 7.3 Micrograph of tool pin and EDS analysis

Fe and O elements in EDS analysis show the influence of adhesion and oxidation wear. As the tool pin is subjected to the highest temperature, adhesion wear is found as the dominant tool degradation mechanism for the tool pin. Farias et al. (2013), Siddiquee & Pandey (2014), and Thompson & Babu (2010) also reported that the adhesion wear mechanism is strongly responsible for the degradation of tool pin. Adhesive wear is mainly driven by the diffusion of the substrate material with the tool material. Another degradation mechanism for tool wear is diffusion at high temperatures. The Fe element strongly influences the dissolution of WC particles present in the $\mathrm{WC}-\mathrm{xCo}$ tools.

$$2WC \leftrightarrow 2W_2C + C \tag{7.1}$$

$$3Fe + 3WC \leftrightarrow Fe_3W_3C + 2C \tag{7.2}$$

which in turn, leads to the formation of $\mathrm{W_2C}$ and $\mathrm{(FeW)_3C}$ (Gu et al. 2015; Siddiquee & Pandey 2014; Thakur et al. 2008). At higher welding temperatures ($\mathrm{T} > 850$ °C), the Fe diffuses into the tool and forms a solid solution with cobalt. According to Lienert et al. (2003), WC undergoes both way diffusion in the temperature range of 850–1200 °C. Diniz et al. (2016) also reported diffusion wear as a prominent mechanism in the machining of steel. Figure *7.4*a–d represents the FESEM micrograph and EDS analysis carried out at the tool shoulder.

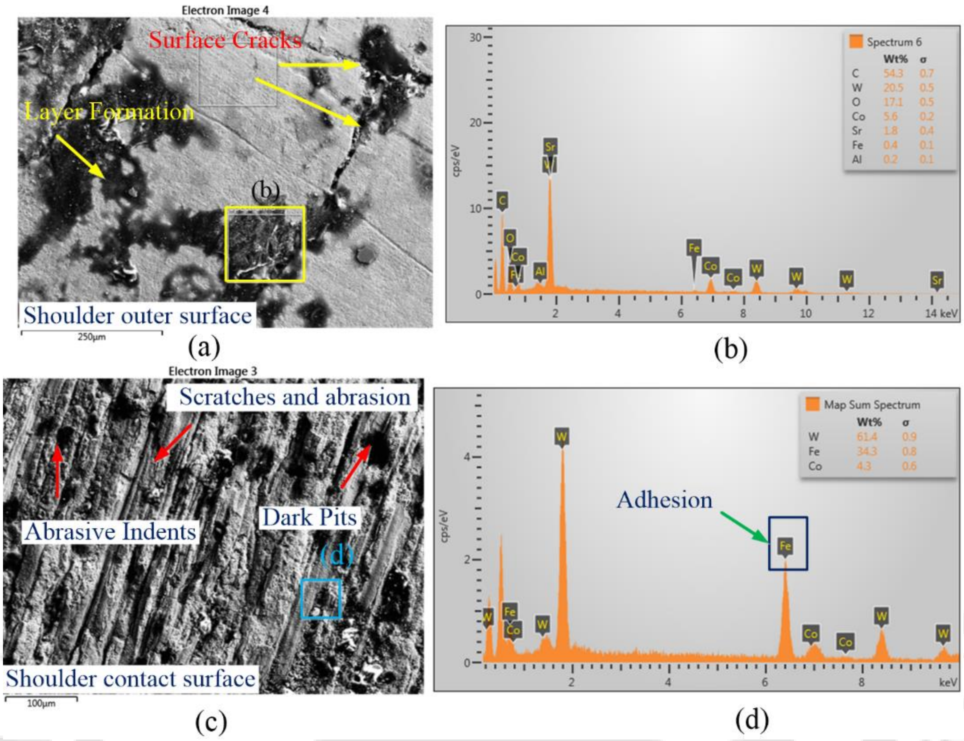

Figure 7.4 (a) Tool shoulder edge of tool A, (b) EDS analysis at the layer formation, (c) micrograph at the shoulder surface showing scratches and abrasion, and (d) EDS analysis at the shoulder contact surface

The micro-cracks are observed at the tool shoulder surface. These cracks are formed due to thermal expansion after welding and shrinkage during rapid cooling under ambient atmosphere. During deformation, the transformation of the ductile FCC structure of Co binder into a brittle HCP structure accelerates the spreading of these cracks. A bluish layer is seen at the tool outer surface. EDS analysis at this layer shows the larger percentage of tungsten (W) as shown in Figure *7.4*c. The groves and scratches on the tool shoulder surface indicate the severe wear due to abrasion. During welding, the workpiece material directly abrades the tool material and this phenomenon gets enhanced, especially at a higher temperature. The abraded particles from both the tool and workpiece further accelerate the abrasion wear of the tool. Due to surface oxidation, a significant reduction in the scratch resistance and the tool's abrasive wear resistance occurred that triggered the abrasive wear mechanism. The micrograph also reveals the presence of small black dark pits on the shoulder surface. This may be due to the diffusion between the steel and tool material. Diffusion as the tool degradation mechanism in FSW of high strength materials is also reported in earlier literature (Siddiquee & Pandey 2014; Tarasov et al. 2014). EDS analysis shows the presence of Fe element on tungsten tool, which indicates adhesion wear, as illustrated in Figure *7.4*d, although adhesion is observed but not found to be as dominant as abrasive wear. This adhesion behavior is reducing towards the shoulder edge. Pradeep & Muthukumaran (2015) also reported less adhesion wear at the shoulder surface compared to that of the pin.

Based on the above observations, tungsten carbide-based tool materials degradation mechanisms have been categorized mainly into five groups, i.e., (i) adhesion wear, (ii) abrasion wear, (iii) crack initiation and propagation, and (iv) chemical erosion (i.e., oxide formation) and (v) diffusion. Tool A $(\mathrm{WC}-6\mathrm{wt.}\%\mathrm{Co})$ experienced brittle fracture at the initial stage, and no further investigation of wear relative to process parameter is carried out.

7.3.2 Characterization of degradation mechanisms in tool material B (WC-10 wt. %Co)

Successful weld joints are obtained by using tool B at different operating conditions, as shown in Table *7.2*. Figure *7.5* shows the surface appearance of the welded joints and the peak temperatures recorded by a non-contacting Infra-Red (IR) camera.

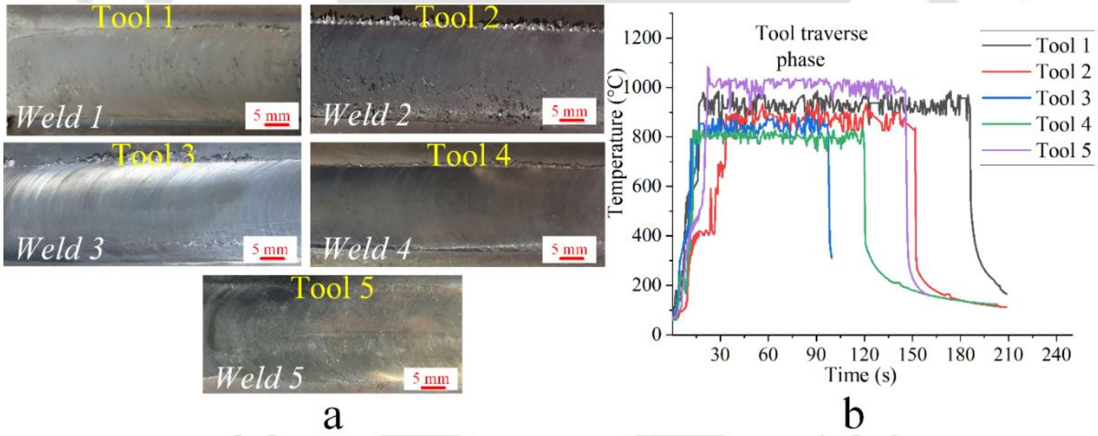

Figure 7.5 Weld joint characterization: (a) top surface appearances of the welded plates at different welding conditions, and (b) transient thermal history of the welding condition using non-contact infrared (IR) camera (The scan was made along the welding direction)

All welds are free from any surface-related flaws as depicted in Figure *7.5*a. Good surface appearance is achieved at low rotational speed (i.e., tool 4) and high traverse speed (i.e., tool 3). It is observed that rotational speed and traverse speed directly affect the weld surface appearance. The weld joint's high surface appearance results in low surface roughness values of the tool, i.e., less wear of the tool. The welds' transient thermal history is recorded by using a non-contacting infra-red (IR) camera, as shown in Figure *7.5*b. The temperature profiles have shown significant variation at five different welding parameters. From the temperature profiles, it is clear that the peak temperature is decreasing with an increase in traverse speed. Similar observations are reported by Saeid et al. (2008) in the FSW of stainless steel. Figure *7.6* indicates the tool micrographs before and after welding and the oxidation behavior of WC − Co tool.

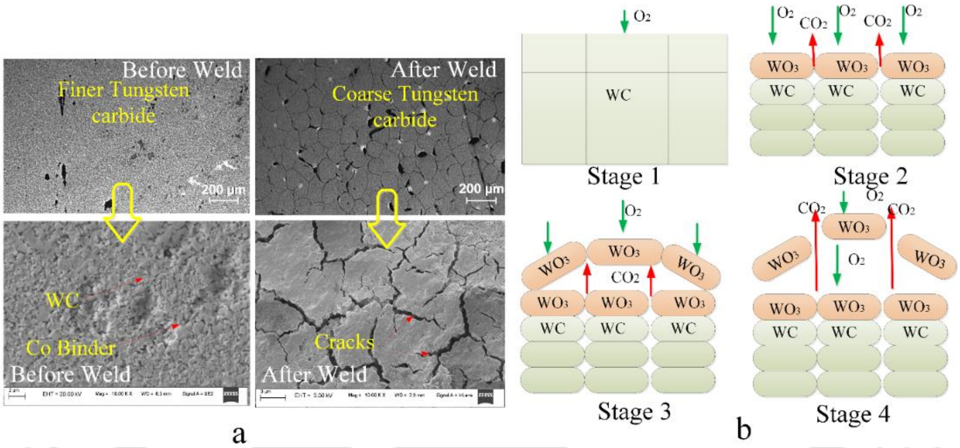

Figure 7.6 (a) Microstructure images of tool representing tungsten carbide and cobalt binder before welding and after welding, and (b) illustration of the oxidation behavior and swelling of W-Co alloys at elevated temperatures

Figure *7.6*a shows the optical and FESEM images of tool microstructure before and after welding. The bright and dark gray regions in the optical microstructure are tungsten carbide and cobalt binder phases, respectively. The grain morphology of the tungsten tool is changed excessively due to the weld thermal cycle. Microstructure images indicate that the bonding between the WC and the Co binder phase appears to be weaker after welding. Brittle WC is closely packed in the ductile cobalt binder. On removal of the ductile binder phase, the abrasive impact can cause further surface cracks and pull out of the WC grains due to abrasion between the contact surfaces. Severe intergranular crack generation is associated with high-temperature tool oxidation. The oxidation of the tool also resulted in the expulsion and swelling of the tungsten tool. Figure *7.6*b shows the schematic diagram explaining the oxidation behavior and swelling of WC material. The tungsten carbide tool's oxidation behavior can be explained as (Lofaj & Kaganovskii 1995):

$$WC+\frac{5}{2}O_2 \rightarrow WO_3 + CO_2 \tag{7.3}$$

$$WC+2O_2 \rightarrow WO_3 + CO \tag{7.4}$$

The oxidation phenomenon in WC alloys is explained well with the schematic diagram. WC reacts with oxygen forms a porous and brittle tungsten oxide phase (WO_3) and CO_2 gas at the outer surface. The formed porous oxide layer further enhances the oxidation process in the adjacent layer. This results in the entrapment of CO_2 inside the WC grains. Porous tungsten oxide (WO_3) and extreme pressures of the CO_2 gas results in the crack formation due to the separation of ductile cobalt binder. It is reported that higher Co content in WC also increases its oxidation behavior (Exner 1979; Exner & Gurland 1970). Additionally, oxidation behavior in WC alloys increases drastically with the temperature at elevated temperatures (Choi et al. 2009b; Liu et al. 2018; Lofaj & Kaganovskii 1995). Hence, it can be concluded that high process temperature during FSW at high rotation speeds and low transverse speeds may drastically decrease the strength of the tool. Figure *7.7* shows sub layer formation at the outer shoulder surface and its EDS analysis.

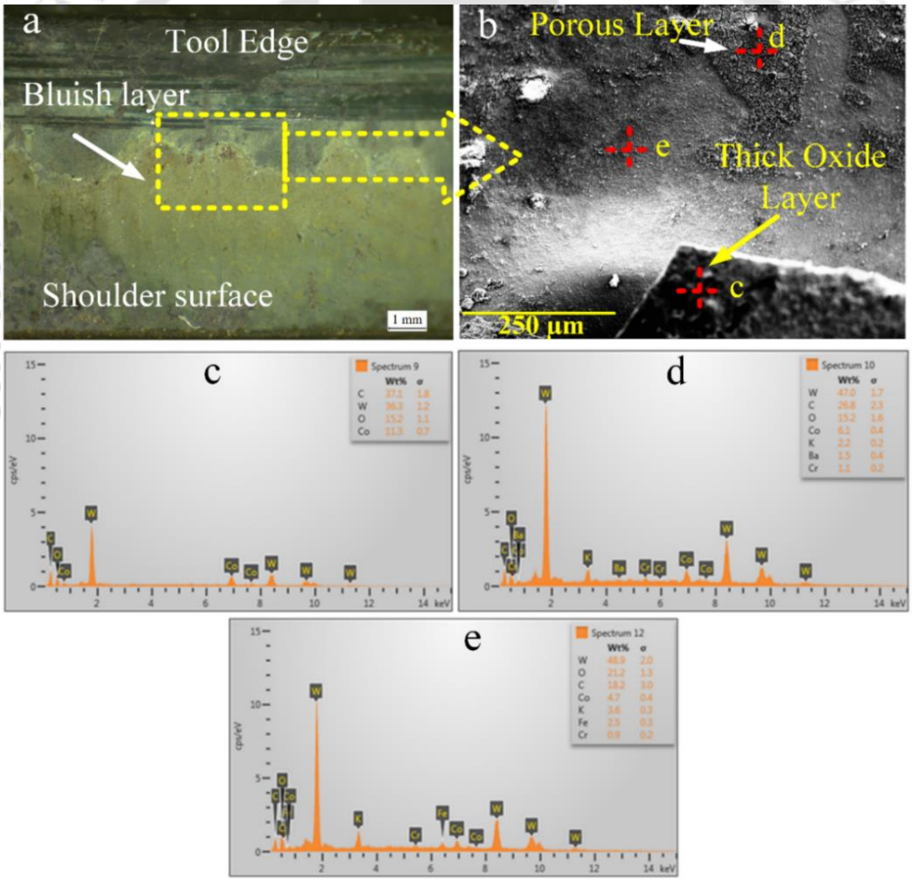

Figure 7.7 Tool wear characterization at non-contact shoulder surface: (a) sub layer formation at non-contact surface due to massive oxidation at elevated temperature, (b) FESEM micrograph indicating different locations for EDS analysis, and (c–e) EDS analysis indicating W, O and Co elements with higher percentage of Co and O elements on the sublayer

Figure *7.7*a shows a bluish layer on the shoulder surface due to the oxidation of tungsten carbide. EDS analysis is carried at the oxide layer and tool surface close to the edge. FESEM-EDS analysis indicates the presence of $\mathrm{W}, \mathrm{Co}, \mathrm{O}, \mathrm{C}$, and Cr as the main elements, as shown in Figure *7.7*c–e. This layer was strongly influenced by the number of weld passes and peak temperature attained in the tool. It is found that the percentage of Co and O elements are higher on the sublayer. In addition, $\%$ of Co element is significantly reduced on the shoulder's non-contact surface (i.e. location d and e shown in Figure *7.77.5b*. These results are in line with those reported by Warren et al. (1996) that the oxidation behavior of $\mathrm{WC}-\mathrm{xCo}$ depends specifically on the cobalt element. The Rockwell (HRC_{150}) hardness measurement is carried out on tool material before and after the FSW process. Figure *7.8*a and Figure *7.8*b show the worn-out tool (top view) and Rockwell hardness indentation at the tool shoulder respectively.

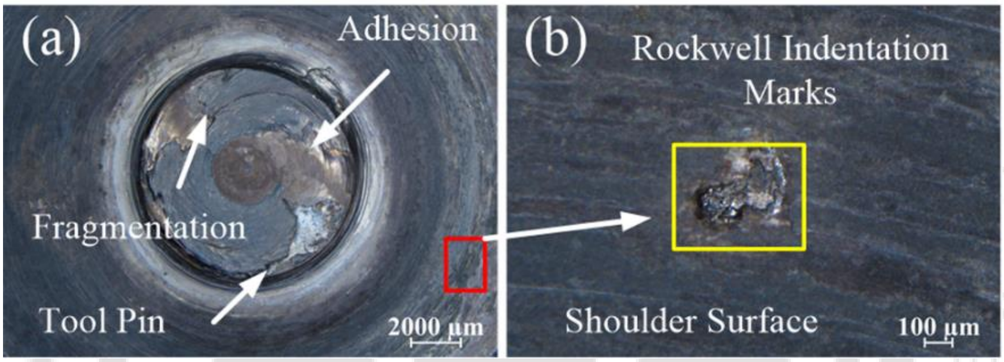

Figure 7.8 (a) Fragmentation and adhesion phenomenon at the tool pin, and (b) indentation mark at tool shoulder after hardness measurement (HRC_{150})

Figure *7.8*a shows the fragmentation and adhesion on the tool pin. This fragmentation of tool material is caused by fracturing along grain boundaries under the shear stress developed on the tool surface. Hardness evaluation is carried out at the shoulder surface. No significant changes are observed in the hardness of the tool after welding. The hardness of the tool material after welding is observed in the range of 79.5–81 HRC_{150}. Figure *7.8*b depicts the hardness indentation mark on the shoulder contact surface. The tool profile is investigated by the projected profile of the tool pin after each successive weld runs as depicted in Figure *7.9*.

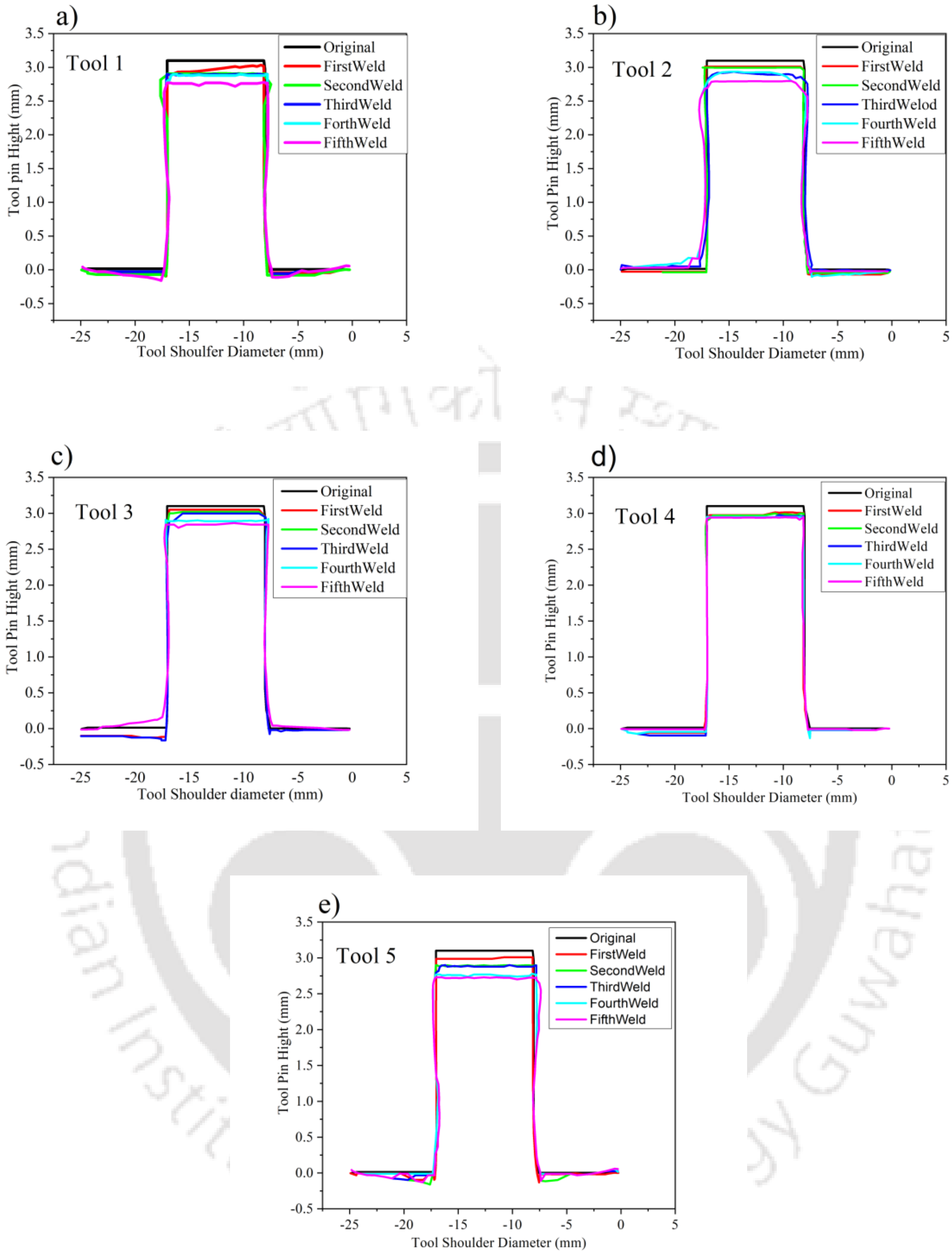

Figure 7.9 Projected profile of tool pin

From Figure *7.9*, it is observed that pin height is reducing after each weld run. The tool pin wear is quantified by measuring the variation in pin length after five weld runs and is evaluated as:

$$\text{Percentage (\%) variation} = \frac{(PL_i - PL_f)}{PL_i} \tag{7.5}$$

where PL_i and PL_f is the initial and final tool pin height after the welding process. Minimum (4%) and maximum (10%) pin length reduction are observed for the tool 4 and tool 5. From the obtained profiles, it is concluded that the wear is less near the pin root and noticeable changes occurred at the pin tip, i.e., reduction of pin height and mushrooming of the tool pin. Tool wear is related to the resistance force from the material to be welded to the tool during FSW. Also, it is observed that the pin length reduction is more at high rotational speed and low traverse speed which indicates a high-temperature tool is more susceptible to wear and degradation. It may be kept to an acceptable level when high process temperatures are avoided. The tool is further characterized by weight loss and surface roughness at the pin and shoulder surface. Figure demonstrates the tool wear characterization by weight loss and surface roughness.

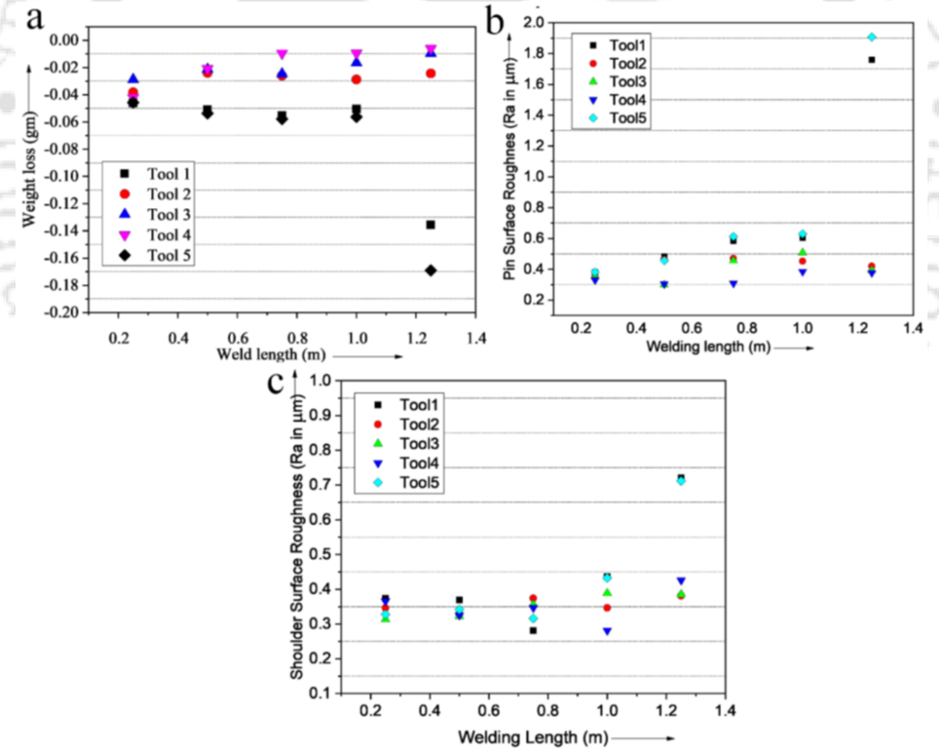

Figure 7.10 Tool wear characterization: (a) weight loss versus weld length, (b) surface roughness after each weld run at tool pin, and (c) surface roughness at tool shoulder surface after each weld run

Figure *7.10*a shows the weight loss versus weld length of FSW tools. The tool weight is measured using weight balance with an accuracy of 0.0001 g. Tool 4 and tool 5 exhibited minimum and maximum weight loss, respectively. The wear rate is strongly influencing by FSW process parameters; i.e., the wear rate is more at higher rotational speed and lower traverse speed. Weight loss shows a decreasing pattern with an increase in traverse speed and a decrease in rotational speed. This phenomenon can be explained as increasing the traverse speed leads to a reduction in tool and workpiece interaction. The increasing rotational speed results in higher relative surface velocities which result in increased tool wear. In addition to that, another important microscopic geometric characteristic i.e. average surface roughness (R_a) is evaluated to characterize the surface integrity of the tungsten tools. Good quality surface finish is of great importance for less wear and higher tool life. Figure *7.10*b & c show the surface roughness variation at the tool pin and shoulder surface with weld length. It is observed that the surface roughness is high at the tool pin surface compared to the tool shoulder surface. The maximum surface roughness is observed for tool 5. It is seen that the surface roughness tends to rise sharply at high rotational speed and low traverse speed due to high heat input. Figure *7.11*shows the surface roughness, micrograph, and EDS analysis at the tool shoulder surface after the welding process.

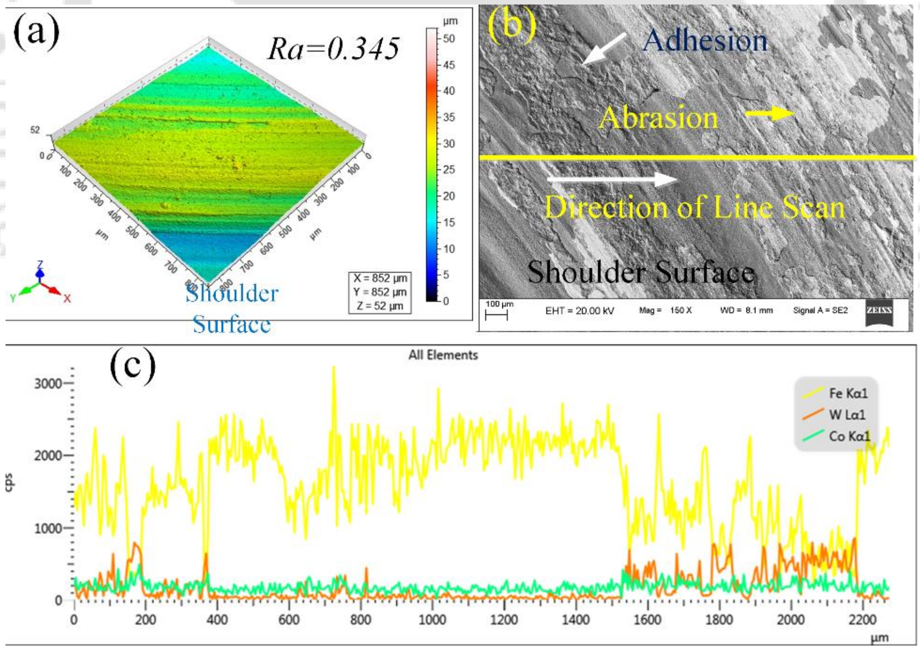

Figure 7.11 Tool shoulder characterization: (a) surface roughness measurement, (b) FESEM micrograph showing abrasion and adhesion wear at the shoulder contact surface, and (c) EDS analysis indicating Fe adhesion on the shoulder contact surface

Figure *7.11a* indicates the surface roughness at the tool shoulder surface. The average surface roughness (R_a) is higher at the tool pin compared to the tool shoulder. Figure *7.11*b shows the micrograph indicating adhesion and abrasion on the tool surface due to the generation of the stick-slip process during relative movement between the tool and workpiece. The surface roughness of the abraded shoulder surface is consistent with the abrasive wear mechanisms. EDS analysis shows the distribution of Fe, W, and Co elements on the shoulder surface. Figure *7.12* shows the surface roughness, micrograph, and the EDS analysis at the tool pin surface after welding.

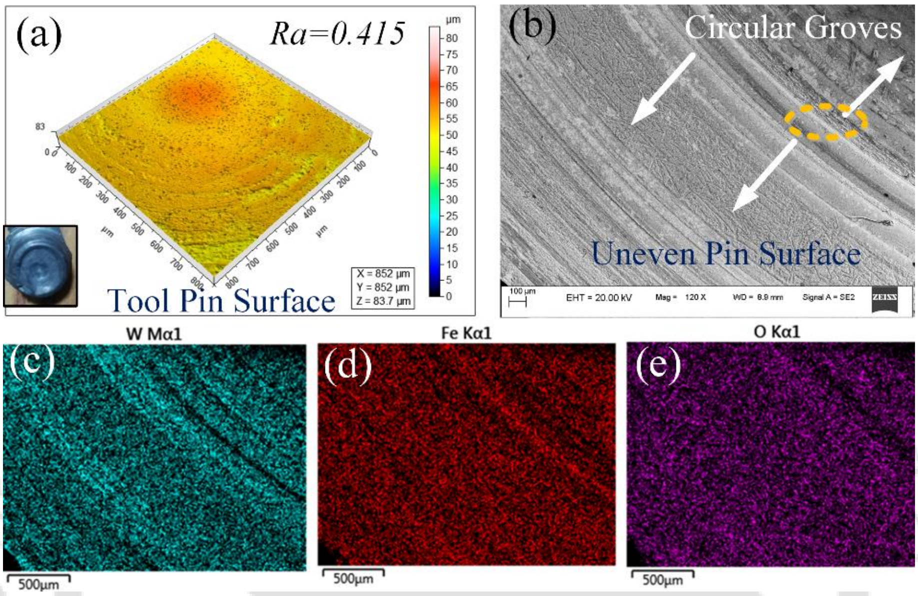

Figure 7.12 Tool pin characterization: (a) surface roughness measurement at tool pin surface, (b) FESEM micrograph indicating non uniform topology with circular grooves, and (c–e) EDS analysis indicating Fe adhesion on the tool pin

Figure *7.12*a shows the surface roughness at the tool pin surface. Adhesion and abrasion are also observed on the pin surface from Figure *7.12*. EDS analysis shows the tungsten (W), iron (Fe), and oxygen (O) elements on the tool pin surface. Diniz et al. (2016) observed that adhesion is the most important wear mechanism in the machining of ductile materials like steel. A qualitative analysis of various precipitate formed on the tool surface is done by XRD phase analysis. Figure *7.13* shows the X-ray diffraction pattern of the tool before and after the welding process within the 2θ range of $10°–80°$. The larger and smaller peaks are indicating tungsten carbide and cobalt, respectively.

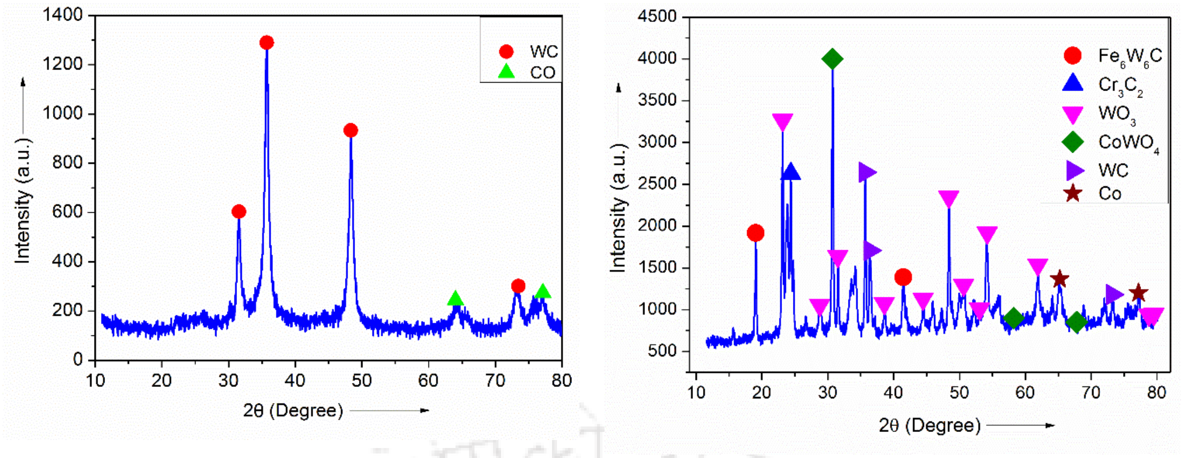

(a) (b)

Figure 7.13 XRD patterns showing different phase's formation on the tool (a) XRD peaks indicating WC and Co peaks before welding, and (b) XRD peaks indicating different oxide and carbide phases after welding

Figure *7.13*b represents the formation of different carbides and oxides phases due to the weld thermal cycle. The interaction of tool material and workpiece yielded carbide phases such as WC, Fe_6W_6C, and Cr_3C_2 at the shoulder surface. The oxide phases of the tungsten tool observed are WO_3 and $CoWO_4$. Tungsten oxide (WO_3) was formed to a weak texture {200} due to the high temperature observed during the welding. Basu & Sarin (1996) also reported the formation of WO_3 oxide phase during oxidation of tungsten carbide. Few peaks are difficult to identify and have not been reported. The formed oxide and carbide phases are responsible for tool life degradation. Degradation of tungsten carbide tool by oxidation is investigated and reported in published literature (Liu et al. 2018; Tarasov et al. 2014; Warren et al. 1996). So, from the XRD analysis, it can be concluded that oxidation is primarily responsible for weakening the Co binder phase, which leads to lower strength of the $WC-Co$ alloy.

7.4 SUMMARY

Cost-effective tungsten carbide tools may be an option to the FSW process since it is possible to improve the tool's wear resistance by controlling the process window to achieve a good quality weld with increased tool life. From the study, the following conclusions are drawn:

- Tool A underwent catastrophic failure, whereas the progressive wear is observed in tool B during welding of high strength steel alloy.
- The grain growth and crack formation is observed in the tungsten carbide tool.

- SEM-EDS analysis revealed cracking, adhesion, abrasion, diffusion, and oxidation as the existing degradation mechanisms.
- At the high rotational speeds, a decreased strength of the binder phase due to the high temperatures may have contributed to severe tool wear through grain pull-outs.
- Adhesion of steel to the tungsten carbide tool is mainly due to the chemical reaction under the compression load at elevated temperatures.
- Abrasion and adhesion wear are responsible for the degradation of the shoulder surface.
- Peaks of WO_3 and $CoWO_4$ in the XRD analysis confirmed the oxidation wear of tungsten tools that resulted in the formation of a porous and brittle-oxide layer.
- The wear rate is strongly influenced by process parameters, i.e., increasing rotational speed and decreasing traverse speed resulted in a higher wear rate. Minimum (4%) and maximum (10%) pin length reductions are observed for tool 4 and tool 5 respectively.
- Weight loss showed a decreasing pattern with an increase in traverse speed and a decrease in rotational speed.
- The average surface roughness is observed higher at the tool pin surface compared to the tool shoulder surface. The maximum surface roughness was observed for tool 5.

:--------------------*--------------------*----------------------:

Chapter 8

8 EXPERIMENTAL INVESTIGATION OF PLASMA ASSISTED FRICTION STIR WELDING OF DH36 STEEL

8.1 INTRODUCTION

In this chapter, a plasma preheating setup is developed with the conventional FSW machine. The plasma torch is fixed with the machine spindle, ahead of the FSW tool, to preheat the workpiece during the plunge and traverse stages efficiently. Preheating of the workpiece is done at three different preheating currents keeping other FSW parameters as constant. The effect of preheating is also compared on the downward z forces at different stages of welding. After performing welds, a comparative study is done between the FSW and PFSW of DH36 steel. The study also extended with the characterization of tool wear during FSW and PFSW. The primary areas of interest were tool wear, z force evaluation, preheating temperatures optimization, cooling rates evaluation, mechanical properties evaluation(i.e., microhardness, tensile properties and impact toughness), and the microstructure characterization. Based on the above investigation during FSW and plasma-assisted FSW, the results revealed that tool wear is significantly reduced during plasma-assisted FSW. The welds produced during PFSW showed different grain morphology as compared to conventional FSW.

8.2 MATERIALS AND METHODOLOGY

Friction stir welding (FSW) is performed on DH36 steel in butt joint configuration. The dimension of the DH36 plates are 240 mm ×100 mm×4 mm. The chemical composition (in wt.%) of DH36 steel is given in Table *8.1*. The tool material and tool design is selected based on trial experiments and the authors' previous research (Tiwari et al. 2020; Tiwari et al. 2019b; Tiwari et al. 2019a). The tool shoulder diameter and tool pin length are 25 mm and 3.5 mm respectively. A tapered pin geometry, tapered from 7 mm at the tool shoulder and 5 mm at the free end, is used in the study. The tool plunge depth is set to be 0.2 mm with a backward tool tilt angle of 2°. The transformation temperatures, i.e., A_1 and A_3 of DH36 steel are calculated to be 731 ± 24 °C and 843 ± 33 °C, respectively (Mishra & Ma, 2005).

Table 8.1 Chemical composition of DH36 steel (wt. %)

C	**Mn**	**Cu**	**Si**	**Cr**	**Mo**	**V**
0.146	1.51	0.14	0.22	0.08	0.02	0.003
Ti	**Al**	**Nb**	**P**	**S**	**Fe**	
0.003	0.017	0.03	0.007	0.001	Bal.	

8.2.1 Experimental setup

A schematic representation of the plasma preheating is depicted in Figure *8.1*. A plasma arc welding machine is used to preheat the workpiece material during the plunge and traverse stages, as illustrated in Figure *8.1*a.The plasma-assisted FSW process is shown in Figure *8.1*b.

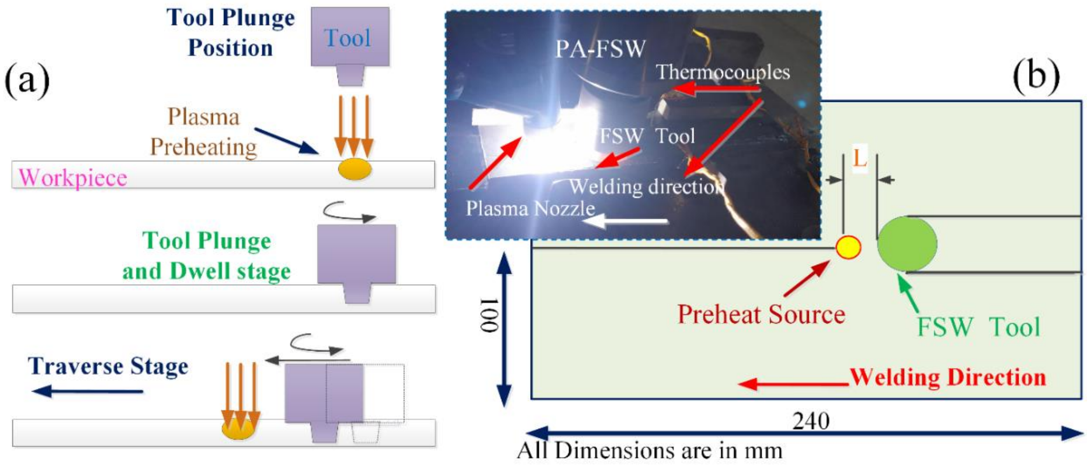

Figure 8.1 Plasma assisted friction stir welding (PFSW) process: (a) illustration of preheating stages of PFSW process, and (b) plasma heat source layout ahead of the FSW tool

Plasma preheat parameters used in this investigation is provided in Table 8.2. Transferred arc mode (i.e., between the tungsten electrode and the workpiece plate) is employed with DCEN polarity in conduction mode. Welding is performed at different plasma preheating currents (i.e., 13A, 15 A & 17A) to check the effect of preheating temperature on tool life and weld quality. The welding was performed at a constant rotational and traverse speed of 600 rpm and 60 mm/min, respectively. From previous research of Ahmad et al. (2019) and Sun et al. (2013), and experimental works carried out in the laboratory; the plasma arc is set at 20 mm ahead of the FSW tool. Process parameters investigated in the present study are summarized in Table 8.3.

Table 8.2 Details of plasma preheating parameters

S. No.	Parameters
Polarity	DCEN
Plasma preheating current (A)	13,15 and 17
Plasma preheating voltage (V)	20.5
Welding speed (mm/min)	60
Shielding gas flow rate (LPM)	12
Nozzle to plate distance (mm)	5
Plasma gas	Argon (99.95 %)
Shielding gas	Argon (99.95 %)
Mode of operation	Conduction mode
Operation type	Automatic

Table 8.3 Welding parameters used in the present study

Operating parameters				
	FSW parameters		**Plasma preheating parameters**	
	Rotational speed (rpm)	**Traverse speed (mm/ min)**	**Preheating Current (A)**	**Voltage (V)**
Weld 1	600	60	-	-
Weld 2			13	20.5
Weld 3			15	20.5
Weld 4			17	20.5

8.2.2 Transient temperature and force measurements

K-type thermocouples are inserted in the weld plates to measure the thermal history, as illustrated in Figure *8.2*. On each plate, holes are drilled of 1 mm diameter, and thermocouples are inserted into these holes. The thermocouples (T_{C1} and T_{C2}) are located in the mid-region (i.e., 2 mm from top and bottom both), and each 8 mm away from the weld centerline, as indicated in Figure *8.2*. Thermocouples connected to channels 1–2 in the data acquisition system (DAQ) to record the transient temperature profiles.

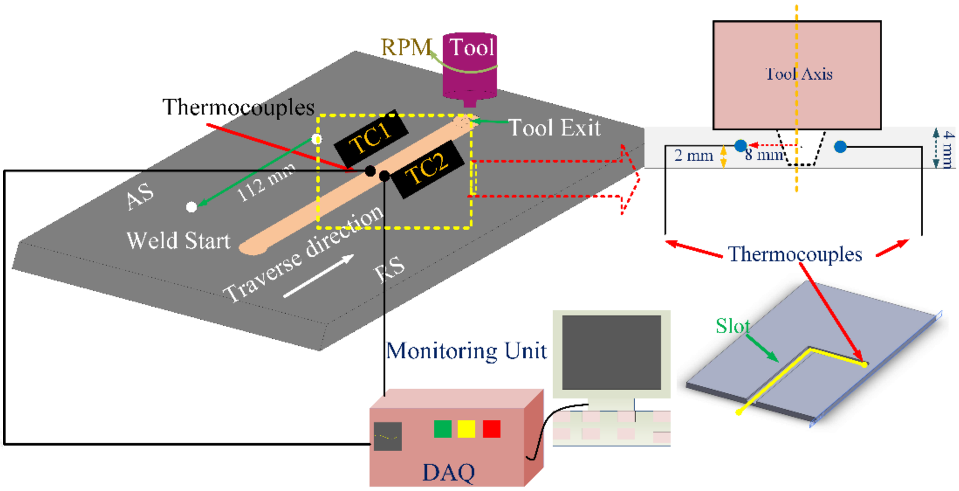

Figure 8.2 Schematic diagram of the thermocouple layout used to record transient thermal history during welding

Strain gages type force sensors are used with a data acquisition system (DAQ) to record the transient force data during the plunge, dwell, and traverse stage. DAQ systems are used to record transient temperature and force data during welding. Welding force was recorded for all FSW stages for with and without preheating cases, as summarized in Table 8.3.

8.2.3 Metallographic and mechanical properties characterization

For the metallographic study, samples are grinded and then polished to mirror-finish using alumina powder. Polished samples are etched with 2% Nital solution for 25 s. The etched specimen are investigated for microstructural study under optical microscope, field emission scanning electron microscope (FESEM), and energy-dispersive analyses (EDS). Microhardness is evaluated at three different layers using a Vickers micro-hardness tester, with a load of 4.9 N for a dwell time of 15 s. Tensile tests are performed at a crosshead speed of 1 mm/min as per ASTM-E8 standards. The Charpy impact test is performed on 4 mm thick specimens at room temperature as per ASTM-E23 standards.

8.3 RESULTS AND DISCUSSION

8.3.1 Surface appearance and force evaluation

Figure *8.3*a shows the welded joints' surface appearance for FSW and PFSW, as illustrated in Table 8.3. The surface appearance of the plasma-assisted welded joints is better than the conventional FSW joints on visual inspection. Surface flaws are absent in the PFSW joints except in weld 4 where excessive flash is generated. This excessive flash may be associated overheating that led to excessive plasticization of the material in weld 4. All the welds are free from visual volumetric defects. The better surface appearance in the energy-assisted FSW is in line with those reported in the literature (Mehta & Badheka, 2017; Padhy et al. 2015; Sun et al. 2014).

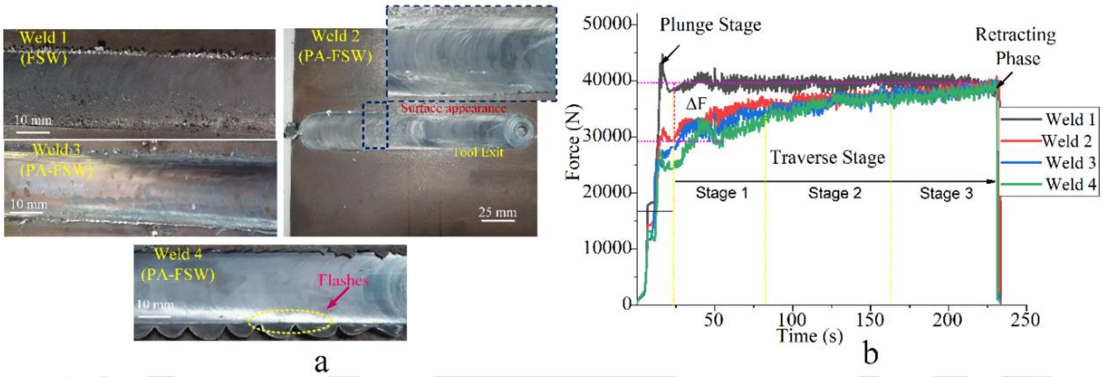

Figure 8.3 (a) Weld top surface appearance at different welding conditions, and (b) the corresponding downward axial force during the welding

Figure *8.3*b shows the downward axial force corresponding to the welding conditions mentioned in Table 8.3. Three welds were performed for repetition, and experimental uncertainty in the measurement of force is predicted to ±8%. In weld 1, the maximum force is observed at the plunge stage due to insufficient thermal softening of the material. The z force decreased during dwelling due to thermal softening of the workpiece material by a steady heat source. The total weld traverse stage is divided into three stages i.e., stage 1, stage 2, and stage 3. At the traverse stage during weld 1, the downward force remains almost constant (i.e., 39.64 kN) during the total weld length (i.e., stage 1 to stage 3). For comparison of the z force for FSW and PFSW cases, change in force is calculated as:

$$\%\Delta F = \frac{F_F - F_P}{F_F} \times 100 \tag{8.1}$$

The downward force calculated by Eqn. 8.1 indicates that the z force is reduced by 31.6% and 5.67% for the plunge stage and traverse stage, respectively, for weld 2. In weld 3 and weld 4, plunge force is reduced by 32.77% and 33.89%, respectively. Since the preheating energy had already softened the workpiece material, plunge force is reduced and huge fluctuations are observed during PFSW cases i.e., weld 2, weld 3 and weld 4. As the tool started traversing, there is steep increase in z force. In traverse stage 3, the welding force is almost numerically the same as the value recorded for weld 1. During the traverse stage of FSW and PFSW, z force difference is significantly less and this effect further diminished at the end of the weld. The impact of plasma preheating is reduced during the traverse stage due to huge heat loss to the FSW bed and fixtures by heat conduction. After stage 1, the effect of preheating diminished, and the downward z forces increased in stage 2, which became stabilized at the end of the weld. The force reduction during the plunge stage is consistent with those reported in previous literature (Ahmad et al. 2019; Álvarez et al. 2014). Sinclair et al. (2010) observed that the z force was less during the thermally-assisted FSW process. They observed that preheating reduced the material flow stress and eased the material transport phenomenon from AS to RS during FSW of steel alloys. Arora et al. (2011) also proposed that preheating at the plunge stage can overcome a pilot hole's need at the plunge stage. Álvarez et al. (2016) found that plunge force was reduced by 30% during induction assisted FSW of super duplex stainless steel. Similarly, Amini & Amiri (2014) and Zhong et al. (2017) also reported that z force is reduced significantly during the UFSW process.

Figure *8.4* shows the macro classification at the weld top surface for the conventional FSW and PFSW. Surface flaw (flash generation) is observed on the top surface, i.e., (shoulder influenced region) in weld 1, which is absent in weld 2 as indicated in Figure 8.4a and 4b. Surface flaws are highly detrimental for joint integrity, especially in case of impact and fatigue loading (Cam 2011; Mishra & Ma 2005; Padhy et al. 2015). PFSW resulted in high degree of plasticization and better surface quality as compared to FSW. Moreover, material splashing is observed on further increasing plasma preheating, as depicted in Figure *8.4*c and Figure *8.4*d.

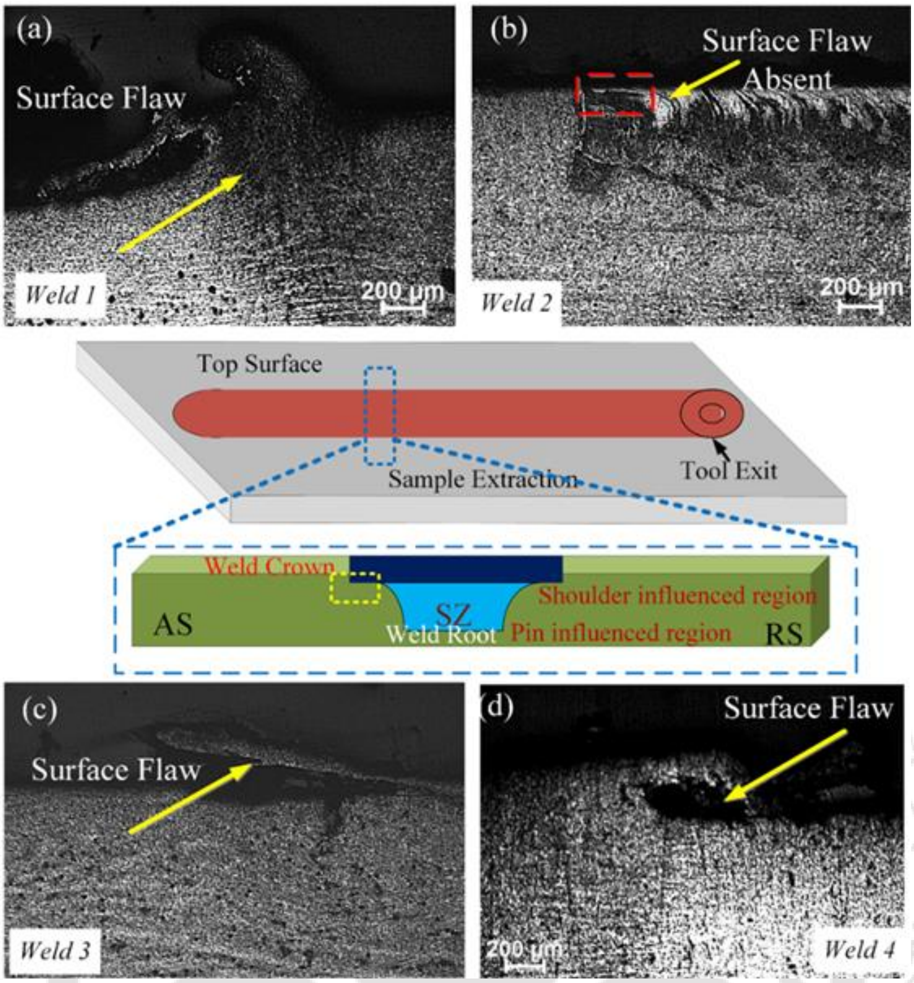

Figure 8.4 Micrograph appearance of weld joints at the top surface: (a) weld 1, (b) weld 2, (c) weld 3, and (d) weld 4

8.3.2 Weld thermal history and the weld microstructures

Figure *8.5*a represents the temperature profiles at 13A, 15A, and 17A by the application plasma preheating on the workpiece material. At 13 A preheating current, the peak temperature is 280 °C, which is increased by18.18% and 39.28% for 15 A and 17A, respectively. From Figure *8.5*b, it is observed that the peak values of thermocouples T_{C1} (i.e., AS) for weld 1 is 697.4 °C. It is observed that the peak temperature increased by 1.14%, 5.65%, 5.81% for weld 2, weld 3, and weld 4, respectively. The heating stage of PFSW is comparatively faster due to the addition of plasma heat energy to the FSW heat energy. The degree of preheating is dependent on the intensity of the preheating current. The thermal history of PFSW exhibits two peaks, i.e., the first peak from the plasma source, and the second peak is the heat generated by the FSW tool as depicted in Figure *8.5*b.

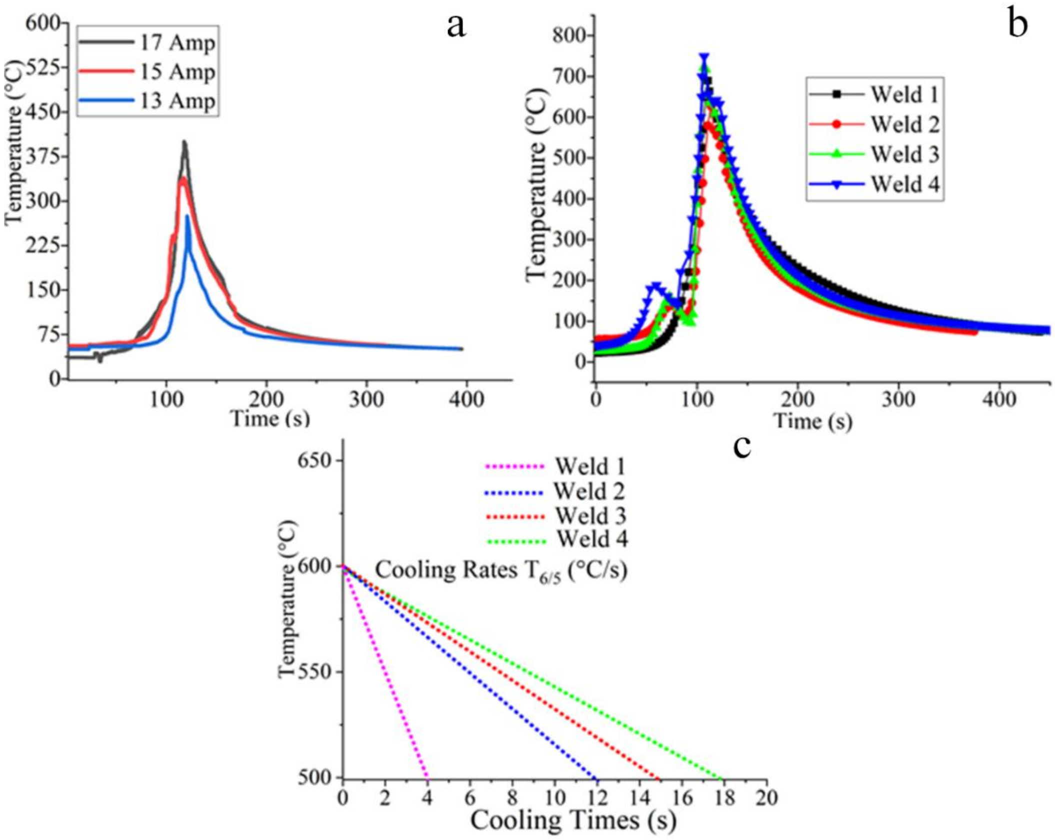

Figure 8.5 Thermal analysis: (a) effect of plasma preheating current, i.e., 13A, 15A, and 17A at a location of 5 mm from the weld line, (b) peak temperatures, and (c) weld cooling rate $T_{6/5}$ for different welding conditions

The maximum temperature reached at the measured location results from the combined effect from both the heat sources, i.e., the plasma preheat source and the FSW tool. Yaduwanshi et al. (2015) reported single peaks in PFSW and observed high process temperature than the conventional FSW of aluminum alloys. In the study of hybrid FSW of aluminum alloys, Amini & Amiri (2014) also reported higher process temperature in the UFSW than conventional FSW. The peak temperatures, cooling rates, and heating rate data determined the microstructural evolution during the FSW of steel. During FSW, heat input (Mishra & Ma, 2005) per unit weld length (Q_F) is expressed as:

$$Q_F = \frac{\frac{4}{3}\pi^2 \mu P N R^3}{U} \tag{8.2}$$

where μ is the friction coefficient, P is the pressure calculated by axial force (z force) divided by tool shoulder area, N is the revolution per second, R is the radius of the shoulder, and v is the welding speed. Heat input for the plasma (Fatima et al. 2016) heat source can be calculated as :

$$Q_P = \frac{\eta_p \times V_v \times I_a}{U} \tag{8.3}$$

where U , V_v, and I_a are the welding speed, voltage, and current, respectively. Plasma efficiency (η_p) was suggested in the range of 0.65-0.75 (Fatima et al. 2016; Liu et al. 2016 Zhang et al. 2014). The peak temperature during FSW (Ghosh et al. 2010; Mishra & Ma 2005; Tiwari et al. 2020) is expressed as:

$$\frac{T_p}{T_m} = K_c \left(\frac{\omega^2}{U \times 10^4} \right)^{\alpha_c} \tag{8.4}$$

where T_p is the maximum temperature reached, T_m is the melting point of the DH36 base plate, ω is the angular velocity of the tool, and U is the welding speed. The constants K_c and α_c have the values lying within the ranges of 0.65–0.79 and 0.04–0.11, respectively, for the FSW of steel (Ghosh et al. 2010; Tiwari et al. 2020). The above relationship predicted the peak temperature of 1093 °C approximately for the conventional FSW, i.e., weld 1. It can be estimated that peak temperatures in PFSW may be higher than FSW due to indirect heat addition during the process. According to Shi et al. (2015), the FSW and the ultra-sonic assisted FSW; temperature difference was less than 20 K. Lv et al. (2018) reported heat added by the ultrasonic-assisted FSW is linear to the conventional FSW. The peak temperature was increased by 40 °C due to an ultrasonic vibration that soften the material. However, few researchers (Padhy et al. 2015; Sun et al. 2013) found that the heat added is not linear to FSW's frictional heat. This phenomenon requires more in-depth investigation, including numerical and analytical approaches, and the current work only focuses on its effect on tool life and weld quality. Moreover, a sharp cooling curve is observed in conventional FSW compared to the plasma-assisted FSW process, as shown in Figure *8.6*c. In general, the cooling rate is not a controllable parameter in FSW. The cooling rate is an outcome that depends on the welding parameters, i.e., rotational and traverse speed and tool plunge depth on a suitable backing plate material. FSW is a fast cooling rate process due to lower peak temperature and high heat loss by the large FSW fixture integrated with the bed. Furthermore, the microstructure of the steel is strongly affected by the cooling rate and peak temperature. Low heat input in the conventional FSW (i.e., weld 1) results in faster cooling rates. Cooling rate from 600-500 °C for weld 1, weld 2, weld 3, and weld 4 is 25 $°C/s$, 8.33 $°C/s$, 6.66 $°C/s$, and 5.55 $°C/s$. Plasma preheating retarded the cooling rate as compared to conventional FSW. Choi et al. (2011) also observed that the additional heat by external heat source prevented the rapid cooling and the hard phases in the weld microstructure.

Figure *8.6* shows the comparison of the stir zone micrograph at different heat input and cooling rate conditions.

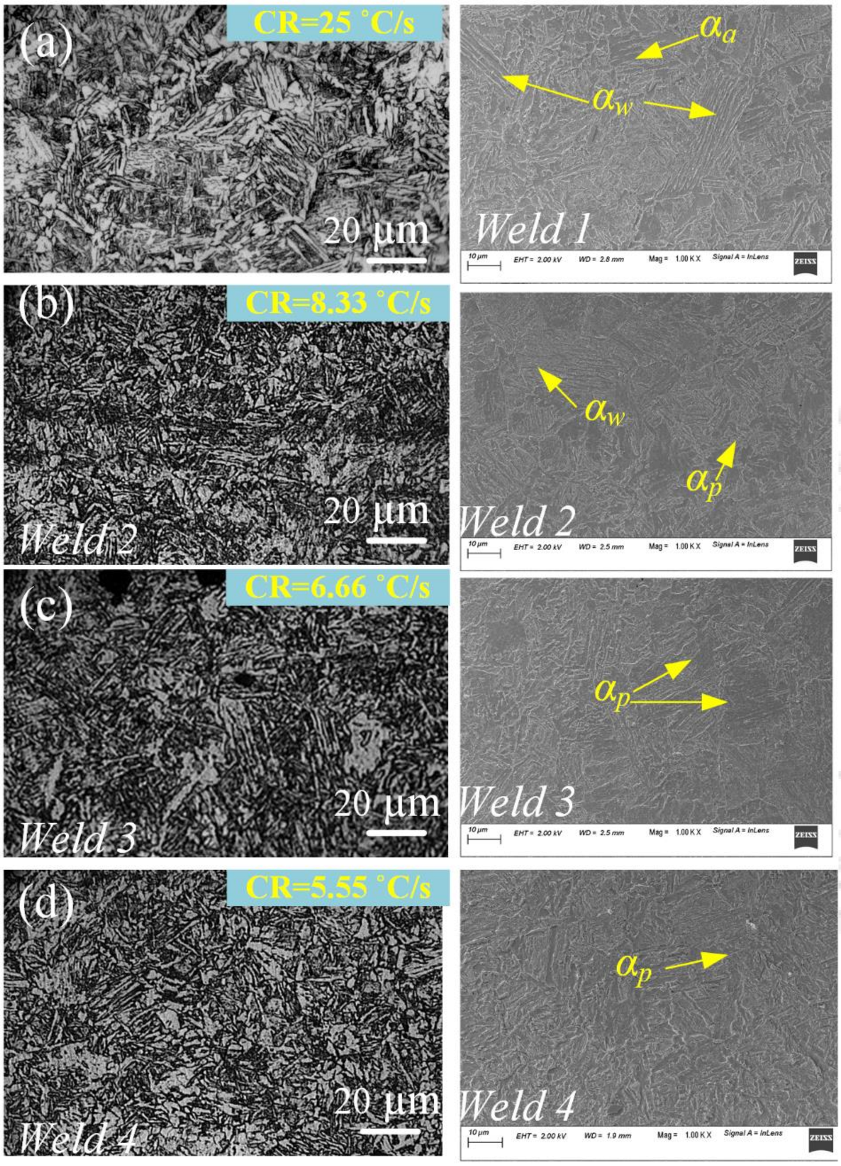

Figure 8.6. Microstructural comparison in the middle of the stir zone under PFSW and conventional FSW: (a) weld 1, (b) weld 2, (c) weld 3, and (d) weld 4

The faster cooling rate (~25 °C/s) of weld 1 results in acicular ferrite (α_a) and Widmanstatten ferrite (α_w) as the major component upon austenite (γ_a) decomposition and less amount polygonal ferrite (α_p) in the SZ microstructure. Microstructural stability is more in acicular ferrite compared to bainite in higher temperatures (Cam 2011; Sorger et al. 2017). The obtained ferrite structures in the SZ microstructures are consistent with the results reported in the literature (Hermenegildo et al. 2018; Wei & Nelson 2012). The low cooling rate welds (~8.33-5.55 $°\mathrm{C/s}$) developed polygonal (α_p) and allotriomorphic ferrite as the major constituents in the stir zone microstructure as depicted in Figure *8.6*b, c and d. Near 5.55 $°\mathrm{C}/s$ i.e. in weld 4, the polygonal (α_p) and allotriomorphic ferrite is larger than the high cooling rate welds, and the ferrite structures that produced is comparatively coarser than that of fast cooling rate. The cooling rate is affected by heat input conditions, i.e. an increase in heat input results in slower cooling rates. The predominant microstructure in the PFSW is polygonal ferrite and allotriomorphic ferrite. These observed microstructures correspond with Toumpis et al. (2014), and Sorger et al. (2017). İpekoğlu et al. (2019) also reported the acicular ferrite as the main structure in the SZ of friction stir welded high strength low alloy steel.

Figure *8.7* illustrates the two existing zones within the heat-affected zone, one is intercritical heat affected zone (ICHAZ), and the other is subcritical heat affected zone (SCHAZ) (G^* : globular cementite) for weld 1 and weld 2 respectively. The FSW of the steel involves allotropic transformation, and a characteristic of TMAZ is lost during phase transformation (Lienert et al. 2003; Mishra & Ma 2005). During FSW, the thermal cycle causes a transformation of the pearlite (α_{fc}) into austenite (γ_a) on heating (with the reverse reaction on cooling) and results in the refinement of pearlite (α_{fc}) colonies and some ferrite grains. ICHAZ during FSW is between the A_1 and the A_3 transformation temperature. As per the continuous cooling time diagram (CCT) of steel, a relatively large time is required to transform from austenite(γ_a) to pearlite (α_{fc}) structure. A normalization heat treatment of the base material is supposed to occur in the ICHAZ region. On the other hand, as illustrated in Figure *8.7*c & Figure *8.7*f, microstructure in SCHAZ consists of spheroidized carbide ($G*$) and ferrite grains. Microstructural observations (Figure *8.7*c & Figure *8.7*f) show that the material in that region of spheroidized carbides experiences sufficient time below the A_1 transformation temperature that allowed partial homogenization and spheroidization of the cementite in SCHAZ. Baker et al. (2019), Wen et al. (2018) and Trinh et al. (2019) also reported similar microstructure in the HAZ region of micro-alloyed steel. Figure *8.7*d & Figure *8.7*g shows the FESEM micrograph of the subcritical HAZ regions of weld 1 and weld 2, respectively. It is believed that a tempering heat treatment takes place in SCHAZ, but the pearlite does not entirely spheroidized due to the thermal cycle being too short for complete spheroidization in that region.

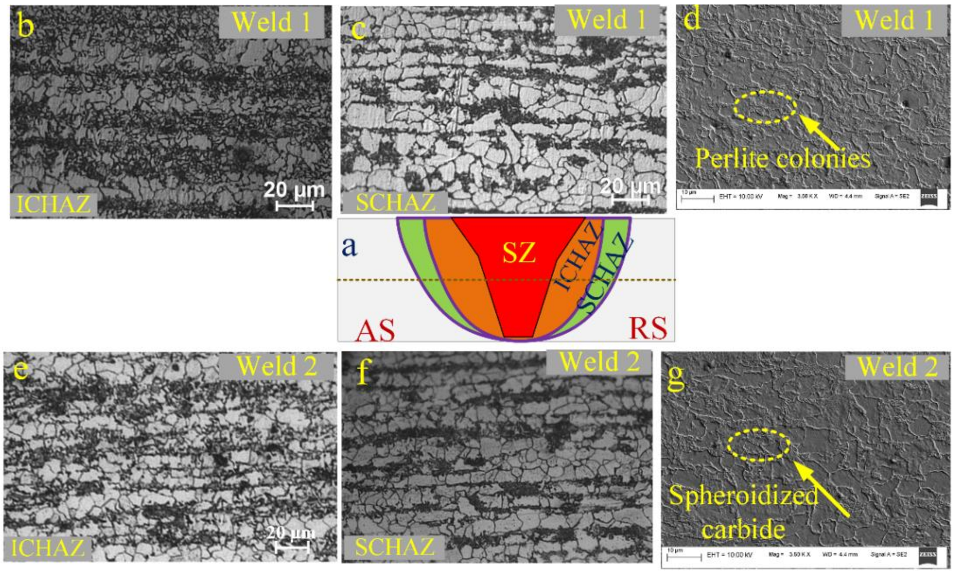

Figure 8.7 Comparison of optical and FESEM micrograph of FSW (i.e., weld 1) and PAFSW (i.e., weld 2): (a) schematic diagram for the heat-affected zone, (b) optical micrograph of intercritical HAZ indicating pearlite dissolution in HAZ region, (c) subcritical HAZ of weld 1 ($G*$: globular cementite), (d) FESEM micrograph of SCHAZ of weld 1,(e) ICHAZ of weld 2 (f) SCHAZ of weld 2, and (g) FESEM micrograph of SCHAZ of weld 2

Figure *8.8* shows the FESEM micrographs and the elemental distribution of the inclusions in the SZ of weld joints. Due to the high temperature and high strain rates in stir zones (Gan et al. 2007; Hamilton et al. 2019; Jain et al. 2019), the presence of tool debris is more likely to occur in this zone. EDS point spectrum analysis suggests that it constitutes 4.5 wt.% W and 0.9 wt.% W in weld 1 and weld 2 as shown in Figure *8.8*a and Figure *8.8*b. EDS mapping in the SZ of weld 1 indicated traces of tungsten (W) particles as depicted in Figure 8.8c-e. Results of earlier publications (Gan et al. 2007; Lienert et al. 2003), reported W particles due to tool wear in the weld microstructure. EDS point spectrum indicates that the SZ of weld 3 and weld 4 consist of significantly low, i.e., 0.5 wt.% W and 0.1 wt.% W, respectively. This can be correlated with preheat; the tool exerts a weaker shear force on DH36 due to the heat-assisted softening of materials.

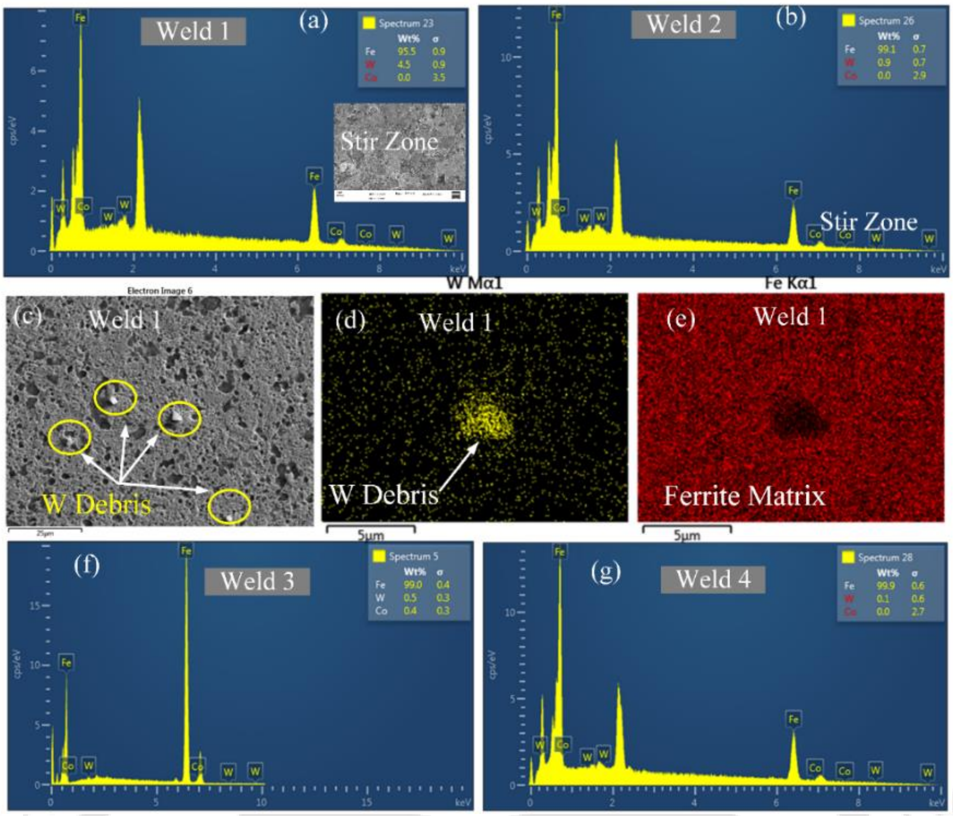

Figure 8.8 Energy dispersive spectrum analysis showing the tungsten (W) percentage in the SZ: (a) weld 1, (b) weld 2, (c-e) elemental mapping indicating tool debris in the SZ, (f) spectrum for weld 3, and (g) spectrum for weld 4

8.3.3 Microhardness distribution

Figure *8.9* demonstrates the microhardness contours and weld macrostructure. The welding condition controlled the weld bead shape and weld zone size. Moreover, the PFSW resulted in the expansion of WZ. D_P and D_F are the weld zone diameters at the top surface during plasma-assisted FSW and FSW. The changes in the weld zone's diameter are calculated as:

$$\%\Delta D = \frac{D_P - D_F}{D_F} \times 100 \qquad \textbf{(8.5)}$$

The weld zone is wider than the tool shoulder's diameter at the top surface. Moreover, the weld zone is expanded by 4.9%, 7.5%, and 7.6% for weld 2, weld 3, and weld 4, respectively. Furthermore, the microhardness contour is plotted from hardness data measured along the transverse cross-section for welded samples at three different layers. The upper layer, the middle layer, and the bottom layers are 0.75, 2, and 3.25 mm away from the joint's top surface.SZ exhibits the highest hardness values, followed by the inner heat affected zone and subcritical heat-affected zone. Hardness is varied from 145 $HV_{0.5}$ in base material to 265.5

$HV_{0.5}$ in the SZ of weld 1. The SZ hardness values for weld 2, weld 3, and weld 4 are 221.5, 220.6, and 219 $HV_{0.5}$, respectively in agreement with the microstructures observed in these regions. Heat-affected softening is not observed in all-welded samples in line with the weld zone's evolved microstructure. On increasing the heat input, the microhardness values are decreased due to the evolution of coarse-grained ferrite carbide aggregate. The above results are supported by the literature of Sun et al. (2013) and Choi et al. (2011) during FSW of steel alloys.

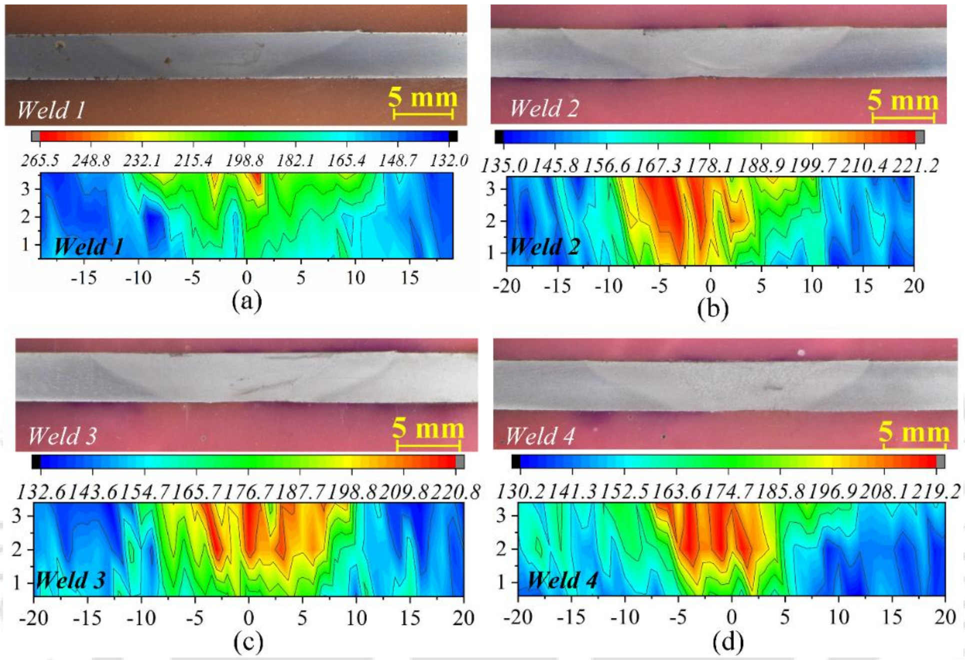

(a)

(b)

(c)

(d)

Figure 8.9 Comparison of microstructure and Vickers microhardness maps: (a) weld 1, (b) weld 2, (c) weld 3, and (d) weld 4

8.3.4 Tensile properties

Figure *8.10*a demonstrates that both the YS and UTS of the welded joints are superior to the base metal. Maximum and minimum tensile strengths are 104.9% and 102.3% of base material for weld 1 and weld 4 respectively. The higher strength of the FSW joint can be attributed to the substantial grain refinement (Hall-Petch effect), high dislocation density (i.e., strain hardening effect), and phases evolution in the SZ (Ghosh et al. 2010). The base elements like Nb, Ti, V, etc., have limited solubility for ferrite and austenite phases, and dispersed precipitate contribute to high strength due to precipitation hardening (Yang et al. 2019). The fracture of tensile specimens corresponds to the transition of the ferrite carbide aggregate region of subcritical HAZ and the base material, as shown in Figure *8.10*b. Figure *8.10*c shows that the elongation of the welded samples is increasing with an increase in the intensity of plasma current. Elongation is increased from ~10% of weld 1 to ~13.8% of weld 4. Figure *8.10*d shows clusters of dimples of different morphology at the fractured surfaces, which indicates that welded samples underwent sufficient plastic deformation before fracture. In dimple failures mode, it is believed that overload remains the principal cause of the fracture and the failure is governed by the coalescence of microvoids.

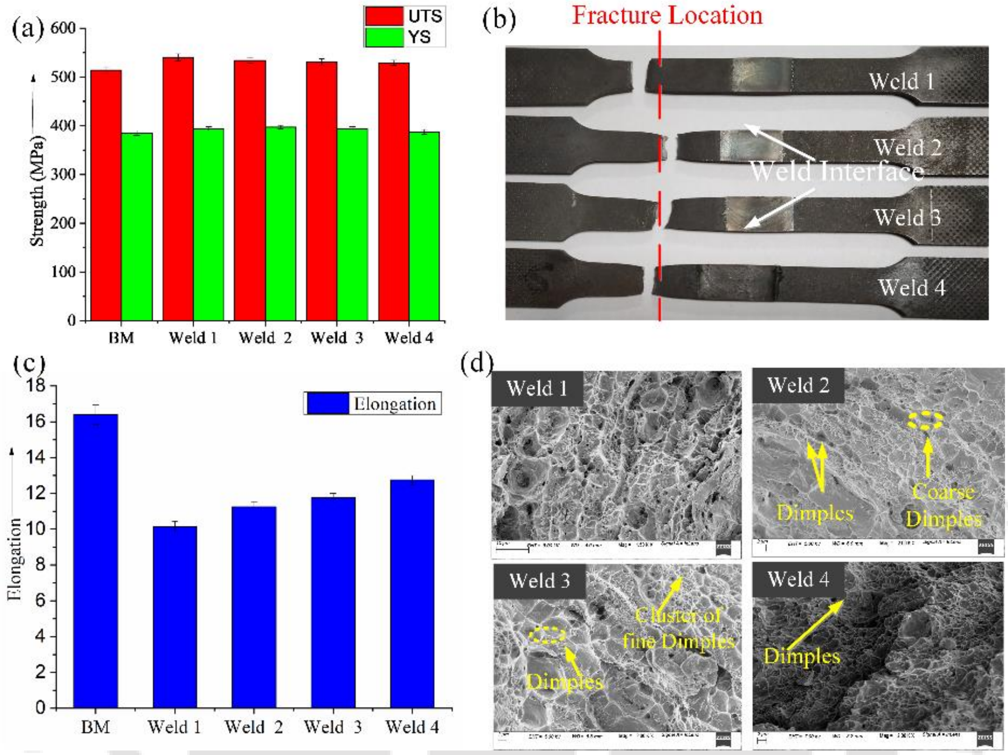

Figure 8.10 Tensile test results: (a) YS and UTS, (b) fracture location, (c) percentage elongation up to fracture point, and (d) FESEM images of fracture surfaces

Figure *8.11*indicates the result of the impact toughness test performed at room temperature. Impact toughness is maximum for weld 4, as depicted in Figure *8.11*a. The welded joints' impact toughness is increased by ~28.9% to ~49.5% from weld 1 to weld 4. This is consistent with the evolved microstructure, as described in section 8.3.2. Cao et al. (2015) and Liu et al. (2011) also reported similar trends of increasing impact strength with the evolved microstructure. Figure *8.11*c shows the comparison of fracture surface morphology of the impact test specimens. Dimples along with quasi cleavage mode of fracture is observed in the fractured impact specimens. Elongated and shallowed dimples are seen on the fractured specimen of weld 4. The cleavage facets appearance on the fractured surface is decreasing slightly from weld 1 to weld 4.

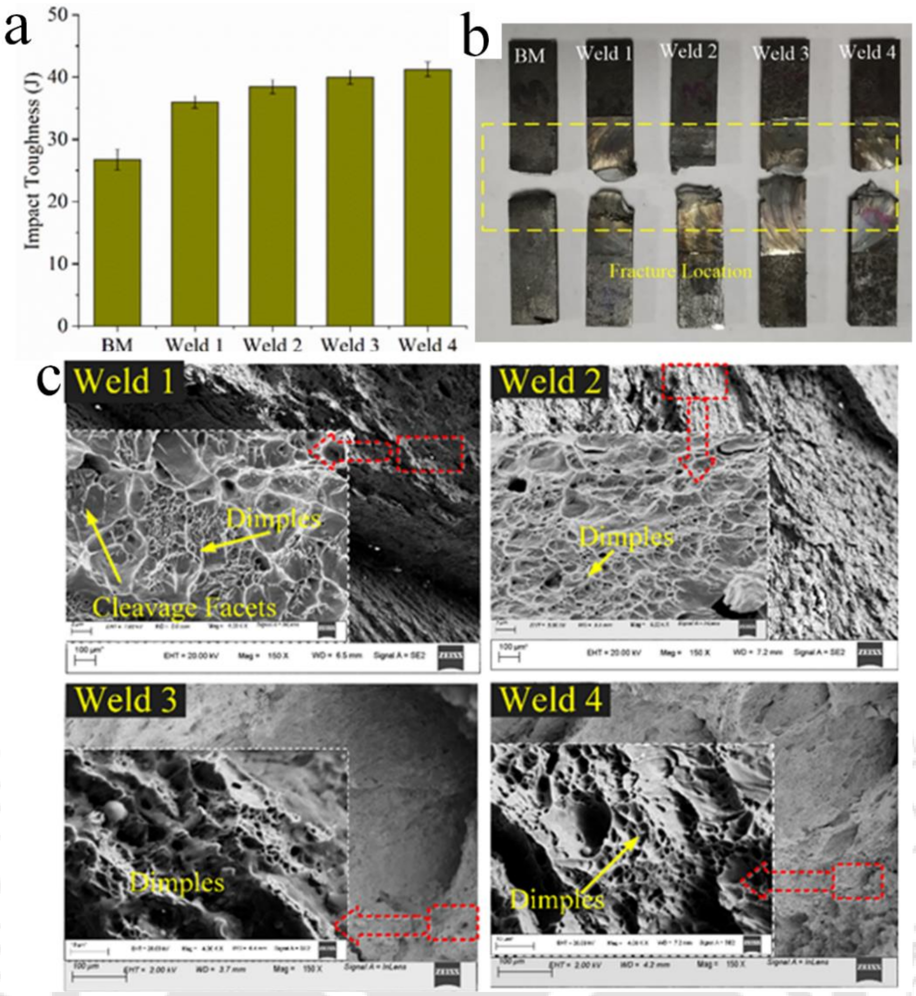

Figure 8.11 Impact test results: (a) comparison on impact toughness of welded specimen with the base material, (b) fracture location of impact specimens, and (c) fracture surface of impact specimens

8.3.5 Tool performance evaluation

Figure *8.12* shows the quantitative and qualitative comparison of the W-Co tools during conventional FSW and PFSW.

From Figure *8.12*a, it can be seen that tool wear is reduced by 58.6% in tool 2 as compared to tool 1. Weight loss is not significant on further increasing the preheating current values as 15A and 17A. It is reported in the earlier studies that tool wear is significantly high during the plunge stage and can be considerably reduced by preheating the workpiece material (Konkol & Mruczek 2007; Lienert et al. 2003; Wei & Nelson, 2012). .In conventional FSW, the tool is exposed to high stresses at elevated temperatures (Gan et al. 2007)’ resulting in either premature tool failure (Tiwari et al. 2019)’ severe tool wear and degradation (Gan et al. 2007), and relatively low welding speed (Yaduwanshi et al. 2015). Figure *8.12*b shows tool profiles measured for pin height and pin diameter using a profile projector. Although little variations are observed at the tool pin height, i.e., it is reduced by 2.7% more in tool 1 than tool 2.

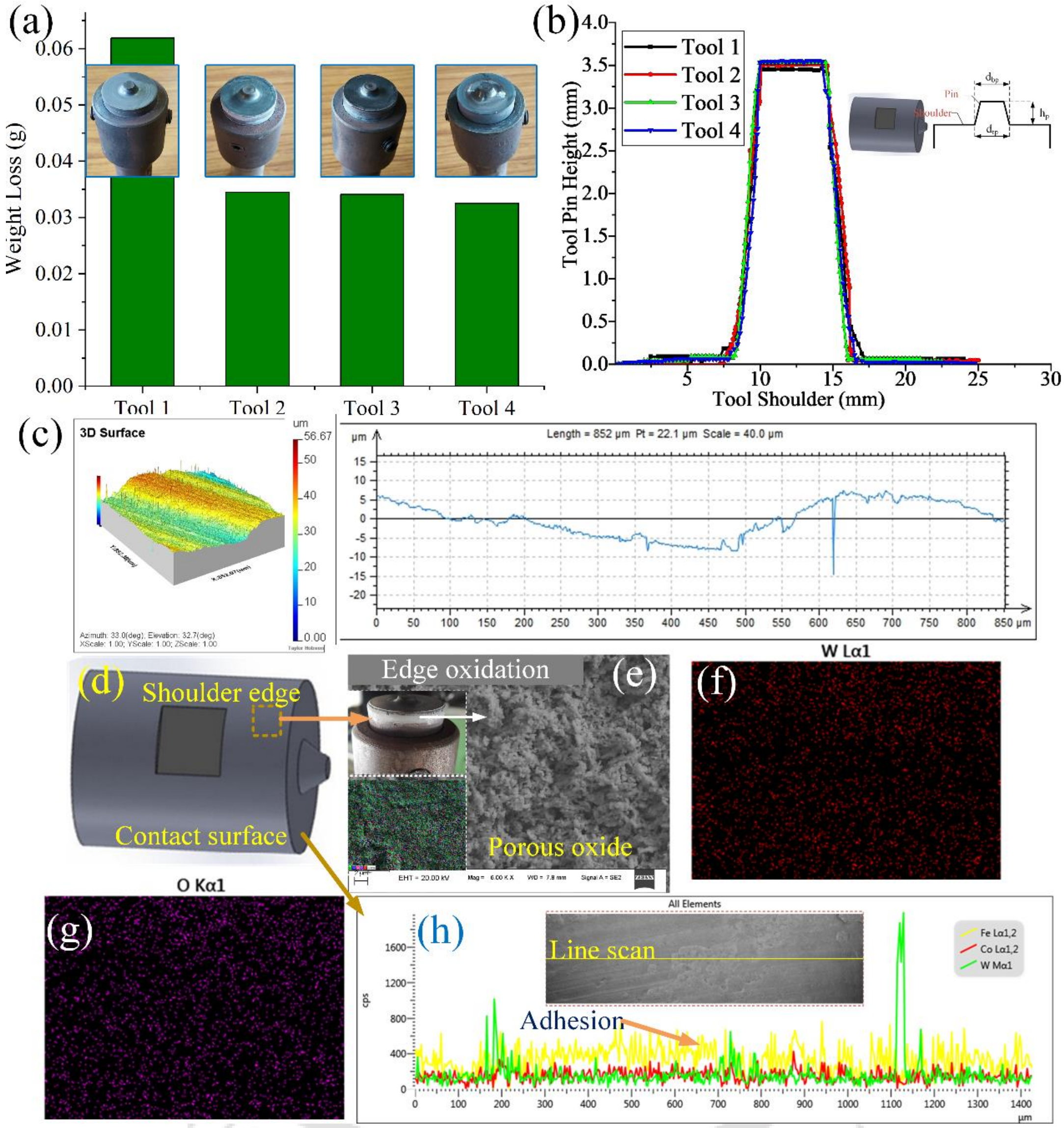

Figure 8.12 Macro characterization of tool: (a) comparison of weight loss, (b) FSW tool profiles (c) 3D surface and surface roughness (R_a) at shoulder for tool 1 (d) tool illustration showing shoulder contact edge and contact surface (e-h) FESEM and EDS analysis showing edge oxidation, and (h) EDS line scan reflecting Fe adhesion on the shoulder contact surface

Unlike in PFSW, tool wear is considerably high in conventional FSW because tool pin contacts with a work plate at ambient temperature. Moreover, the tool pin bottom shows more wear than the tool pin root, since the effect of frictional heat by tool shoulder is comparatively less at the bottom region. This cooler part (i.e., bottom region) of the workpiece leads to substantial tool pin wear during the welding. It is found that the tool shoulder did not show any significant changes. The overall surface profile remains relatively flat, which indicates no plastic deformation is observed at the contact edge. Average surface roughness (R_a) values are 0.53 μm and 0.41 μm for tool 1 and tool 2 respectively as shown in Figure *8.12*c. Moreover, it seems that the pin is broken/chipping occurred at the pin bottom region in the tool 1. This chipping at the tool pin bottom can trigger the abrasive wear mechanism which may results in the brittle/catastrophic fracture due to the presence of the internal defects, voids, porosity and surface defects developed on the tool. Figure *8.12*d shows the primary area of concern i.e. shoulder edge and shoulder contact surface, regarding tool wear and degradation. The oxidation layer is visible at the shoulder edge as shown in Figure *8.12*e-g. Frequently heating and cooling the tool may influence the material's oxidation behavior and fracture toughness. Tungsten tool material is susceptible to cracking induces due to differences of thermal cycles (i.e., heating and cooling rates) of tool pin and shoulder (Tiwari et al. 2019). Besides, loss in ductile cobalt binder and abraded tool particles at the contact interface also triggers the abrasive wear mechanism at elevated temperatures. This abrasion wear agrees with the microstructural studies of the tungsten carbide tool by Tiwari et al. (2019). From previous literature (Gan et al. 2007; Tiwari et al. 2019), it is also confirmed that the high process temperatures are more detrimental to the tool life rather than high stresses. The cobalt extrusion followed by carbide removal or carbide fracture may be the dominant wear mechanism at the tool contact surface. The EDS line scan, shown in Figure 12h, indicates a more in-depth on W tools' adhesion behavior where Fe element from workpiece sticks on the parent W and Co elements.

8.4 SUMMARY

The FSW and PFSW of DH36 steel are performed using WC-10wt.% Co tool. PFSW has a significant effect on weld quality and tool life. From the study, following conclusions are drawn

- The welded joints produced by PFSW has shown a good surface appearance as compared to the conventional FSW. Faying defects at the top surface are minimum in the PFSW. PFSW resulted in good quality weld due to thermal softening of the material and the high degree of plasticization.
- The flash is generated at high axial force and high preheating currents, as this increased the heat input and resulted in excessive plasticization of material.
- The downward force is reduced by 31.6% and 6.25% during the plunge and traverse stage, respectively for weld 2. During PFSW, the temperature is increased by 1.14%, 5.65%, and 5.81% for weld 2, weld 3, and weld 4, respectively.

- Weld zone microstructure revealed grain refinement and ferrite phase evolution during FSW and PFSW. The microstructural analysis in PFSW illustrated significant changes in the grains' structural morphology, controlled by the cooling rate and heat input.
- The plasma preheating source's additional heat input delayed the cooling rate, which affected the phase evolution in the SZ of the PFSW joints. The maximum hardness value in the SZ is reduced by 16% in weld 2 as compared to the weld 1. Further increase in plasma current from i.e., weld 3 and weld 4 has shown no significant reduction in the SZ hardness.
- The YS and UTS of all-welded joints are higher than the base material. The mechanical properties like strength and hardness are increased due to the grain size strengthening (Hall-Petch effect), moderately acicular/widmanstatten ferrite formation, and slightly attributed to the increased dislocation density.
- Tool wear is reflected by tool profile, surface characteristics, abrasion, and adhesion wear mechanisms. Plasma preheating reduced the tool force by 31% and tool wear by 58% due to the material softening.

:--------------------*--------------------*----------------------

Chapter 9

9 CONCLUSIONS AND THE FUTURE SCOPE OF THE WORK

9.1 CONCLUSIONS OF THE PRESENT WORK

Joining steel by FSW is more challenging, unlike softer materials because of the high temperature and stresses generated during the process that increased the tool wear. In addition to that high power requirement, robust fixture, costly tool material, tool geometry, tool forces, and process parameters are needed to be investigated in detail. In order to support the current research trend and rapid growth of FSW of steel, deep insights of the complex microstructure evolution and effect of tool wear need to be addressed. The present thesis address some of these pertinent issues and elaborate fundamental knowledge in joining similar and dissimilar low carbon steels using tungsten tool. In the purview of this general theme, the major topics addressed in the present thesis work are as follows:

- Development and characterization of friction stir welding technology of low-carbon steel plates using tungsten carbide $(\mathrm{WC}-10\mathrm{wt.\%Co})$ tool.
- Investigation on friction stir welding of dissimilar steels, i.e., AIS304 stainless steel and mild steel.
- CFD modelling of temperature distribution and material flow investigation during FSW of DH36 shipbuilding grade steel.
- Friction stir welding of DH36 steel using two different grades of tool material i.e., tool A $(\mathrm{WC}-6\ \mathrm{wt.\%Co})$ and tool B $(\mathrm{WC}-10\ \mathrm{wt.\%Co})$.
- Effect of plasma preheating on weld quality and tool life during friction stir welding of DH36 steel.

The overall thesis outcomes are briefly summarized below

- Friction stir welding of low carbon steel(UNS G10060) yielded higher strength and hardness albeit less ductility than the base material.
- During FSW of low carbon steel, it is seen that material flow on the AS is more complex and chaotic at both top and bottom regions than the material flow on the RS.

- FSW of low carbon steel resulted in the formation of “onion ring”, “banded structure” and the “swirl zone” that reflects the complex material movement during the process.
- In FSW of low carbon steel, the finest grains size (i.e. 7.9 μm) is observed in TMAZ.

✓ **From the FSW of dissimilar steel, the following conclusions are drawn**

- In joining of dissimilar steel, successful joints are produced from tool offset of 0.6 mm to 1.2 mm towards the mild steel side, at rotational speeds of 600 rpm and 875 rpm.
- The effect of tool offset on mechanical properties i.e. tensile strength, microhardness and impact toughness is more significant at a low rotational speed.
- Tensile strength of the welded joint is between the tensile strength of both materials i.e. higher than the tensile strength of the mild steel and lower than the tensile strength of stainless steel.
- In FSW of dissimilar steel, complex intermixing is observed in the weld region with higher intermixing on the advancing side that resulted in both mechanical interlocking at macro scale and metallurgical bonding at micro scale.
- In FSW of dissimilar steel, it is seen that tool debris are present in the weld zone microstructure especially in the SZ and in the AS-SZ.

✓ **From the FSW of DH36 steel plates following conclusions are drawn**

- From the FSW of DH36 steel, it is confirmed that the tool wear is significantly high as compared to FSW of similar and dissimilar steels.
- Tungsten tools with fracture toughness greater than 3750 N/mm^2 produced successful welds with minimum tool wear.
- It is also seen that the degradation mechanisms of the tungsten-based tool are adhesion, abrasion, diffusion, oxidation, deformation, and cracking.
- Among these degradation mechanisms, oxidation wear is one of the major wear mechanism that resulted in the pull out of ductile cobalt binder and formation of a porous and brittle-oxide layer at the tool shoulder surface.
- Moreover during FSW of DH36 steel, at high process temperatures, tungsten carbide tools are more prone to oxidation wear that reduces the tool life drastically.
- It is also observed that abrasion wear and adhesion wear is more significant on the shoulder surface and tool pin surface respectively.
- From the FSW of DH36 steel, process temperature has more detrimental effect on tool wear rather than process forces. i.e., increasing rotational speed and decreasing traverse speed resulted in a higher wear rate.

- ✓ **From CFD modeling of FSW of DH36 steel, the following conclusions are drawn**
- ➢ The CFD model shows that the temperature distribution is asymmetric and skewed at the advancing trailing region and this asymmetry reduced on increasing traverse heat input ratio (THIR).
- ➢ The temperature, velocity and strain rate are maximum on the shoulder-workpiece interface that decreased through the plate thickness drastically.
- ➢ It is observed that the strain rates are different on AS and RS due to differences in relative velocity.
- ➢ It is also seen that the material flow and material mixing occurs at the retreating side and the advancing side of the joint respectively. Moreover, material flow drastically changes in the advancing side that resulted in the formation of swirl zone in that region.
- ✓ **From plasma-assisted FSW of DH36 steel plates, the following conclusions are drawn**
- ➢ Preheating of DH36 steel reduced the downward force by 31.6% and 6.25% during the plunge and traverse stage respectively.
- ➢ The maximum hardness value in the stir zone was reduced by 15% in PFSW as compared to the FSW.
- ➢ The tensile strength gradually decreased with the increase in plasma preheating temperature.
- ➢ Preheating during FSW retarded the cooling rate which affected the second phase evolution in the stir zone microstructure of the PFSW joints.
- ➢ Preheating of the workpiece material reduced the wear of the tungsten tool by 58% compared to conventional FSW.

9.2 SCOPE OF FUTURE WORK

In the present study, FSW of low carbon steel (UNS G10060, UNS G10080, UNS S30400 and DH36 steel) is explored experimentally and numerically. To overcome the problem of wear, an attempt is made to preheat the workpiece by plasma torch during FSW of DH36 steel. More in-depth analysis is required to understand the complex thermal phenomenon during plasma assisted FSW of steel. The following areas can be explored in the future investigations

- ❖ In this study preheating is done by plasma torch, other energy assisted FSW processes like Induction assisted FSW, laser assisted FSW and ultrasonic assisted FSW can be studied on FSW of DH36 steel.

- Prediction of residual stresses using numerical and experimental techniques during FSW of DH36 steel.
- Tribological properties of tool pin can be enhanced to withstand the high process temperatures and process forces.
- Experimental and numerical fatigue analysis of FS welded joints can be explored.
- Numerical modelling of plasma assisted FSW is required to get more insights in the complex thermal interaction during plasma assisted FSW process.
- Mathematical model for the effect of preheating on weld quality and tool wear can be explored.

:--------------------*--------------------*----------------------:

REFERENCES

Able, N., & Pfefferkorn, F. (2005). Laser-assisted friction stir lap welding of aluminum. *In Heat Transfer Summer Conference Systems*, 425–429.

Ahmad, B., Galloway, A., & Toumpis, A. (2019). Numerical optimisation of laser assisted friction stir welding of structural steel. *Science and Technology of Welding & Joining*, *24*(6), 548–558.

Ahmadnia, M., Seidanloo, A., Teimouri, R., Rostamiyan, Y., & Titrashi, K. G. (2015). Determining influence of ultrasonic-assisted friction stir welding parameters on mechanical and tribological properties of AA6061 joints. *The International Journal of Advanced Manufacturing Technology*, *78*(9–12), 2009–2024.

Al-moussawi, M., Smith, A. J., & Faraji, M. (2017). Friction Stir Welding of EH46 Steel Grade at Dwell Stage :Microstructure Evolution. *Metallography, Microstructure, and Analysis*, *6*(6), 489–501.

Al-Moussawi, M., & Smith, A. J. J. (2018). Defects in Friction Stir Welding of Steel. *Defects in Friction Stir Welding of Steel*, *7*(2), 19–202.

Al-Moussawi, M., Smith, A. J., Young, A., Cater, S., & Faraji, M. (2017). Modelling of friction stir welding of DH36 steel. *Int. Journal of RefractoryMetals and HardMaterialsnt. Journal of RefractoryMetals and HardMaterials*, *92*(1–4), 341–360.

Álvarez, A. I., Cid, V., Pena, G., Sotelo, J., & Verdera, D. (2016). Assisted Friction Stir Welding of Carbon Steel: Use of Induction and Laser as Preheating Techniques. In *Friction Stir Welding and Processing VII* (pp. 117–126). Springer, Cham.

Álvarez, A. I., García, M., Pena, G., Sotelo, J., & Verdera, D. (2014). Evaluation of an induction-assisted friction stir welding technique for super duplex stainless steels. *Surface and Interface Analysis*, *46*(10–11), 892–896.

Amini, S., & Amiri, M. R. (2014). Study of ultrasonic vibrations' effect on friction stir welding. *International Journal of Advanced Manufacturing Technology*, *73*(1–4), 127–135.

Arora, A., De, A., & Debroy, T. (2011). Toward optimum friction stir welding tool shoulder diameter. *Scripta Materialia*, *64*(1), 9–12.

Arora, A., Nandan, R., Reynolds, A. P., & DebRoy, T. (2009). Torque, power requirement and stir zone geometry in friction stir welding through modeling and experiments. *Scripta Materialia*, *60*(1), 13–16.

Arora, A., Zhang, Z., De, A., & DebRoy, T. (2009). Strains and strain rates during friction stir welding. *Scripta Materialia*, *61*(9), 863–866.

Ashish, B., Saini, J. S., & Sharma, B. (2016). A review of tool wear prediction during friction stir welding of aluminium matrix composite. *Transactions of Nonferrous Metals Society of China*, *26*(8), 2003–2018.

Assidi, M., & Fourment, L. (2009). Accurate 3D Friction Stir Welding simulation tool based on friction model calibration. *International Journal of Material Forming*, *2*(1), 327–330.

Assidi, M., Fourment, L., Guerdoux, S., & Nelson, T. (2010). Friction model for friction stir welding process simulation: Calibrations from welding experiments. *International Journal of Machine Tools and Manufacture*, *50*(2), 143–155.

Aydin, H., & Nelson, T. W. (2013). Microstructure and mechanical properties of hard zone in friction stir welded X80 pipeline steel relative to different heat input. *Materials Science and Engineering A*, *586*, 313–322.

Baker, T. N., Rahimi, S., He, K., & Mcpherson, N. (2019). Evolution of microstructure during double-sided friction stir welding of microalloyed steel. *Metallurgical and Materials Transactions A*, *50*(6), 2748–2764.

Bang, H., Bang, H., Song, H., & Joo, S. (2013). Joint properties of dissimilar Al6061-T6 aluminum alloy/Ti-6%Al-4%V titanium alloy by gas tungsten arc welding assisted hybrid friction stir welding. *Materials and Design*, *51*, 544–551.

Bang, H. H., Bang, H. H., Jeon, G., Oh, I., & Ro, C. (2012). Gas tungsten arc welding assisted hybrid friction stir welding of dissimilar materials Al6061-T6 aluminum alloy and STS304 stainless steel. *Materials and Design*, *37*, 48–55.

Bang, H. S., Bang, H. S., Hong, J. H., Jeon, G. H., Kim, G. S., & Kaplan, A. F. H. (2016). Effect of Tungsten-Inert-Gas Preheating on Mechanical and Microstructural Properties of Friction Stir Welded Dissimilar Al Alloy and Mild Steel. *Strength of Materials*, *48*(1), 152–159.

Barnes, S. J., Bhatti, A. R., Steuwer, A., Johnson, R., Altenkirch, J., & Withers, P. J. (2012). Friction Stir Welding in HSLA-65 Steel : Part I . Influence of Weld Speed and Tool Material on Microstructural Development. *Metallurgical and Materials Transactions A*, *43*(7), 2342–2355.

Basu, S. N., & Sarin, V. K. (1996). Oxidation behavior of WC-Co. *Materials Science and Engineering: A*, *209*(1–2), 206–212.

Batalha, G. F., Farias, A., Magnabosco, R., Delijaicov, S., & Adamiak, M. (2012). Evaluation of an AlCrN coated FSW tool. *Journal of Achievements in Materials and Manufacturing Engineering*, *55*(2), 607–615.

Bilgin, M. B., & Meran, C. (2012). The effect of tool rotational and traverse speed on friction stir weldability of AISI 430 ferritic stainless steels. *Materials and Design*, *33*(1), 376–383.

Bilgin, M. B., Meran, C., & Canyurt, O. E. (2015). Optimization of strength of friction stir welded joints for AISI 430 ferritic stainless steels by genetic algorithm. *International Journal of Advanced Manufacturing Technology*, *77*(9–12), 2221–2233.

Cam, G. (2011). Friction stir welded structural materials: Beyond Al-alloys. *International Materials Reviews*, *56*(1), 1–48.

Campanelli, S. L., Casalino, G., Casavola, C., & Moramarco, V. (2013). Analysis and comparison of friction stir welding and laser assisted friction stir welding of aluminum alloy. *Materials*, *6*(12), 5923–5941.

Cao, R., Li, J., Liu, D. S., Ma, J. Y., & Chen, J. H. (2015). Micromechanism of Decrease of Impact Toughness in Coarse-Grain Heat-Affected Zone of HSLA Steel with Increasing Welding Heat Input. *Metallurgical and Materials Transactions A*, *46*(7), 2999–3014.

Casalino, G., Campanelli, S., Ludovico, a D., Contuzzi, N., & Angelastro, A. (2012). Study of a fiber laser assisted friction stir welding process. *In High Power Laser Materials Processing: Lasers, Beam Delivery, Diagnostics, and Applications (Vol. 8239, p. 823913). International Society for Optics and Photonics.*

Chang, W.-S. S., Rajesh, S. R., Chun, C.-K. K., & Kim, H.-J. J. (2011). Microstructure and Mechanical Properties of Hybrid Laser-Friction Stir Welding between AA6061-T6 Al Alloy and AZ31 Mg Alloy. *Journal of Materials Science & Technology*, *27*(3), 199–204.

Chao, Y. J., Qi, X., & Tang, W. (2003). Heat Transfer in Friction Stir Welding—Experimental and Numerical Studies. *Journal of Manufacturing Science and Engineering*, *125*(1), 138–145.

Chen, C. M., & Kovacevic, R. (2004). Joining of Al 6061 alloy to AISI 1018 steel by combined effects of fusion and solid state welding. *International Journal of Machine Tools and Manufacture*, *44*(11), 1205–1214.

Chen, G., Ma, Q., Zhang, S., Wu, J., Zhang, G., & Shi, Q. (2018). Computational fluid dynamics simulation of friction stir welding : A comparative study on different frictional boundary conditions. *Journal of Materials Science & Technology*, *34*(1), 128–134.

Chen, Y. C., Fujii, H., Tsumura, T., Kitagawa, Y., Nakata, K., Ikeuchi, K., Matsubayashi, K., Michishita, Y., Fujiya, Y., & Katoh, J. (2009). Friction stir processing of 316L stainless steel plate. *Science and Technology of Welding and Joining*, *14*(3), 197–201.

Cheng, C., Lin, H., Lin, J., Cheng, C., Lin, H., & Lin, J. (2013). Friction stir welding of ductile iron and low carbon steel Friction stir welding of ductile iron and low carbon steel. *Science and Technology of Welding & Joining*, *15*(8), 706–711.

Cho, H.-H., Kim, D.-W., Hong, S.-T., Jeong, Y.-H., Lee, K., Cho, Y.-G., Kang, S. H., & Han, H. N. (2015). Three-Dimensional Numerical Model Considering Phase Transformation in Friction Stir Welding of Steel. *Metallurgical and Materials Transactions A*, *46*(12), 6040–6051.

Cho, H., Hong, S., Roh, J., Choi, H., & Hoon, S. (2013). Three-dimensional numerical and experimental investigation on friction stir welding processes of ferritic stainless steel. *Acta Materialia*, *61*(7), 2649–2661.

Choi, D.-H. H., Lee, C.-Y. Y., Ahn, B.-W. W., Yeon, Y.-M. M., Park, S.-H. h. C., Sato, Y.-S. Y. S., Kokawa, H., & Jung, S.-B. B. (2010). Effect of fixed location variation in friction stir welding of steels with different carbon contents. *Science and Technology of Welding & Joining*, *15*(4), 299–304.

Choi, D. H., Ahn, B. W., Yeon, Y. M., Park, S. H. C., Sato, Y. S., Kokawa, H., & Jung, S. B. (2011). Microstructural Characterizations Following Friction Stir Welding of Dissimilar Alloys of Low- and High-Carbon Steels. *Materials Transactions*, *52*(7), 1500–1505.

Choi, D. H., Lee, C. Y., Ahn, B. W., Choi, J. H., Yeon, Y. M., Song, K., Hong, S. G., Lee, W. B., Kang, K. B., & Jung, S. B. (2011). Hybrid Friction Stir Welding of High-carbon Steel. *Journal of Materials Science and Technology*, *27*(2), 127–130.

Choi, D. H., Lee, C. Y., Ahn, B. W., Choi, J. H., Yeon, Y. M., Song, K., Park, H. S., Kim, Y. J., Yoo, C. D., & Jung, S. B. (2009). Frictional wear evaluation of WC – Co alloy tool in friction stir spot welding of low carbon steel plates. *International Journal of Refractory Metals and Hard Materials*, *27*(6), 931–936.

Chung, Y. D., Fujii, H., Sun, Y., & Tanigawa, H. (2011). Interface microstructure evolution of dissimilar friction stir butt welded F82H steel and SUS304. *Materials Science and Engineering A*, *528*(18), 5812–5821.

Chung, Y. D., Fujii, H., Ueji, R., & Tsuji, N. (2010). Friction stir welding of high carbon steel with excellent toughness and ductility. *Scripta Materialia*, *63*(2), 223–226.

Colegrove, P. A., & Shercliff, H. R. (2006). CFD modelling of friction stir welding of thick plate 7449 aluminium alloy. *Science and Technology of Welding and Joining*, *11*(4), 429–441.

Colegrove, P. A., Shercliff, H. R., & Zettler, R. (2007). Model for predicting heat generation and temperature in friction stir welding from the material properties. *Science and Technology of Welding and Joining*, *12*(4), 284–297.

Constantin, M. A. ., Bosneag, A., Nitu, E. ;, & Iordache, M. (2018). Orientation of process parameter values of TIG assisted FSW of copper to obtain improved mechanical properties. *In IOP Conference Series: Materials Science and Engineering (Vol. 400, No. 2, p. 022017). IOP Publishing.*

Constantin, M. A., Boșneag, A., Nitu, E., & Iordache, M. (2017). Experimental investigations of tungsten inert gas assisted friction stir welding of pure copper plates. *In CAR 2017.*

Cui, L., Fujii, H., Tsuji, N. and, & Nogi, K. (2007). Friction stir welding of a high carbon steel. *Scripta Materialia*, *56*(7), 637–640.

Cui, L., Fujii, H., Tsuji, N., Nakata, K., Nogi, K., Ikeda, R., & Matsushita, M. (2007). Transformation in Stir Zone of Friction Stir Welded Carbon Steels with Different Carbon Contents. *ISIJ International*, *47*(2), 299–306.

da Cunha, P. H. C. P., Lemos, G. V. B., Bergmann, L., Reguly, A., dos, Santos, J., Marinho, R. R., & Paes, M. T. P. (2018). Effect of welding speed on friction stir welds of GL E36 shipbuilding steel. *Journal of Materials Research and Technology*, *8*(1), 1041–1051.

Daftardar, S. (2009). *Laser Assisted Friction Stir Welding: Finite Volume Method and Metaheuristic Optimization*. *M*(May), 93.

Darvazi, A. R., & Iranmanesh, M. (2014). Prediction of asymmetric transient temperature and longitudinal residual stress in friction stir welding of 304L stainless steel. *Materials and Design*, *55*, 812–820.

de Queiroz Caetano, G., Silva, C. C., Motta, F. M., Miranda, C. H., Farias, P. J., Bergmann, A. L., & Santos, J. F. dos. (2018). Influence of rotation speed and axial force on the friction stir welding of AISI 410S ferritic stainless steel. *Journal of Materials Processing Tech.*, *262*, 430–436.

Dialami, N., Chiumenti, M., Cervera, M., & Agelet de Saracibar, C. (2016). Challenges in Thermo-mechanical Analysis of Friction Stir Welding Processes. *Archives of Computational Methods in Engineering*, *24*(1), 189–225.

Diniz, A. E., Machado, Á. R., & Corrêa, J. G. (2016). Tool wear mechanisms in the machining of steels and stainless steels. *International Journal of Advanced Manufacturing Technology*, *87*(9–12), 3157–3168.

Exner, H. (1979). Physical and chemical nature of cemented carbides. *International Materials Reviews*, *24*(1), 149–173.

Exner, H. E., & Gurland, J. (1970). A review of parameters influencing some mechanical properties of tungsten carbide-cobal alloys. *Powder Metallurgy*, *13*(25), 13–31.

Fall, A., Fesharaki, M., Khodabandeh, A., & Jahazi, M. (2016). Tool Wear Characteristics and Effect on Microstructure in Ti-6Al-4V Friction Stir Welded Joints. *Metals*, *6*(11), 275.

Farias, A., Batalha, G. F., Prados, E. F., Magnabosco, R., & Delijaicov, S. (2013). Tool wear evaluations in friction stir processing of commercial titanium Ti – 6Al – 4V. *Waer*, *302*(1–2), 1327–1333.

Fatima, S., Khan, M., Jaffery, S. H. I., Ali, L., Mujahid, M., & Butt, S. I. (2016). Optimization of process parameters for plasma arc welding of austenitic stainless steel (304 L) with low carbon steel (A-36). *Proceedings of the Institution of Mechanical Engineers, Part L: Journal of Materials Design and Applications*, *230*(2), 640–653.

Fei, X., Jin, X., Ye, Y., Xiu, T., & Yang, H. (2016). Effect of pre-hole offset on the property of the joint during laser-assisted friction stir welding of dissimilar metals steel and aluminum alloys. *Materials Science and Engineering A*, *653*, 43–52.

Fei, X., Ye, Y., Jin, L., Wang, H., & Lv, S. (2018). Special welding parameters study on Cu/Al joint in laser-heated friction stir welding. *Journal of Materials Processing Technology*, *256*, 160–171.

Fowler, S., Toumpis, A., & Galloway, A. (2016). Fatigue and bending behaviour of friction stir welded DH36 steel. *International Journal of Advanced Manufacturing Technology*, *84*(9–12), 2659–2669.

Frigaard, Ø., Grong, Ø., & Midling, O. T. (2001). A process model for friction stir welding of age hardening aluminum alloys. *Metallurgical and Materials Transactions A*, *32*(5), 1189–1200.

Fujii, H, Cui, L., Nakata, K., & Nogi, K. (2008). Mechanical properties of friction stir welded carbon steel joints - Friction stir welding with and without transformation. *Welding in the World*, *52*(9–10), 75–81.

Fujii, H, Tatsuno, T., Tsumura, T., Ueji, R., Nakata, K., & Nogi, K. (2008). Hybrid Friction Stir Welding of Carbon Steel. *In Materials Science Forum (Vol. 580, Pp. 393-396). Trans Tech Publications Ltd.*

Fujii, Hidetoshi, Cui, L., Tsuji, N., Maeda, M., Nakata, K., & Nogi, K. (2006). Friction stir welding of carbon steels. *Materials Science and Engineering A*, *429*(1–2), 50–57.

Gan, W., Li, Z. T., & Khurana, S. (2007). Tool materials selection for friction stir welding of L80 steel. *Science and Technology of Welding and Joining*, *12*(7), 610–613.

Ghosh, M., Kumar, K., & Mishra, R. S. (2010). Analysis of microstructural evolution during friction stir welding of ultrahigh-strength steel. *Scripta Materialia*, *63*(8), 851–854.

Ghosh, M., Kumar, K., & Mishra, R. S. (2011). Friction stir lap welded advanced high strength steels: Microstructure and mechanical properties. *Materials Science and Engineering A*, *528*(28), 8111–8119.

Gu, L., Huang, J., Tang, Y., Xie, C., & Gao, S. (2015). Influence of different post treatments on microstructure and properties of WC-Co cemented carbides. *Journal of Alloys and Compounds*, *620*, 116–119.

Guo, G. and, & Shen, Y. (2019). Friction stir welding of dissimilar stainless steels : evaluation of flow pattern , microstructure and mechanical properties. *Materials Research Express*, *6*(5), 056510.

Hajian, M., Abdollah-zadeh, A., Rezaei-Nejad, S. S. S., Assadi, H., Hadavi, S. M. M. M. M., Chung, K., & Shokouhimehr, M. (2015). Microstructure and mechanical properties of friction stir processed AISI 316L stainless steel. *Materials and Design*, *67*, 82–94.

Hamilton, C., Kopyściański, M., Węglowska, A., Pietras, A., & Dymek, S. (2019). Modeling, microstructure, and mechanical properties of dissimilar 2017A and 5083 aluminum alloys friction stir welds. *Proceedings of the Institution of Mechanical Engineers, Part B: Journal of Engineering Manufacture*, *233*(2), 553–564.

Hanke, S., Lemos, G. V. ., Bergmann, L., Martinazzi, D., dos Santos, J. F., & Strohaecker, T. R. (2017). Degradation mechanisms of pcBN tool material during Friction Stir Welding of Ni-base alloy 625. *Wear*, *376*, 403–408.

Hasan, A. F., Bennett, C. J., & Shipway, P. H. (2015). A numerical comparison of the fl ow behaviour in Friction Stir Welding (FSW) using unworn and worn tool geometries. *Materials and Design*, *87*, 1037–1046.

Hasan, A. F., Bennett, C. J., Shipway, P. H., Cater, S., & Martin, J. (2017). A numerical methodology for predicting tool wear in Friction Stir Welding. *Journal of Materials Processing Technology*, *241*, 129–140.

Hermenegildo, T. F., Santos, T. F., Torres, E. A., Afonso, C. R., & Ramirez, A. J. (2018). Microstructural Evolution of HSLA ISO 3183 X80M (API 5L X80) Friction Stir Welded Joints. *Metals and Materials International*, *24*(5), 1120–1132.

Husain, M. M., Sarkar, R., Pal, T. K., Prabhu, N., & Ghosh, M. (2015). Friction Stir Welding of Steel: Heat Input, Microstructure, and Mechanical Property Co-relation. *Journal of Materials Engineering and Performance*, *24*(9), 3673–3683.

İpekoğlu, G., Tevfik Küçükömeroğl, Semih M Aktarer, D Murat Sekban, & GürelÇam. (2019). Investigation of microstructure and mechanical properties of friction stir welded dissimilar St37/St52 joints. *Materials Research Express*, *6*(4), 046537.

Iqbal, Z., Shuaib, A. N., Al-Badour, F., Merah, N., & Bazoune, A. (2014). Microstructure and Hardness of Friction Stir Weld Bead on Steel Plate Using W-25%Re Pin Tool. *In Engineering Systems Design and Analysis (Vol. 45851, p. V003T14A015). American Society of Mechanical Engineers.*

Iqbal, Zafar, Saheb, N., & Shuaib, A. R. (2016). W-25%Re-HfC composite materials for Pin tool material applications: Synthesis and consolidation. *Journal of Alloys and Compounds*, *674*, 189–199.

Iqbal, Zafar, Shuaib, A. R., Al-Badour, F., Merah, N., & Bazoune, A. (2014). Experimental Evaluation of Wear Features of W-25%Re Pin Tool Used in Friction Stir Welding Mild Steel. *In ASME International Mechanical Engineering Congress and Exposition (Vol. 46445, p. V02BT02A010). American Society of Mechanical Engineers.*

Jafarzadegan, M., Abdollah-zadeh, A., Feng, A. H. H., Saeid, T., Shen, J., & Assadi, H. (2013). Microstructure and Mechanical Properties of a Dissimilar Friction Stir Weld between Austenitic Stainless Steel and Low Carbon Steel. *Journal of Materials Science & Technology*, *29*(4), 367–372.

Jain, R., Pal, S. K., & Singh, S. B. (2019). Investigation on effect of pin shapes on temperature, material flow and forces during friction stir welding: A simulation study. *Proceedings of the Institution of Mechanical Engineers, Part B: Journal of Engineering Manufacture*, *233*(9), 1980–1992.

Joo, S. (2013). Joining of dissimilar AZ31B magnesium alloy and SS400 mild steel by hybrid gas tungsten arc friction stir welding. *Metals and Materials International*, *19*(6), 1251–1257.

Kadian, A. K., & Biswas, P. (2015). A Comparative Study of Material Flow Behavior in Friction Stir Welding Using Laminar and Turbulent Models. *Journal of Materials Engineering and Performance*, *24*(10), 4119–4127.

Karami, S., Jafarian, H., Eivani, A. R., & Kheirandish, S. (2016). Engineering tensile properties by controlling welding parameters and microstructure in a mild steel processed by friction stir welding. *Materials Science and Engineering A*, *670*, 68–74.

Khandkar, M. Z. H., Khan, J. A., & Reynolds, A. P. (2003). Prediction of temperature distribution and thermal history during friction stir welding: input torque based model. *Science and Technology of Welding and Joining*, *8*(3), 165–174.

Kheireddine, A. H., Ammouri, A. H., & Hamade, R. F. (2013). *Finite element modeling of laser assisted friction stir welding of carbon steels for enhanced sustainability of welded joints*.

Kim, Y. G., Kim, J. S., & Kim, I. J. (2014). Effect of process parameters on optimum welding condition of DP590 steel by friction stir welding. *Journal of Mechanical Science and Technology*, *28*(12), 5143–5148.

Klingensmith, S., DuPont, J. N., & Marder, A. R. (2005). Microstructural characterization of a double-sided friction stir weld on a superaustenitic stainless steel. *Welding Journal*, *84*(5), 77s-85s.

Konkol, P. J., & Mruczek, M. F. (2007). Comparison of Friction Stir Weldments and Submerged Arc Weldments in HSLA-65 Steel. *Welding Journal*, *86*(7), 187s-195s.

Küçükömero, T., Aktarer, S. M., Güven, İ., & Çam, G. (2018). Microstructure and mechanical properties of friction-stir welded St52 steel joints. *International Journal of Minerals, Metallurgy and Materials*, *25*(12), 1457–1464.

Kumar, K., & Kailas, S. V. (2008). The role of friction stir welding tool on material flow and weld formation. *Materials Science and Engineering A*, *485*(1–2), 367–374.

Lakshminarayanan, A. K., Balasubramanian, V., & Salahuddin, M. (2010). Microstructure, tensile and impact toughness properties of friction stir welded mild steel. *Journal of Iron and Steel Research International*, *17*(10), 68–74.

Lemos, G. V. B., Hanke, S., Dos Santos, J. F., Bergmann, L., Reguly, A., & Strohaecker, T. R. (2017). Progress in friction stir welding of Ni alloys. *Science and Technology of Welding and Joining*, *22*(8), 643–657.

Lienert, T. J., Stellwag, JR., W. L., Grimmett, B. B., & Warke, R. W. (2003). Friction stir welding studies on mild steel. *Welding Journal-New York*, *82*(1), 1-S.

Liu, D., Cheng, B., & Luo, M. (2011). Microstructure And Impact Fracture Behaviour of HAZ of F460 Heavy Ship Plate With High Strength And Toughness. *Acta Metallurgica Sinica*, *47*(10), 1233–1240.

Liu, H. J., Feng, J. C., Fujii, H., & Nogi, K. (2005). Wear characteristics of a WC – Co tool in friction stir welding of AC4A C 30 vol % SiCp composite. *International Journal of Machine Tools and Manufacture*, *45*, 1635–1639.

Liu, X. C., & Wu, C. S. (2016). Elimination of tunnel defect in ultrasonic vibration enhanced friction stir welding. *Materials and Design*, *90*, 350–358.

Liu, Y., Wang, Z., Sun, Q., Yin, B., Cheng, J., Zhu, S., Yang, J., Qiao, Z., & Liu, W. (2018). Tribological behavior and wear mechanism of pure WC at wide range temperature from 25 to 800 °C in vacuum and air environment. *International Journal of Refractory Metals and Hard Materials*, *71*, 160–166.

Liu, Z., Ji, S., & Meng, X. (2018). Joining of magnesium and aluminum alloys via ultrasonic assisted friction stir welding at low temperature. *The International Journal of Advanced Manufacturing Technology*, *97*(9–12), 4127–4136.

Liu, Z. M., Cui, S. L., Luo, Z., Zhang, C. Z., Wang, Z. M., & Zhang, Y. C. (2016). Plasma arc welding: Process variants and its recent developments of sensing, controlling and modeling. *Journal of Manufacturing Processes*, *23*, 315–327.

Liu, Zhenlei, Meng, X., Ji, S., Li, Z., & Wang, L. (2018). Improving tensile properties of Al/Mg joint by smashing intermetallic compounds via ultrasonic-assisted stationary shoulder friction stir welding. *Journal of Manufacturing Processes*, *31*, 552–559.

Lofaj, F., & Kaganovskii, Y. S. (1995). Kinetics of WC-Co oxidation accompanied by swelling. *Journal of Materials Science*, *30*(7), 1811–1817.

Logan, B. P., Toumpis, A. I., Galloway, A. M., McPherson, N. A., & Hambling, S. J. (2016). Dissimilar friction stir welding of duplex stainless steel to low alloy structural steel. *Science and Technology of Welding and Joining*, *21*(1), 11–19.

Lv, X., Wu, C. S., Yang, C., & Padhy, G. K. (2018). Weld microstructure and mechanical properties in ultrasonic enhanced friction stir welding of Al alloy to Mg alloy. *Journal of Materials Processing Technology*, *254*, 145–157.

Manvatkar, V., De, A., Svensson, L. E., & DeBroy, T. (2015). Cooling rates and peak temperatures during friction stir welding of a high-carbon steel. *Scripta Materialia*, *94*, 36–39.

Mao, Y., Ke, L., Liu, F., Liu, Q., Huang, C., & Xing, L. (2014). Effect of tool pin eccentricity on microstructure and mechanical properties in friction stir welded 7075 aluminum alloy thick plate. *Materials and Design*, *62*, 334–343.

Matlan, M. J. B., Mohebbi, H., Pedapati, S. R., Awang, M. B., Ismail, M. C., Kakooei, S., & Dan, N. E. (2018). Dissimilar Friction Stir Welding of Carbon Steel and Stainless Steel : Some Observation on Microstructural Evolution and Stress Corrosion Cracking Performance. *Transactions of the Indian Institute of Metals*, *71*(10), 2553–2564.

Mehta, K. P., & Badheka, V. J. (2017). Hybrid approaches of assisted heating and cooling for friction stir welding of copper to aluminum joints. *Journal of*

Materials Processing Technology, *239*, 336–345.

Meran, C., & Canyurt, O. E. (2010). Friction Stir Welding of austenitic stainless steels. *Journal of Achievements in Materials and Manufacturing Engineering*, *43*(1), 432–439.

Merklein, M., & Giera, A. (2008). Laser assisted Friction Stir Welding of drawable steel-aluminium tailored hybrids. *International Journal of Material Forming*, *1*(1), 1299–1302.

Meshram et al., 2013. (2013). Friction stir welding of maraging steel (Grade-250). *Materials & Design*, *49*, 58–64.

Micallef, D., Camilleri, D., & Mollicone, P. (2013). Simplified Thermo-Elastoplastic Numerical Modelling Techniques Applied to Friction Stir Welding of Mild Steel. *In ASME International Mechanical Engineering Congress and Exposition(Vol. 56185, p. V02AT02A094). American Society of Mechanical Engineers.*

Miles, M. P., Nelson, T. W., Steel, R., Olsen, E., & Gallagher, M. (2009). Effect of friction stir welding conditions on properties and microstructures of high strength automotive steel. *Science and Technology of Welding and Joining*, *14*(3), 228–232.

Miles, M. P., Pew, J., Nelson, T. W., & Li, M. (2006). Comparison of formability of friction stir welded and laser welded dual phase 590 steel sheets. *Science and Technology of Welding and Joining*, *11*(4), 384–388.

Miles, M. P., Ridges, C. S., Hovanski, Y., Peterson, J., Santella, M. L., & Steel, R. (2011). Impact of tool wear on joint strength in friction stir spot welding of DP 980 steel. *Science and Technology of Welding and Joining*, *16*(7), 642–647.

Mishra, R. S., & Ma, Z. Y. (2005). Friction stir welding and processing. *Materials Science and Engineering R: Reports*, *50*(1–2), 1–78.

Miyazawa, T., Iwamoto, Y., Maruko, T., & Fujii, H. (2011). Development of Ir based tool for friction stir welding of high temperature materials. *Science and Technology of Welding and Joining*, *16*(2), 188–192.

Mohan, D. G., & Gopi, S. (2018). Induction assisted friction stir welding : a review Induction assisted friction stir welding : a review. *Australian Journal of Mechanical Engineering*, *18*(1), 119–123.

Morisada, Y., Fujii, H., Kawahito, Y., Nakata, K., & Tanaka, M. (2011). Three-dimensional visualization of material flow during friction stir welding by two pairs of X-ray transmission systems. *Scripta Materialia*, *65*(12), 1085–1088.

Morisada, Yoshiaki, Imaizumi, T., Fujii, H., Matsushita, M., & Ikeda, R. (2014).

Three-Dimensional Visualization of Material Flow During Friction Stir Welding of Steel and Aluminum. *Journal of Materials Engineering and Performance*, *23*(11), 4143–4147.

Murr, L. E. (2010). A review of FSW research on dissimilar metal and alloy systems. *Journal of Materials Engineering and Performance*, *19*(8), 1071–1089.

Nandan, R., Debroy, T., & Bhadeshia, H. K. D. H. D. H. (2008). Recent Advances in Friction Stir Welding – Process, Weldment Structure and Properties. *Progress in Materials Science*, *53*(6), 980–1023.

Nandan, R., Roy, G. G., & Debroy, T. (2006). Numerical Simulation of Three-Dimensional Heat Transfer and Plastic Flow During Friction Stir Welding. *Metallurgical and Materials Transactions A*, *37*(4), 1247–1259.

Nandan, R., Roy, G. G., Lienert, T. J., & Debroy, T. (2007). Three-dimensional heat and material flow during friction stir welding of mild steel. *Acta Materialia*, *55*(3), 883–895.

Nandan, R., Roy, G. G., Lienert, T. J., & DebRoy, T. (2006). Numerical modelling of 3D plastic flow and heat transfer during friction stir welding of stainless steel. *Science and Technology of Welding and Joining*, *11*(5), 526–537.

Nathan, S. R. ., Malarvizhi, S., & Rao, A. G. (2015). Effect of welding processes on mechanical and microstructural characteristics of high strength low alloy naval grade steel joints. *Defence Technology, 11*(3), 308–317.

Nathan, S. R., Balasubramanian, V., Malarvizhi, S., & Rao, A. G. (2016a). An investigation on metallurgical characteristics of tungsten based tool materials used in friction stir welding of naval grade high strength low alloy steels. *International Journal of Refractory Metals and Hard Materials*, *56*, 18–26.

Nathan, S. R., Balasubramanian, V., Malarvizhi, S., & Rao, A. G. (2016b). Effect of Tool Shoulder Diameter on Stir Zone Characteristics of Friction Stir Welded HSLA Steel Joints. *Transactions of the Indian Institute of Metals*, *69*(10), 1861–1869.

Nelson, T. W., & Rose, S. A. (2016). Controlling hard zone formation in friction stir processed HSLA steel. *Journal of Materials Processing Technology*, *231*, 66–74.

Nemat-Nasser, S., & Guo, W. G. (2003). Thermomechanical response of DH-36 structural steel over a wide range of strain rates and temperatures. *Mechanics of Materials*, *35*(11), 1023–1047.

Neto, D. M., & Neto, P. (2013). Numerical modeling of friction stir welding process: A literature review. *International Journal of Advanced*

Manufacturing Technology, *65*(1–4), 115–126.

Ozekcin, A., Jin, H. W., Koo, J. Y., Bangaru, N. V., Ayer, R., Vaughn, G., Steel, R., & Packer, S. (2004). A microstructural study of friction stir welded joints of carbon steels. *International Journal of Offshore and Polar Engineering*, *14*(4), 284–288.

Padhy, G. K., Wu, C. S., & Gao, S. (2015). Auxiliary energy assisted friction stir welding – status review. *Science and Technology of Welding and Joining*, *20*(8), 631–649.

Padmanaban, R., Kishore, V. R., & Balusamy, V. (2014). Numerical Simulation of Temperature Distribution and Material Flow During Friction Stir Welding of Dissimilar Aluminum Alloys. *Procedia Engineering*, *97*, 854–863.

Pal, S., & Phaniraj, M. P. (2015). Determination of heat partition between tool and workpiece during FSW of SS304 using 3D CFD modeling. *Journal of Materials Processing Technology*, *222*, 280–286.

Park, H., Youn, H., Ryu, J., Son, H.-T., Bang, H., Shon, I., & Oh, I.-H. (2012). Fabrication and mechanical properties of WC-10 wt .% Co hard materials for a friction stir welding tool application by a spark plasma sintering process. *Journal of Ceramic Processing Research*, *13*(6), 705–712.

Park, K., Kim, B., & Ni, J. (2009). Numerical Simulation of Plunge Force During the Plunge Phase of Friction Stir Welding and Ultrasonic Assisted Fsw. *Proceedings of the ASME 2008 International Mechanical Engineering Congress and Exposition. Volume 4: Design and Manufacturing*, 1–6.

Pradeep, A., & Muthukumaran, S. (2015). Study of sub-shoulder tool wear on friction stir welded steel plates using two modes of metal transfer phenomenon. *The International Journal of Advanced Manufacturing Technology*, *84*(5–8), 1153–1162.

Pradeep, A., Muthukumaran, S., & Dhanush, P. R. (2013). Subshoulder formation during friction stir welding of steel using tungsten alloy tool. *Science and Technology of Welding and Joining*, *18*(8), 671–679.

Prasanna, P., Rao, B. S., & Rao, G. K. M. (2010). Finite element modeling for maximum temperature in friction stir welding and its validation. *The International Journal of Advanced Manufacturing TechnologyI*, *51*(9–12), 925–933.

Rahimi, S., Konkova, T. N., Violatos, I., & Baker, T. N. (2019). Evolution of Microstructure and Crystallographic Texture During Dissimilar Friction Stir Welding of Duplex Stainless Steel to Low Carbon-Manganese Structural Steel. *Metallurgical and Materials Transactions A*, *50*(2), 664–687.

Rai, R., De, A., Bhadeshia, H. K. D. H., & DebRoy, T. (2011). Review: friction stir welding tools. *Science and Technology of Welding and Joining*, *16*(4), 325–342.

Ramesh, R., Dinaharan, I., Kumar, R., & Akinlabi, E. T. (2017). Microstructure and mechanical characterization of friction stir welded high strength low alloy steels. *Materials Science and Engineering: A*, *687*, 39–46.

Reynolds, A. P. (2000). Visualisation of material flow in autogenous friction stir welds. *Science and Technology of Welding and Joining*, *5*(2), 120–124.

Reynolds, A. P., Tang, W., Posada, M., & Deloach, J. (2003). Friction stir welding of DH36 steel. *Science and Technology of Welding and Joining*, *8*(6), 455–460.

Sadeghian, B., Taherizadeh, A., & Atapour, M. (2018). Simulation of weld morphology during friction stir welding of aluminum- stainless steel joint. *Journal of Materials Processing Technology*, *259*(6), 96–108.

Saeid, T., Abdollah-zadeh, A., Assadi, H., & Malek Ghaini, F. (2008). Effect of friction stir welding speed on the microstructure and mechanical properties of a duplex stainless steel. *Materials Science and Engineering A*, *496*(1–2), 262–268.

Sampath, K. (2006). An understanding of HSLA-65 plate steels. *Journal of Materials Engineering and Performance*, *15*(1), 32–40.

Sato, Y. S., Arkom, P., Kokawa, H., Nelson, T. W., & Steel, R. J. (2008). Effect of microstructure on properties of friction stir welded Inconel Alloy 600. *Materials Science and Engineering A*, *477*(1–2), 250–258.

Sato, Y. S., Yamanoi, H., Kokawa, H., & Furuhara, T. (2007). Microstructural evolution of ultrahigh carbon steel during friction stir welding. *Scripta Materialia*, *57*(6), 557–560.

Schmidt, H., & Hattel, J. (2004). A local model for the thermomechanical conditions in friction stir welding. *Modelling and Simulation in Materials Science and Engineering*, *13*(1), 77–93.

Schmidt, H., & Hattel, J. (2005). Modelling heat flow around tool probe in friction stir welding. *Science and Technology of Welding and Joining*, *10*(2), 176–186.

Scutelnicu, E., Birsan, D. A. N., & Cojocaru, R. (2011). Research on Friction Stir Welding and Tungsten Inert Gas assisted Friction Stir Welding of Copper. *Recent Advances in Manufacturing Engineering*, *1*, 97–102.

Seidel, T. U., & Reynolds, A. P. (2003). Two-dimensional friction stir welding process model based on fluid mechanics. *Science and Technology of Welding and Joining*, *8*(3), 175–183.

Sekban, D. M., Aktarer, S. M., Xue, P., Ma, Z. Y., & Purcek, G. (2016). Impact toughness of friction stir processed low carbon steel used in shipbuilding. *Materials Science and Engineering: A*, *672*, 40–48.

Sellars, C. M., & Tegart, W. J. M. (1972). Hot Workability. *International Metallurgical Reviews*, *17*(1), 1–24.

Selvaraj, M. ., Murali, V. ., & Rao, S. R. K. . (2013). Thermal model for friction stir welding of mild steel. *Multidiscipline Modeling in Materials and Structures*, *9*(1), 49–61.

Sharma, G., & Dwivedi, D. K. (2017a). Structure and Properties of Friction Stir Weld Joints of Structural Steel. *Transactions of the Indian Institute of Metals*, *70*(1), 201–208.

Sharma, G., & Dwivedi, D. K. (2017b). Study on microstructure and mechanical properties of dissimilar steel joint developed using friction stir welding. *The International Journal of Advanced Manufacturing Technology*, *88*(5–8), 1299–1307.

Sheppard, T., & Wright, D. S. (1979). Determination of flow stress: Part 1 constitutive equation for aluminium alloys at elevated temperatures. *Metals Technology*, *6*(1), 215–223.

Shi, L., Wu, C. S., & Liu, H. J. (2014). Modeling the material flow and heat transfer in reverse dual-rotation friction stir welding. *Journal of Materials Engineering and Performance*, *23*(8), 2918–2929.

Shi, L., Wu, C. S., & Liu, X. C. (2015). Modeling the effects of ultrasonic vibration on friction stir welding. *Journal of Materials Processing Technology*, *222*, 91–102.

Shi, L., Wu, C. S., & Sun, Z. (2018). An integrated model for analysing the effects of ultrasonic vibration on tool torque and thermal processes in friction stir welding. *Science and Technology of Welding and Joining*, *23*(5), 365–379.

Shindo, D. J., Rivera, A. R., & Murr, L. E. (2002). Shape optimization for tool wear in the friction-stir welding of cast AI359-20 % SiC MMC. *Journal of Materials Science*, *37*(23), 4999–5005.

Siddiquee, A. N., & Pandey, S. (2014). Experimental investigation on deformation and wear of WC tool during friction stir welding (FSW) of stainless steel. *International Journal of Advanced Manufacturing Technology*, *73*(1–4), 479–486.

Sinclair, P. C., Longhurst, W. R., Cox, C. D., Lammlein, D. H., Strauss, A. M., & Cook, G. E. (2010). Heated Friction Stir Welding: An Experimental and Theoretical Investigation into How Preheating Influences Process Forces. *Materials and Manufacturing Processes*, *25*(11), 1283–1291.

Singh, D. K., Sahoo, G., Basu, R., Sharma, V., & Mohtadi-Bonab, M. A. (2018). Investigation on the microstructure—mechanical property correlation in dissimilar steel welds of stainless steel SS 304 and medium carbon steel EN 8. *Journal of Manufacturing Processes*, *36*, 281–292.

Song, K. H., & Nakata, K. (2010). Effect of precipitation on post-heat-treated Inconel 625 alloy after friction stir welding. *Materials and Design*, *31*(6), 2942–2947.

Song, K. H., Tsumura, T., & Nakata, K. (2009). Development of Microstructure and Mechanical Properties in Laser-FSW Hybrid Welded Inconel 600. *Materials Transactions*, *50*(7), 1832–1837.

Song, M., & Kovacevic, R. (2003). Thermal modeling of friction stir welding in a moving coordinate system and its validation. *International Journal of Machine Tools & Manufacture*, *43*(6), 605–615.

Sorger, G., Lehtimäki, E., Hurme, S., Remes, H., Molter, L., Vilaça, P., & Molter, L. (2017). Microstructure and fatigue properties of friction stir welded high-strength steel plates. *Science and Technology of Welding and Joining*, *23*(5), 380–386.

Steuwer, A., Barnes, S. J., Altenkirch, J., Johnson, R., & Withers, P. J. (2012). Friction Stir Welding of HSLA-65 Steel: Part II. The Influence of Weld Speed and Tool Material on the Residual Stress Distribution and Tool Wear. *Metallurgical and Materials Transactions A*, *43*(7), 2356–2365.

Stevenson, R., Toumpis, A., & Galloway, A. (2015). Defect tolerance of friction stir welds in DH36 steel. *Materials and Design*, *87*, 701–711.

Sun, Y. F., Konishi, Y., Kamai, M., & Fujii, H. (2013). Microstructure and mechanical properties of S45C steel prepared by laser-assisted friction stir welding. *Materials and Design*, *47*, 842–849.

Sun, Y. F., Shen, J. M., Morisada, Y., & Fujii, H. (2014). Spot friction stir welding of low carbon steel plates preheated by high frequency induction. *Materials and Design*, *54*, 450–457.

Sun, Z., & Wu, C. S. (2020). Influence of tool thread pitch on material flow and thermal process in friction stir welding. *Journal of Materials Processing Technology*, *275*, 116281.

Sundqvist, J., Kim, K. H., Bang, H. S., Bang, H. S., & Kaplan, A. F. H. (2017). Numerical simulation of laser preheating of friction stir welding of dissimilar metals. *Science and Technology of Welding and Joining*, *23*(4), 351–356.

Tarasov, S. Y., Rubtsov, V. E., & Kolubaev, E. A. (2014). A proposed diffusion-controlled wear mechanism of alloy steel friction stir welding (FSW) tools used on an aluminum alloy. *Wear*, *318*(1–2), 130–134.

Tello, K. E., Gerlich, A. P., & Mendez, P. F. (2010). Constants for hot deformation constitutive models for recent experimental data. *Science and Technology of Welding and Joining*, *15*(3), 260–266.

Thakur, D., Ramamoorthy, B., & Vijayaraghavan, L. (2008). Influence of different post treatments on tungsten carbide-cobalt inserts. *Materials Letters*, *62*(28), 4403–4406.

Thomä, M., Wagner, G., Straß, B., Conrad, C., Wolter, B., Benfer, S., & Fürbeth, W. (2016). Recent Developments for Ultrasonic-Assisted Friction Stir Welding: Joining, Testing, Corrosion - an Overview. *IOP Conference Series: Materials Science and Engineering*, *118*(March), 8.

Thomas, W. M., Threadgill, P. L., & Nicholas, E. D. (1999). Feasibility of friction stir welding steel. *Science and Technology of Welding and Joining*, *4*(6), 365–372.

Thomas, W. M., Wiesner, C. S., Marks, D. J., & Staines, D. G. (2009). Conventional and bobbin friction stir welding of 12% chromium alloy steel using composite refractory tool materials. *Science and Technology of Welding and Joining*, *14*(3), 247–253.

Thompson, B., & Babu, S. S. (2010). Tool Degradation Characterization in the Friction Stir Welding of Hard Metals. *Welding Journal*, *89*(12), 256s-261s.

Tingey, C., Galloway, A., Toumpis, A., & Cater, S. (2015). Effect of tool centreline deviation on the mechanical properties of friction stir welded DH36 steel. *Materials and Design*, *65*, 896–906.

Tiwari, A., Pankaj, P., Bharadwaj, A., Singh, P., Biswas, P., & Kore, S. D. (2019). Friction Stir Welding of Shipbuilding Grade DH36 Steel. In A.-B. N. (eds) Sharma V., Dixit U. (Ed.), *Manufacturing Engineering*. (pp. 17–34). Singapore:Springer .

Tiwari, A., Pankaj, P., Biswas, P., Kore, S. D., & Rao, A. G. (2019). Tool performance evaluation of friction stir welded Shipbuilding grade DH36 steel butt joints. *The International Journal of Advanced Manufacturing Technology*, *33*(10), 4931–4938.

Tiwari, A., Pankaj, P., Suman, S., & Biswas, P. (2020). CFD Modelling of Temperature Distribution and Material Flow Investigation During FSW of DH36 Shipbuilding Grade Steel. *Transactions of the Indian Institute of Metals*, *73*(9), 2291–2307.

Tiwari, A., Singh, P., Biswas, P., & Kore, S. D. (2019). Friction Stir Welding of Low-Carbon Steel. In P. Sahoo & J. P. Davim (Eds.), *Advances in Materials, Mechanical and Industrial Engineering* (pp. 209–226). Cham:Springer.

Tiwari, A., Singh, P., Pankaj, P., Biswas, P., & Kore, S. D. (2019). FSW of low carbon steel using tungsten carbide (WC-10wt .% Co) based tool material. *Journal of Mechanical Science and Technology*, *33*(10), 4931–4938.

Tiwari, A., Singh, P., Pankaj, P., Biswas, P., Kore, S. D., & Pal, S. (2019). Effect of Tool Offset and Rotational Speed in Dissimilar Friction Stir Welding of AISI 304 Stainless Steel and Mild. *Journal of Materials Engineering and Performance*, *28*(10), 6365–6379.

Toumpis, A., Galloway, A., Cater, S., & McPherson, N. (2014). Development of a process envelope for friction stir welding of DH36 steel - A step change. *Materials and Design (1980-2015)*, *62*, 64–75.

Toumpis, A. I., Galloway, A. M., Arbaoui, L., & Poletz, N. (2014). Thermomechanical deformation behaviour of DH36 steel during friction stir welding by experimental validation and modelling. *Science and Technology of Welding and Joining*, *19*(8), 653–663.

Tribe, A., & Nelson, T. W. (2015). Study on the fracture toughness of friction stir welded API X80. *Engineering Fracture Mechanics*, *150*, 58–69.

Trinh, D., Frappart, S., Rückert, G., & Cortial, F. (2019). Effect of friction stir welding process on microstructural characteristics and corrosion properties of steels for naval applications. *Corrosion Engineering, Science and Technology*, *54*(4), 353–361.

Ueji, R., Fujii, H., Cui, L., Nishioka, A., Kunishige, K., & Nogi, K. (2006). Friction stir welding of ultrafine grained plain low-carbon steel formed by the martensite process. *Materials Science and Engineering A*, *423*(1–2), 324–330.

Ulysse, P. (2002). Three-dimensional modeling of the friction stir-welding process. *International Journal of Machine Tools and Manufacture*, *42*(14), 1549–1557.

Vashishtha, H., Taiwade, R. V., Sharma, S., & Patil, A. P. (2017). Effect of welding processes on microstructural and mechanical properties of dissimilar weldments between conventional austenitic and high nitrogen austenitic stainless steels. *Journal of Manufacturing Processes*, *25*, 49–59.

Wan, L., Huang, Y., Guo, W., Lv, S., & Feng, J. (2014). Mechanical Properties and Microstructure of 6082-T6 Aluminum Alloy Joints by Self-support Friction Stir Welding. *Journal of Materials Science and Technology*, *30*(12), 1243–1250.

Wang, H., Wang, K., Wang, W., Huang, L., Peng, P., & Yu, H. (2019). Microstructure and mechanical properties of dissimilar friction stir welded type 304 austenitic stainless steel to Q235 low carbon steel. *Materials Characterization*, *155*, 109803.

Wang, J., Su, J., Mishra, R. S., Xu, R., & Baumann, J. A. (2014). Tool wear mechanisms in friction stir welding of Ti – 6Al – 4V alloy. *Wear*, *321*, 25–32.

Warren, A., Nylund, A., & Olefjord, I. (1996). Oxidation of tungsten and tungsten carbide in dry and humid atmospheres. *International Journal of Refractory Metals and Hard Materials*, *14*(5–6), 345–353.

Wei, L., & Nelson, T. W. (2012). Influence of heat input on post weld microstructure and mechanical properties of friction stir welded HSLA-65 steel. *Materials Science and Engineering A*, *556*, 51–59.

Wen, C., Wang, Z., Deng, X., Wang, G., & Misra, R. D. K. (2018). Effect of Heat Input on the Microstructure and Mechanical Properties of Low Alloy Ultra-High Strength Structural Steel Welded Joint. *Steel Research International*, *89*(6), 1700500.

Yaduwanshi, D. K:, Bag, S., & Pal, S. (2015). Heat transfer analyses in friction stir welding of aluminium alloy. *Proc IMechE Part B: J Engineering Manufacture*, *229*(10), 1722–1733.

Yaduwanshi, D. K., Bag, S., & Pal, S. (2014). Effect of Preheating in Hybrid Friction Stir Welding of Aluminum Alloy. *Journal of Materials Engineering and Performance*, *23*(10), 3794–3803.

Yaduwanshi, D. K., Bag, S., & Pal, S. (2017). On the effect of tool offset in hybrid-FSW of copper-aluminium alloy. *Materials and Manufacturing Processes*, *33*(3), 277–287.

Yaduwanshi, D. K, Bag, S., & Pal, S. (2016). Numerical modeling and experimental investigation on plasma-assisted hybrid friction stir welding of dissimilar materials. *Materials and Design*, *92*, 166–183.

Yang, W., Shi, X., Wei, B., Duan, S., & Guo, H. (2019). Effect of sulphur content on precipitates and properties of DH36 structural steel. *Ironmaking & Steelmaking*, *46*(6), 550–556.

Yu, Z., Feng, Z., Hoelzer, D., Tan, L., & Sokolov, M. A. (2015). Friction Stir Welding of ODS and RAFM Steels. *Metallurgical and Materials Transactions E*, *2*(3), 164–172.

Zandsalimi, S., Heidarzadeh, A., & Saeid, T. (2018). Dissimilar friction-stir welding of 430 stainless steel and 6061 aluminum alloy: Microstructure and mechanical properties of the joints. *Proceedings of the Institution of Mechanical Engineers, Part L: Journal of Materials: Design and Applications*, *233*(9), 1791–1801.

Zhang, H., Zhang, Z., Chen, J. (2007). 3D modeling of material flow in friction stir welding under different process parameters. *Journal of Materials*

Processing and Technology, *183*(1), 62–70.

Zhang, Q. L., Yang, C. L., Lin, S. B., & Fan, C. L. (2014). Horizontal welding of aluminium alloys by soft plasma arc. *Proceedings of the Institution of Mechanical Engineers, Part B: Journal of Engineering Manufacture*, *228*(11), 1481–1490.

Zhang, Y. N., Cao, X., Larose, S., & Wanjara, P. (2012). Review of tools for friction stir welding and processing. *Canadian Metallurgical Quarterly*, *51*(3), 250–261.

Zhong, Y. B., Wu, C. S., & Padhy, G. K. (2017). Effect of ultrasonic vibration on welding load, temperature and material flow in friction stir welding. *Journal of Materials Processing Technology*, *239*, 273–283.

Zhou, L., Zhang, R. X., Li, G. H., Zhou, W. L., Huang, Y. X., & Song, X. G. (2018). Effect of pin profile on microstructure and mechanical properties of friction stir spot welded Al-Cu dissimilar metals. *Journal of Manufacturing Processes*, *36*, 1–9.

Zhu, X. K., & Chao, Y. J. (2004). Numerical simulation of transient temperature and residual stresses in friction stir welding of 304L stainless steel. *Journal of Materials Processing Technology*, *146*(2), 263–272.

:-------------------*-------------------*---------------------:

Appendix A

A.1 FSW MACHINE SPECIFICATIONS

Spindle	BT 40
FSW tool holder	BT 40 Arbor
Spindle motor	20 HP/440V
Feed motor	3 HP 960 RPM
Z axis thrust	6500 kgf/65kN (max.) (adjustable in steps of 100 kgf)
Feed motor	3HP – preferably 960 RPM
Feed Requirements:	
Quill stroke	100 mm by hydraulic pressure
X axis stroke	1000 mm (feed rate 20 − 300)
X axis feed	23-300 minimum 15−18 levels
Y axis stroke	200 mm/manual
Z axis stroke	300 mm (feed rate 2 mm −50 mm) 18 steps
Table size	1800 × 400 mm
Table surface	′T' Slot as per standard
Hydraulic System	
Hydraulic power pack motor	Minimum 5HP/440V
Hydraulic tank capacity	100 ltrs
Hydraulic oil	ISO 68

Lubrication System	
Lubrication	Centralized lubrication system
Lubrication oil	SAE40
Vibration	Anti-vibration pad

A.2 MACHINE’S SPECIFICATIONS USED FOR CHARACTERIZATION

Machine Name	Make and Model	Specifications
Dynamic UTM	Instron, UK	• Hydraulic power pack pumping capacity 25ltr/min • Testing Method: Load control and position control (strain and displacement)
Micro hardness tester	Make: Buehler, Model:Micrometer-2101	• Indentation force 50,100,300,500,2000 gF • Dwell time:5 to 60 s at interval of 60s
Drop weight impact tester	Make: IEICOS, Model: IDWITM	• Impact energy scale:30−120 Joules • Height of impact: 0.3 −1.7 m • CNC controlled with data acquisition system • Test: Impact energy, impact force
Stereomicroscope	Make: Nikon, Model:SMZ25	• Zoom ratio:25: 1 • Magnification range:0.63X −15.75X • Motorized zoom • Zooming observation: BF/DF/FL/Simple polarizing
Optical microscope	Make: Carl Zeiss, Model: Axiotech-100HD, 3D	• Magnification: 50X−5000X • Table movement: 3 −axis measuring system, reflecting light measuring step 75 mm ×55 mm ×50 mm • Lens: Binocular photo type, 20°/23 • Camera: Axio-Cam and Axiovision 4.8.2 software (in built)
Field emission scanning electron microscope (FESEM)	Make: Zeiss, Model: Sigma	• Specimen chamber : 330 mm inner dia, 270 mm height • Specimen weight: upto 0.5 kg tilted; up to 2kg not tilted • Movement: $\frac{X}{Y}$ =125 mm, Z =50 mm, T = −10° to 360°, R = 360° continues • Specimen stage: 5 axis motorized cartesian
Infrared (IR) camera	Make: INFRATECH, Model: Variocam-hr − 400	• Frequency range:1−8 Hz • Emissivity range:0.01−1

XRD	PANalytical, X-pert	• 3 kW generator and direct optical positioning • Pre-FIX incident and diffracted beam • X ray lens with attenuator, fixed divergence slits 1/32° • High resolution goniometer with optically encoded sample positioning enables a minimum step of 0.0001°

Appendix B

B.1 LIST OF PARAMETERS USED IN THE SIMULATION

N (MPa)	$(\text{Axial force})/\pi \cdot \text{R}_1$
Tool material	$\text{WC} - 10\ \text{wt.}\ \%\ \text{Co}$
Density of tool material (kg/m^3)	19400
R_s (mm)	12.5
R_p (mm)	3.5-2.5
Pin length(mm)	3.4
Work piece density (kg/m^3)	7860
Workpiece material	DH36 steel
Workpiece thickness (mm)	4
Workpiece length (mm)	200
Workpiece width (mm)	100
Rotational speed (rpm)	600, 450, 300
Welding speed (mm/s)	1, 1.5, 2
A_e, material constant (s^{-1})	2.36e^{13}
α_mat, material constant (MPa^{-1})	1.76e^{-8}
n_mat ,material constant	4.32

(R_g), Universal gas constant ($JK^{-1}mol^{-1}$)	8.314
Q, Activation energy (kJ/mol)	371
μ_0	0.3
μ_f	0.3-0.12
δ_o	0.4
λ	0.405
η_{mech}	0.4
ε	0.26
h_b (W/m^2 K)	2000
h_s (W/m^2 K)	175
h_t (W/m^2 K)	30

B.2 AN ANALYTICAL MODEL FOR THE HEAT GENERATION IN THE TAPERED PIN PROFILE FSW TOOL

An analytical expression for the heat generation equations for the tapered pin profile are formulated. This includes heat generation contributions from specific tool surfaces i.e. shoulder surface (SS), pin bottom surface (PBS) and pin side surface (PSS).

(i) Heat generation at shoulder workpiece interface (Q_{ss})

(ii) Heat generation at pin bottom interface(Q_{pb})

(iii) Heat generation at pin taper interface (Q_{pt})

The total heat generation by the FSW tool can expressed as

$$Q_T = Q_{ss} + Q_{pb} + Q_{pt} \tag{B2.1}$$

Heat generation at shoulder workpiece interface

During FSW process, the tool workpiece interface is defined as the heat source, and it contains three parts: shoulder surface (ss), pin side surface (pt) and pin bottom surface(pb). In present case, a tool with flat cylindrical shoulder surface and a tapered pin profile is selected. The heat generated at tool work interface i.e. tool shoulder, taper pin and the pin is calculated. Figure B1 shows the schematic diagram for the calculation of heat generation at the tool workpiece interface. T and H is the thickness of the workpiece material and the tool pin length respectively. N is the normal reaction force at contact surface as shown in Figure B1. R_1 R_2 and R_3 are the radii at the tool shoulder, pin radius at the shoulder surface and pin radius at the free end respectively. The tapered angle of the tool pin is assumed as α_l. On the flat shoulder surface an infinitesimal small element δr is taken at a radial distance r from the tool center as shown in Figure B1 (b). Similarly, an infinitesimal small element δh is considered at a distance of h mm from shoulder surface as depicted in Figure B1(c).

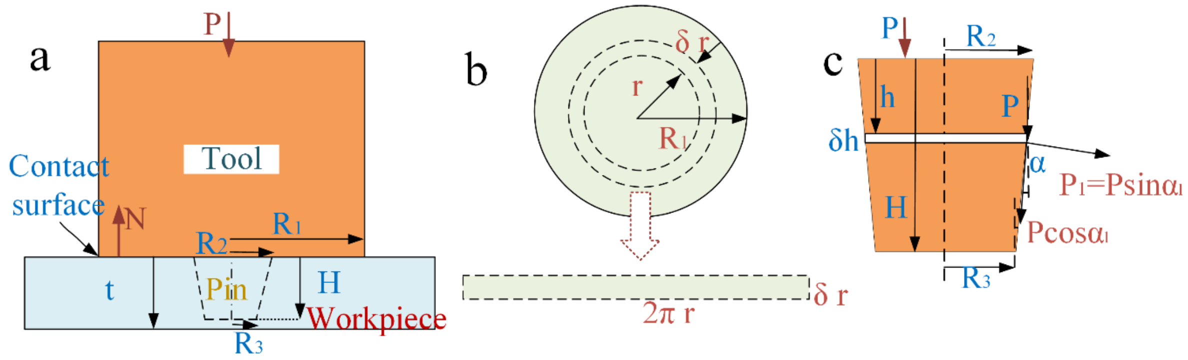

Figure. B1 Heat generation at tool work contact interface: (a) cylindrical shoulder with tapered tool pin, (b) elementary area on the tool shoulder for heat generation calculation, and (c) elementary area on the tool taper surface for heat generation calculation

The thickness of the elemental area is δr. Hence, the area of elemental ring can be written as

$$\delta A = 2\pi r\delta r \qquad \mathbf{(B2.2)}$$

The normal force acting on the elemental ring δA area is given as

$$\delta N = P2\pi r\delta r \qquad (\boldsymbol{B2.3})$$

Consider μ be the coefficient of friction between shoulder workpiece interfaces, for this condition the frictional force can be written as

$$\delta F = \mu P2\pi r\delta r \qquad \mathbf{(B2.4)}$$

The heat generated in the elemental ring area

$$\delta Q = \mu P 2\pi r \delta r \omega r \qquad (\boldsymbol{B2.5})$$

Integrating both sides

$$\int_{R_2}^{R_1} \delta Q = 2\pi\mu\omega P \int_{R_2}^{R_1} r^2\, \delta r \qquad (\boldsymbol{B2.6})$$

The final expression for the heat generation at the shoulder contact

$$Q_s = \frac{2}{3}\pi\mu\omega P({R_1}^3 - {R_2}^3) \qquad (\boldsymbol{B2.7})$$

The yield shear stress τ_{yield} is estimated to be $\frac{\sigma_{yield}}{\sqrt{3}}$, where σ_{yield} is yield strength of the material. Considering the sliding and sticking factor δ for heat generation where δ signifies the amount of sliding. The heat generated at tool work interface can be written as:

$$Q_{sf} = Q_{sl} + (1-\delta)Q_{st} \qquad (\boldsymbol{B2.8})$$

The final expression for frictional heat generation at the tool work interface can be written as

$$Q_{ss} = [\delta\mu P + (1-\delta)\eta_{mech}\tau_{yield}]\frac{2}{3}\pi\omega({R_1}^3 - {R_2}^3) \qquad (\boldsymbol{B2.9})$$

This final expression can estimate the heat generation for $0 < \delta < 1$, corresponding to sliding when $\boldsymbol{\delta} = 0$, sticking when $\delta = 1$ and partial sliding/sticking when $0 < \delta < 1$.

Heat generation at tool pin bottom surface

Similarly the heat generation at the tool pin bottom interface can be described as

$$\delta Q = \mu P 2\pi r \delta r \omega r \qquad (\boldsymbol{B2.10})$$

Integrating both sides between the limits 0 to R_3

$$\int_{0}^{R_3} \delta Q = 2\pi\mu\omega P \int_{0}^{R_3} r^2\, \delta r \qquad (\boldsymbol{B2.11})$$

$$Q_{pb} = \frac{2}{3}\pi\mu\omega P({R_3}^3) \qquad (\boldsymbol{B2.12})$$

The yield shear stress τ_{yield} is estimated to be $\frac{\sigma_{yield}}{\sqrt{3}}$, where $\sigma_{\ yield}$ is yield strength of workpiece material. Considering extent of slip δ for heat generation the heat generation equation for pin bottom surface can be expressesd as

$$Q_{pb} = [\delta\mu P + (1-\delta)\eta_{mech}\tau_{yield}]\frac{2}{3}\pi\omega({R_3}^3) \qquad (\boldsymbol{B2.13})$$

Similary, the above mentioned expression can estimate the heat generation at pin bottom surface for $0 < \delta < 1$, corresponding to sliding when $\delta = 0$, sticking when $\delta = 1$ and partial sliding/sticking when $0 < \delta < 1$.

Heat generation at taper surface

At pin taper surface, both the friction and deformation are significant for heat generating. The heat generated at the pin tapered surface Q_{pt} is written as:

$$Q_{pt} = \delta\omega \int_0^H 2\pi(R_3 + htan\alpha_l)^2\,\pi_w dh\left({R_2}^3 - {R_3}^3\right) \qquad (\boldsymbol{B2.14})$$

$$+ (1-\delta)H\int_0^H \mu P_1 2\pi\,(R_3 + htan\alpha_l)^2\frac{dh}{cos\alpha_l}$$

$$Q_{pt} = \frac{2\delta\pi\omega\eta_{mech}\tau_{yield}}{3tan\alpha_l}\left({R_2}^3 - {R_3}^3\right) + \frac{2}{3}(1-\delta)\frac{\pi\mu P_1\omega}{sin\alpha_l}({R_2}^3 - {R_3}^3) \qquad (\boldsymbol{B2.15})$$

where δ is the contact state variable; H is the tool pin height; h is the height variable and α_l is the conic angle; P_1 is measured approximately equal to the plunge pressure P.

--------------------*--------------------*----------------------:

LIST OF PUBLICATIONS

International SCI Journal Publication (Published/Accepted)

- **Tiwari, A.,** Singh, P., Pankaj, P., Biswas, P., & Kore, S. D. (2019). FSW of low carbon steel using tungsten carbide ($WC-10wt.\%\,Co$) based tool material. Journal of Mechanical Science and Technology, 33(10), 4931-4938.
- **Tiwari, A.,** Singh, P., Pankaj, P., Biswas, P., Kore, S. D., & Pal, S. (2019). Effect of tool offset and rotational speed in dissimilar friction stir welding of $AISI$ 304 stainless steel and mild steel. Journal of Materials Engineering and Performance, 28(10), 6365-6379.
- **Tiwari, A.,** Pankaj, P., Suman, S., & Biswas, P. (2020). CFD Modelling of Temperature Distribution and Material Flow Investigation during FSW of $DH36$ Shipbuilding Grade Steel. Transactions of the Indian Institute of Metals, 73(9), 2291-2307.
- **Tiwari**, **A**., Pankaj, P., Biswas, P., Kore, S. D., & Rao, A. G. (2019). Tool performance evaluation of friction stir welded shipbuilding grade $DH36$ steel butt joints. The International Journal of Advanced Manufacturing Technology, 103(5-8), 1989-2005.
- **Tiwari, A.,** Pankaj, P., Suman, S., Singh, P., Biswas, P., Pal, S., & Rao, A. G. (2021). Effect of plasma preheating on weld quality and tool life during friction stir welding of DH36 steel. Proceedings of the Institution of Mechanical Engineers, Part B: Journal of Engineering Manufacture, 0954405421990139.

Book Chapters/Procedia (Published/Accepted)

- **Tiwari, A.,** Singh, P., Biswas, P., & Kore, S. D. (2018, January). Friction stir welding of low-carbon steel. In *International Conference on Mechanical Engineering* (pp. 209-226). Springer, Cham.
- **Tiwari, A.,** Pankaj, P., Bharadwaj, A., Singh, P., Biswas, P., & Kore, S. D. (2019). Friction stir welding of shipbuilding grade DH36 steel. In *Manufacturing Engineering* (pp. 17-34). Springer, Singapore.

List of International conferences

- Tiwari A., Pankaj P., Singh P., Biswas P., “Effect of Heat Input And Cooling Rate On Mechanical Properties And Microstructural Evolution In Friction Stir Welding Of DH36 Steel In Naval Application”, International Conference on Advanced Materials and Processes for Defence Applications (ADMAT 2019), Hyderabad, October 23-25, 2019.

- Tiwari A., Singh P., Biswas P., Kore S.D., “Effect of traverse speed in FSW of AISI 1006 steel” International Congress 2017 of the International Institute of Welding, Chennai, December 07-09, 2017.
- Tiwari A., Singh P., Biswas P., Kore S.D, “Feasibility studies in FSW of low carbon steel” INCOM18: Proceedings of the 1st International Conference on Mechanical Engineering Jadavpur University, Kolkata, January 4 – 6, 2018.
- Tiwari A., Pankaj P., Singh P., Biswas P., Kore S.D, Weld joint quality evaluation in FSW of shipbuilding grade DH36steel” Vth International Conference on Production and Industrial Engineering, CPIE-2018, Bangkok, Thailand, June 26-29, 2018.

:-------------------*--------------------*----------------------: